

UNIVERSITY OF SOUTHAMPTON

Faculty of Social Sciences
School of Mathematical Sciences

**Modelling the Impedance Response of
Perovskite Solar Cells**

by

Laurence John Bennett

ORCID: 0000-0002-0152-1401

*A thesis for the degree of
Doctor of Philosophy*

June 2022

University of Southampton

Abstract

Faculty of Social Sciences
School of Mathematical Sciences

Doctor of Philosophy

Modelling the Impedance Response of Perovskite Solar Cells

by Laurence John Bennett

Perovskite solar cells (PSCs) are a promising new photovoltaic technology that have the potential to provide low-cost renewable energy on a global scale. Whilst significant problems, particularly in terms of stability and toxicity, remain to be overcome before this technology can be exploited on a wide scale, the full potential of PSCs cannot be reached without a correct description of their fundamental workings. Impedance spectroscopy (IS) is a simple and powerful technique that can be used to probe the fundamental properties and behaviour of PSCs both in situ and in the lab. As such, it can be used to assess changes in device behaviour associated with degradation. However, the results obtained using this technique are poorly understood because of the additional complexity of device behaviour that ensues from ion motion in the perovskite.

In this thesis, a method of simulating impedance spectroscopy measurements is developed based on a drift-diffusion modelling approach, that includes the effects of both mobile ions and charge carriers. The impedance simulations reproduce the features and trends observed in experiment, enhancing our understanding of their physical origin. Systematic asymptotic methods are applied to the drift-diffusion model and used to obtain an analytic simplified model of the impedance response of a PSC. This analytic model consists of simple relations for the key features of impedance spectra of a PSC. Excellent agreement is demonstrated between the analytic model and the more complex drift-diffusion model from which it is derived, in a regime where the applied voltage is close to the open-circuit voltage, including the maximum power point. This analytic model is compared to the impedance response of an RC - RC circuit and is used to derive expressions for resistances and capacitances of the cell in terms of physical parameters in the drift-diffusion model. It is found that the shape of the impedance spectra obtained near open-circuit can be related to the dominant source of recombination loss in the cell.

An ideality factor (termed the *electronic* ideality factor) n_{el} is identified that can be obtained through measurements of the high frequency impedance. Unlike the standard ‘ideality factor’ that is typically measured and misinterpreted, n_{el} is not dependent on the ionic properties of the cell and serves as an analogue for the ideality factor in conventional solar cells in which mobile ions are absent. Determination of the electronic ideality factor allows the dominant recombination mechanism within the PSC to be identified. The methods developed in this thesis to interpret impedance spectra provide much needed insight into the impedance response of PSCs and allow physical parameters to be extracted from the data. This enables researchers to more effectively employ IS, characterise key properties and identify losses, helping to develop more efficient and stable PSCs.

Contents

List of Publications	ix
List of Figures	xi
List of Tables	xiii
Declaration of Authorship	xv
Acknowledgements	xvii
Nomenclature	xix
1 Introduction	1
1.1 Thesis motivation	1
1.2 Thesis overview	2
1.3 Contributions	2
2 Perovskite solar cells	5
2.1 Background and theory	5
2.2 Challenges	9
2.2.1 Stability and environmental impact	9
2.2.2 Ionic motion	11
2.3 Summary	15
3 Impedance spectroscopy and the ideality factor	17
3.1 The ideality factor and PSCs	17
3.2 IS background and theory	21
3.3 Equivalent circuit models	23
3.4 Impedance spectra of PSCs	27
3.4.1 High frequency feature	29
3.4.2 Low frequency feature	30
3.4.3 Intermediate frequency features	31
3.4.4 Trends of the low and high frequency features	33
3.5 Prominent models	33
3.6 Summary	38
4 IS modelling and results	41
4.1 The drift-diffusion equations for PSC modelling	42
4.2 Numerical solution	50

4.2.1	IonMonger IS module	51
4.3	Results and comparison to experiment	54
4.3.1	DC voltage	56
4.3.2	Illumination	59
4.3.3	Reproducing experimental spectra using the IS module	63
4.4	Understanding the impedance response	66
4.4.1	Ultra-low frequency regime	67
4.4.2	Intermediate frequency regime	70
4.4.3	Ultra-high frequency regime	73
4.4.4	Low frequency feature	74
4.4.5	High frequency feature	75
4.5	Conclusion	76
5	Deriving an analytic model for IS simulation	79
5.1	The surface polarisation model	80
5.1.1	Model description	80
5.1.2	Drift-diffusion equations within the surface polarisation model	84
5.1.3	The total current	86
5.1.4	Summary of the surface polarisation model	87
5.2	Boltzmann approximation to the carrier densities	87
5.3	Recombination current	92
5.4	Linearisation and impedance spectroscopy	97
5.4.1	Impedance parameters	100
5.4.2	Resistances, capacitances, and an RC - RC circuit	102
5.5	Summary	104
6	Analytic model results	107
6.1	Comparison between the analytic and numerical drift-diffusion models.	108
6.1.1	DC voltage and illumination	109
6.1.2	Recombination mechanisms	112
6.1.3	Analytic model accuracy	115
6.2	Qualitative behaviour of the IS response	116
6.2.1	High frequency feature	117
6.2.2	Low frequency feature	118
6.3	Ideality factors	121
6.3.1	Electronic ideality factor	121
6.3.2	The ectypal factor	123
6.3.3	Comparison between the ectypal and the electronic ideality factors	125
6.4	General recombination mechanisms	127
6.5	Conclusion	129
7	Summary and Conclusions	133
7.1	Further research	136
Appendix A	Multiple concurrent recombination mechanisms	139
Appendix A.1	The low and high frequency resistances and capacitances	139
Appendix A.2	The electronic ideality factor	140

References

143

List of Publications

1. W. Clarke, **L.J. Bennett**, Y. Grudeva, J.M. Foster, G. Richardson, and N. E. Courtier. IonMonger 2.0: Software for free, fast and versatile simulation of current, voltage and impedance response of planar perovskite solar cells. Work in preparation.
2. R. García-Rodríguez, A.J. Riquelme, M. Cowley, K. Valadez-Villalobos, G. Oskam, **L.J. Bennett**, M.J. Wolf, J.A. Anta, P.J. Cameron, and A.B. Walker. Inverted hysteresis in n-i-p and p-i-n perovskite solar cells. Under consideration for publication by *Energy Technology*.
3. A. Castro-Chong, A.J. Riquelme, T. Aernouts, **L.J. Bennett**, G. Richardson, G. Oskam, and J.A. Anta. Illumination intensity dependence of the recombination mechanism in mixed perovskite solar cells. *ChemPlusChem*, 86(9):1347-1356, 2021. [1]
4. **L.J. Bennett**, A.J. Riquelme, N.E. Courtier, J.A. Anta, and G. Richardson. A new ideality factor for perovskite solar cells and an analytical theory for their impedance spectroscopy response. *arXiv preprint. arXiv:2105.11226*, 2021. [2]
5. A.J. Riquelme, **L.J. Bennett**, N.E. Courtier, M.J. Wolf, L. Contreras-Bernal, A.B. Walker, G. Richardson, and J.A. Anta. Identification of recombination losses and charge collection efficiency in a perovskite solar cell by comparing impedance response to a drift-diffusion model. *Nanoscale*, 12(33):17385-17398, 2020. [3]

Conference Contributions

Poster presentation

- 1 **L.J. Bennett**, A.J. Riquelme, N.E. Courtier, J.A. Anta and, G. Richardson. The electronic ideality factor and the impedance response of perovskite solar cells. *CDT-PV Showcase*, September 2021.

Oral presentation

- 2 **L.J. Bennett**, A.J. Riquelme, N.E. Courtier, J.A. Anta and, G. Richardson. An analytic model that describes the impedance response of perovskite solar cells near open-circuit. *SIAM conference on mathematical aspects of materials science. Minisymposium on modelling and simulation of charge transport in perovskites*, May 2021.

Poster presentation

- 3 **L.J. Bennett**, A.J. Riquelme, N.E Courtier, M.J. Wolf, L. Contreras-Bernal, A.B. Walker, G. Richardson, and J.A. Anta. Modelling the impedance response of perovskite solar cells. *CDT-PV Winter Event*, February 2020.

Poster presentation

- 4 **L.J. Bennett**, N.E Courtier, and G. Richardson. Modelling the impedance response of perovskite solar cells. *Perovskite solar cells and optoelectronics conference*, October 2019.

List of Figures

2.1	Crystal structure of perovskite.	6
2.2	Architecture of a typical planar perovskite solar cell.	6
2.3	Scanning electron microscope image of a planar perovskite solar cell.	7
2.4	A current-voltage curve showing hysteresis.	12
2.5	A sketch to describe ionic vacancies.	13
3.1	Illustration of the potential distribution across a PSC.	20
3.2	Apparatus for an impedance spectroscopy measurement.	21
3.3	Applied voltage and current output during an impedance measurement.	22
3.4	Impedance spectrum for an RC element.	25
3.5	Three-dimensional frequency-Nyquist plot for a semicircular feature.	25
3.6	Nyquist and frequency plot for an impedance spectrum with two semicircular features.	26
3.7	Equivalent circuit diagrams for spectra with two semicircles.	27
3.8	Example of a Nyquist plot of a PSC impedance spectrum.	28
3.9	Frequency plot of a PSC impedance spectrum.	28
3.10	Example of PSC impedance spectra with negative LF features.	31
3.11	Examples of impedance spectra from PSCs that show exotic features.	32
3.12	Equivalent circuit model for the impedance response of a PSC proposed by Ghahremanirad <i>et al.</i>	37
4.1	Schematic showing the geometry of a PSC with generation and recombination.	43
4.2	Simulated Nyquist plot at three DC voltages.	56
4.3	Frequency plot showing R and X at three DC voltages.	57
4.4	Frequency plot showing $ Z $ and θ at three DC voltages.	58
4.5	Low and high frequency current response in time and as a Lissajous figure.	59
4.6	Nyquist plot of impedance spectra at different open-circuit voltages.	60
4.7	Frequency plots of impedance spectra at different open-circuit voltages.	61
4.8	Trends of the high and low frequency features with open-circuit voltage.	62
4.9	Comparison of solutions from the drift-diffusion model to experimental J - V and impedance measurements.	63
4.10	Examples of simulated impedance spectra showing unusual intermediate frequency features.	65
4.11	Frequency plot showing the three frequency regimes for PSCs.	67
4.12	Electric potential within the ultra-low frequency regime.	68
4.13	Anion vacancy density within the ultra-low frequency regime.	69
4.14	Electron and hole densities within the ultra-low frequency regime.	70

4.15	Electric potential for frequencies within and above the intermediate frequency regime.	70
4.16	Anion vacancy density for frequencies within and above the intermediate frequency regime.	71
4.17	Frequency plots for the electric field and Debye layer charge.	72
4.18	Electron and hole densities for frequencies within and above the intermediate frequency regime.	73
4.19	Frequency plot of the total current and its components.	74
5.1	Schematic illustrating the potential across a PSC at steady-state.	81
5.2	Schematic illustrating the potential across a PSC with a bulk electric field. . . .	82
5.3	Non-linear capacitance relation from the surface polarisation model [4–6]. . . .	83
5.4	Relationship between the Debye layer charge, potential drops and applied voltage. .	84
5.5	Boltzmann approximation for the electron and hole densities at different voltages. .	89
5.6	Verification of the Boltzmann approximation for the electron and hole densities at open-circuit.	90
5.7	Verification of the Boltzmann approximation for the electron and hole densities at maximum power point and with a lower anion vacancy density.	91
5.8	Approximate error of the Boltzmann approximation at different DC voltages. . .	91
5.9	Comparison between full impedance relations and an RC - RC circuit.	103
6.1	Nyquist plot verifying analytic solutions for different DC voltages.	110
6.2	Frequency plot verifying analytic solutions for different DC voltages.	110
6.3	Trends of the resistances, capacitances and time constants with open-circuit voltage.	111
6.4	Simulated impedance spectra for a cell with a reduced anion vacancy density. .	111
6.5	Simulated impedance spectra for a cell at and below maximum power point. . .	112
6.6	Analytic and numerical impedance spectra with different recombination mechanisms at 0.1-Sun.	113
6.7	Frequency plot comparing different recombination mechanisms at 0.1-Sun. . .	113
6.8	Impedance spectra with different recombination mechanisms under 1-Sun . . .	114
6.9	Frequency plot of the spectra presented in Figure 6.8.	114
6.10	Analytic and numerical impedance spectra with different recombination mechanisms at maximum power point.	115
6.11	Approximate error of the analytic model at different DC voltages.	116
6.12	Schematic of the electric potential across a PSC during high frequency impedance measurements.	118
6.13	Schematic of the electric potential across a PSC during ultra-low frequency impedance measurements.	119
6.14	Illustration of how the shape of an impedance spectrum is related to n_{el} and \bar{n}_{ec} . .	120
6.15	Current-voltage measurements and the ectypal and electronic ideality factors. .	125
6.16	Electronic and ectypal factors at different open-circuit voltages.	126
6.17	Electronic and ectypal factors for different recombination mechanisms. . . .	127
6.18	Electronic and ectypal factors for different recombination mechanisms with modified device parameters.	127
6.19	Nyquist plot for a simulated cell with multiple recombination mechanisms. . .	128
6.20	Frequency plot for a simulated cell with multiple recombination mechanisms. .	129

List of Tables

3.1	Recombination type and the ideality factor.	20
3.2	Equivalent circuit components and their impedances.	24
4.1	Constants and parameter definitions for the drift-diffusion equations.	55
4.2	Recombination mechanisms and parameters.	56
5.1	Full and approximate recombination mechanisms and parameters.	93
5.2	Recombination type and the electronic ideality factor.	93
6.1	Relationship between the low frequency feature and the recombination mechanism.	120

Declaration of Authorship

I declare that this thesis and the work presented in it is my own and has been generated by me as the result of my own original research.

I confirm that:

1. This work was done wholly or mainly while in candidature for a research degree at this University;
2. Where any part of this thesis has previously been submitted for a degree or any other qualification at this University or any other institution, this has been clearly stated;
3. Where I have consulted the published work of others, this is always clearly attributed;
4. Where I have quoted from the work of others, the source is always given. With the exception of such quotations, this thesis is entirely my own work;
5. I have acknowledged all main sources of help;
6. Where the thesis is based on work done by myself jointly with others, I have made clear exactly what was done by others and what I have contributed myself;
7. None of this work has been published before submission

Signed:.....

Date:.....

Acknowledgements

Firstly, I would like to thank my supervisor Dr Giles Richardson for his guidance and belief in both me and the project. I would also like to thank Dr Nicola Courtier who always had time to help and offer great advice. I wish to thank Prof. Alison Walker, Prof. Petra Cameron and Prof. Laurie Peter from the University of Bath for their useful discussions and introducing me to impedance spectroscopy. I thank Prof. Giampaolo D'Alessandro for his detailed feedback over the years. My thanks also go to Antonio Riquelme and Prof. Juan Anta for the valuable help and perspective that they have provided.

This work has been supported by an EPSRC funded studentship from the CDT in New and Sustainable Photovoltaics (reference EP/L01551X/1). I gratefully acknowledge the training and the opportunity provided by the CDT. I wish to thank Alison, Ken, Asim, Alan and all those involved for the creation and running the CDT. I am pleased to have shared these great experiences with all of C4.

I would like to thank my Dad and the rest of my family for being there for me and getting me to this point. Finally, I wish to thank Hannah for the amazing support and motivation that she has given me throughout my PhD and time at university.

Nomenclature

Symbols

A	Cell area
b	Perovskite layer width
b_E	ETL width
b_H	HTL width
B	Susceptance (imaginary component of the admittance $Y = 1/Z(\omega)$)
C_{HF}	High frequency capacitance
C_{LF}	Low frequency capacitance
d_E	Effective doping density in the ETL
d_H	Effective doping density in the HTL
D_E	Electron diffusion coefficient within the ETL
D_H	Hole diffusion coefficient within the HTL
D_n	Electron diffusion coefficient in perovskite
D_p	Hole diffusion coefficient in perovskite
D_+	Ionic vacancy diffusion coefficient
E	Uniform bulk electric field
E_C	Perovskite conduction band level
E_{cE}	Conduction band minimum of the ETL
E_V	Perovskite valence band level
E_{vH}	Valence band maximum of the HTL
f	Frequency
F_i	Potential barrier to recombination
F_{ph}	Incident photon flux
F_T	Total potential drop across the Debye layers
g_c	Perovskite conduction band density of states
g_{cE}	Effective conduction band density of states within the ETL
g_v	Perovskite valence band density of states
g_{vH}	Effective valence band density of states within the HTL
G	Conductance (real component of the admittance $Y = 1/Z(\omega)$)
G_{bulk}	Bulk generation rate
G_+	Ionic conductance per unit area
i	Imaginary unit

j_d	Displacement current density
j_n	Electron current density
j_p	Hole current density
j_P	Ionic current density
j_{rec}	Recombination current density
j_{R_i}	Recombination current prefactor
j_{gen}	Photocurrent density
J	Current density
k_B	Boltzmann constant
k_l	Deep trap constant for recombination on the ETL/perovskite interface
k_r	Deep trap constant for recombination on the perovskite/HTL interface
k_E	Ratio of electron density in the perovskite to that in the ETL
k_H	Ratio of hole density in the perovskite to that in the HTL
k_{SRH}	Deep trap constant for bulk SRH recombination
L_D	Debye length
n	Electron density within the perovskite layer
n_{ec}	Ectypal factor
\bar{n}_{ec}	Measured ectypal factor
n_{el}	Electronic ideality factor
n_i	Intrinsic carrier density within the perovskite
$n_{ETL}^{(l)}$	Electron density within the ETL at the ETL/perovskite interface
$n^{(r)}$	Electron density within the perovskite at perovskite/HTL interface
N_0	Ionic vacancy density
p	Hole density within the perovskite
$p^{(l)}$	Hole density within the perovskite at the ETL/perovskite interface
$p_{HTL}^{(r)}$	Hole density within the HTL at the perovskite/HTL interface
q	Charge of a proton
Q	Ionic surface charge density
Q_{DC}	Steady-state/DC ionic surface charge density
r_{SRH}	Ratio of SRH recombination current to the total recombination current
R	Resistance (real component of impedance $Z(\omega)$)
R_b	Bimolecular recombination rate
R_{bulk}	Bulk recombination rate
R_l	ETL/perovskite interfacial SRH recombination rate
R_n	Electron-limited bulk SRH recombination rate
R_p	Hole-limited bulk SRH recombination rate
R_r	Perovskite/HTL interfacial SRH recombination rate
R_s	Series resistance
R_{HF}	High frequency resistance
R_{LF}	Low frequency resistance
t	Time

T	Temperature
v_{nE}	Electron recombination velocity for SRH at ETL/perovskite interface
v_{nH}	Electron recombination velocity for SRH at perovskite/HTL interface
v_{pE}	Hole recombination velocity for SRH at ETL/perovskite interface
v_{pH}	Hole recombination velocity for SRH at perovskite/HTL interface
V_1	Potential drop across the left Debye layer within the ETL
V_2	Potential drop across the left Debye layer within the Perovskite
V_3	Potential drop across the right Debye layer within the Perovskite
V_4	Potential drop across the right Debye layer within the HTL
V_{bi}	Built-in voltage
V_{DC}	Steady-state/DC voltage
V_{oc}	Open-circuit voltage
V_p	Perturbation amplitude
V_T	Thermal voltage
$V(t)$	Applied voltage
x	Spatial parameter
X	Reactance (imaginary component of the impedance $Z(\omega)$)
Y	Admittance ($1/Z(\omega)$)
Z	Impedance
α	Perovskite absorption coefficient
β	Bimolecular recombination rate in the bulk
δ	Ratio of perturbation amplitude to thermal voltage
ε_0	Permittivity of free space
ε_E	Permittivity of the ETL
ε_H	Permittivity of the HTL
ε_p	Permittivity of the perovskite
ω	Angular frequency
ω_{HF}	Characteristic high frequency
ω_{LF}	Characteristic low frequency
Ω_E	ETL doping and permittivity parameter from the SPM
Ω_H	HTL doping and permittivity parameter from the SPM
τ_n	Electron pseudo-lifetime for SRH recombination
τ_p	Hole pseudo-lifetime for SRH recombination
\mathcal{V}	Capacitance relation from the surface polarisation model

Abbreviations

AM	Air mass
DC	Direct current
ETL	Electron transport layer
HF	High frequency
HTL	Hole transport layer
IMPS	Intensity modulated photocurrent spectroscopy
IMVS	Intensity modulated photovoltage spectroscopy
IF	Intermediate frequency
IS	Impedance spectroscopy
LF	Low frequency
MA	Methylammonium
MAPI	Methylammonium lead iodide ($\text{CH}_3\text{NH}_3\text{PbI}_3$)
MPP	Maximum power point
ODE	Ordinary differential equation
PDE	Partial differential equation
PSC	Perovskite solar cell
PV	Photovoltaic
Spiro	2,2',7,7'-Tetrakis[N,N-di(4-methoxyphenyl)amino]-9,9'-spirobifluorene
SRH	Shockley-Read-Hall
TL	Transport layer
UHF	Ultra-high frequency
ULF	Ultra-low frequency

Chapter 1

Introduction

1.1 Thesis motivation

Global energy demand is set to continue to rise over the next decade despite the effects of climate change from the use of fossil fuels becoming ever more apparent [7, 8]. Consequently, there is great urgency to produce significant proportions of energy from low-carbon sources to reduce overall greenhouse gas emissions.

Solar energy capture using photovoltaic (PV) systems, delivers renewable and low-emission electricity that can be utilised to generate a significant proportion of the global electricity demand. To accelerate the rate of commercial deployment of terawatt-scale solar PV, the total system cost needs to be reduced and the efficiency improved [9]. Over the last decade there has been a significant global increase in the rate of installations of solar photovoltaics [10–12]. Silicon solar cells currently dominate the global photovoltaic market in the form of mono-crystalline and multi-crystalline single junction cells [12]. In 2020, multi- and mono-crystalline silicon accounted for around 15% and 80% of global photovoltaics production respectively, leaving thin-film technologies at only 5% [12]. The market dominance of silicon technology has been facilitated by the falling cost of silicon feedstock and the improved economy of scale in production [10, 13].

The theoretical maximum conversion efficiency from solar radiation to electrical power (the Shockley-Queisser limit) for a single junction solar cell is greatest for a semiconductor with a band gap of 1.34 eV [14, 15]. Crystalline silicon has a band gap of 1.1 eV and is therefore not optimal for solar PV applications [14]. Additionally, this band gap is indirect, resulting in a low optical absorption coefficient [14]. Semiconductor materials with direct band gaps are termed ‘thin-film’ as only a thin layer of these materials are required to absorb the sun’s radiation effectively [16]. As a result, thin-film materials can be cheaper to produce as less raw material is required in their production. Another disadvantage of silicon PV is that their performance relies upon high temperature processing to produce silicon of extremely high purity, increasing their

cost and energy payback time [14, 17, 18]. Despite the relative success of silicon solar cells, these drawbacks continue to drive the quest for more efficient photovoltaic technologies.

Most importantly, to be commercially competitive against silicon PV any alternative must offer greater efficiency, or be able to be produced at a significantly lower cost. Perovskite solar cells (PSCs) are a new PV technology that has the potential to deliver both of these features, sparking significant excitement and research into their development [19–21].

1.2 Thesis overview

This thesis is set out as follows. Chapters 2 and 3 detail the relevant background for the subsequent technical chapters. Firstly, in Chapter 2, a brief overview of the properties and operation of PSCs is given. Some of the main challenges that need to be overcome before PSCs can be commercialised are also discussed. This includes the impact of mobile ions within the perovskite on device operation. Next, in Chapter 3, an introduction into ideality factors for PSCs is given, followed by the theory and application of impedance spectroscopy. The interpretations for PSC impedance spectra, and the models currently available, are reviewed.

Chapter 4 is the first technical chapter and details a drift-diffusion model of a planar PSC that includes mobile ions. The simulation tool *IonMonger*, which numerically solves this coupled ionic-electronic charge transport model, is extended to enable simulation of impedance spectroscopy measurements. These numerical solutions are shown to be concordant with experimental impedance measurements, validating the underlying drift-diffusion model. In Chapter 5, this drift-diffusion model is systematically approximated to facilitate analytic solution. Employing the ‘surface polarisation model’, in addition to other suitable approximations, enables simple analytic relations to be derived that describe the fundamental impedance response of PSCs. In Chapter 6, these relations are shown to be accurate by comparing them to numerical solutions determined from the full drift-diffusion model. This analytic model justifies the use of a particular equivalent circuit and defines the associated resistance and capacitances in terms of cell properties. The new interpretations for the impedance response of PSCs provided by the analytic relations are explored, including how efficiency losses can be identified and understood from impedance measurements. Finally, in Chapter 7, the main findings and conclusions of this thesis are summarised and opportunities for further research are discussed.

1.3 Contributions

Sections 3.1 and 3.4.4 in Chapter 3 contain excerpts verbatim from the pre-published material in ref. [2]. This manuscript was written by myself and Dr Giles Richardson and edited by Antonio J. Riquelme, Dr Nicola E. Courtier and Dr Juan A. Anta.

In Section 4.1, the drift-diffusion equations and their description have been published in ref. [3] and its supplementary information. The material used in this thesis from ref. [3] was written by myself and all authors contributed to editing. Any results presented from this paper are appropriately referenced.

Significant portions of Chapters 5 and 6 are reproduced verbatim from ref. [2] and its supplementary information. This manuscript was written by myself and Dr Giles Richardson and edited by Antonio J. Riquelme, Dr Nicola E. Courtier and Dr Juan A. Anta.

Chapter 2

Perovskite solar cells

This chapter provides an overview of the field of PSC research and sets the context for later chapters. In Section 2.1, the history and development of PSCs is outlined, in addition to a basic description of their operation. In Section 2.2, the broad challenges that need to be overcome for PSCs to become a viable and competitive solar technology are discussed. This includes stability issues and their environmental impact. Furthermore, the challenges associated with ionic motion within the perovskite layer are considered and their effect on device operation is outlined. Finally, a brief summary is presented in Section 2.3.

2.1 Background and theory

Perovskite is the name given to any material which adopts the general crystal structure, ABX_3 [19]. The perovskite structure is shown in Figure 2.1 where A and B are large and small cations respectively and X is an anion. In the context of photovoltaics, the prototypical perovskite absorber is methylammonium lead tri-iodide or $MAPbI_3$, often abbreviated to MAPI [22]. MA is a methylammonium cation ($CH_3NH_3^+$) at the A site, lead (Pb^{2+}) is the B site cation, and iodide (I^-) the X site anion. When a vast number of atoms bond to form a crystal structure, like a repeating ABX_3 lattice, the discrete set of permitted energy levels of the electrons form a ‘continuum’ or ‘band’ structure. These bands can split to form a band gap (E_g) which is simply defined as the energy difference (at absolute zero) between an electron in the highest occupied energy state (top of the valence band) and the energy of the lowest unoccupied energy state (bottom of the conduction band). A schematic of the band structure of a PSC is shown in Figure 2.2.

The energy band gap is critical in determining the properties of a material. A material with a very small band gap ($E_g < 0.5$ eV) is a conductor, whilst a material with a large band gap ($E_g > 3$ eV) is an insulator [14]. MAPI has a band gap of around 1.6 eV [24], making it a semiconductor. This is important as a photon can be ‘absorbed’ by the material to excite an electron from the

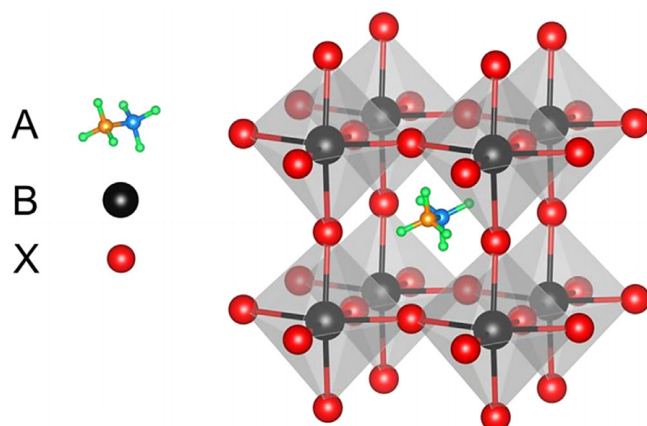


FIGURE 2.1: Crystal structure of perovskite with a general structure of the form ABX_3 . For MAPI perovskite, A is methylammonium (MA), B is lead (Pb) and X is iodine (I). Reprinted from [23], with permission from Elsevier.

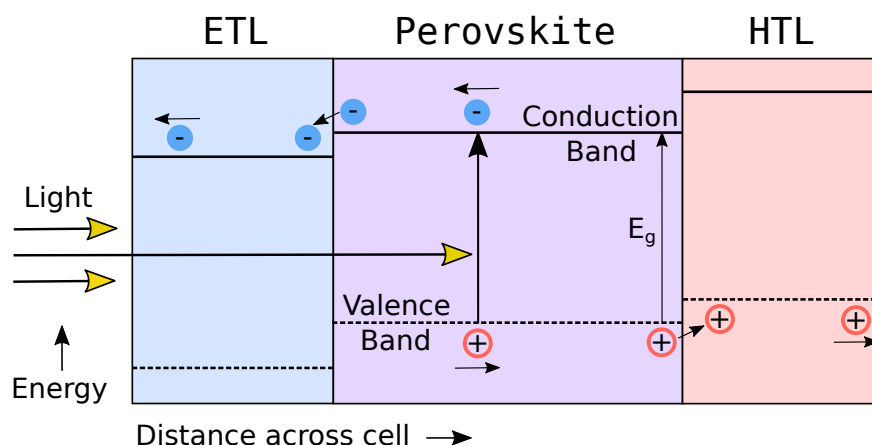


FIGURE 2.2: A simplified representation of the band structure of a typical planar perovskite solar cell. Light generates free electrons in the conduction band and electron holes in the valence band of the perovskite. Holes refer to the vacancy left by an electron. The absence of a negative charge, which moves as a neighbouring electron fills the vacancy to leave another vacancy, can be described as a positively charged quasiparticle, i.e. a hole. The band energy alignments enable collection of the electrons via the electron transport layer (ETL) and holes from the hole transport layer (HTL).

valence to conduction band. This leaves a positively charged hole in the valence band. This hole can be described as a quasiparticle, that moves in the opposite direction that the electrons move to fill it. Without a band gap, any excited electrons in the conduction band would rapidly ($\sim 10^{-15}$ s [14]) dissipate their energy by thermalisation back down to the lowest unoccupied energy level in the valence band. Instead, excited electrons thermalise to the bottom of the conduction band. From there, recombination pathways that occur on much longer timescales are required for the electrons to relax back to lower energy states. Devices can be designed to separate electrons and holes before they recombine between bands, and transport them to an external circuit where their energy can be utilised.

In an ideal semiconductor, there are no electron states available with energies that lie between the valence and conduction bands. Consequently, photons of energy less than the band gap cannot be absorbed. Photons with energies greater than the band gap excite electrons to high energy levels, however, they quickly thermalise back down to the bottom of the conduction band. As a result, the energy that can be harnessed from any excited electron is equal to the semiconductor's band gap. This highlights the importance of a semiconductor's band gap when used as absorbers in photovoltaic devices.

To create a planar PSC, an electron transport layer (ETL) is added to a transparent conducting oxide. This is followed by a perovskite layer and a hole transport layer (HTL). Finally a metallic contact is added. In PSCs that employ MAPI, titanium dioxide (TiO_2) and spiro-OMeTAD (2,2',7,7'-tetrakis(N,N-di-p-methoxy-phenylamine)-9,9'-spiro-bifluorene) are often used as ETLs and HTLs respectively [25–27]. An electron microscope image of a planar PSC is shown in Figure 2.3. In this 'standard' configuration, light enters the cell to reach the perovskite layer through the ETL. In contrast, for 'inverted' configurations the light is directed through the HTL. The approximations required to model the rough interfaces and inhomogeneities of planar devices as part of a one-dimensional model are discussed in Section 4.1

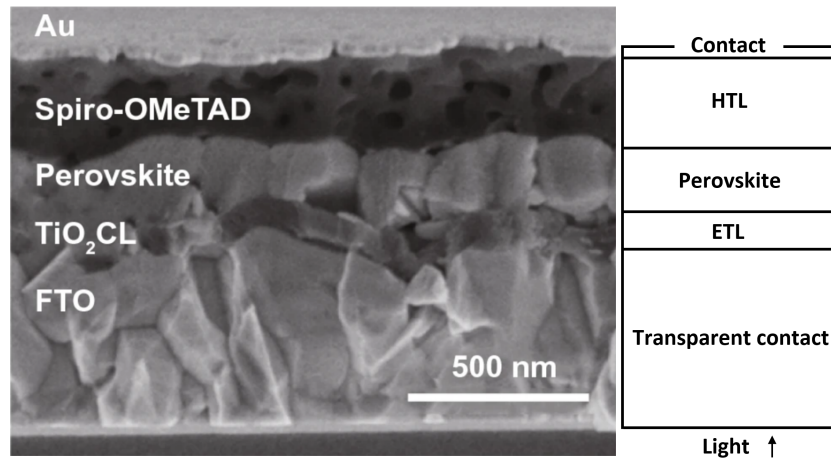


FIGURE 2.3: Cross-sectional field emission scanning electron microscope image of a planar perovskite solar cell. CL refers to a 'compact layer' of TiO_2 and FTO stands for fluorine doped tin oxide which is used as the transparent electrical contact. Image adapted from ref. [27] and licensed under CC BY 4.0.

Under operation, the perovskite material absorbs incident photons with energies greater than the band gap to produce excitons. These excitons are bound states of excited electrons and holes due to their Coulomb attraction [14]. In perovskites, they are weakly bound (< 50 meV [28, 29]) and the thermal energy available at room temperature (~ 25 meV) causes the rapid dissociation into free electrons in the conduction band and holes in the valence band. The free electrons and holes then move by diffusion, from higher concentrations to lower concentrations, and drift, in response to an electric field, to their respective transport layers. The device is designed such that the ETL and HTL band energies provide an energy barrier to the opposing charge carrier. This is demonstrated in Figure 2.2, as it is energetically favourable for electrons (holes) to move downwards (upwards) on the band diagram. The alignment and bending of the bands

also establishes a ‘built-in’ voltage and an electric field across the device, which works to drive charge carriers to their respective transport layer.

In perovskites used in PV applications, lead (Pb^{2+}) is primarily the B site cation, but tin (Sn^{2+}) is sometimes used. In MAPI, the iodine can be replaced by another halide anion, most commonly bromide (Br^-) or chloride (Cl^-) [30]. Mixed halide perovskites have been shown to improve device performance and stability, and a commonly used formulation is $\text{MAPb}(\text{I}_{1-x}\text{Br}_x)_3$ where $x < 1$ [30, 31]. Furthermore, the large MA cation at the A site is often partially or fully replaced by formamidinium ($\text{NH}_2\text{CHNH}_2^+$) in ‘hybrid’ perovskites, or caesium (Cs^+) is used at the A site in all inorganic formulations [32–36]. Mixing the species of cations at site A and the halides at site X enables the formation of perovskite materials with a wide range of properties. These blended formulations, often termed hybrid metal halide perovskites, can be optimised to produce cells with improved efficiency, better stability and reduced hysteresis [34]. From here onwards, we use the general term ‘perovskite’ to refer to perovskite materials that are useful in photovoltaic applications.

The first reported use of perovskites in PV applications was in 2006 by Miyasaka *et al.* who produced cells with an efficiency of 2.2% using MAPbBr_3 perovskite as a sensitizer in dye-sensitised solar cells [37]. In 2009, they achieved a power conversion efficiency of 3.8% by substituting bromide for iodide to produce MAPbI_3 (MAPI) [38]. In 2012, Kim *et al.* [39] replaced the liquid electrolyte in a dye-sensitised solar cell for the solid hole transport material spiro-OMeTAD and obtained an efficiency of 9.7%. Simultaneously, Lee *et al.* [40] announced success producing 10.9% efficient ‘meso-superstructured’ solar cells. This new solar cell design used an insulating Al_2O_3 ‘scaffold’ in which a mixed halide perovskite was coated. Critically, they found that perovskites were capable of transporting both electrons and holes to their respective transport materials [22]. Following this, in early 2013, Ball *et al.* [41] demonstrated an efficiency of 9.1% when the mesoporous scaffold was removed and the depth of the perovskite absorber layer was increased. This established an efficient PSC with a ‘conventional’ thin-film architecture. The architectures of the best performing PSCs are typically based on a thin-film planar ‘n-i-p’ structure or a mesoporous TiO_2 scaffold [30, 42].

MAPI has an optical band gap of approximately 1.6 eV and a maximum theoretical efficiency of around 31% under an AM (air-mass) 1.5 spectrum [24, 43]. AM 1.5 corresponds to the solar spectrum received at ground level after it has passed through 1.5 times the thickness of the atmosphere [15]. By varying the mix of halides and cations at the A site, the band gap can be tuned between 1.48–2.3 eV [35]. This enables the band gap of perovskites to be tuned for optimal efficiency depending on their application [44, 45]. For example, perovskite absorbers with band gaps in this range can be used in multi-junction solar cells [22]. In particular, silicon-perovskite tandem devices show great commercial potential, with the record certified efficiency currently standing at 29.5% [36, 46]. Perovskites exhibit very high optical absorption, with a steep absorption onset and have very long charge carrier diffusion lengths [31, 47]. As a result, a thin film of perovskite material (~100–600 nm) can effectively capture the incident AM 1.5 spectrum, generating mobile charges that diffuse and drift to their respective transport

layers before they can recombine. A wide range of fabrication techniques for PSCs, including many low temperature methods (sub-150°C), enable the possibility of large-scale and low cost manufacturing [25, 26, 48–50].

These properties make perovskite an excellent material for thin-film PV applications and have enabled the extremely rapid increase in power conversion efficiencies for PSCs to just above 25% [46, 51, 52]. This increase in power conversion efficiency within such a short time is remarkable for a new PV technology [20, 46]. Whilst PSCs have the potential to compete with silicon, issues of toxicity, stability, and the effects of ion motion need to be addressed before large-scale commercial deployment can be achieved [36, 53, 54]. These issues are discussed in the following section.

2.2 Challenges

To provide an overview of the field of perovskite solar cells, this section outlines some of the challenges faced by researchers that need to be overcome before PSCs can be commercialised. These include the relatively poor inherent stability of PSCs compared to traditional silicon PV as well as concerns over the toxicity of the materials used in its manufacturing. Evidence of mobile ionic species within perovskites and their effect on measurements and performance is also discussed.

2.2.1 Stability and environmental impact

Commercial solar modules are expected to pass international performance standards (IEC 61215 [55]). These standards include stability tests that simulate harsh and accelerated weather testing. For example, the modules need to be able to withstand many cycles between -40 and 85 °C, 1000 hours at 85 °C at 85% relative humidity and high levels of UV exposure [55–57]. It is crucial to overcome the inherent instability of PSCs and demonstrate that these tests can be passed.

Heat [58, 59], moisture [60, 61], light [62, 63] and oxygen under light irradiance [62, 64] are all factors that have been shown to cause degradation of PSCs [65]. Depending on the exact perovskite formulation, exposure to these factors can cause degradation within hours or even minutes, significantly reducing power conversion efficiencies [61, 62, 64, 66]. It has also been demonstrated that the generation, accumulation and depletion of ions within the perovskite lattice can stimulate degradation of the materials [67–72].

Degradation caused by exposure to extrinsic factors such as moisture, oxygen and UV can be prevented by encapsulation and UV protective coatings [66]. Hydrophobic layers [73, 74], mixed perovskite formulations [75, 76] and the use of different materials as transport layers [64, 75, 77, 78] further improve stability and reduce the reliance on encapsulants. Heat is an intrinsic factor that cannot be mitigated by encapsulation. Therefore, it is essential to reduce

material susceptibility to degradation from high temperatures. It has been established that high temperature stability is improved by using specific mixed perovskite formulations [79] as well as employing novel transport layers [80] and the addition of buffer layers [81, 82]. Blocking layers, that work by inhibiting ion migration into and out of transport layers, have also been shown to eliminate degradation pathways associated with mobile ionic species [65, 83]. Ionic modelling and further experimental study will provide insight and help to advance progress towards designing long-term stable devices [4, 67].

While there is still a long way to go before 25 year stable PSCs are fully realised, the stability of state of the art PSCs has improved tremendously since 2012 [36]. Groups have reported devices capable of maintaining efficiencies above 20% after 50 days operation under 1-Sun and capable of passing the high temperature and humidity tests required for IEC 61215 certification [82, 84, 85].

With the development of a new technology, it is important to consider its overall environmental impact. In comparison to other solar photovoltaic technologies, PSCs have the potential to deliver the shortest energy payback time [17]. However, an obvious concern is their lead content, which is required to make the most efficient perovskite formulations [86]. As a heavy metal, it poses a threat to human health and the environment through, its production from raw lead ore, fabrication into cells, leakage into the environment during cell operation, and at the end of life disposal. Fortunately, efficient PSCs only need a perovskite absorber layer of around 100-600 nm in thickness. This corresponds to around a few hundred milligrams of lead per square meter [53]. Even to satisfy the production of PSCs at the terawatt-scale, which is of the order required to become the world's primary energy source, the current rate of lead production would not need to be significantly increased [36]. Nonetheless, concerns over the health and environmental impacts refining of raw lead ore for PSCs can be mitigated through the use of recycled lead, for instance from lead-acid car batteries, which has been shown not to significantly impact cell performance [87].

Fabrication of PSCs can involve the use of toxic solvents, which may have a much greater human toxicity potential than lead. This risk can be reduced by using less hazardous solvents, which have been shown to be effective in device preparation with relatively minor reductions in efficiency (versus the hazardous alternatives) [88]. Once deployed, or at their end-of-life, the perovskite can degrade into lead compounds, which are more bioavailable and therefore more toxic than metallic lead [53, 60, 89]. Replacement of lead with tin (or other cations) in the perovskite formulation has been proposed. However, the lower efficiencies of these formulations mean that theoretical and experimental advances are required for these to be viable alternatives to lead-based PSCs [90]. Furthermore, there are also concerns over the toxicity of tin [89].

Commercially available solar cells use encapsulation to provide a barrier from the outside elements. As such, for PSCs encapsulation serves to benefit both device stability and environmental contamination risks, namely, by inhibiting degradation due to the ingress of water and oxygen, and to safeguard against leaching of hazardous chemicals into the environment [53].

Additionally, degradation can be directly monitored through efficiency measurements of cells in operation. Thus, defective or damaged cells, at risk of contaminating the environment can be appropriately handled and removed [53]. Finally, end-of-life recycling and safe disposal is essential. As demonstrated by cadmium telluride (CdTe) solar cell manufacturing, this is an economically viable option that can be implemented in practice [91].

Overall, high quality encapsulation, refinement of perovskite formulation and the use of novel blocking and transport layers should be sufficient to deliver safe and stable PSCs, as required to meet the standards for commercial applications.

2.2.2 Ionic motion

When performing standard characterisation measurements for photovoltaic cells, perovskite solar cells can exhibit unusual behaviour. Perhaps most strikingly, current-voltage (J - V) measurements of PSCs often show a significant difference in the measured current between scanning from above open-circuit to short-circuit and back again to above open-circuit. This difference in measured values depending on transient conditions and the history of the cell is termed ‘hysteresis’. These dynamic effects, occurring on timescale of around seconds, are an unusual characteristic for a solar cell to have. Understanding the cause of this behaviour is one of the keys to unlocking the full potential for perovskite solar cells.

Figure 2.4 shows an example of hysteresis for current-voltage measurements of a MAPI solar cell. Current-voltage curves are measured by sweeping through an applied voltage and measuring the current output of the cell. The voltage sweep typically involves performing a ‘reverse scan’ from around 1.2 V to 0 V, followed by a ‘forward scan’ from 0 V back to 1.2 V. This measurement may be performed with no light incident onto the cell or under irradiance. A standardised measure of efficiency is obtained when a J - V measurement is performed for a cell that is exposed to an air-mass (AM) 1.5 spectrum at 100 mW cm^{-2} irradiance [92].

Hysteretic effects mean that J - V scans of PSCs do not probe the steady-state output of the cell under different applied biases. Consequently, the efficiencies calculated from them are ambiguous or unreliable. Scan rate and direction, light and voltage history have all been shown to affect the hysteresis observed in J - V curves of PSCs [93, 94]. Transience has also been observed in measurements of photoluminescence intensity, photovoltage and photocurrent [95, 96]. Efforts have been made to ensure protocols of measurements are well documented and that stabilised efficiencies are obtained using a maximum power point tracking method [97, 98]. Maximum power point tracking is a method that maximises the power output of the solar cell under illumination by dynamically modifying the applied load (or equivalently applied voltage) such that the product $J \cdot V$ is maximal [14]. Solar arrays are typically operated using maximum power point tracking and efficiencies obtained using this method can offer far more realistic measures of efficiency than the maximum power point of a J - V curve.

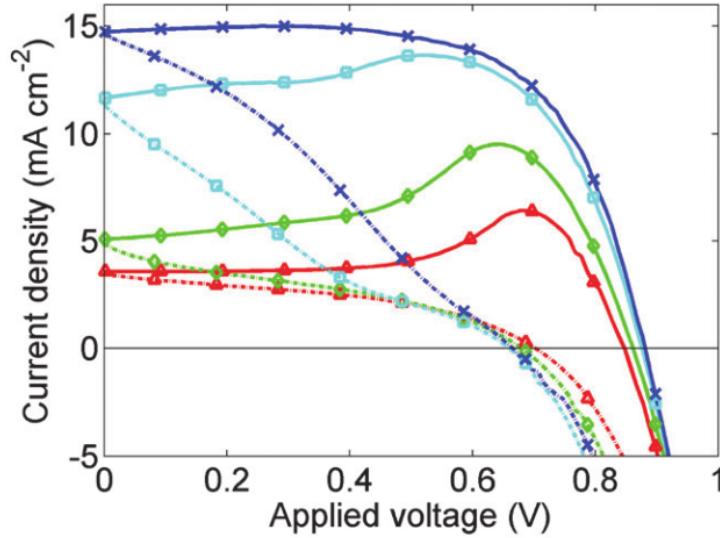


FIGURE 2.4: Experimental current-voltage measurement of a MAPI solar cell with varying scan rates. Scan rates are 0.5 V s^{-1} for blue crosses, 0.25 V s^{-1} for cyan squares, 0.1 V s^{-1} for green diamonds and 0.05 V s^{-1} for red triangles. Solid lines represent the reverse scan from 1.2 V to 0 V and dotted lines represent the forward scan back to 1.2 V. The cell was held at 1.2 V for 5 seconds prior to measurement. Figure reproduced from ref. [6] and licensed under CC BY 3.0.

The exact cause of hysteresis in PSCs has been highly debated since its recognition in a paper by Snaith *et al.* in 2014 [92]. In this paper, they described the anomalous behaviour and proposed the following explanations: (i) a ferroelectric polarisation of the perovskite; (ii) filling and saturation of electronic trap states at the perovskite-transport layer interfaces; (iii) mobile ions within the perovskite [92].

Subsequently, these hypotheses have been thoroughly investigated. (i) It has been shown that MAPI is not ferroelectric at room temperature as polarisation of ferroelectric domains only holds for very short timescales [99–101]. This is much too fast for the relatively slow timescales that hysteresis is observed (around 10^{-3} to 10^3 seconds) [67, 92, 94, 96]. (ii) Electronic mobility is very high in perovskites and so transport is of the order 10^{-9} s. This is much faster than that of hysteresis; however, trapping and detrapping could occur on timescales that match more closely [6]. (iii) The presence of mobile halide ions in the perovskites used in PV has been extensively confirmed in the literature [69, 101–103]. Furthermore, experiment and modelling show that ion motion can account for the observed hysteresis in PSCs [5, 6, 102, 104–106].

Even before their popularity as photovoltaic materials, it was documented that inorganic perovskites with formulations CsPbCl_3 and CsPbBr_3 had mobile halide ions [107, 108]. Halide vacancies within the perovskite lattice allow the motion of halides to the empty sites. As an analogy to an electron vacancy being described as a hole, it is equivalent to describe this motion of halide ions (anions⁻) as halide vacancies with positive charge (cations⁺) that move in the opposite direction through the perovskite material. A sketch of this is given in Figure 2.5. Density functional theory calculations have been employed to model the perovskite structure and have shown that iodide ions can move via vacancies under normal operating conditions in

MAPI [69, 70]. Eames *et al.* and Walsh *et al.* predict a density of vacancies of around $1 \times 10^{25} \text{ m}^{-3}$ [69, 109]. Furthermore, density functional theory calculations have estimated the activation energy of methylammonium and formamidinium cation vacancies, indicating that the barrier is low enough for them to be mobile within perovskites [70, 110]. This results in transient behaviour on timescales longer than 10^3 seconds, much longer than that of the halide vacancies motion [67].

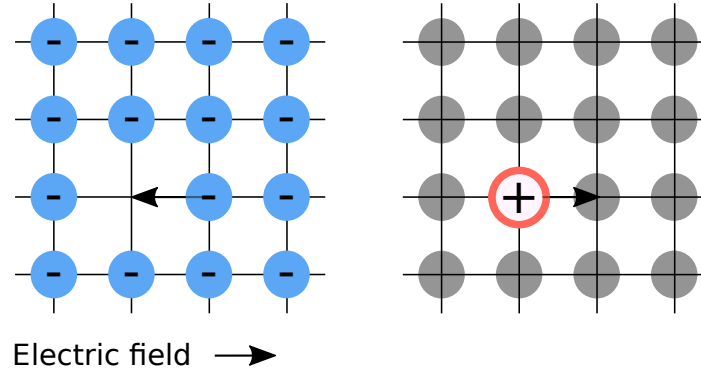


FIGURE 2.5: Left: a sketch of a crystal lattice with a single ionic vacancy. In response to the electric field, a negatively charged ion can ‘hop’ to the left to fill the vacancy. Right: an equivalent description of the system, in which the ionic vacancy is a positively charged quasiparticle that hops to the right.

Some experimental evidence indicates that the lead cation in MAPI could also be mobile [111]; however, this requires further investigation as calculations by Eames *et al.* had previously ruled this out [69]. The possibility of two or more mobile species within the perovskite materials adds further complexity to modelling and understanding the ramifications for their performance as solar cells.

At the high densities predicted by density functional theory calculations, mobile ionic vacancies can redistribute to fully screen the electric field from the bulk of the perovskite layer [4, 5, 69, 109]. As a result, at steady-state the electrons and holes (charge carriers) do not drift in response to an electric field across the bulk of the perovskite. This limits the rate of collection as they must diffuse to their respective transport layers. Importantly, if the applied voltage varies over the same timescale in which the ions adjust their distribution to screen the field, then there is a difference between the currents measured on the forward and reverse scans. Hysteresis-free J - V measurements are expected for very high scan rates as the ions are effectively static on the timescale of the scan. Additionally, for very slow scan rates, the ions have sufficient time to equilibrate with the applied potential so that the system is in a quasi-steady-state throughout the measurement, resulting in identical current outputs during forward and reverse scans.

The magnitude of hysteresis has been shown to be strongly dependent on temperature and scan rate [94, 112, 113]. It is also reported that the severity of hysteresis is influenced by the grain sizes in the perovskite active layer and the structure of the electron transport layer (typically TiO_2) [114]. Furthermore, with identical perovskite active layers, changing the transport layers of PSCs to different materials has been shown to impact hysteresis. For example, Kim *et al.*

report changing TiO_2 to PCBM and spiro-MeOTAD to NiO results in a hysteresis-free MAPI cell [115]. Similar results are reported for interfacial passivation, which may reduce hysteretic effects in the same way by reducing recombination at the interfaces [116, 117]. Collectively, these factors seem to indicate a different, or additional process to ion motion to account for the observed hysteresis, especially the dependence on transport layers. However, the combination of ion motion and its impact on recombination has been proposed as the mechanism that most fully accounts for the wide ranging factors that influence the observed hysteresis in PSCs [4, 5, 118]. Mobile ions within the perovskite layer may also penetrate or react with the neighbouring transport layers, adding additional complexity to understanding PSC physics [64, 119, 120].

Since the recognition of the presence of hysteresis in PSCs, there have been many reports of so-called ‘low-hysteresis’ or ‘hysteresis-free’ devices [73, 115, 117, 121–123]. In these reports, it can be unclear whether hysteresis is truly absent owing to the device modifications or simply missed as it is not probed at the relevant temperatures or timescales [112, 124]. Recent literature, that presents the results of models including ionic motion, has provided considerable insight into the processes that cause hysteresis and the implications of mobile ions within devices [4, 124]. The literature often speculates that hysteresis can be eliminated through improved device processing and as performance is further improved. However, ionic vacancies seem to be an intrinsic property of the popular perovskite formulations and therefore can’t be entirely eliminated through improved sample processing. Additionally, ionic vacancies may be generated under light exposure (photo-generation) or during longer-term operation of devices. It is therefore critical to develop methods capable of probing the ionic properties of PSCs to better understand the ionic behaviour of PSCs.

The hysteresis displayed in the J - V curves of PSCs can be probed by conducting multiple measurements at different scan rates. However, conducting many J - V measurements is time consuming and it can be challenging to appropriately quantify the amount of hysteresis. Impedance spectroscopy is a technique that measures the current of a device in response to small sinusoidal voltage perturbations applied at different frequencies. The theory of impedance spectroscopy and how to interpret the impedance spectra of PSCs is presented in the following chapter. A J - V measurement is conducted across a wide voltage range for a single scan rate. In contrast, impedance spectroscopy is conducted at a given voltage across a wide frequency range.

Jacobs *et al.* demonstrate how impedance measurements can determine the scan rates that hysteresis will arise for so-called ‘hysteresis-free’ devices [125]. Broadly, both very fast J - V scan rates and high frequency impedance measurements probe the response of a PSC with the ions remaining approximately static. At slow scan rates and very low frequencies, the ions move and remain in equilibrium with the applied voltage. While both J - V and impedance measurements simply involve applying a voltage to a device and measuring its current output, both are useful characterisation tools, that provide very different insights into the operation of solar cells.

2.3 Summary

Perovskite solar cells display excellent optoelectronic properties. This includes low non-radiative recombination rates, strong optical absorption and a tunable band gap. Additionally, the perovskite absorber layer can be processed at low cost and temperatures and does not require rare-earth materials. These favourable properties have spurred significant research interest. In only a decade, excellent efficiencies have been obtained, with 25.5% and 29.5% for single-junction and perovskite silicon tandem cells respectively [46, 51].

In this light, PSCs have great potential. However, concerns remain over their environmental impact and susceptibility to degradation through exposure to heat, moisture and oxygen. Risks due to toxicity can be mitigated via the use of less hazardous solvents, careful monitoring during operation and end-of-life recycling. Significant advances have been made in achieving device stability through the use of mixed perovskite formulations, improved transport layers and the use of blocking and buffer layers. Furthermore, it seems likely that high quality encapsulation will play a key role in limiting the risks of both degradation and environmental contamination.

Theoretical and experimental studies have identified the presence of a high density of mobile ionic vacancies within PSCs. This adds significant complexity to their fundamental operation and makes interpretation of standard characterisation techniques more challenging. Notably, current-voltage measurements display hysteresis that is dependent on the voltage scan rate and history of the cell. Impedance spectroscopy is a technique which is commonly employed to characterise solar cells and is currently under-utilised for PSCs, largely because PSC impedance data is poorly understood and so frequently misinterpreted. This will be explored in the next chapter.

Chapter 3

Impedance spectroscopy and the ideality factor

Impedance spectroscopy (IS) is a relatively simple measurement to perform that uses equipment that is commonplace in labs. With correct interpretation, IS can provide valuable information about cell properties and performance. Additionally, determining the ideality factor of a solar cell is a common method of characterisation that allows key properties of the cell to be inferred. Both of these are straightforward methods to characterise the performance of solar cells. However, when applied to PSCs, their results are often misinterpreted due to the unusual physics of PSCs. As a result, specialised models need to be employed that suitably account for the properties of PSCs, including the high density of mobile ionic vacancies. In this chapter, the theory of ideality factors and impedance spectroscopy, as required for later chapters, is discussed. Following this, the high, low, and intermediate frequency features observed in the IS response are detailed. Upon reviewing the PSC models currently employed, an opportunity for an impedance model based on a drift-diffusion approach is identified.

This chapter is set out as follows. Section 3.1 outlines the diode equation and the ideality factor for solar cells. Its application to PSCs is then reviewed. Section 3.2 describes the basic theory of impedance spectroscopy and how it is performed. In Section 3.3, equivalent circuit models as tools to interpret and extract useful information from impedance spectra are introduced. Section 3.4 details the types of features observed in the impedance spectra of perovskite solar cells and discusses their physical origin. Section 3.5 reviews the leading models currently employed to interpret PSC impedance spectra. Finally, in Section 3.6 an overview of this chapter is given.

3.1 The ideality factor and PSCs

From classical solar cell theory, derived to describe semiconductor p - n junctions, the current response of a photovoltaic diode can be approximated by the (non-ideal) diode equation [14,

126]

$$J(V) = j_{\text{gen}} - j_{\text{dark}}(V), \quad (3.1)$$

$$= j_{\text{gen}} - j_0 \left[\exp \left(\frac{V}{n_{\text{id}} V_T} \right) - 1 \right], \quad (3.2)$$

where J is the total current density, V is the applied voltage, j_{gen} is the photo-generated current density, j_{dark} is the dark current density, j_0 is the dark saturation current density and n_{id} is the diode ideality factor. The thermal voltage is given by $V_T = k_B T / q$, where q is the positive unit of electric charge, k_B is the Boltzmann constant and T is temperature. All symbols are defined on page xix.

The diode equation (3.2) is derived from the conservation equations for the electron and hole densities and Poisson's equation within a p - n junction [14]. The generation current density j_{gen} is independent of voltage, and corresponds to the current produced from the incident light. The dark current density j_{dark} is the current that flows in the opposite direction to the photocurrent. This current, also termed the recombination current, describes the diodic behaviour of a solar cell. In forward bias (positive applied voltage) the dark current grows exponentially, whereas in reverse bias (negative applied voltage) the dark current does not flow, except for a small leakage current j_0 . For solar cell technologies such as silicon, the diode equation is commonly employed and provides a good approximation for their current output as a function of the applied voltage. However, as discussed later, it is generally not appropriate for PSCs.

The diode ideality factor n_{id} is a dimensionless number that typically takes a value between 1 and 2. It is a measure of how diodic the cell response is, such that an ideality factor of 2 means that the current depends more weakly on the applied voltage. The specific value can be related to the type of recombination losses that occur. An ideality factor of 1 can indicate that the primary mechanism is bimolecular radiative recombination, in which free electrons in the conduction band recombine with holes in the valence band and emit a photon. An ideality factor of 2 can indicate a monomolecular non-radiative recombination process, for example Shockley-Read-Hall (SRH) recombination in which carriers recombine at a trap within the band gap; however, this relies on the recombination being limited by both carrier types [14, 126, 127]. Non-integer values are expected when multiple recombination mechanisms limit the performance, with the closeness to 1 or 2 indicating the relative amount of each type of recombination.

To determine the ideality factor from devices, measurements such as Suns- V_{oc} or dark- J - V are performed. For the Suns- V_{oc} method, the open-circuit voltage V_{oc} of the cell is measured at different levels of illumination and the ideality factor can be derived from the formula

$$\frac{1}{n_{\text{id}}} = V_T \frac{d \ln(F_{ph})}{dV_{\text{oc}}}, \quad (3.3)$$

where F_{ph} is the illumination intensity. This Suns- V_{oc} method assumes that the photo-generated current is proportional to the illumination intensity and, on account of neglecting the -1 term in equation (3.2), is only valid for voltages above around 0.1 V. For the dark- J - V method, the

ideality factor is determined by measuring the current-voltage curve of a solar cell in the dark via

$$\frac{1}{n_{id}} = V_T \frac{d \ln(j_{\text{dark}})}{dV}. \quad (3.4)$$

This relation can be obtained from eq.(3.2), with $J(V) = j_{\text{dark}}$. Similarly this is only valid at voltages above around 0.1 V. Naturally, these relatively simple and well-established methods have been applied to PSCs. However, literature reports have found values of the ‘ideality factor’, determined for PSCs using the techniques outlined above, that are voltage dependent and that range from around 0.9 to greater than 5 [128–131]. Various authors have attempted to relate the value of the ‘ideality factor’ to specific recombination processes for PSCs [128, 132–134]. Yet, a comprehensive framework for interpreting these ideality factor measurements in PSCs has not been established.

It has been highlighted that applying classical solar cell theory is not appropriate for PSCs [134, 135]. This is due to the high density of mobile ions, that redistribute to screen the bulk electric field and accumulate at the perovskite/transport layer (TL) interfaces, resulting in an electric potential profile that can be approximately described by Figure 3.1. To address this, Courtier has produced a PSC model, derived from drift-diffusion theory, which aims to quantify the steady-state performance of PSCs via a replacement for the diode ideality factor, termed the ectypal factor [135]. This work explains why measurements of the ‘ideality factor’ for PSCs cannot be interpreted using the standard diode theory. Instead, (when carried out near the built-in voltage of the cell) the ‘ideality factor’ determined by the Suns- V_{oc} or dark- J - V methods for PSCs is actually the ectypal factor, defined by [135], as

$$n_{ec}(V) = \frac{V_{bi} - V}{F_i(V_1, V_2, V_3, V_4)}, \quad (3.5)$$

where, V_{bi} is the built-in voltage of the cell and F_i is the potential barrier to recombination, defined in Table 3.1. The built-in voltage is formed due to the difference in the Fermi levels of the ETL and HTL at equilibrium, as defined in eq.(4.29) [14]. The size of the potential barrier F_i depends on the type of recombination occurring (assuming a single source dominates) and the size of the potential drops V_{1-4} . Figure 3.1 labels the location of the potential drops V_{1-4} across a PSC. The types of recombination considered here are discussed in Section 4.3. Note that in general, it is the *measured* ectypal factor \bar{n}_{ec} that is determined from experiment, which is given by [135]

$$\bar{n}_{ec}(V) = n_{ec}(V_{DC}) \left[1 - \frac{V - V_{bi}}{n_{ec}} \frac{dn_{ec}}{dV} \right]^{-1}. \quad (3.6)$$

When the applied voltage is close to the built-in voltage of the cell, the measured ectypal factor is approximately equal to the true ectypal factor. A more detailed description of the potential distribution across a PSC is provided in Section 5.1.

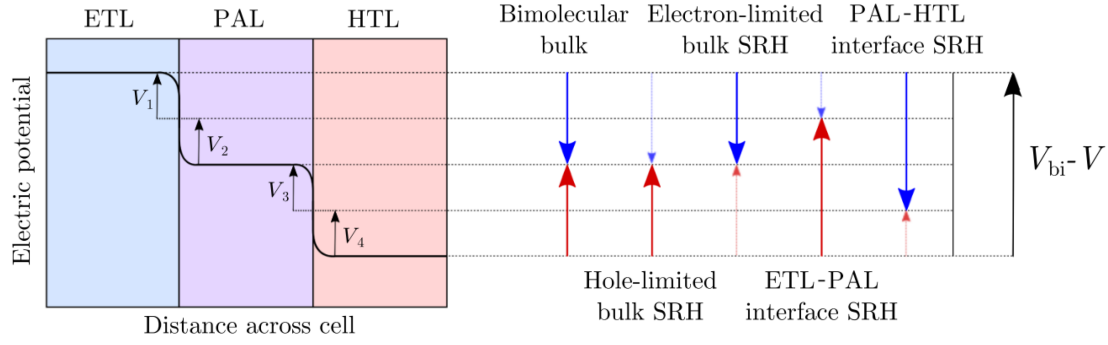


FIGURE 3.1: Illustration of the potential distribution across a PSC. At steady-state, as shown, there is no bulk electric field and the potential distribution can be split into the four potential drops V_{1-4} . The large arrows on the right indicate the potential drops that control the rate of recombination and hence the value of the ectypal factor for each recombination type. PAL stands for perovskite absorber layer and SRH stands for Shockley-Read-Hall (recombination).

Figure reproduced from ref. [135] and licensed under CC BY 4.0.

Recombination Type	$F_i(V_1, V_2, V_3, V_4)$	n_{ec}
Bimolecular	$V_1 + V_2 + V_3 + V_4$	1
Hole-limited SRH	$V_3 + V_4$	$\frac{V_1 + V_2 + V_3 + V_4}{V_3 + V_4}$
Electron-limited SRH	$V_1 + V_2$	$\frac{V_1 + V_2 + V_3 + V_4}{V_1 + V_2}$
ETL/perovskite interfacial	$V_2 + V_3 + V_4$	$\frac{V_1 + V_2 + V_3 + V_4}{V_2 + V_3 + V_4}$
Perovskite/HTL interfacial	$V_1 + V_2 + V_3$	$\frac{V_1 + V_2 + V_3 + V_4}{V_1 + V_2 + V_3}$

TABLE 3.1: Recombination types and the corresponding value of the ectypal factor, defined in equation (3.5). The function $F_i(V_1, V_2, V_3, V_4)$ is the potential barrier to recombination. The total potential drop across the cell at steady state is given by $V_1 + V_2 + V_3 + V_4 = V_{bi} - V$.

From Table 3.1, a measurement of a cell with a large potential drop at the ETL/perovskite interface, for example $V_1 + V_2 = 4 \cdot (V_3 + V_4)$, would identify an ectypal factor of $n_{ec} \approx 1.25$ if the dominant recombination mechanism were electron limited SRH in the perovskite, or $n_{ec} \approx 5$ if the dominant recombination were hole-limited SRH in the perovskite. The ectypal diode theory provides a framework to understand the voltage dependence and the high values for $n_{id} > 3$ as reported in experiment. In ref. [135], this theory is validated against numerical solutions to a drift-diffusion model, in which simulated Suns- V_{oc} and dark- $J-V$ measurements are performed. It is found that the values determined from these simulated measurements are concordant with those predicted for the ectypal factor, as defined in eq.(3.5), for each recombination mechanism.

In contrast to classical diode theory, the ectypal diode theory accounts for the ionic distribution of a PSC, which is necessary to provide a correct description of its steady-state performance. Measurement of the ectypal factor provides a way to determine the relative size of the potential drop that controls recombination. With knowledge of the sizes of the potential drops across the

cell, it may be possible to infer the recombination mechanism that limits performance. However, in practice it may be challenging to obtain an accurate picture of the potential distribution such that the exact recombination mechanism can be unambiguously determined. As such, there is a need for an equivalent to an ideality factor, applicable to PSC cell theory, that can be used to diagnose the type of recombination occurring within a perovskite solar cell.

3.2 IS background and theory

Impedance spectroscopy (IS) is a measurement technique that is widely used to study solar cells [96, 136] and many other systems, including lithium-ion batteries [137, 138], fuel cells [139, 140], corrosion [141], coatings, and paints [142, 143]. When applied to systems that involve ionic or chemical processes, such as PSCs, impedance spectroscopy is often specified as *electrochemical* impedance spectroscopy. The equipment required to measure impedance is fairly simple and inexpensive. Figure 3.2 shows an example of the apparatus used to measure the impedance of a solar cell. With suitable models to interpret the spectra, IS can provide significant insight into the properties and functionality of perovskite solar cells. In particular, the effects of ion motion can be interrogated, making it a particularly valuable technique to use in the study of PSCs.



FIGURE 3.2: Example of the apparatus required for an impedance spectroscopy measurement. Left image shows a cell under illumination with wire connections to an ‘Autolab/PG-STAT302N’ potentiostat (right) which applies the voltage perturbation and measures the current response. A frequency response analyser module is used to extract the phase and amplitude from the current response.

Impedance spectroscopy is performed by perturbing a device in steady-state with a low-amplitude alternating voltage and measuring its current response. The applied voltage, consisting of a constant (or ‘DC’) component and a sinusoidal component, can be expressed in the general form

$$V(t) = V_{\text{DC}} + V_p \cos(\omega t), \quad (3.7)$$

where V_{DC} is the steady-state voltage, V_p is the amplitude and ω is the angular frequency of the voltage perturbation. By design, the amplitude of the applied voltage perturbation is small so

that a linear current response is obtained [144]. For solar cells, a linear response is obtained for perturbation amplitudes approximately below the thermal voltage ($V_T \approx 25$ mV at room temperature). The resulting current response takes the general form

$$J(t) = J_{DC} + J_p(\omega) \cos(\omega t - \theta(\omega)). \quad (3.8)$$

Here, J_{DC} is the steady-state current density (dependent on V_{DC} and other conditions such as illumination), J_p is the amplitude of the sinusoidal component of the current density and θ is its phase relative to the voltage perturbation. The phase and amplitude of the current response is dependent on the frequency of the applied voltage perturbation. Figure 3.3 illustrates the applied voltage and current response for an impedance measurement. The complex impedance

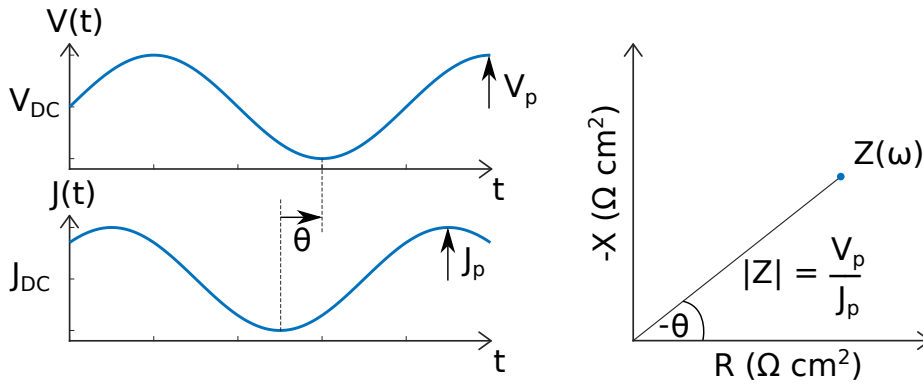


FIGURE 3.3: Left: illustration of the applied voltage and current response during an impedance measurement. Right: Nyquist plot, or Argand diagram, showing the impedance at a given frequency.

$Z(\omega)$ can be represented in the form [145]

$$Z(\omega) = |Z(\omega)|e^{i\theta(\omega)}, \quad (3.9)$$

where θ is the phase of the current density relative to the applied voltage and the magnitude

$$|Z(\omega)| = \frac{V_p}{J_p(\omega)}. \quad (3.10)$$

The real component of the impedance $R(\omega)$, is termed the resistance and the imaginary component $X(\omega)$, is termed the reactance so that the impedance can also be written in the form¹

$$Z(\omega) = R(\omega) + iX(\omega). \quad (3.11)$$

Calculating the impedance using the current *density* (as above), results in the impedance having units $\Omega \text{ cm}^2$. In the context of solar cells, this is a more general and useful representation as it enables the spectra obtained from cells with different active area sizes to be more easily compared. Impedance provides a measure of the opposition of a system to a change in voltage, and

¹Alternatively the notation Z' and Z'' is often used to represent the real and complex components of impedance respectively.

thus provides a more complete description of a system's behaviour than resistance alone. Figure 3.3 illustrates the complex impedance, determined at a given frequency, and its representation in the complex plane. The imaginary component of the impedance is typically negative and therefore it is usual to plot $-X(\omega)$ against $R(\omega)$. An impedance spectrum can be determined by performing measurements of impedance at many different frequencies, that span a wide range (typically from \sim mHz to MHz). Each impedance measurement corresponds to a point on the complex plane. The impedance of the system, measured over a wide frequency range, often traces features such as semicircles, lines or loops on the complex plane. These plots are typically called Nyquist plots [136, 146]. Frequency plots, in which the magnitude $|Z|$, phase θ , real R or imaginary X components of impedance are plotted against frequency f , more directly show a system's response at a given frequency. Examples of the Nyquist (complex plane) and frequency plots for impedance spectra are given in the following section (for example, see Figures 3.4 and 3.6). The maxima observed in the frequency plots correspond to time constants of the system. For example, these time constants may relate to particular transport or chemical processes [96]. Further information can be obtained from spectra by investigating the dependence of these time constants on temperature, illumination and voltage. [96, 147].

Impedance spectroscopy is a very powerful technique, enabling a system's response to be probed over an extremely wide range of timescales (10^{-6} to 10^4 s [144, 148]). High precision measurements can be made as the measurement can be averaged over very long periods [144]. Furthermore, perturbing the system with a low amplitude signal, gives a linear response, significantly reducing the complexity of the analysis required to interpret the results [136, 149]. In general, the current (or voltage) response of PSCs to large amplitude stimuli is highly non-linear, in part owing to the complex ionic-electronic interaction [96]. This makes IS, that obtains linear or pseudo-linear responses, a particularly useful technique. However, the additional complexity of the ionic-electronic interaction in PSCs means that the models developed for traditional and other thin-film technologies are not applicable to this technology. The following section discusses the use of equivalent circuit models to interpret and extract useful information from impedance spectra.

3.3 Equivalent circuit models

Equivalent circuits are composed of idealised electrical elements, such as resistors and capacitors, that represent a given electrical system. These simple equivalent circuit models can support interpretation and analysis of the response of electrical systems. Accordingly, experimental impedance spectra are commonly analysed using equivalent circuit models. The impedance spectra of PSCs are usually displayed in the form of Nyquist plots. In this representation, one or more semicircles are typically observed (see Figures 3.8 and 4.2 presented later for experimental and simulated impedance spectra respectively). Table 3.2 shows the symbols used to represent resistors, capacitors and inductors as well as their respective impedances.

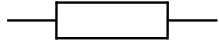
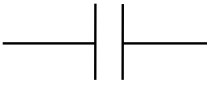

	Resistor	Capacitor	Inductor
Symbol			
Impedance	$Z_R = R_1$	$Z_C = \frac{1}{i\omega C_1}$	$Z_L = i\omega L_1$

TABLE 3.2: Equivalent circuit components and their impedances.

The total impedance within a circuit can be calculated using the same rules as those for classical resistance. For example, the total impedance for series combination is given by

$$Z_{tot} = Z_1 + Z_2 + \dots, \quad (3.12)$$

while the parallel combination of impedance gives

$$1/Z_{tot} = 1/Z_1 + 1/Z_2 + \dots. \quad (3.13)$$

In terms of equivalent circuit components, a semicircular feature is produced by a parallel combination of a resistor (R_1) and capacitor (C_1). As listed in Table 3.2, the impedance of a resistor Z_R is a constant (real) value equal to the value of its classical resistance. The impedance of a capacitor Z_C is purely imaginary and is inversely proportional to frequency. The total impedance for the parallel combination of Z_R and Z_C (as illustrated in Figure 3.4), often termed RC element, is given by

$$Z_{RC} = \frac{R_1}{1 + R_1^2 C_1^2 \omega^2} - i \frac{R_1^2 C_1 \omega}{1 + R_1^2 C_1^2 \omega^2}. \quad (3.14)$$

The impedance for this RC element is plotted in Figure 3.4 for a 50Ω resistor and a $10 \mu\text{F}$ capacitor. Adding a resistor R_s in series with the RC element shifts the semicircle along the R -axis by an amount R_s . Equation (3.14) can be recognised as an equation of a semicircle (parameterised by ω) in the R - X plane, with radius $R_1/2$ centred at $R_1/2$. The product $R_1 \cdot C_1$ corresponds to a time constant of the system, given by

$$\tau_1 = R_1 C_1 \quad (3.15)$$

$$= 1/\omega_1. \quad (3.16)$$

Consequently, distinct semicircles that appear in Nyquist plots of the impedance spectra can each be attributed to physical processes occurring on different timescales [146].

Literature often presents impedance spectra on Nyquist plots. This is convenient as slight variations to the impedance of cells can result in significant changes to the shape and size of the plots. However, they remain somewhat abstract and information about frequency is lost or, at best, limited. Complementing Nyquist plots with frequency plots and relating the spectra to

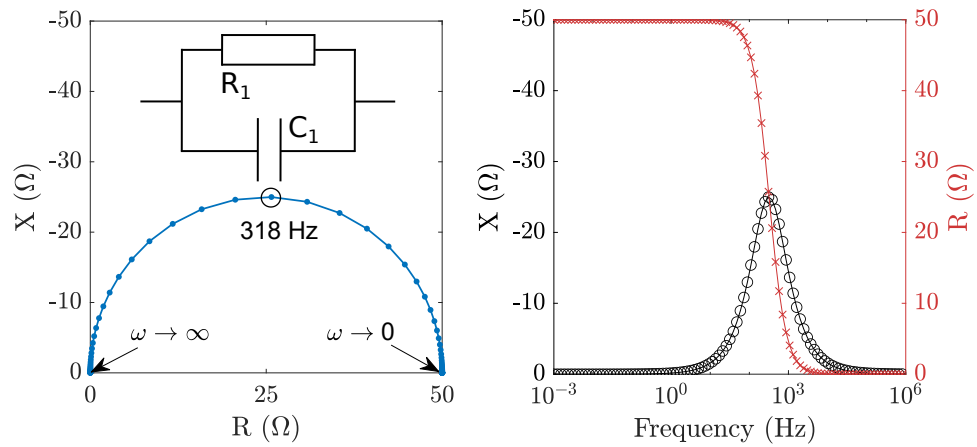


FIGURE 3.4: Impedance spectra displayed in the form of Nyquist (left) and frequency plot (right) for the RC equivalent circuit shown. The Nyquist plot displaying a semicircular spectrum is parameterised by the (angular) frequency ω . Equivalent circuit parameters: $R_1 = 50 \, \Omega$, $C_1 = 10 \, \mu\text{F}$. Time constant $\tau_1 = 0.5 \, \text{ms}$. Data points are connected with lines to aid the eye. Reactance X and resistance R are displayed as black circles and blue crosses respectively.

equivalent circuit models is essential to getting the most from impedance data. Figure 3.5 displays a three-dimensional frequency-Nyquist plot to show the relationship between the two data representations. Owing to the limited representation of frequency, two very different impedance spectra can give identical Nyquist plots. This highlights the importance of labelling frequencies and including frequency plots if necessary.

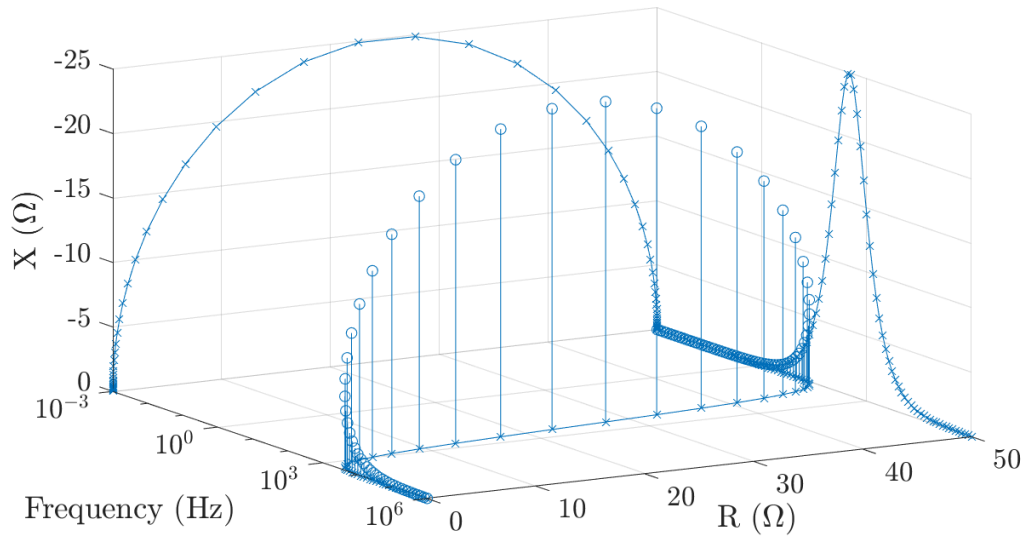


FIGURE 3.5: Three-dimensional frequency-Nyquist plot with projections onto the X - f , R - f and X - R planes. Equivalent circuit parameters: $R_1 = 50 \, \Omega$, $C_1 = 10 \, \mu\text{F}$ with 100 sample frequencies.

Nyquist plots of impedance spectra that display two semicircles can be modelled by the series combination of two RC elements (as shown in Figure 3.6c)). Calculating the impedance for this

‘ RC - RC ’ circuit, one obtains

$$Z_{RC-RC} = R_{RC-RC} + iX_{RC-RC}, \quad (3.17)$$

$$R_{RC-RC} = \frac{R_1}{1 + \omega^2 R_1^2 C_1^2} + \frac{R_2}{1 + \omega^2 R_2^2 C_2^2}, \quad (3.18)$$

$$X_{RC-RC} = -\frac{\omega R_1^2 C_1}{1 + \omega^2 R_1^2 C_1^2} - \frac{\omega R_2^2 C_2}{1 + \omega^2 R_2^2 C_2^2}. \quad (3.19)$$

Figure 3.6c) shows this RC - RC circuit and a), b) and d) plot its impedance according to equations (3.17)-(3.19). The RC elements have been labelled to indicate the high and low frequency time constants. For $\tau_{HF} \ll \tau_{LF}$ the semicircles are distinct, as is shown in Figure 3.6. However, if the time constants differ by two orders of magnitude or less, then the high and low frequency features are not distinct and the resulting semicircles may overlap, appear as a single misshapen semicircle, or one with a bulge.

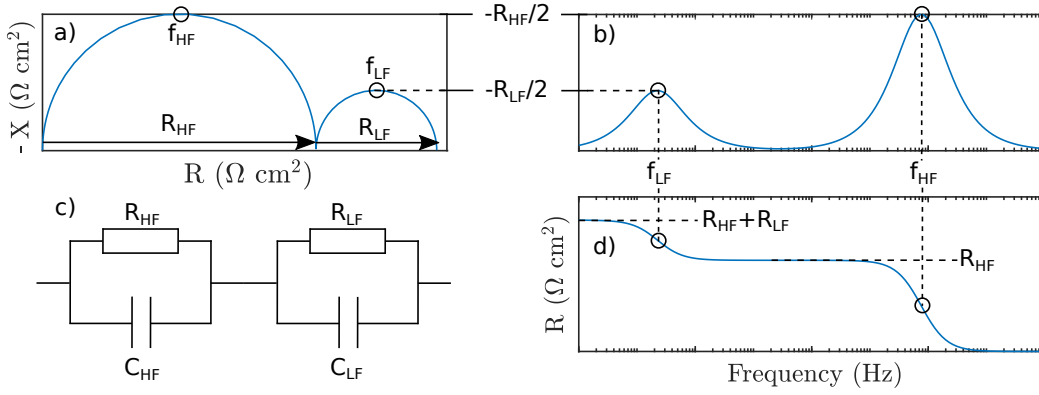


FIGURE 3.6: a) Nyquist, b) and d) frequency plots with key impedance parameters labelled for the impedance spectrum of c) an RC - RC equivalent circuit. The labelled frequencies are related to the angular frequencies via $f = \omega/2\pi$.

A series resistance R_s as $\omega \rightarrow \infty$ is regularly observed in the impedance spectra of solar cells [96, 150]. On the J - V curve, a large series resistance reduces the gradient at the open-circuit voltage [14]. This series resistance is attributable to the resistance of the contact layers as well as the experimental apparatus [151]. Consequently, a series resistor is added to the circuit shown in Figure 3.6. This equivalent circuit has been used to model the full impedance spectra of PSCs [152].

It is important to note that the Nyquist plot shown in Figure 3.6 is not unique to the RC - RC circuit shown in Figure 3.6c). Other equivalent circuits with two time constants, also produce identical Nyquist plots [152, 153]. Examples of such circuits are shown in Figure 3.7b and c). The particular configuration of elements should be justified in relation to the physical system being modelled.

With an appropriate cell model, fitting equivalent circuits to impedance measurements enables useful cell parameters to be determined. It should be noted that fitting equivalent circuit models to the feature rich impedance spectra of PSCs is generally inexact. This is because equivalent

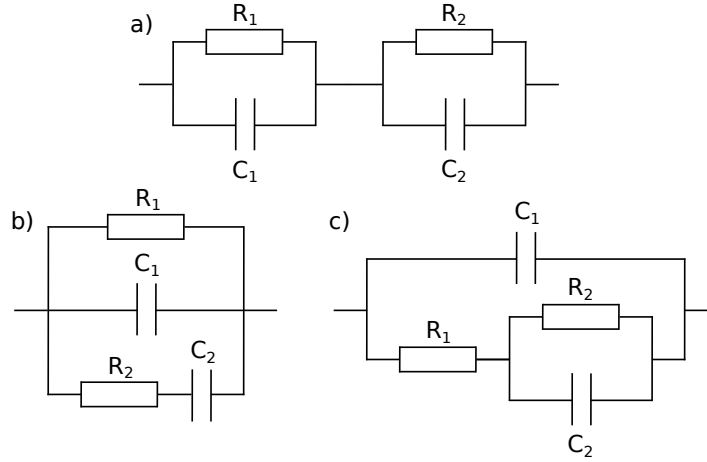


FIGURE 3.7: Equivalent circuit diagrams that can each model an impedance spectrum that exhibits two semicircles [152, 153].

circuit model representation is not unique and additional components can be included to significantly improve fit to data; however, they may have no relation to the solar cell's operation. Whilst it is important to understand their limitations, equivalent circuit models are a valuable tool to extract useful information and can be used to improve physical understanding of the system. Providing a mathematical argument for a particular equivalent circuit model is critical to justify their use as an analogue of physical systems.

3.4 Impedance spectra of PSCs

Throughout the development of PSCs, impedance spectroscopy has been widely used to study their properties. This has been facilitated by the extensive experience developed by research groups using these techniques to study dye-sensitised solar cells and other thin-film photovoltaic devices [154, 155]. However, owing to the unusual features seen for PSCs, and a lack of suitable models, there remains uncertainty as to how to correctly interpret spectra and extract physical parameters from them.

Generally, although not always, IS is performed on full perovskite devices that include transport layers and contacts [156]. The applied voltage typically ranges from short-circuit to the open-circuit voltage of the device under light and in the dark. The frequency range of the applied perturbation is typically around 10^{-2} - 10^6 Hz and its amplitude V_p is ~ 20 mV [95, 131, 147, 154, 157–162]. In practice, the amplitude of the voltage perturbation is a balance between obtaining a linear response and having a reasonable signal to noise ratio. Spectra can vary quite considerably across measurement protocols, device composition and architectures. Overall, spectra plotted on Nyquist diagrams loosely share the same form as that of Figure 3.6 [147]. Examples of real PSC impedance spectra obtained at V_{oc} under illumination are shown in Figures 3.8 and 3.9.

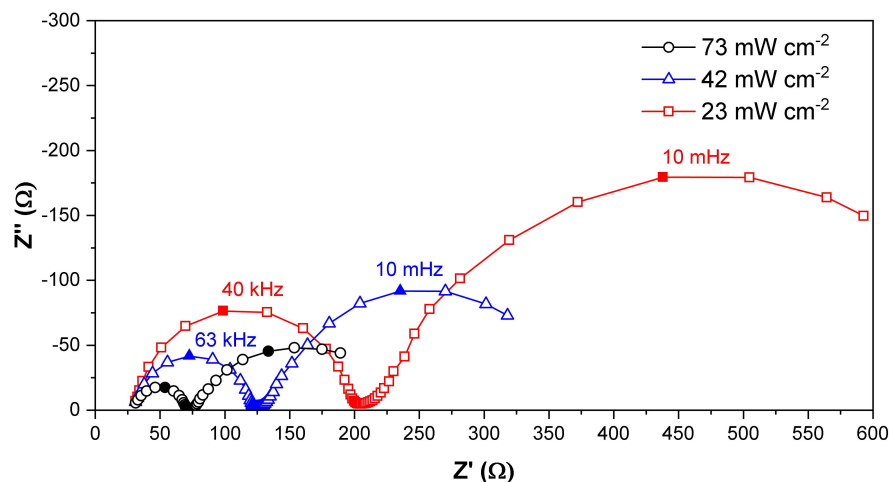


FIGURE 3.8: Nyquist plots showing examples of impedance spectra for a PSC ($\text{TiO}_2/\text{MAPbI}_{3-x}\text{Cl}_x/\text{Spiro}$). Measured at open-circuit under blue LED illumination at three different intensities. Z' and Z'' correspond to the real and imaginary components of impedance respectively. The 73 mW cm^{-2} intensity produced a photocurrent equivalent to 1-Sun AM 1.5 illumination. Figure reproduced from ref. [163] with permission.

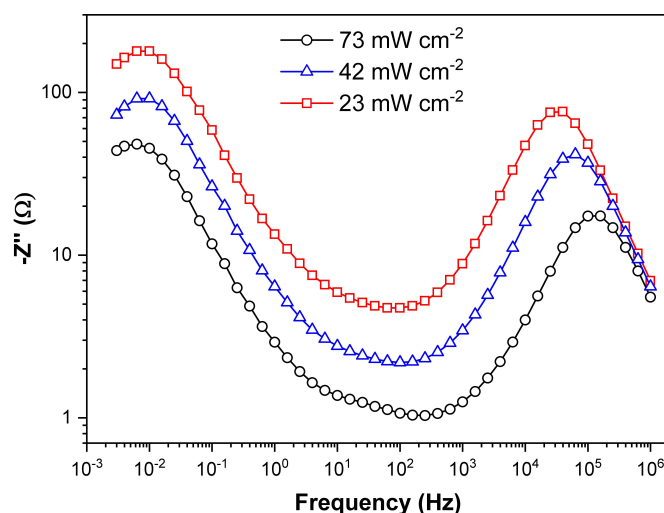


FIGURE 3.9: Corresponding frequency plot for the impedance spectra presented in Figure 3.8. The imaginary component of the impedance is plotted against frequency. Figure reproduced from ref. [163] with permission.

Increasing from low to high frequencies, the semicircular features are traced from right to left. These semicircles vary in radius, relative size to one another, and may only be partially resolved [131, 151]. Interestingly, the low frequency feature can lie below the axis, which corresponds to positive reactances [158, 159, 164]. Furthermore, other features are occasionally observed at intermediate frequencies, including loops and bulges [95, 96, 154, 157, 161]

It is evident here, and in the literature, that the radii of the semicircles are reduced as the voltage is increased towards open-circuit [163]. This can be understood by considering the gradient of a J - V curve (e.g. see Figure 2.4) [165]. Near short-circuit, the gradient is shallow corresponding to a large resistance. As the voltage is increased to near open-circuit, small changes in voltage

result in significant changes in current output and hence there is a low associated resistance. Some literature presents results of IS over a limited frequency range. This can result in features only being partially traced and not fully captured. Care must be taken when interpreting these features. The following subsections detail the features observed in PSC impedance spectra and discuss their origin.

3.4.1 High frequency feature

When plotting the impedance spectra for PSCs on a Nyquist diagram, a semicircular feature is traced over frequencies around 10^4 - 10^6 Hz [96, 147]. For example, this feature corresponds to the left semicircle, for a given illumination, in Figure 3.8. Given that this feature is approximately semicircular, there is a resistance associated with the diameter of the semicircle and a capacitance related to the frequency that it is observed. The origin of this feature, henceforth referred to as the high frequency (HF) feature, has been attributed to many mechanisms. For the capacitance, this includes; geometric [96, 125, 131, 166], double-layer [167], chemical [159] and depletion capacitances [162]. The resistance associated with the HF feature R_{HF} has been attributed to; recombination [96, 131], electron and hole transport [157, 168] and ion motion resistances [151]. The present understanding is that this feature arises from the geometric capacitance and recombination resistance of the cell [96, 125, 131, 157]. The geometric, also termed junction or contact capacitance, is given by [157, 166]

$$C_{\text{Geo}} = \frac{\epsilon_p \epsilon_0}{b}, \quad (3.20)$$

where ϵ_p is the relative permittivity of the perovskite, ϵ_0 the vacuum permittivity and b is the perovskite width. This geometric capacitance (per unit area) is equivalent to parallel-plate capacitance, where the perovskite is the dielectric material and the transport layers or contacts function as the parallel plates [157, 166]. Pockett *et al.* found that the measured capacitance of the HF feature remains constant across different applied voltages [96]. Independence of the HF capacitance C_{HF} with illumination has also been demonstrated [147]. Guerrero *et al.* also measured this capacitance with varying perovskite width, finding that it is inversely proportional to the perovskite width [157]. These findings are consistent with the geometric capacitance, as defined in eq.(3.20).

The value of the HF capacitance has been found to be around 100 - 650 nF cm⁻² [96, 131, 147]. Notably, predictions of the HF capacitance via eq.(3.20) can result in values too small by a factor of up to around 10. This discrepancy can be reconciled via a ‘roughness factor’ that accounts for the imperfect and rough planar interfaces between the perovskite layer and the adjacent transport layers in a PSC, in comparison to an idealised parallel plate capacitor [131]. As such, including a roughness factor (in the numerator of eq.(3.20)) means that the value predicted from a geometric capacitance is in line with experimental measurements.

The recombination resistance is defined [129, 169]

$$R_{\text{rec}} = \left(\frac{dJ}{dV} \right)^{-1}. \quad (3.21)$$

As defined above, the recombination resistance scales linearly with illumination intensity. Given that the resistance extracted from the HF feature R_{HF} also displays a linear dependence on the light intensity, this suggests that R_{HF} is proportional to a recombination resistance [96, 129, 131, 169].

3.4.2 Low frequency feature

The low frequency (LF) feature is observed in the impedance spectra at frequencies around 10^{-2} - 10^1 Hz [96, 147, 170]. This is perhaps the most unusual feature of the impedance response of PSCs. This is because it is indicative of a slow process, occurring roughly on the timescale of seconds, which is unusual for solar cells, whose response are typically only governed by electronic processes occurring over much faster timescales. This LF feature is usually apparent as a semicircle to the right of the HF feature on a Nyquist plot, or a peak in the reactance versus frequency plot. An example of a LF feature observed in a PSC impedance spectra is shown in Figure 3.8. In the Nyquist plot representation, a semicircular feature above the axis usually corresponds to a process with an associated capacitance. Interestingly, the LF feature can lie below the axis on the Nyquist plot, which can be associated to a ‘negative capacitance’ or an inductive feature [171–175]. An example of an impedance spectrum with a ‘negative’ LF feature is shown in Figure 3.10. Some references refer to this feature as an ‘inductive loop’ [174]; however, to ensure clarity for later discussion of a different ‘loop’ feature, henceforth this is referred to as a negative LF feature. The negative LF feature is observed for regular and inverted cell configurations [175] [174], and for cells without transport layers [164]. Here, we note that the semicircles displayed on Nyquist plots for experimental spectra are often imperfect, or ‘flattened’. In contrast, those determined from the equivalent circuit models presented in Section 3.3, or drift-diffusion models, are typically exact semicircles. The possible cause for this discrepancy is discussed in Section 4.3.1.

Extracting the capacitance from the (positive) low frequency feature yields extremely high capacitances. These can be as large as 10^{-2} - 10^0 F cm⁻² [115, 147, 162]. This capacitance was first reported as a so-called ‘photoinduced giant dielectric constant’ [177]. This report garnered significant interest and stimulated considerable debate over its physical origin [99, 178, 179]. Some of the proposed explanations include; giant dielectric effects and relaxation [95, 167, 168, 177], electronic and ionic accumulation at contacts [157], electrochemical reactions [164], ionic diffusion [151], ionic motion and its impact on recombination and charge injection [96, 125] and trap states [180–182].

Evidence indicates that this LF feature is a result of ions moving in response to the voltage perturbation, which effects the charge injection/extraction and recombination of electrons and

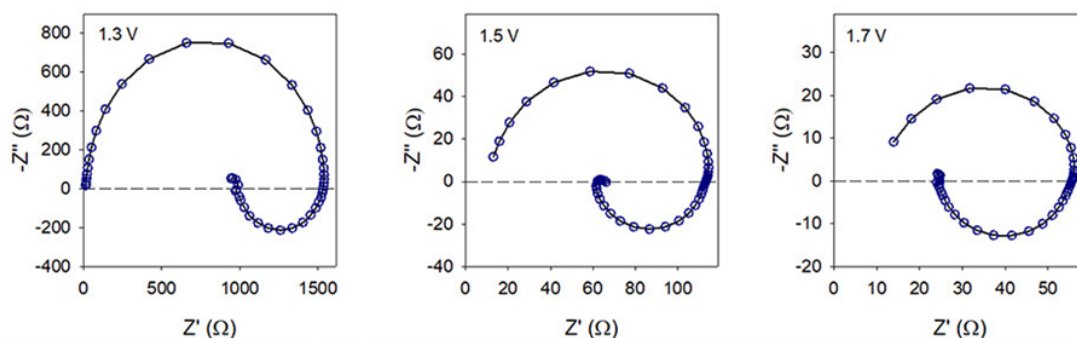


FIGURE 3.10: Examples of experimental impedance spectra of a PSC with negative low frequency features. Measured for a complete methylammonium lead bromide perovskite solar cell under an inert atmosphere at different DC voltages. Adapted with permission from [176]. Copyright 2021 American Chemical Society.

holes [96, 125, 158, 183]. This interpretation is justified as the resistance associated with the LF feature has approximately the same dependence on light intensity as the HF resistance [96, 147]. Additionally, groups have performed IS measurements at a range of temperatures and extracted an activation energy for the associated mechanisms responsible for the LF feature [96, 147, 184]. These activation energies are in line with other calculations of activation energies for iodide ($\sim 0.45 - 0.6$ eV) and MA^+ ($\sim 0.5 - 0.85$ eV) [70, 110] vacancy migration.

The proposed physical origin of the LF feature as an ionic modulation of the current output demonstrates that the capacitance (and negative capacitance) associated with the LF feature is not a true capacitance, i.e. not the result of charge storage. Although the probable physical mechanisms for the low and high frequency features have been identified, the precise conditions for when a negative LF feature is observed are yet to be established. Additionally, it is not yet clear how to extract device properties from the spectra. This highlights the importance of physics-based PSC device models to specify the exact impedance response of PSCs.

3.4.3 Intermediate frequency features

More exotic features, other than the high and low frequency features discussed so far, can be observed in the Nyquist plots of impedance spectra for PSCs. For example, these include a third semicircle between the low and high frequency features, or a bulge to one of the semicircles [185, 186]. Additionally, loops between the low and high frequency semicircles have also been observed [157, 161, 175], as well as ‘spirals’ [95, 176] or multiple negative features [171, 173, 175]. Henceforth, we refer to this varied group of exotic features as intermediate frequency (IF) features. Examples of some of these IF features that have been observed in experiment are displayed in Figure 3.11.

When resolved, IF features can be observed at a wide range of frequencies, 10^{-1} - 10^4 Hz [96, 175, 175, 185]. The exact physical origins for these features have yet to be conclusively determined. One possibility is that some of these features are an artefact of performing IS under

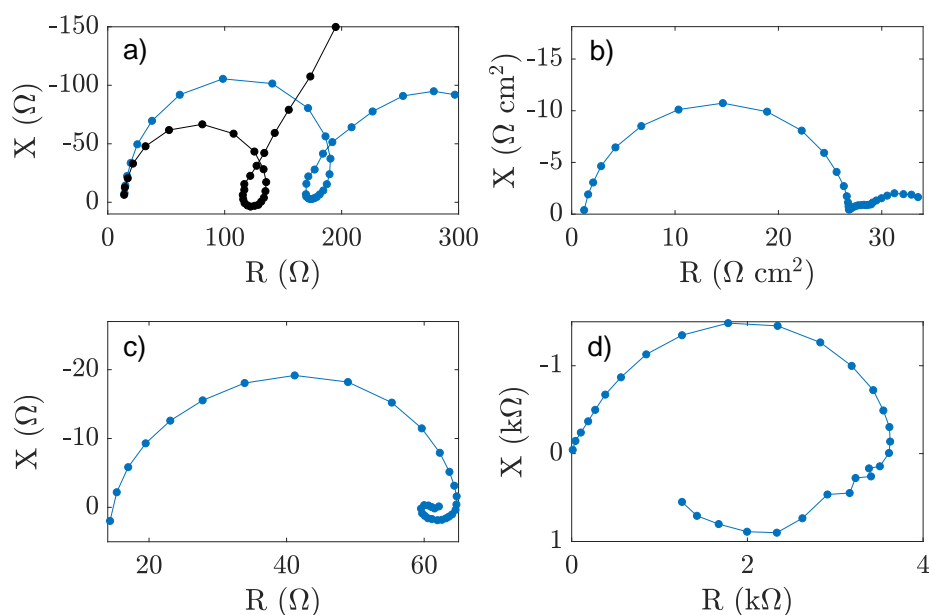


FIGURE 3.11: Representative examples of impedance spectra from PSCs that show intermediate frequency, or ‘exotic’, features. a) loop feature, reproduced from IS data presented in ref. [157]. b) ‘bulge’ feature shown in data obtained from ref. [186]. c) ‘spiral’ feature, reproduced from data from ref. [95]. d) two negative features, data sourced from ref. [173].

non-steady-state conditions [158, 187]. Moia *et al.* demonstrate that loops between the LF and HF features can be observed, when otherwise are not apparent, for spectra obtained with insufficient stabilisation prior to measurement [158]. This could be a result of residual ion motion from a cell that is not properly stabilised before, or degradation during, the measurement. The inherent instability of PSCs and the transient effects of ion motion means that extra care should be taken to ensure reproducibility of the impedance measurements. These results indicate that loops between the LF and HF features are not an intrinsic part of the impedance response for PSCs. However, Jacobs *et al.* demonstrate that loops can be exhibited using a drift-diffusion model of a PSC in certain parameter regimes [125]. Given that the simulation can be guaranteed to be at steady-state, this suggests that loops may indeed be a true feature of the impedance response of some PSCs.

Pockett *et al.* demonstrate that the IF feature, arising as a bulge to the LF feature has an associated activation energy and shares the same dependency on light as the LF feature. This leads them to a similar interpretation for its origin [96]. They propose that the two activation energies, determined from the LF and IF features, may correspond to I^- and MA^+ , or a single ionic species that diffuses at a different rate depending on its location (e.g. within the bulk or along grain boundaries) [96]. Fully understanding the mechanism responsible for this IF feature could enable information about the number of mobile ionic species and their mobilities.

Inductors have been employed in the equivalent circuit modelling of negative capacitances and

loop features [161, 171, 174]. The inductance, or negative capacitance, observed is a consequence of other mechanisms that resemble these components. As such, their physical interpretation should remain distinct [125]. Furthermore, it is important to note that these IF features are not always observed. The ability to resolve these features within the spectra is highly dependent on the light and bias of measurement, as well as device composition. This variability between the spectra obtained by different groups has hindered progress towards understanding their physical origin. The complex effect of ionic distribution on recombination and charge injection has been put forward to explain these features, as well the LF features [125, 158]. Whilst this seems most probable, this interpretation still requires considerable investigation to determine the exact physics responsible.

3.4.4 Trends of the low and high frequency features

While the impedance response of PSCs display a rich variety of features, that are sensitively dependent on device composition and experimental conditions, Contreras-Bernal *et al.* identify the following commonly observed characteristics [147]:

- i) Two (or more) features, corresponding to time constants that are visible as peaks in frequency plots or semicircles/arcs in Nyquist plots.
- ii) The characteristic frequency of the LF feature is independent of DC voltage, whereas the characteristic frequency of the HF feature increases exponentially with DC voltage.
- iii) Both of the resistances associated with the low and high frequency features (R_{LF} and R_{HF} respectively) decrease exponentially with DC voltage.
- iv) The capacitance associated with the HF feature is independent of DC voltage, for low voltages, while the capacitance associated with the LF feature increases exponentially with open-circuit voltage. This is implicit given ii-iii) and that the time constant $\tau = RC$.

The low and high frequency resistances and capacitances are determined via fitting to an RC - RC equivalent circuit, as shown in Figure 3.6c. Note that i-iv) are compatible with cells that display a negative LF feature. These trends with DC voltage (or illumination) appear to be characteristic features of the impedance spectra of PSCs [96, 147, 163]. Therefore, these should be reproduced by models that aim to describe the fundamental impedance response of PSCs.

3.5 Prominent models

Accurate device models are essential to interpret and extract useful information from the results of impedance spectroscopy measurements. The complex operation of PSCs has hindered efforts to derive device models that can suitably capture the fundamental operation of PSCs. In this

section, four notable models that have been developed to interpret the impedance spectra of PSCs are reviewed.

In the work by Neukom *et al.* the simulated impedance response of a PSC is compared to experimental measurements [183]. The simulated measurements are produced using the PSC simulation tool, SETFOS from FLUXiM [183, 188]. In addition, the impact of mobile ions and device parameters on various simulated measurements and overall efficiency are studied. With a single parameter set, they demonstrate that the drift-diffusion model can realistically reproduce the general response of a PSC to a number of different measurement protocols.

The simulated measurements are obtained using the commercial software package, SETFOS from FLUXiM [183, 188]. This tool numerically solves a one-dimensional drift-diffusion model for the three core layers of a planar PSC. In this study, one negative and one positive species of mobile ions are modelled within the perovskite layer. Neukom and coworkers conduct comparison of many different experimental measurements and simulations for a planar PSC (TaTm/MAPi/C₆₀). These characterisation techniques include J - V , intensity modulated photocurrent spectroscopy (IMPS), impedance spectroscopy, Suns- V_{oc} and transient photocurrent measurements. The impedance spectroscopy results are presented in the form of capacitance versus frequency plots and are conducted under illumination, and in the dark at 0 V. The simulated results for IS and the other characterisation methods show reasonable agreement with experiment. However, given the broad scope of the paper, only a limited number of impedance results are presented. Notably, it was found that mobile ions within the perovskite layer were required for the simulated measurements to reproduce the experimental measurements they conducted on TaTm/MAPi/C₆₀ cells. Additionally, SRH recombination and low interfacial recombination were necessary to reproduce their measurements. Interestingly, they show that simulations with only mobile anion vacancies do not differ significantly from those with both mobile anion and cation vacancies.

Jacobs *et al.* [125] use numerical simulations of a coupled ionic-electronic drift-diffusion model, based on the work of various groups, to describe the impedance response of PSCs [6, 105, 118]. They focus on interpreting the impedance spectra of PSCs in terms of the AC capacitive component $C = \omega^{-1} \text{Im}(Y(\omega))$, where susceptance $Y(\omega) = 1/Z(\omega)$. As such, they consider the continuity equation for the electron density within the device to derive an expression for the apparent capacitance. This is found to have two contributions. The first, they label C_Q , corresponds to the usual (classical) definition of capacitance involving physically stored charge. The second, A_R , still with units of capacitance, corresponds to a phase-delayed recombination current. This component can be positive or negative, which they reason is responsible for the negative capacitance and loop features observed in IS of PSCs. This distinction between apparent capacitance arising from physically stored charge and phase-delayed capacitance greatly aids interpretation of IS data and enables reasonable explanations to be formed. This is the primary focus of their work and, on analysing their numerical solutions, they reach similar but

more general conclusions than Pockett *et al.* [96], by describing the low and intermediate features observed in the impedance spectra of PSCs in terms of the ionic distribution's ability to increase or decrease recombination and injection/extraction.

While the model equations are not explicitly stated, this work is reported to employ a one-dimensional coupled ionic-electronic drift-diffusion model in line with the models developed by van Reenan *et al.* [118], Richardson *et al.* [6] and Calado *et al.* [105]. With the exception of Fig. 1 in ref. [125], one mobile ionic species is modelled and constrained to the perovskite layer. The adjacent transport layers are also modelled. Numerical solutions were obtained using COMSOL Multiphysics integrated with MATLAB [189, 190] and the impedance was calculated using a Fourier transformation of the current [125]. Upon research, the exact PSC drift-diffusion model equations used in this work could not be found.

Interestingly, Jacobs *et al.* investigated how the impedance spectra could deliver information about hysteresis, which is typically quantified from J - V measurements [125]. Specifically, they plot $\text{Im}(Y(\omega))$ versus frequency (where $Y(\omega) = 1/Z(\omega)$) and compare this to different hysteresis indices for J - V curves measured at various scan rates. Converting scan rates to frequencies, they observed that below $\sim 10^3$ Hz, the frequency dependence of the magnitude of $\text{Im}(Y(\omega))$ generally corresponds to that of the measured hysteresis. The benefits of employing IS instead of J - V measurements is the simplicity of measurement as well as being able to probe frequencies that are difficult to reach in J - V measurements. Furthermore, IS can be carried out at the maximum power point of the cell, providing information that is more relevant to the real world operation of the cell [125].

Using their numerical model, Jacobs and coworkers were able to reproduce the so-called giant LF capacitance and negative capacitances that are observed in experiment [125]. To reproduce the loops between the LF and HF features that are sometimes seen in experiment, Jacobs *et al.* note that the density of carriers within the perovskite needed to be increased significantly in their simulations [125]. They reason that the loops, like the LF feature, are due to the component of apparent capacitance arising from a phase-delayed recombination current. To obtain dark LF capacitances as high as observed in their experimental measurements (above $50 \mu\text{F cm}^{-2}$), surface states needed to be added at the perovskite/transport layer interfaces, which are hard to justify physically. This was to increase the ionic charge stored at the interfaces.

Unlike drift-diffusion models, analytic models are able to justify the use of a particular equivalent circuit model and directly show the relationship between specific device parameters and their impact on the impedance spectra. However, the complexity of the coupled ionic-electronic response has meant that it is challenging to derive an accurate analytic model. Two notable papers that propose equivalent circuit models via examination of the underlying physics of operation of PSCs are the works by Moia *et al.* [158] and Ghahremanirad *et al.* [161].

Moia *et al.* propose an equivalent circuit model that incorporates transistors to couple the effect of ionic motion to the electrical output of the cell [158]. Through comparison to both simulated impedance from a drift-diffusion model and experimental measurements, they demonstrate that

transistors enable the general impedance response of a PSC to be reproduced effectively. The treatment of the interfaces as transistors provides a more realistic picture of the coupled ionic-electronic physics of operation for PSCs than a simple diode model. This helps to deliver insight into the impedance response of PSCs and offers an alternative to numerical drift-diffusion models for the simulation of PSC behaviour.

To arrive at an equivalent circuit model, Moia *et al.* apply detailed balance at equilibrium to determine relations that describe the current as a function of potential drops at the interfaces [158]. They identify these current equations to be analogous to those that describe bipolar transistors. The transistors, one at each interface, are controlled by the ionic environment within the perovskite and the externally applied bias. As a result, the ionic distribution controls the flow of current at the perovskite/TL interfaces. Based upon this argument, an equivalent circuit model is proposed with either one or two transistors (depending on whether the cell response is controlled by a single or both interfaces). The transistors are controlled by an ionic circuit branch that modulates the electronic circuit. This equivalent circuit model is shown to fit impedance spectra measured for hybrid metal halide PSCs. Additionally, the equivalent circuit was fitted to simulated impedance measurements obtained using the open-source software, Driftdiffusion [105, 191, 192]. This tool numerically solves the charge transport model described by Calado *et al.* [105], which is equivalent to other drift-diffusion models of a planar PSC, based on a single mobile ion species in the perovskite layer and mobile charge carriers throughout the device. [4, 118, 183].

Their equivalent circuit model, and drift-diffusion model, reproduce the characteristics of the HF and LF features in addition to the LF ‘inductance’ or negative capacitance as observed in experiment. In these models, the LF response is reproduced via the coupling of the ionic distribution with the recombination and electronic charge injection. These interpretations for the apparent capacitance are in line with Jacobs *et al.* [125]. Interestingly, extension of their equivalent circuit model to include the penetration of ions into, and reversible chemical reactions at, a perovskite/TL interface predicts both positive and negative apparent capacitances.

Whilst this equivalent circuit model is intuitively appealing, and based on reasonable physical assumptions, it lacks formal justification and hence it is not possible to directly relate the parameters of the devices connected in the equivalent circuit to real physical parameters of the PSC. Indeed, attempting to formally derive such an equivalent circuit model (based on transistors) from a drift-diffusion model of a PSC, using formal asymptotics, could potentially result in an interesting and valuable contribution to the field.

Ghahremanirad *et al.* propose an equivalent circuit model to explain the negative capacitance and loops observed in the impedance spectra of PSCs [161]. In their work, they employ a surface polarisation model, developed by Ravishankar *et al.* [193], to justify a particular equivalent circuit model and help understand the physical processes responsible for the exotic features.

The surface polarisation model employed by Ghahremanirad *et al.* [161] was previously used to simulate hysteresis and other transient techniques and models the accumulation of holes and

positive ionic charge at the ETL/perovskite interface [193]. The accumulation of charge forms an energy barrier that modifies the recombination current. They show that with parameter fitting, the surface polarisation model can reproduce the experimentally observed hysteresis. Using semiconductor diode theory and applying this surface polarisation model, Ghahremanirad *et al.* transform to the frequency domain to determine an expression for impedance [161]. They attribute the model parameters to resistors, capacitors and an inductor to form the equivalent circuit model shown in Figure 3.12. They show that by fitting the seven component values, this circuit can reproduce the experimental spectra of MAPI cells that display loops between the LF and HF features and negative LF features.

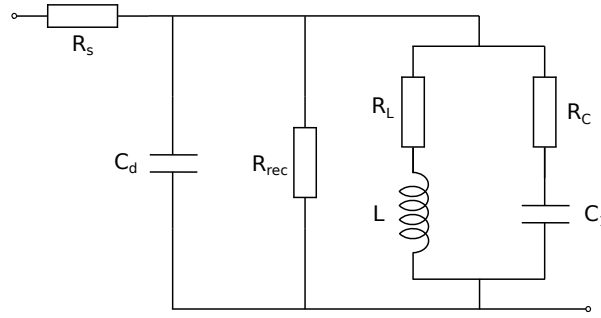


FIGURE 3.12: Equivalent circuit model for the impedance response of a PSC proposed by Ghahremanirad *et al.* [161].

Figure 3.12 shows the equivalent circuit model derived by Ghahremanirad *et al.* [161]. The capacitor C_d was added empirically to represent the capacitance associated with the high frequency bulk dielectric or surface properties of the cell. From the underlying surface polarisation model, Ghahremanirad *et al.* find that increasing the charge stored for a given voltage (i.e. capacitance), as well as the relaxation constant (which quantifies the lag between the applied voltage and the internal surface polarisation voltage), results in a loop forming between the high and low frequency features. Increasing these further, the low frequency feature dips below the axis to form a semicircle corresponding to ‘negative capacitance’.

The experimental spectra that Ghahremanirad *et al.* [161] fit their equivalent circuit model to were obtained from MAPI cells with modified electron transport layers [194]. Specifically, alternate layers of compact TiO_2 and mesoporous SnO_2 were stacked on top of the FTO contact before MAPI was deposited. The porosity of these layers means that the perovskite can fill the mesostructure. The impedance spectra of these cells display distinct loops between the LF and HF feature, that can dip below the axis. The size of the loops are roughly proportional to the number of TiO_2 and SnO_2 layers [194]. This modified MAPI architecture lends itself to the surface polarisation model derived by Ravishankar *et al.* [193], in which a larger energy barrier is expected at the ETL/Perovskite interface. However, Kelvin probe force microscopy (KPFM) measurements have shown that in general, the electric potential is distributed across both perovskite/TL interfaces [195–197]. Therefore, the equivalent circuit model proposed by Ghahremanirad *et al.* may not be a suitable analogue for the impedance response of PSCs. The surface polarisation model developed by Richardson *et al.* [6] and Courtier *et al.* [4, 5], is entirely

consistent with the underlying drift-diffusion model of the ionic-electronic motion in the cell. It therefore provides a much better representation of evolution of the electric potential in a PSC, as shown in Figures 3.1a) and 5.2.

The benefit of the equivalent circuit model presented in Figure 3.12, is that the resistor, capacitor and inductor values are related to device parameters such as the recombination current and ionic relaxation times [161]. However, this equivalent circuit is not properly derived from their phenomenological surface polarisation model, which in itself is only capable of capturing cell behaviour in a very broad sense. Furthermore, an additional parameter was added in order to obtain a better fit to experiment. A more general underlying device model is required to define this parameter.

3.6 Summary

This chapter introduces the ideality factor and describes the experimental impedance measurements for PSCs. It thus sets the context for the remaining chapters. Measurement of an ideality factor is a widely used technique to evaluate the performance and infer the type of efficiency loss occurring within a solar cell. However, when techniques such as the Suns- V_{oc} or dark- $J-V$ methods are applied to PSCs, high $n_{id} > 3$ and voltage dependent values have been reported [128–131]. These values can be explained using ectypal diode theory, as opposed to classical diode theory, which accounts for the ionic distribution of a PSC [135]. With this framework, typical methods to determine the ideality factor in fact return the ectypal factor, which is defined as the ratio of the total potential drop across the cell to the potential that forms a barrier to recombination. If the sizes of the potential drops across the cell are known, then it may be possible to infer the recombination mechanism that limits performance through the value of the ectypal factor. However, in practice, determining the potential distribution to a high enough accuracy may be challenging. As such, this motivates us to formulate a method to determine a true ideality factor for PSCs. This is described in further detail in Chapter 6.

Impedance spectroscopy is a measurement technique that involves the application of a DC voltage with an additional small sinusoidal perturbation and measuring the sinusoidal current response. By analysing the response of a cell at many different frequencies, spanning a range from mHz to MHz, important device properties can be determined. This analysis is often performed by fitting to an equivalent circuit, which enables resistances, capacitances, and time constants to be extracted from the impedance spectra. For more established solar cell technologies, these equivalent circuits have been derived from fundamental theory, and enable the characteristics extracted from spectra to be related to device properties. However, for PSCs it is not yet clear which equivalent circuit should be used, or how the resistances and capacitance are related to fundamental device properties.

Advancement towards even a qualitative understanding of the impedance response has been challenging due to the varied and unconventional impedance response that PSCs exhibit. Spectra

generally display two features, corresponding to a high frequency response and a low frequency response. The HF feature, is typically observed at around 10 to 100 kHz and is apparent as a semicircular feature above the axis on a Nyquist plot [96, 147]. The overall consensus is that the associated resistance and capacitance has been attributed to the recombination resistance and geometric capacitance of the cell [96, 125, 131, 157]. The properties of the low frequency feature are particularly unusual for a solar cell. Observed at frequencies around 10 mHz to 10 Hz, this feature is approximately semicircular and can lie either above or below the axis on a Nyquist diagram [96, 147, 170, 176]. The very high positive (or negative) capacitance associated with this feature is not a true capacitance. Instead, evidence indicates that the LF feature is a result of ions moving in response to the voltage perturbation, which affects the charge injection/extraction and recombination of electrons and holes [96, 125, 158, 183]. This proposed ionic modulation of the current output can account for the very high, and negative, capacitances extracted from PSC impedance spectra.

Furthermore, exotic or intermediate frequency features have been observed. These include loops between the low and high frequency semicircles, or additional semicircles that lie above or below the axis on a Nyquist plot. If apparent in the spectra, these features can be observed between around 0.1 Hz to 10 kHz [96, 175, 175, 185]. It has been demonstrated that insufficient stabilisation can cause loops; however, some evidence suggests these may be a fundamental feature of the impedance response of PSCs [125, 158]. The exact physical processes responsible for these features have yet to be conclusively determined.

While accurate device models are essential to extract all of the information from impedance spectra, the development of models for PSCs has been hindered due to the complexity of their operation. In Section 3.5, the leading models that include the physics of mobile ions are reviewed. Overall, there are a limited set of numerical simulation tools available for researchers to use and better understand the impedance response of PSCs. Additionally, an analytic model has yet to be systematically derived from a coupled-ionic electronic drift-diffusion model. This would justify a particular equivalent circuit and enable the extraction of physical parameters from the impedance spectra of PSCs. Finally, a dedicated study on how recombination impacts the impedance spectra of PSCs has not been performed.

In summary, this chapter details the impedance response of PSCs, as reported in the literature. An opportunity for drift-diffusion modelling to provide further insight into the impedance response of PSCs is identified. In the following chapter, a method of simulating impedance spectroscopy measurements is formulated based on a charge transport model of the cell. This drift-diffusion modelling approach is shown to reproduce the features observed in experiment. Chapters 5 and 6 present the derivation and results of an analytic model derived via approximations to the model set out in the following chapter.

Chapter 4

IS modelling and results

In addition to applications in semiconductor physics [198, 199], drift-diffusion, or equivalently, charge-transport equations can be applied to a broad range of systems. Some of these applications include modelling the electrodiffusion of ions in biological systems [200, 201], electrolytes and ionic diffusion in chemical systems [202–204], and the dynamics of fluids in electric fields [205]. Rather than modelling the kinetics of individual charged particles, which is impractical on device scales, drift-diffusion models provide a macroscopic description of the charge densities and potential within the system. This approach is capable of modelling the steady-state and time-dependent operation of perovskite solar cells and enables current-voltage measurements of PSCs to be simulated [6, 105, 118].

A lack of appropriate models for the impedance of PSCs has meant that impedance spectroscopy is underused, and its results are often misinterpreted. In this chapter, we detail a drift-diffusion model that includes the coupled ionic-electronic dynamics required to suitably describe the response of PSCs during impedance measurements. We summarise the formulation of an ‘IS module’ for the open-source PSC simulator, `IonMonger` [106, 206]. This adds the capability of simulating IS measurements via numerical solution to the drift-diffusion model. A selection of impedance spectra are presented for different simulated measurement conditions. The low and high frequency features, as observed in experiment, are reproduced by the model. This includes the so-called ‘giant’ LF capacitance, that can either be positive or negative. The trends with illumination, universally observed in experiment, are also reproduced. Additionally, we demonstrate that under particular conditions, the model predicts the intermediate frequency features that have been observed in experiment, including loops and additional arcs. These results validate the underlying charge transport model as a means to describe the impedance response of PSCs. Finally, we present a framework to better understand the fundamental response of PSCs during IS measurements.

In the first section of this chapter, a drift-diffusion model for a PSC is specified. In Section 4.2, a

module for `IonMonger` is detailed, which enables simulation of impedance spectroscopy measurements. Section 4.3 presents simulated impedance spectra under different voltages and illuminations and comparisons are made to experimental impedance spectra, validating the underlying charge-transport model. In Section 4.4, a framework for the interpretation of the impedance response is established. Finally, in Section 4.5, the concluding remarks are given and the context is set for the following chapters.

4.1 The drift-diffusion equations for PSC modelling

As described in Chapter 2 and depicted in Figure 4.1, a planar perovskite solar cell consists of an electron transport layer (ETL) and a hole transport layer (HTL) that sandwich a photoactive perovskite layer. Electrical connection is made using metallic or transparent conducting layers that contact the outer surfaces of the transport layers. Given the symmetry of a planar cell, the system can be described by a one-dimensional drift-diffusion model. Further description of the drift-diffusion equations and approximations for semiconductor modelling without mobile ions, can be found in [14].

A one-dimensional planar model is an approximation for the structure of a PSC. While two-dimensional models are available for semiconductor simulation [207, 208], to account for these more complex geometries, compromises often need to be made regarding the device physics that can be modelled in order to overcome the additional computational costs. For example, mesoporous structures have been simulated in two-dimensions for PSCs; however, the ionic vacancies are fixed in position [125].

For a one-dimensional model, the width of each layer is approximated as uniform across the plane and the rough interfaces (as shown in Figure 2.3) are approximated as perfectly flat. To produce cells that perform well, the layer widths are carefully controlled to optimise for maximising light absorption and minimising charge transport distances. Therefore, it is expected that for high efficiency cells (i.e. those in which we wish to model) the layers are free from major defects and their thicknesses do not vary too significantly. On device scales, these variations can be modelled via parasitic resistances [14]. The impact of the interface roughness on impedance spectra is discussed in Sections 3.4.1 and 6.2.1.

A further limitation of a one-dimensional model is that grain boundaries, other inhomogeneities or mesoporous structures that occur within three-dimensional polycrystalline materials cannot be explicitly modelled. Whilst certainly a limitation, these inhomogeneities and structures can be accounted for via modification to model parameters that approximate material properties. For example, by using the diffusion coefficient for ion vacancy migration measured experimentally, which may occur primarily via grain boundaries rather than through the grains themselves [209].

Additionally, it is found that these geometries, or structures, do not need to be explicitly modelled within a drift-diffusion model to reproduce the key features observed in current-voltage and impedance measurements [3, 4, 125, 158].

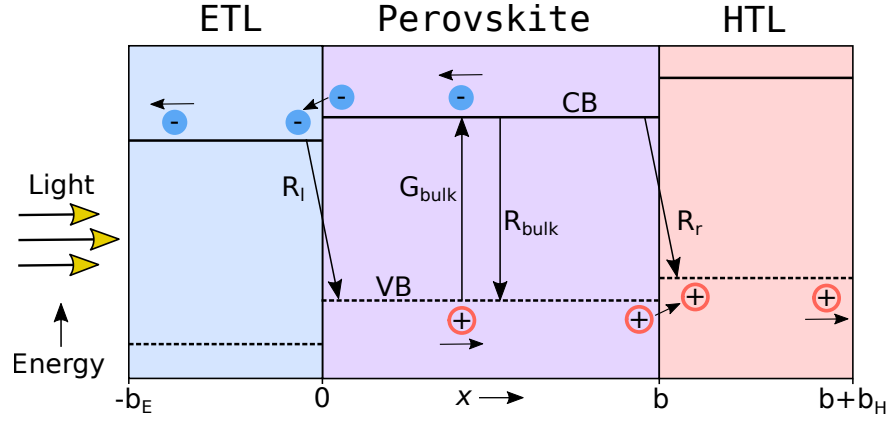


FIGURE 4.1: Schematic showing the geometry of a PSC. Incident light excites an electron into the conduction band (CB) and leaves a hole in the valence band (VB). The generation of charge carriers (electrons and holes) is shown by G_{bulk} . Recombination in the bulk of the perovskite is shown by R_{bulk} and at the ETL/perovskite and perovskite/HTL interfaces by R_l and R_r , respectively.

The system of partial differential equations that make up a drift-diffusion model describe the conservation of charges within the device and their coupling to Poisson's equation (which relates the electric potential to charge densities). In this work, we use the one-dimensional, 'single-layer' coupled ionic-electronic drift-diffusion model established by Richardson *et al.* [6] and later extended to a 'three-layer' model (ETL/perovskite/HTL) by Courtier *et al.* [4]. A more complete description of the drift-diffusion model is presented in [210]. Other established formulations are given in [105, 118, 183].

In the context of this work, it is sufficient to consider only one mobile ionic species, specifically mobile iodide ions. This is in line with the calculations by Eames *et al.* [69], where the diffusion coefficient for anion (iodide) vacancies is much greater than that for cation (MA or Pb) vacancies [69]. Accordingly, the cation vacancy density is set as a constant (N_0) across the cell width, equal to the anion vacancy density, to conserve the neutral charge of the device. Mobile cations can be included in the drift-diffusion equations and should be considered when simulating PSC operation over long timescales such as hours or days. While there is some evidence of ions penetrating the transport layers, we do not model this here [119, 211]. Therefore, in this model, the mobile anion vacancies are constrained to the perovskite layer. In what follows, we adopt the formulation of the drift-diffusion equations for PSC modelling given by Courtier *et al.* [4].

The perovskite layer ($0 < x < b$)

Within the perovskite layer the density of electrons in the conduction band, holes in the valence band, and ionic vacancies are modelled. The positively charged ionic vacancies are constrained to the perovskite layer. Additionally, the generation of electrons and holes by the absorption of light and their recombination occurs solely within the perovskite layer (and at the interfaces).

The electron and hole densities, n and p respectively, are governed in time t and one spatial dimension x via [4]

$$\frac{\partial n}{\partial t} - \frac{1}{q} \frac{\partial j_n}{\partial x} = G_{\text{bulk}}(x, t) - R_{\text{bulk}}(n, p), \quad (4.1)$$

$$\frac{\partial p}{\partial t} + \frac{1}{q} \frac{\partial j_p}{\partial x} = G_{\text{bulk}}(x, t) - R_{\text{bulk}}(n, p), \quad (4.2)$$

$$j_n = qD_n \left(\frac{\partial n}{\partial x} - \frac{n}{V_T} \frac{\partial \phi}{\partial x} \right), \quad (4.3)$$

$$j_p = -qD_p \left(\frac{\partial p}{\partial x} + \frac{p}{V_T} \frac{\partial \phi}{\partial x} \right). \quad (4.4)$$

Here, j_n and j_p are the electron and hole currents, ϕ is the electric potential, D_n and D_p are the electron and hole diffusion coefficients respectively, V_T is the thermal voltage, G_{bulk} is the charge carrier generation rate (per unit volume) and R_{bulk} is their recombination rate. The mobile anion vacancy density P , satisfies the conservation equation

$$\frac{\partial P}{\partial t} + \frac{\partial \mathcal{F}_P}{\partial x} = 0, \quad (4.5)$$

$$\mathcal{F}_P = -D_+ \left(\frac{\partial P}{\partial x} + \frac{P}{V_T} \frac{\partial \phi}{\partial x} \right), \quad (4.6)$$

where \mathcal{F}_P and D_+ are the anion vacancy flux and diffusion coefficient respectively. The electric potential satisfies Poisson's equation [14]

$$\frac{\partial^2 \phi}{\partial x^2} = \frac{q}{\varepsilon_p} (N_0 - P + n - p), \quad (4.7)$$

where ε_p is the permittivity of the perovskite and N_0 is the (uniform) density of cation vacancies. A constant value for ε_p is in line with measurements of MAPI perovskite, which have determined that the real component of the permittivity is approximately independent of frequency [212]. It is also assumed that the permittivity is not dependent on the direction or magnitude of the applied field. This is reasonable because a more complex description of the permittivity is not required to describe the general current-voltage and impedance response of PSCs [3, 4, 125, 158]. However, we note that a slight frequency dependence of the permittivity may be needed in order to explain some of the minor features of PSC impedance spectra, such as the flattening of the semicircles or high geometric capacitances, that models are yet to reproduce.

The generation and recombination rates, as well as other parameters that appear in the drift-diffusion equations, are given at the end of this section once the model has been detailed.

The electron transport layer ($-b_E < x < 0$)

Within the ETL, the equations that describe the conservation of electrons are

$$\frac{\partial n}{\partial t} - \frac{1}{q} \frac{\partial j_n}{\partial x} = 0, \quad j_n = qD_E \left(\frac{\partial n}{\partial x} - \frac{n}{V_T} \frac{\partial \phi}{\partial x} \right), \quad (4.8)$$

where D_E is the diffusion coefficient for electrons in the ETL. Note that there are no source terms to generate or recombine electrons within the ETL (or HTL). No generation of carriers occurs because the transport layers do not absorb photons to produce carriers. Recombination is not expected to be significant in the ETL (HTL) because the hole density (electron density) is assumed to be extremely small within the ETL (HTL) [14]. This is a reasonable approximation because the semiconducting transport layers are highly doped and have large band gaps. As a result, they have very low minority carrier densities and effectively block minority carriers entering from the perovskite layer. This justifies only explicitly modelling the majority carriers in each of the transport layers. Poisson's equation within the ETL is thus well-approximated by

$$\frac{\partial^2 \phi}{\partial x^2} = \frac{q}{\varepsilon_E} (n - d_E), \quad (4.9)$$

where ε_E is the permittivity of the ETL and d_E is the effective doping density of the ETL.

The hole transport layer ($b < x < b + b_H$)

Equivalently to the ETL, there is no significant generation or recombination in the HTL. Hence

$$\frac{\partial p}{\partial t} + \frac{1}{q} \frac{\partial j_p}{\partial x} = 0, \quad j_p = -qD_H \left(\frac{\partial p}{\partial x} + \frac{p}{V_T} \frac{\partial \phi}{\partial x} \right), \quad (4.10)$$

where D_H is the diffusion coefficient for holes in the HTL. Poisson's equation within the HTL is given by

$$\frac{\partial^2 \phi}{\partial x^2} = \frac{q}{\varepsilon_H} (d_H - p), \quad (4.11)$$

where ε_H and d_H are the permittivity and effective doping density of the HTL respectively.

Boundary and continuity conditions

Poisson's equation and the conservation equations require suitable boundary conditions. At the outer edges of the transport layers ($-b_E$ and $b + b_H$) the metal layers form ohmic contact. This gives rise to the following boundary conditions

$$\phi|_{x=-b_E} = -\frac{V(t) - V_{bi}}{2}, \quad \phi|_{x=b+b_H} = \frac{V(t) - V_{bi}}{2}, \quad (4.12)$$

$$n|_{x=-b_E} = d_E, \quad p|_{x=b+b_H} = d_H. \quad (4.13)$$

Additionally, on the internal interfaces at $x = 0$ and $x = b$, the ionic flux is subject to the following boundary conditions

$$\mathcal{F}_P|_{x=0} = 0, \quad \mathcal{F}_P|_{x=b} = 0. \quad (4.14)$$

This restricts the ionic vacancies to stay within the perovskite layer. At the perovskite/transport layer interfaces, the hole and electron currents are specified by

$$j_p|_{x=0} = -qR_l, \quad j_n|_{x=b} = -qR_r, \quad (4.15)$$

where R_l and R_r are the rate of recombination (per unit area) on the $x = 0$ and $x = b$ interfaces respectively. The continuity equations at the internal interfaces for the electric potential are given by

$$\phi|_{x=0^-} = \phi|_{x=0^+}, \quad \phi|_{x=b^-} = \phi|_{x=b^+}, \quad (4.16)$$

$$\varepsilon_E \frac{\partial \phi}{\partial x}|_{x=0^-} = \varepsilon_p \frac{\partial \phi}{\partial x}|_{x=0^+}, \quad \varepsilon_p \frac{\partial \phi}{\partial x}|_{x=b^-} = \varepsilon_H \frac{\partial \phi}{\partial x}|_{x=b^+}, \quad (4.17)$$

representing continuity of electric potential and the normal component of electric displacement on the internal interfaces. Here, 0^- and 0^+ notation is to indicate evaluation within the ETL at $x = 0$ and the perovskite at $x = 0$ respectively. Similarly, b^- and b^+ is used to denote evaluation at $x = b$ within the perovskite and the HTL respectively. The ratio of the carrier densities across their respective TL/perovskite interface are specified as

$$k_E n|_{x=0^-} = n|_{x=0^+}, \quad p|_{x=b^-} = k_H p|_{x=b^+}, \quad (4.18)$$

where the parameters k_E and k_H ensure the Fermi level is continuous across the interface and are defined in (4.27) and (4.28) respectively. Lastly, the electron and hole currents are subject to the interface conditions

$$j_n|_{x=0^-} = j_n|_{x=0^+} - qR_l, \quad j_p|_{x=b^-} = j_p|_{x=b^+} + qR_r, \quad (4.19)$$

where R_l and R_r are the interfacial recombination rates at the ETL/perovskite (left) and perovskite/HTL (right) interfaces respectively and together with (4.15) represent charge conservation conditions on the two interfaces.

Generation, recombination and additional parameters in the drift-diffusion model

Electrons and holes are generated within the perovskite via the Beer-Lambert law for a single wavelength of light [14]

$$G_{\text{bulk}}(x) = F_{ph} \alpha e^{-\alpha x}, \quad (4.20)$$

where F_{ph} is the flux of photons incident on the device with energy above the band gap and α is the absorption coefficient of the perovskite. This describes the attenuation of light as it penetrates the uniform perovskite layer. It is assumed that the transparent contact and the ETL does not significantly absorb the incident light. In general, the generation of rate can be a function of time; however, for the purposes of impedance spectroscopy simulation only a constant illumination is required.

The two main forms of recombination that occur within the perovskite are trap-assisted Shockley-Read-Hall (R_{SRH}) and bimolecular, or radiative, (R_b) recombination. Shockley-Read-Hall (SRH) recombination models the recombination that occurs at traps (or, equivalently the available energy states) that lie within the band gap of the perovskite. This process involves one carrier type relaxing to the lower energy state of the trap. Recombination occurs when an opposing carrier also relaxes to the trap state and annihilates the pair. Bimolecular recombination is the reverse of generation. This is the direct recombination of carriers across the band gap, resulting in the emission of a photon. This is an unavoidable form of recombination; however, under typical operating conditions it is expected that recombination in the bulk occurs predominantly via trap-assisted SRH for PSCs [213]. These recombination mechanisms are modelled by [14]

$$R_{\text{bulk}}(n, p) = \underbrace{\beta (np - n_i^2)}_{R_b} + \underbrace{\frac{np - n_i^2}{\tau_p n + \tau_n p + k_{SRH}}}_{R_{SRH}}. \quad (4.21)$$

Here, β is the bimolecular rate constant and τ_n and τ_p are the SRH pseudo-lifetimes for electrons and holes respectively. For simplicity, it is assumed that the spatial distribution of traps are uniform and their density is not dependent on temperature. Although trap states are likely to be located at energies throughout the band gap, when the carrier densities are similar it is the ‘deep traps’ near the centre of the band gap that contribute most to the recombination rate. This warrants the use of the ‘deep-level trap’ approximation which neglects the smaller contribution from traps away from the centre of the band gap. With this approximation, k_{SRH} is defined

$$k_{SRH} = (\tau_n + \tau_p) n_i. \quad (4.22)$$

This constant is typically small compared to the other terms in the denominator. See Nelson [14] for a complete description. The intrinsic carrier density, n_i , is defined by [14]

$$n_i = \sqrt{g_c g_v} \exp\left(-\frac{E_g}{2qV_T}\right). \quad (4.23)$$

Here, g_c and g_v are the effective density of states in the conduction and valence bands respectively and E_g is the band gap of the perovskite. The intrinsic carrier density is included in the recombination rates to account for thermal generation of carriers. At thermal equilibrium, the recombination rate is zero.

Recombination can occur at the interfaces between the perovskite and the transport layers. For example, this is significant when the material interfaces contain a high density of traps due to crystal defects at the boundary [14]. Similarly to the recombination in the bulk caused by traps, the interfacial recombination rate at the ETL/perovskite (left) interface is modelled by the trap-assisted SRH law of the form

$$R_l(n|_{x=0-}, p|_{x=0+}) = \frac{n|_{x=0-} p|_{x=0+} - n_i^2/k_E}{p|_{x=0+}/v_{nE} + n|_{x=0-}/v_{pE} + k_l}, \quad (4.24)$$

where, v_{nE} and v_{pE} are the electron and hole recombination velocities at the ETL/perovskite interface respectively. This rate is dependent on the electron density within the ETL at the interface and the hole density within the perovskite at the interface. Similarly, the interfacial recombination rate at the perovskite/HTL (right) interface is dependent on the electron density within the perovskite at the interface and the hole density within the HTL at the interface. Hence

$$R_r(n|_{x=b^-}, p|_{x=b^+}) = \frac{n|_{x=b^-} p|_{x=b^+} - n_i^2/k_H}{p|_{x=b^+}/v_{nH} + n|_{x=b^-}/v_{pH} + k_r}, \quad (4.25)$$

where, v_{nH} and v_{pH} are the electron and hole recombination velocities at the perovskite/HTL interface respectively. As for the bulk SRH recombination rate, it is assumed that the traps that contribute most to recombination at the interfaces have energies close to the centre of the band gap. Therefore [14]

$$k_l = \left(\frac{1}{k_E v_{pE}} + \frac{1}{v_{nE}} \right) n_i, \quad k_r = \left(\frac{1}{k_H v_{nH}} + \frac{1}{v_{pH}} \right) n_i. \quad (4.26)$$

While these terms are included in the interfacial recombination rates, they are typically negligible. The factors k_E , and k_H above are related to the band energies and density of states via

$$k_E = \frac{g_c}{g_{cE}} \exp \left(-\frac{E_c - E_{cE}}{qV_T} \right), \quad (4.27)$$

$$k_H = \frac{g_v}{g_{vH}} \exp \left(-\frac{E_{vH} - E_v}{qV_T} \right). \quad (4.28)$$

Here, g_c and g_v are the effective conduction and valence band density of states in the perovskite respectively, E_c and E_v are the energies of the valence and conduction band edges in the perovskite respectively, g_{cE} is the effective conduction band density of states in the ETL, g_{vH} is the effective valence band density of states in the HTL, E_{cE} is the conduction band energy of the ETL and E_{vH} is the valence band energy of the HTL. The factors given by (4.27) and (4.28) are small, resulting in a much larger majority carrier density at $x = 0^-$ and $x = b^+$ compared to that within the perovskite at the interface [214, 215]. The built-in voltage, as required for the boundary conditions in (4.12), is defined by [14]

$$V_{bi} = \frac{1}{q} (E_{fE} - E_{fH}), \quad (4.29)$$

where the Fermi levels of the ETL and the HTL are given by

$$E_{fE} = E_{cE} - V_T \ln \left(\frac{g_{cE}}{d_E} \right), \quad E_{fH} = E_{vH} + V_T \ln \left(\frac{g_{vH}}{d_H} \right). \quad (4.30)$$

A full list of the symbols used in this thesis is given in the nomenclature on page xix.

Deriving the total current from the model

Arguably the most important output from the solution of the drift-diffusion model is the total

current extracted from the cell. This can easily be compared to experimental measurements and enables the impedance to be calculated. In order to determine the total current output of the device, we note that eq.(4.2) – eq.(4.1) gives

$$\frac{\partial}{\partial t} (q(p - n)) + \frac{\partial}{\partial x} (j_p + j_n) = 0. \quad (4.31)$$

Rearranging Poisson's equation (4.7) as follows

$$q(p - n) = q(N_0 - P) - \epsilon_p \frac{\partial^2 \phi}{\partial x^2}, \quad (4.32)$$

this can be substituted into eq.(4.31) to give

$$\frac{\partial}{\partial t} \left(qN_0 - qP - \epsilon_p \frac{\partial^2 \phi}{\partial x^2} \right) + \frac{\partial}{\partial x} (j_p + j_n) = 0. \quad (4.33)$$

Noting that the cation vacancy density N_0 is constant and rearranging eq.(4.5) such that

$$-q \frac{\partial P}{\partial t} = \frac{\partial j_P}{\partial x}, \quad (4.34)$$

where the anion vacancy current density $j_P = q\mathcal{F}_P$, eq.(4.33) can be written as

$$\frac{\partial}{\partial t} \left(-\epsilon_p \frac{\partial^2 \phi}{\partial x^2} \right) + \frac{\partial}{\partial x} (j_p + j_n + j_P) = 0. \quad (4.35)$$

Finally, on noting that the electric field $E = -\frac{\partial \phi}{\partial x}$, this gives

$$\frac{\partial}{\partial x} \left(j_p + j_n + j_P + \epsilon_p \frac{\partial E}{\partial t} \right) = 0. \quad (4.36)$$

Therefore, the total current density is given by

$$J(t) = j_n(x, t) + j_p(x, t) + j_d(x, t) + j_P(x, t). \quad (4.37)$$

where the *displacement current density* is defined

$$j_d(x, t) = \epsilon_p \frac{\partial E(x, t)}{\partial t}. \quad (4.38)$$

The total current density $J(t)$ is the current measured from experiment (subject to series and shunt resistance losses). The total current density can be evaluated at any point within the perovskite layer and consists of contributions from the free electron, hole and anion vacancy currents as well as the displacement current. The displacement current arises from polarisation of free space (the vacuum), which is independent of material properties, and the dielectric polarisation of the material itself. This is due to the induction of dipoles that align with the electric field across the device, which act to reduce the magnitude of the electric field. The magnitude of the displacement current is only large when the electric field varies rapidly. At typical scan rates for current-voltage measurements, the displacement current induced is negligible. However, for

very high scan rates and impedance measurements it can be significant. The anion vacancy current density j_P , resulting from the motion of ions across the perovskite width, is negligible under typical operation.

Note that the same method as detailed above can be used to calculate the total current in the transport layers, resulting in

$$J(t) = j_n(x, t) + \epsilon_E \frac{\partial E(x, t)}{\partial t}, \quad (4.39)$$

in the ETL and

$$J(t) = j_p(x, t) + \epsilon_H \frac{\partial E(x, t)}{\partial t}, \quad (4.40)$$

in the HTL. Equations (4.37-4.40) enable the total current density to be evaluated at any point across the three-layer device.

4.2 Numerical solution

The set of partial differential equations detailed above describe the electric potential and charge transport within a PSC. Given that the drift-diffusion equations (without applying simplifications) are highly non-linear coupled PDEs, solutions must be found numerically. Numerical solutions can be determined using the method of lines. Employing this technique involves discretising the spatial derivatives, leaving a system of coupled ordinary differential equations for the charge densities and algebraic equations for the electric potential [106, 206]. This set of differential-algebraic equations can be solved in time using a suitable integration algorithm.

These PDEs are particularly challenging to solve numerically with realistic device parameters [5, 106]. This is due to their severe spatial *and* temporal stiffness, which means that standard solution techniques require extremely small time steps, and fine spatial grids in order to determine accurate solutions. Spatial stiffness is a result of the formation of four Debye layers (also termed boundary or double layers) which are of the order of ~ 2 nm. These narrow layers are formed due to the accumulation and depletion of ionic vacancies within the perovskite at the perovskite/TL interfaces. This steep variation in charge density (and hence potential) at the outer edges of the perovskite layer is accompanied by steep changes in the majority carrier density in the transport layers, which form adjacent Debye layers [4]. Temporal stiffness occurs due to the vastly different timescales at which the electronic and ionic charges move [5, 106].

To deal with the stiffness in space, Courtier *et al.* use a non-uniform spacing to position the grid points most closely at the Debye layers [106]. This provides sufficient resolution at the interfaces without wasting computational power solving at this resolution throughout the device, where distributions vary less sharply. Additionally, a numerical integrator capable of dealing with stiff

problems is employed. These approaches enable accurate numerical solutions to be obtained rapidly on a desktop computer.

4.2.1 IonMonger IS module

`IonMonger` is an open-source planar perovskite solar cell simulator developed by Courtier *et al.* [206]. Written in MATLAB, this application numerically solves the coupled ionic-electronic drift-diffusion equations, as detailed in Section 4.1. Specifically, the numerical solutions are obtained using a finite element scheme to discretise the spatial derivatives [206]. The resulting system of differential-algebraic equations are integrated using `ode15s`, which is a built-in routine that is capable of dealing with stiff numerical problems [216, 217].

By specifying device parameters, as well as the illumination and applied voltage in time, `IonMonger` can be used to simulate current-voltage measurements of PSCs. With a high density of mobile ionic vacancies, as predicted by Eames *et al.* [69], simulations reproduce the hysteresis that is observed in experimental J - V curves [6]. The numerical solutions include the carrier and vacancy distributions, as well as the electric potential, across the cell in time. This provides detailed information about the physics of operation that can't otherwise be easily determined from experimental measurements.

`IonMonger` is highly optimised to obtain accurate solutions quickly, with realistic planar PSC device parameters, on a modern personal computer. It contains the relevant physics to simulate impedance spectroscopy measurements. This includes electronic processes occurring within less than a microsecond to ionic redistribution occurring over hundreds of seconds. These features mean that `IonMonger` is well suited for adaptation to simulate impedance spectroscopy measurements.

To model impedance spectroscopy measurements, we have developed an additional 'module' for `IonMonger` [*release paper currently in preparation by W. Clarke, L.J Bennett, G. Richardson, and N. E. Courtier*]. This module routinely employs the core numerical solver of `IonMonger`, adding the ability to simulate IS measurements for PSCs. Impedance spectra can be calculated at different DC voltages, illumination conditions and temperatures. With realistic device parameters (Table 4.1) and experimental protocols, this enables IS measurements for physical PSCs to be simulated.

Impedance simulation

Firstly, the measurement protocol is defined. This includes the DC voltage, perturbation amplitude, frequency range and the number of frequencies. The DC (or constant level of) illumination is also specified. These inputs are used to construct an applied voltage protocol $V(t)$ for each frequency of the form

$$V(t) = V_{\text{DC}} + V_p \cos(\omega t), \quad (3.7 \text{ reprinted})$$

which specifies the boundary condition (4.12). The voltage protocols are passed to the numerical solver, `IonMonger`, together with values for the device and recombination parameters (see Tables 4.1 and 4.2 respectively). `IonMonger` then numerically solves the drift-diffusion equations (Section 4.1) for each frequency. The solutions for the current density, $J(t)$, are analysed using a Fourier transform to extract their phase and amplitude. Finally, the impedance for each frequency is calculated and a spectrum can be constructed.

Calculating the impedance as a function of frequency

An important part of the IS module is the extraction of the phase and amplitude of the current output for each frequency of perturbation. This is in order to calculate the impedance, given by eq.(3.9). Using the trigonometric Fourier series, a general current response is given by

$$J(t) = J_{\text{DC}} + \sum_{n=1}^{\infty} (a_n \cos(n\omega t) + b_n \sin(n\omega t)), \quad (4.41)$$

where

$$J_{\text{DC}} = \frac{1}{T} \int_{-T/2}^{T/2} J(t) dt, \quad (4.42)$$

$$a_n = \frac{2}{T} \int_{-T/2}^{T/2} J(t) \cos(n\omega t) dt, \quad b_n = \frac{2}{T} \int_{-T/2}^{T/2} J(t) \sin(n\omega t) dt. \quad (4.43)$$

The period T is related to the angular frequency via $T = 2\pi/\omega$. Given that the applied voltage is of a single angular frequency ω and that the response (as required for impedance measurements) is linear, the only non-zero coefficients are for $n = 1$. Therefore, the general current output in response to an applied voltage with angular frequency ω can be written

$$J(t) = J_{\text{DC}} + a_1 \cos(\omega t) + b_1 \sin(\omega t), \quad (4.44)$$

where a_1 and b_1 are determined using (4.43). Using a trigonometric addition formula¹ the current can be rewritten in the form

$$J(t) = J_{\text{DC}} + J_p \cos(\omega t - \theta), \quad (3.8 \text{ reprinted})$$

where

$$J_p = \sqrt{a_1^2 + b_1^2}, \quad \theta = \arctan\left(\frac{b_1}{a_1}\right). \quad (4.45)$$

¹Expressing equation (4.44) in the form (3.8):

$$J_p \cos(\omega t - \theta) = \underbrace{J_p \cos(\theta)}_{a_1} \cos(\omega t) + \underbrace{J_p \sin(\theta)}_{b_1} \sin(\omega t)$$

Therefore the impedance is given by

$$Z(\omega) = |Z|e^{i\theta}, \quad (3.9 \text{ reprinted})$$

where $|Z| = V_p/J_p$. Here we note that for impedance it is conventional to define the current such that an increase in voltage results in an increase in current. This is contrary to how the current is defined in this work, which is such that the current is positive within the power generating regime. The effect of $J(t) \rightarrow -J(t)$ on impedance representation is to shift the phase by π rad. By using numerical integration to determine a_1 and b_1 , the phase and amplitude, as required for impedance calculations, can be determined for a sinusoidal current $J(t)$. This method is in line with that used by Moia *et al.* [158]. The accuracy of this calculation can be improved by increasing the number of time points per period. As standard, two periods of $J(t)$ for integration and 100 time points per period are used.

Optimisation methods

`IonMonger` is heavily optimised to produce solutions for J - V measurements. A given J - V solution only takes around 5 seconds on a moderately fast personal computer. However, even with this speed, effectively 50 (or more) of these J - V solutions are required to produce an impedance spectrum. This leads to computational times of around 5 minutes (or longer). This is fast considering the complexity of the numerical problem. However, to investigate device parameters and their impact on spectra, tens, or even hundreds, of spectra need to be produced. For this reason, optimisation to improve computational speed is critical.

The main technique that has been employed to improve the speed of the IS module is to make use of MATLAB's parallel computing capabilities [218]. The IS module is constructed such that the solutions at different frequencies can be solved independently of one another. Therefore the multiple cores on a CPU can be utilised, with each used to solve the PDEs for a given frequency in parallel. This greatly reduces the time required to generate an impedance spectrum, with the time reduction dependent on the number of cores available. Additionally, the steady-state solution at V_{DC} is calculated only once, at the beginning of the operation. This steady-state solution is then used as the initial condition for each frequency perturbation. This avoids wasting computational effort solving for the steady-state solution at each frequency.

Implementing these methods results in very fast simulation times. With a high specification laptop (2018 Intel i7-8750H 6 core processor at 2.2 GHz (4.1 GHz max) and 16 GB RAM) the spectra presented in Figure 4.2 take 65-70 seconds each to simulate. These are produced with 300 grid points in the perovskite layer, with the device parameters from Table 4.1 and are composed of 128 frequencies each. We note that doubling the number of spatial grid points, results in identical spectra and thus indicates that with the adaptive mesh used in `IonMonger`, there is enough spatial resolution to properly resolve the problem.

4.3 Results and comparison to experiment

In this section, the impedance spectra obtained via numerical solution to the drift-diffusion equations are presented. These are obtained using the impedance spectroscopy module for `IonMonger`, as detailed in Section 4.2. The parameters that describe material properties and physical constants, as required to determine solutions to the drift-diffusion equations, are given in Table 4.1. The specific values for the parameters are chosen to be in line with experimental impedance data and known ranges of parameter values for a prototypical perovskite solar cell, i.e. a MAPI absorber layer sandwiched between a TiO_2 ETL and a Spiro HTL. In Figures 4.2-4.5, SRH recombination in the bulk is simulated. Specifically, electron-limited SRH recombination (which we label R_n) is modelled with the electron and hole pseudo-lifetimes given in Table 4.2. SRH recombination is electron-limited when the electron SRH pseudo-lifetime is much greater than the hole SRH pseudo-lifetime (i.e. $\tau_n \gg \tau_p$). In this case, the full SRH recombination rate, given in (4.21), is approximately monomolecular and controlled by the electron density. Correspondingly, if $\tau_p \gg \tau_n$, then the SRH recombination is hole-limited. While these rates can be accurately approximated, as is done in the following chapter, the numerical solutions obtained throughout employ the full recombination rates given by (4.21)-(4.25).

Simulation protocol

As standard, for each spectrum obtained from numerical solution to the drift-diffusion equations, the impedance is calculated at 128 frequencies. These frequencies are logarithmically spaced across a range of 1 mHz to 10 MHz. This frequency range is chosen as it captures the LF and HF behaviour, as observed in experiment. Typically, experimental measurements are only able to probe frequencies up to 1 MHz, which is a limitation of the measurement apparatus [224]. Here, a frequency limit of 10 MHz was chosen for the numerical simulations in order to fully resolve the HF feature across all parameter and measurement regimes. The lower limit of 1 mHz is approximately the limit of experimental measurements, beyond which would require hours to days of continuous measurement. The simulation can probe frequencies well below 1 mHz; however, no additional response is observed for the material parameters used in Table 4.1. The perturbation amplitude is 10 mV throughout. Unless otherwise stated, the impedance spectra are calculated under an illumination equivalent to 0.1-Sun. More specifically, the photon flux is monochromatic (520 nm) with an intensity that produces a photocurrent equivalent to 0.1-Sun at AM1.5.

Symbol	Description	Value	Source
Constants			
k_B	Boltzmann constant	$8.62 \times 10^{-5} \text{ eV K}^{-1}$	
q	Charge of a proton	$1.60 \times 10^{-19} \text{ C}$	
ε_0	Permittivity of free space	$8.85 \times 10^{-12} \text{ F m}^{-1}$	
MAPbI₃ properties			
b	Width	300 nm	[160]
α	Absorption coefficient	$1.3 \times 10^7 \text{ m}^{-1}$	[219]
ε_p	Permittivity	$24.1\varepsilon_0$	[220]
E_C	Conduction band level	-3.8 eV	[221]
E_V	Valence band level	-5.4 eV	[221]
g_c	Conduction band DoS	$8.1 \times 10^{24} \text{ m}^{-3}$	[220]
g_v	Valence band DoS	$5.8 \times 10^{24} \text{ m}^{-3}$	[220]
D_n	Electron diffusion coefficient	$1.7 \times 10^{-4} \text{ m}^2 \text{ s}^{-1}$	[222]
D_p	Hole diffusion coefficient	$1.7 \times 10^{-4} \text{ m}^2 \text{ s}^{-1}$	[222]
D_+	Ionic vacancy diffusion coefficient	$1 \times 10^{-16} \text{ m}^2 \text{ s}^{-1}$	[69]
N_0	Ionic vacancy density	$1.6 \times 10^{25} \text{ m}^{-3}$	[109]
ETL properties (compact-TiO₂)			
b_E	Width	100 nm	
d_E	Effective doping density	$5 \times 10^{24} \text{ m}^{-3}$	
ε_E	Permittivity	$10\varepsilon_0$	
D_E	Electron diffusion coefficient	$1 \times 10^{-5} \text{ m}^2 \text{ s}^{-1}$	
g_{cE}	Effective conduction band DoS	$1 \times 10^{26} \text{ m}^{-3}$	
E_{cE}	Conduction band minimum	-4.1 eV	[223]
HTL properties (Spiro)			
b_H	Width	200 nm	
d_H	Effective doping density	$5 \times 10^{24} \text{ m}^{-3}$	
ε_H	Permittivity	$3\varepsilon_0$	
D_H	Hole diffusion coefficient	$1 \times 10^{-6} \text{ m}^2 \text{ s}^{-1}$	
g_{vH}	Effective valence band DoS	$1 \times 10^{26} \text{ m}^{-3}$	
E_{vH}	Valence band maximum	-5.1 eV	[221]
Other			
T	Temperature	298 K	
V_T	Thermal voltage (at 298 K)	25.7 mV	
F_{ph}	Incident photon flux (1 sun equivalent)	$1.4 \times 10^{21} \text{ m}^{-2} \text{ s}^{-1}$	
V_{bi}	Built-in voltage	0.85 V	

TABLE 4.1: Constants and parameter definitions for the drift-diffusion equations. Unless otherwise stated, these values are used throughout.

Recombination Type	Full Form	Parameter Values
Bimolecular, R_b	$R_{\text{bulk}} = \beta (np - n_i^2)$	$\beta = 10^{-12} \text{ m}^3 \text{ s}^{-1}$
Hole-limited SRH, R_p	$R_{\text{bulk}} = \frac{np - n_i^2}{\tau_n p + \tau_p n + k_{SRH}}$	$\tau_n = 3 \times 10^{-10} \text{ s}$ $\tau_p = 3 \times 10^{-8} \text{ s}$
Electron-limited SRH, R_n	$R_{\text{bulk}} = \frac{np - n_i^2}{\tau_n p + \tau_p n + k_{SRH}}$	$\tau_n = 3 \times 10^{-8} \text{ s}$ $\tau_p = 3 \times 10^{-10} \text{ s}$
ETL/Perovskite interfacial SRH, R_l	$R_l = \frac{n_{\text{ETL}}^{(l)} p^{(l)} - n_i^2 / k_E}{p^{(l)} / v_{nE} + n_{\text{ETL}}^{(l)} / v_{pE} + k_l}$	$v_{nE} = 10^5 \text{ m s}^{-1}$, $v_{pE} = 5 \text{ m s}^{-1}$
Perovskite/HTL interfacial SRH, R_r	$R_r = \frac{n^{(r)} p_{\text{HTL}}^{(r)} - n_i^2 / k_H}{p_{\text{HTL}}^{(r)} / v_{nH} + n^{(r)} / v_{pH} + k_r}$	$v_{nH} = 5 \text{ m s}^{-1}$ $v_{pH} = 10^5 \text{ m s}^{-1}$

TABLE 4.2: List of all recombination types considered in this work. Unless otherwise stated, the recombination parameter values used are those specified here. If, for example, R_n is quoted then electron-limited SRH is calculated in the bulk using $\tau_n = 3 \times 10^{-8} \text{ s}$ and $\tau_p = 3 \times 10^{-10} \text{ s}$ (all other recombination rates are zero). The intrinsic carrier density n_i , and the parameters k_{SRH} , k_l and k_r are defined in (4.22)-(4.28).

4.3.1 DC voltage

Figures 4.2-4.4 show the simulated impedance response of a PSC at three DC voltages, including open-circuit. These figures plot the different forms of the complex impedance, which are defined by equations (3.9-3.11). Specifically, Figure 4.2 shows a Nyquist plot of the spectra, in which two distinct semicircles above the axis are observed for each of the DC voltages. Traversing from the left semicircle to the right corresponds to decreasing frequencies. The leftmost semicircle corresponds to the high frequency (HF) feature and the rightmost semicircle is the low frequency (LF) feature. The characteristic frequencies of these features are labelled on the Nyquist diagrams. The high and low frequency features are visible on the frequency plots, Figures 4.3 and 4.4, as peaks or transitions between two flat regions.

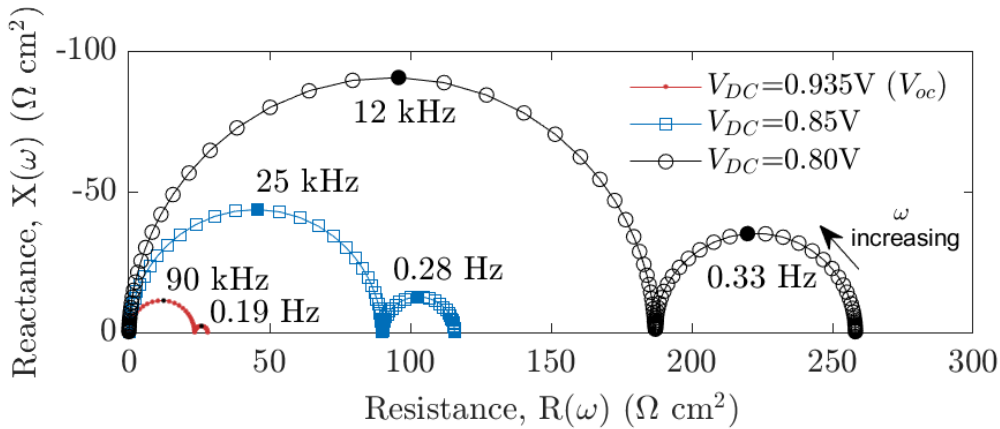


FIGURE 4.2: Nyquist plot representation of simulated impedance spectra for a PSC at three DC voltages. The illumination is 0.1-Sun equivalent and the perturbation amplitude is 10 mV. Recombination is electron-limited SRH in the bulk (R_n). Device parameters and recombination lifetimes are listed in Tables 4.1 and 4.2 respectively. Figures 4.3 and 4.4 show the corresponding frequency plots for these spectra.

The characteristic frequencies of around 10^4 - 10^5 Hz and 10^{-1} - 10^0 Hz for the high and low frequency features respectively are in line with those determined from experimental measurements [96, 147, 170]. The diameter of, and hence resistances associated with, both the LF and HF semicircles are strongly dependent on the DC voltage. Reducing the DC voltage from open-circuit towards short circuit, the semicircles on the Nyquist plots increase in diameter. This can be understood by considering the gradient of the steady-state J - V curve at each DC voltage. At open-circuit, the gradient is steep, corresponding to a low impedance (as a small change in voltage results in a large change in current). As the DC voltage is reduced, the gradient flattens and thus the impedance is higher. In this case, although not in general, the LF feature remains above the axis (capacitive) and increases in size roughly proportionally to the HF feature. We note that the numerical solutions show that the low frequency feature is sensitive to the recombination process occurring. This is studied comprehensively in Section 6.1. As shown in Figure 4.4, at high frequencies the phase tends to 90° . This is because there is no series resistance as the drift-diffusion model is one-dimensional (R_s is inversely proportional to the cross-sectional area). Additionally, contact and experimental apparatus resistances are not accounted for.

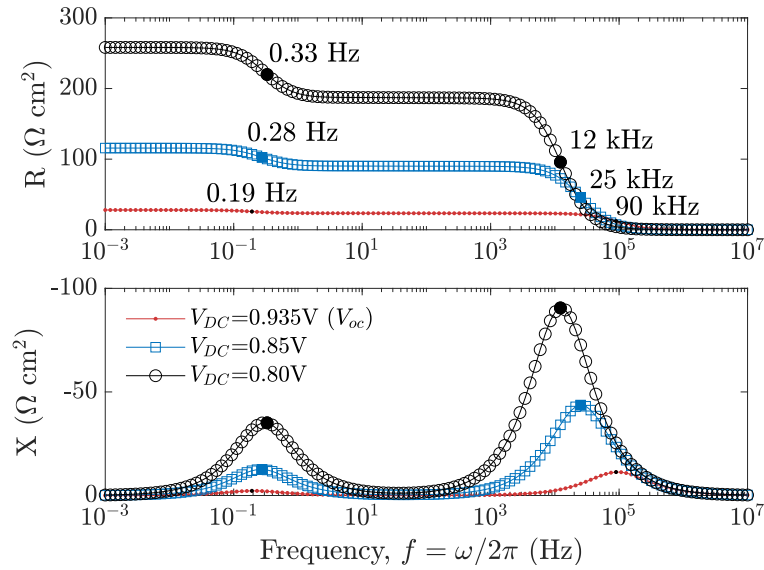


FIGURE 4.3: Frequency plots showing the real component, resistance R and imaginary component, reactance X of impedance versus frequency for the spectra presented in Figure 4.2.

The frequency plots are shown in addition to the Nyquist figures to aid interpretation. While the characteristic frequencies are labelled on the Nyquist figures, frequency information is still highly limited. Additionally, trends can be more clearly depicted. Bode plots ($|Z(\omega)|$ and $\theta(\omega)$ versus frequency) are more typically presented when analysing impedance. However, in this work it is better to present frequency plots that display the resistance $R(\omega)$ and reactance ($X(\omega)$) versus frequency. This is because the reactance more clearly shows the characteristic frequency of the peaks and is not strongly affected by an additional series resistance.

Figure 4.5 shows the current response in time due to a voltage perturbation at two different frequencies. This is helpful in relating the somewhat abstract frequency response to the more straightforward temporal response. Specifically, an ultra-low frequency and a high frequency

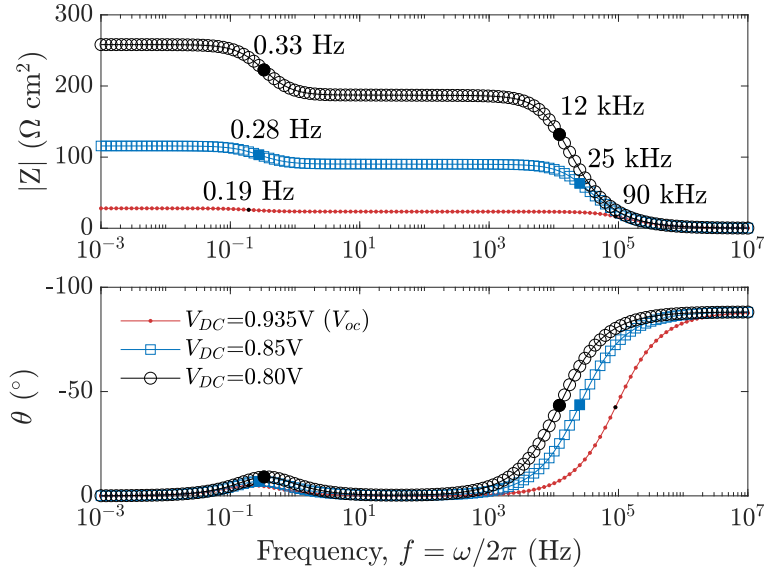


FIGURE 4.4: Frequency plots showing the magnitude, $|Z|$ and phase, θ versus frequency for the spectra presented in Figure 4.2.

response is shown at a DC applied voltage of 0.8 V for impedance spectra presented in Figures 4.2-4.4. The ultra-low frequency response, at 1 mHz, shows the current responds in phase with the applied voltage. Representing this as a Lissajous diagram (current versus voltage) simply results in a straight line. Conversely, at 12 kHz which corresponds to the characteristic frequency of the HF response, there is a clear phase shift and hence the Lissajous trace is an oval. In this form, the responses can be related to the Nyquist plot. For example, the high frequency response is greater (i.e. a larger amplitude) than the low frequency response. This corresponds to a lower impedance, as $|Z| \propto 1/J_p$.

The Lissajous diagrams shown in Figure 4.5 are helpful to determine if the response to a perturbation is linear and stable. For a stable response the Lissajous trace for two different periods overlap. A non-linear response is shown as a curved line for zero phase, or if there is a phase, then the oval is non-symmetric [153]. This representation is particularly useful during experimental measurements. Here, we note the Lissajous figures show that the response for a 10 mV perturbation amplitude is not perfectly linear; however, this does not significantly impact the calculation of impedance.

The impedance spectra produced from the drift-diffusion model, and those from the equivalent circuits in Section 3.3, display perfect semicircles when viewed on a Nyquist plot. However, impedance spectra obtained from physical devices often display semicircles that are ‘imperfect’ or flattened (see, for example, Figures 3.8 and 3.10). There is uncertainty over the cause of the flattened semicircles, which could be a result of the measurement not being carried out under steady-state conditions (i.e. light or temperature variations, or the devices degrading). Additionally, they could be due to additional physical process occurring that are not typically included in drift-diffusion models; for example, the presence of more than one mobile ionic

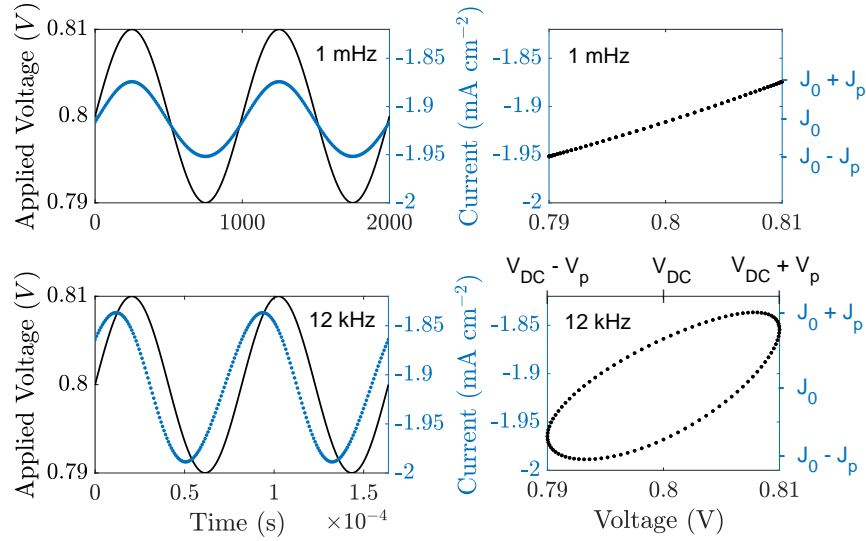


FIGURE 4.5: Left: applied voltage (left axis with black line) and the resulting current response (right axis with blue data points) versus time. Right: corresponding Lissajous plots (current versus voltage). The two frequencies show current responses in phase (top = 1 mHz) and out of phase (bottom = 12 kHz). The 12 kHz response is indicated on the impedance spectra (Figures 4.2-4.4) at 0.8 V DC applied voltage. Note that here we take the convention that the photogenerated current is negative.

species within the perovskite layer [125]. It has also been proposed that the flattened semicircles may be due to inhomogeneities of the devices such as interface roughness or porous structures [225], that a one-dimensional model does not capture.

While their exact cause may yet to be fully understood, flattened semicircles can be modelled using constant phase elements (or, equivalently non-ideal capacitors), as part of equivalent circuit models [187, 226]. The additional fitting parameters enable the equivalent circuit models to better match the non-idealised behaviour of PSC impedance spectra; however, without a physics-based model that defines the additional parameters, these do not provide any further understanding for the physical cause of this behaviour. Further study using a drift-diffusion model under simulated non-equilibrium conditions could help elucidate the cause of the flattened semicircles. Otherwise, the limitations of a one-dimensional model, as discussed in Section 4.1, may be the cause.

4.3.2 Illumination

In this section numerical solutions are presented that simulate impedance spectroscopy measurements at open-circuit voltage under different levels of illumination. These measurements are commonly performed as the dependence on illumination can be used to help identify the physical processes responsible for each feature [147]. Additionally, ideality factors and activation energies can be calculated from these trends [96, 131]. This is discussed further in Chapter 6.

Figures 4.6 and 4.7 show Nyquist and frequency plots for simulated impedance spectra at open-circuit under various illuminations. Here, the cell parameters are the same as those used in the previous section, from Table 4.1. The only change has been to the type of recombination occurring. Previously, electron-limited SRH recombination (R_n) was modelled, and the resulting spectra show positive LF features. Here, in contrast, hole-limited SRH recombination (R_p) is simulated and the resulting spectra have negative LF features. This shows how the drift-diffusion model can reproduce the negative or ‘inductive’ features as have been reported in the literature [175, 186]. Note that for simplicity, the monochromatic photon flux that results in a short-circuit photocurrent equivalent to 1-Sun illumination has been labelled 1000 Wm^{-2} . The other levels of illumination have been scaled from 1-Sun accordingly.

Higher illuminations significantly reduce the diameters of both the high and low frequency semicircles. Across all illuminations, the LF feature lies below the axis and its size relative to the HF semicircle remains roughly constant. As can be seen in the peaks of the reactance X in Figure 4.7, the characteristic frequency of the LF feature remains somewhat independent of illumination. Whereas the HF feature shifts to higher frequencies with increased illumination.

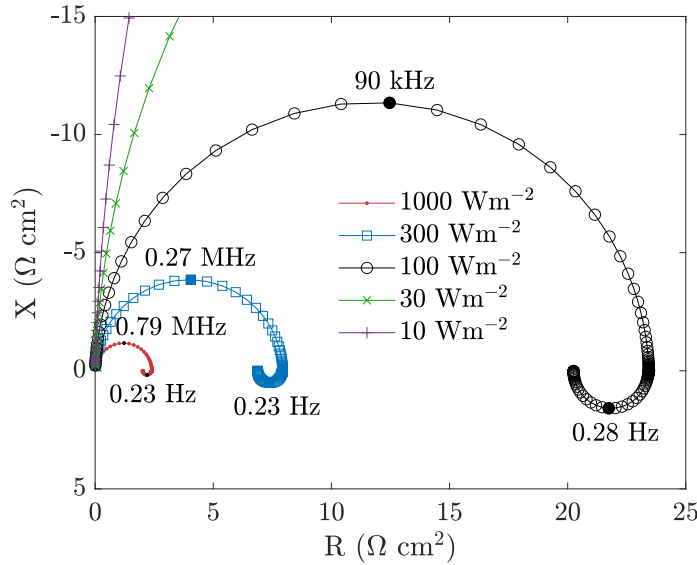


FIGURE 4.6: Nyquist plots for simulated impedance spectra at open-circuit voltages under different illumination intensities. Recombination is hole-limited SRH in the bulk, R_p with lifetimes from Table 4.2 and cell parameters from Table 4.1.

The trends with illumination are more easily understood by plotting the key features of the spectra versus open-circuit voltage, which is a proxy for illumination intensity (high V_{oc} corresponding to high illumination), as shown in Figure 4.8. In this case, the key features such as the characteristic frequencies, resistances and capacitances are obtained by ‘reading off’ the values from the spectra. For example, the resistance of the high and low frequency features are simply the diameters of the respective semicircles. The characteristic frequencies f_i are obtained from the peaks in the reactance versus frequency plots and are related to the time constants τ_i via

$$\tau_i = \frac{1}{2\pi f_i} \quad (4.46)$$

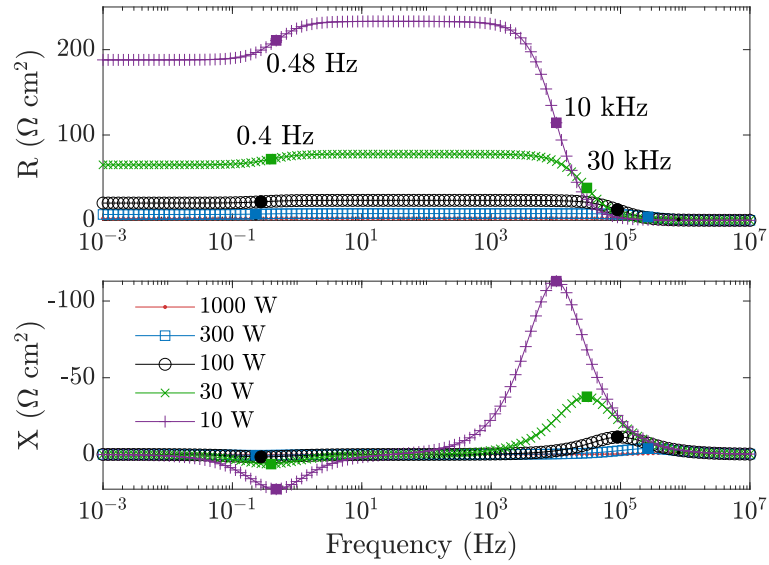


FIGURE 4.7: Frequency plots for the spectra presented in Figure 4.2.

where $\omega_i = 2\pi f_i$. The capacitance associated with each feature is related to the time constant and resistance via

$$C_i = \frac{\tau_i}{R_i}. \quad (3.15 \text{ reprinted})$$

In practice, this method of ‘reading off’ the values of the resistances or characteristic frequencies is built into the `IonMonger` IS module (for spectra with one or two semicircular features). The spectra are analysed to find the number of local maxima and minima in the reactance versus frequency data. This is used to classify the impedance spectrum, i.e. determine the number of features and their position above or below the axis. For simple spectra that show a high and low frequency feature, the diameter of each semicircle (equal to R_i) is simply twice the value of the peak in reactance $X(\omega_i)$. This is shown in Figure 3.6. While basic, this is all that is required to extract the impedance parameters from spectra with two semicircular features. For impedance spectra with more features, dedicated equivalent circuit model fitting software, such as `Zview`, should be used. The impedance parameters obtained using this method (for two distinct semicircular features) are equivalent to fitting to an RC - RC circuit². This circuit is shown in Figure 3.6c). Fitting to equivalent circuits is common in the literature, however equivalent circuits (and the values of the components found from fitting) do not have a physical meaning without a suitable physical model to justify their use. This becomes acutely clear when negative resistances and capacitances are obtained from fitting, as is the case for negative LF features. While resistors and capacitors with negative values are clearly unphysical, the mathematics that describes the impedance of an RC - RC equivalent circuit is compatible with

²Using a non-linear least squares method to fit experimental impedance spectra to an equivalent circuit model is more appropriate to extract resistances and time constants than ‘reading them off’ from the spectra. This is because fitting can account for signal noise, non-ideal components, a low number of sample frequencies and extrapolate impedance spectra to beyond the minimum and maximum frequencies. Additionally, when more than two features are present the values of the impedance parameters cannot be simply read off from the spectra.

such negative component values. In this sense, the equivalent circuit is simply a tool to extract key data from the spectra such as ‘resistances’ and ‘capacitances’.

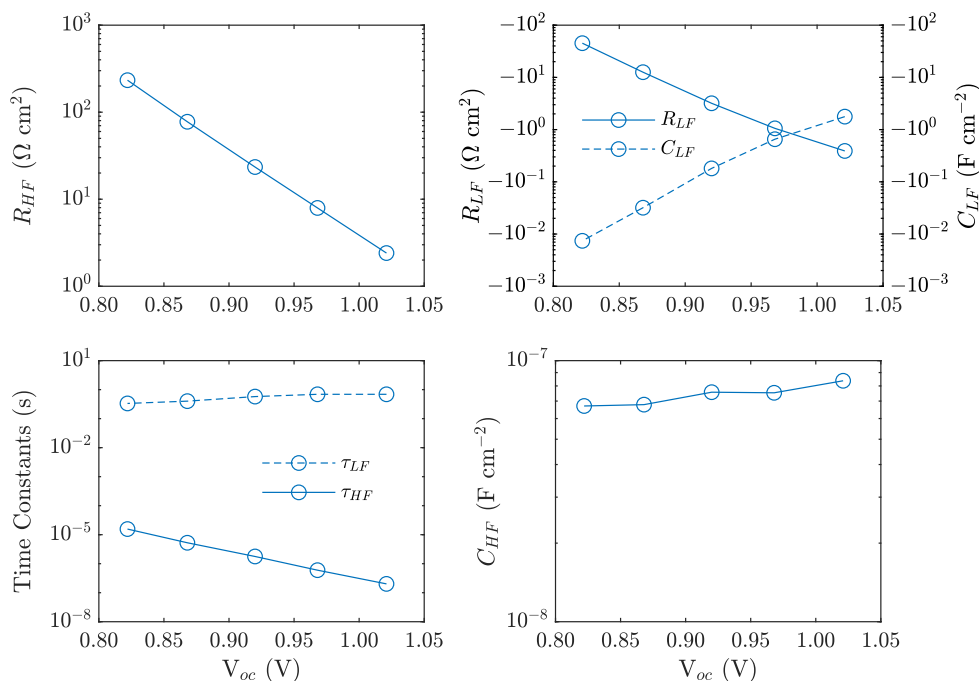


FIGURE 4.8: High and low frequency resistances, capacitances and time constants calculated from impedance spectra (Figures 4.6 and 4.7) at different illumination intensities (and therefore open-circuit voltages). These equivalent circuit parameters are determined by fitting to an RC - RC circuit or reading off the resistances and frequencies from the Nyquist and frequency plots. Capacitance is obtained via $C_i = \tau_i/R_i$. The ‘ideality factor’ obtained from the gradient of the HF resistance is approximately 1.7. Note that the low frequency resistances and capacitances are negative.

Figure 4.8 clearly shows that the high frequency resistance decreases exponentially with increasing open-circuit voltage. The gradient of $\log(R_{HF})$ with V_{oc} gives an ‘ideality factor’ of approximately 1.7. In Section 6.3.2, it is shown that the ‘ideality factor’ extracted using this method is in fact the rectification factor. Similarly to the HF resistance, although not as strictly, the magnitude of the low frequency resistance also decreases exponentially with open-circuit voltage. Correspondingly, the magnitude of the LF capacitance increases exponentially with open-circuit voltage. Hence the LF time constant is approximately independent of open-circuit voltage. On the other hand, the HF time constant decreases exponentially with illumination. The position of the HF peak is therefore strongly influenced by the level of illumination. Notably, the HF capacitance is almost independent of open-circuit voltage. This indicates that this is a geometric capacitance, as defined in eq.(3.20).

The qualitative trends of the resistances, capacitances and (implicitly) the time constants shown by Figure 4.8 are consistent with those of experimental impedance measurements for PSCs [96, 131, 147] (i.e. points i-iv in Section 3.4.4). Additionally, we note that these general trends

are consistently reproduced for spectra simulated with different device parameters (inverted configurations [3]) and recombination types. This provides validation that the underlying drift-diffusion model contains enough of the relevant physics to appropriately model the operation of PSCs.

4.3.3 Reproducing experimental spectra using the IS module

Riquelme *et al.* employed a combined modelling and experimental approach to better understand the impedance response of PSCs [3]. *IonMonger*, which numerically solves the drift-diffusion model detailed in Section 4.1, was used to simulate J - V and Suns- V_{oc} measurements and the IS module was used to generate impedance spectra. They demonstrate that with their standard parameter set, for a MAPI PSC with a mesoporous TiO_2 ETL, the IS model can reproduce the trends of impedance spectra with illumination, as described in Section 3.4.4. Additionally, they show that these trends are matched for the device parameters used by Neukom *et al.* [183] for an inverted cell configuration. Most notably, with meticulous parameter fitting they are able to obtain a semi-quantitative fit to experimental J - V , Suns- V_{oc} and impedance measurements for a mesoporous PSC. This is shown in Figure 4.9, with experimental measurements in black and two different simulated solutions from *IonMonger* in red and blue.

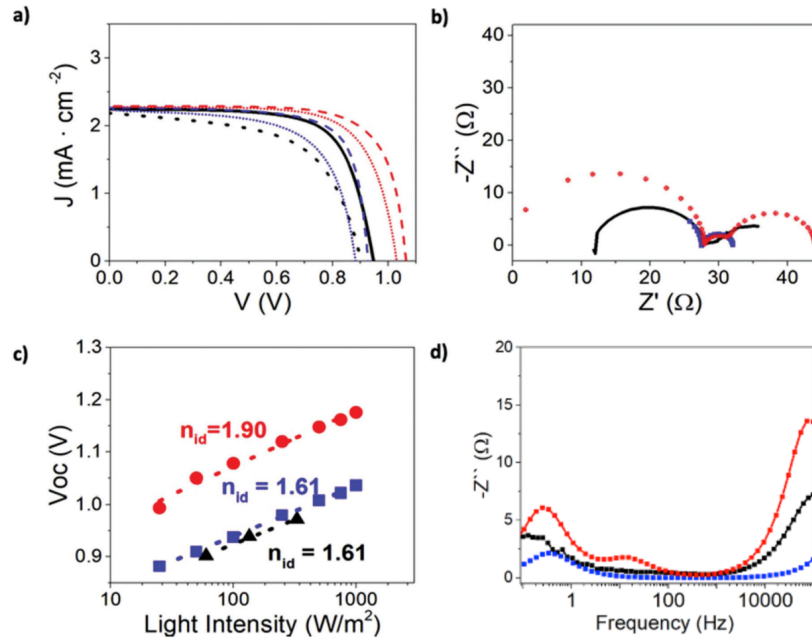


FIGURE 4.9: Experimental (black), and simulated (red and blue) a) J - V curve, b) Nyquist plot, c) Suns- V_{oc} and d) imaginary component of the impedance versus frequency. The red and blue data are for a mesoporous cell parameter set before and after parameter fitting respectively. The fitting to better match experiment involved the inclusion of interfacial recombination and modification of the diffusion coefficients in the perovskite layer. Figure adapted from ref. [3] and licensed under CC BY 3.0.

The standard parameter set for the drift-diffusion model, in red, is based on direct measurements and values in line with those reported in the literature. Recombination consists of bimolecular and electron-limited SRH. The blue data correspond to solutions obtained after modification of the standard parameter set to fit the experimental measurements. This parameter fitting involved the introduction of interfacial recombination at both perovskite/TL interfaces in order to obtain the same ‘ideality factor’ from Suns- V_{oc} measurements. Additionally, the anion vacancy density and density of states in the perovskite were increased, and the diffusion coefficients of all mobile charge in the perovskite were reduced. These changes were made to reproduce the open-circuit voltage and hysteresis, displayed by the experimental J - V curve.

As discussed in Section 4.1, the one-dimensional planar model is a considerable approximation for the mesoporous structure of some PSC architectures, including those measured for the data represented in Figure 4.9. Nonetheless, the particular transport properties of mesoporous cells can be approximately accounted for via modification of the input parameters. In contrast to planar cells, the mesoporous cells are modelled with reduced diffusion coefficients for electrons, holes and anion vacancies. Additionally, increased rates of interface recombination were required at the perovskite/ETL interface, perhaps as a result of the higher surface area at the mesoporous interface.

It is clear that the numerical solutions closely match the hysteresis and the gradient of the Suns- V_{oc} measurement. Riquelme *et al.* also show that the dependence of the open-circuit voltage on temperature is matched very well by the fitted parameter set. In contrast, the agreement is not as favourable between the simulated and experimental impedance spectra. The magnitude of the (real) impedance at intermediate frequencies (between the HF and LF features) matches very closely. However, there is a disparity between the size of the LF features, and as shown in Figure 4.9d, the characteristic frequency of the HF feature in the simulated spectrum is much greater than that for the experimental spectrum. In the latter case, this discrepancy can be accounted for via a ‘roughness factor’. Finally, we note that a series and shunt resistance has not been explicitly modelled.

This subsection demonstrates that the IS model reproduces the key PSC impedance features, and their dependence on illumination, for parameters other than those listed in Table 4.1, i.e. for mesoporous cells and inverted configurations. With extensive parameter fitting, Riquelme and coworkers were able to semi-quantitatively match both experimental J - V and impedance spectra using the drift-diffusion model [3]. In order to obtain similar simulation results to the measurements, (for a PSC with a mesoporous TiO_2 ETL), interfacial recombination was required. Manual parameter fitting is a difficult and time consuming process. There is opportunity for automated and optimised parameter searching, for example using machine learning [227]. Furthermore, analytic relations that describe the impedance response of a PSC would more directly show the impact of each parameter on the spectrum. This would greatly improve understanding of the impedance response of PSCs, and enable more straightforward fitting to impedance measurements. Overall, these results provide further validation of the ability of the drift-diffusion model to reproduce the impedance response of PSCs.

Intermediate frequency features

Thus far, we have focused on spectra with two features, corresponding to a low and high frequency time constant. While these are the most commonly observed features, other ‘exotic’ or intermediate frequency features have been reported in the literature. Representative examples of some of these features are given in Figure 3.11. These features include; (a) a loop between the two (positive) high and low frequency semicircles, (b) a ‘bulge’ or additional arc on the (positive) LF semicircle, (c) a ‘spiral’ where a negative LF feature extends back above the axis, and (d) two negative LF features (similar to the ‘bulge’ but below the axis). Notably, these exotic features are observed in impedance spectra obtained using the `IonMonger` IS module. Figure 4.10 shows examples of simulated impedance spectra that exhibit the four intermediate frequency features described above. These spectra are all simulated with a single concurrent recombination mechanism. Specifically, the recombination is either electron or hole-limited SRH.

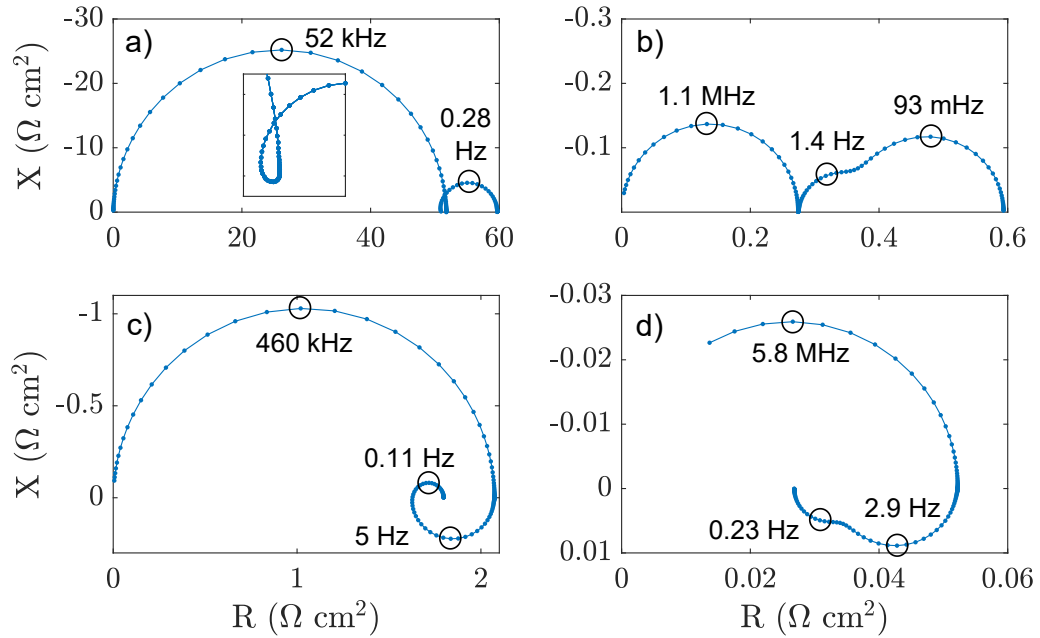


FIGURE 4.10: Examples of simulated PSC impedance spectra showing exotic intermediate frequency features. See Figure 3.11 for examples of these features in experiment. a) loop feature, simulated with modified parameters from Table 4.1 at 0.9 V. These parameters are the same as those used in Table 4.1 but with the following changes: $b = 400$ nm, $E_{cE} = -4.0$ eV and recombination is SRH with lifetimes $\tau_n = 3 \times 10^{-7}$ s and $\tau_p = 3 \times 10^{-9}$ s. b) ‘bulge’ feature determined using parameters from Table 4.1 with R_n recombination from Table 4.2 at 1.2 V. c) ‘spiral’ feature, obtained with the same parameters as a) but at 1.1 V. d) two negative features, obtained with the same parameters as b) but with R_p recombination. All spectra are simulated with 1-Sun equivalent illumination. Simulation protocol and the other parameters remain the same as those used throughout.

With the parameters stated (see the caption of Figure 4.10), these intermediate frequency features are observed at around 1-10 Hz. This is concordant with experimental reports [96, 228]. As detailed in Section 3.4.3, there has been significant speculation over their physical origin. It

has been suggested that loops are the result of measurements taking place under non-steady-state conditions [158, 229]. This has even been demonstrated experimentally (see the SI of ref. [158]) where cells show loops between LF and HF features when measured after insufficient stabilisation prior to measurement, which disappear when measured after sufficient time. Additionally, the degradation of cells, or other variations to measurement conditions, may also result in loop features. However, the drift-diffusion simulations presented here, and in [3, 125], demonstrate that loop features can be reproduced without invoking non-steady-state conditions or additional processes. Therefore, loops may indeed be a genuine feature of the impedance response of PSCs, but care should be taken to ensure impedance spectra are free from artefacts caused by non-steady-state measurement conditions.

The spectra presented in Figure 4.10 are particularly interesting because it has been proposed that these features may be the result of multiple mobile ionic species, or a single ionic species that diffuses at a different rate within the bulk or along grain boundaries [96]. However, these results demonstrate that a drift-diffusion model of a PSC, with a single mobile ionic species constrained to the perovskite layer, is sufficient to reproduce the rich variety of features observed in experiment. We note that this does not necessarily mean that IF features can not be produced by multiple mobile ionic species. For example, the intermediate frequency feature observed by García-Rodríguez *et al.* shows a dependence on the relative proportion of bromide versus iodide in the perovskite formulation [185]. In this case, the IF feature has a characteristic frequency closer in frequency to the HF feature, as opposed to the LF feature in Figure 4.10.

Additionally, we note that to generate the distinct IF features in simulations, as shown in Figure 4.10, this required a significant amount of fine-tuning of the parameters. The size and shape of these features are strongly dependent on the simulated experimental conditions, as well as cell and recombination parameters. In general, these features are not commonly observed in the simulations and, if observed, are less pronounced than the HF and LF features. A brief discussion of the origin of these features is given in Section 4.5.

4.4 Understanding the impedance response

To gain further insight into the response of a PSC during impedance measurements, it is helpful to examine the spatial distribution of charge and potential over the course of voltage perturbations. This helps to relate the temporal response to the frequency response captured by impedance measurements. The response of a PSC can be classified according to the frequency of the voltage perturbation. This motivates the classification of frequency ‘regimes’, in which the impedance response is approximately constant and is the result of particular physical processes. These regimes are indicated in Figure 4.11.

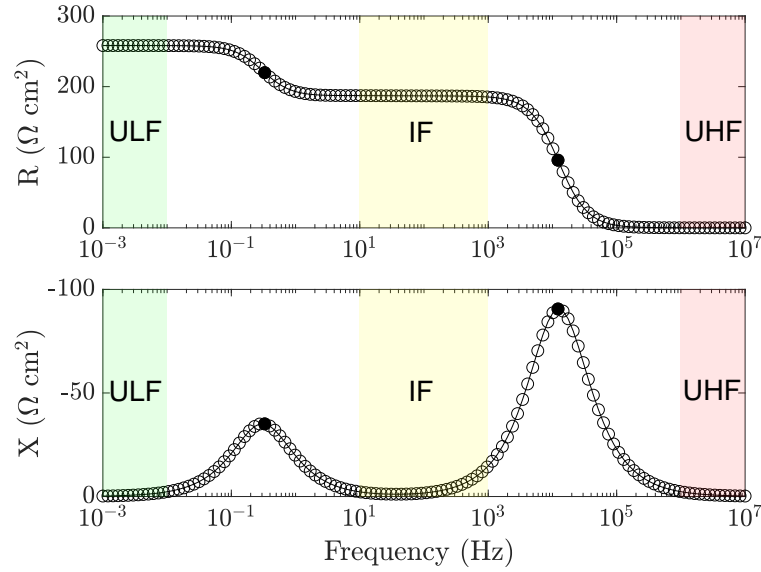


FIGURE 4.11: Frequency plot indicating the ultra-low frequency (ULF), intermediate frequency (IF), and ultra-high frequency (UHF) regimes. These regimes classify the three distinct responses of a PSC during impedance measurements. This spectra is the same as that presented in Figures 4.2 and 4.3. Specifically, $V_{DC} = 0.8$ V with electron limited SRH recombination in the bulk (R_n) under 0.1-Sun equivalent illumination. Cell and recombination parameters are listed in Tables 4.1 and 4.2 respectively.

The following frequency regimes categorise the impedance response of a PSC:

- **Ultra-low frequency regime:** $f \lesssim 10^{-2}$ Hz
 - Low frequency feature: $10^{-1} \lesssim f \lesssim 10^0$ Hz
- **Intermediate frequency regime:** $10^1 \lesssim f \lesssim 10^3$ Hz
 - High frequency feature: $10^4 \lesssim f \lesssim 10^5$ Hz
- **Ultra-high frequency regime:** $f \gtrsim 10^6$ Hz

The exact range of frequencies that these regimes span is dependent on the cell parameters as well as illumination and DC voltage. The low and high frequency features have also been indicated. These features are the result of the cell transitioning between different regimes that dominate the (frequency) response of the cell. The following sections describe the general response of a PSC within each of these regimes, followed by interpretations for the low and high frequency features.

4.4.1 Ultra-low frequency regime

The ultra-low frequency regime describes the response of a PSC for voltage perturbations of frequencies below around 10 mHz. Within this ultra-low frequency regime, the electric potential

across a PSC over a period of perturbation is described by Figure 4.12. This figure shows the electric potential across the three core layers of a PSC at five equally spaced time points during an ultra-low frequency impedance measurement. The electric field within the bulk of the transport layers as well as the bulk of the perovskite layer remains flat over the course of the perturbation. To compensate for the applied voltage perturbation, the potential drops at the perovskite/TL interfaces grow and shrink over a period. The flat potential across the bulk of the perovskite shows that there is virtually no electric field to drive the electrons and holes to their respective contacts.

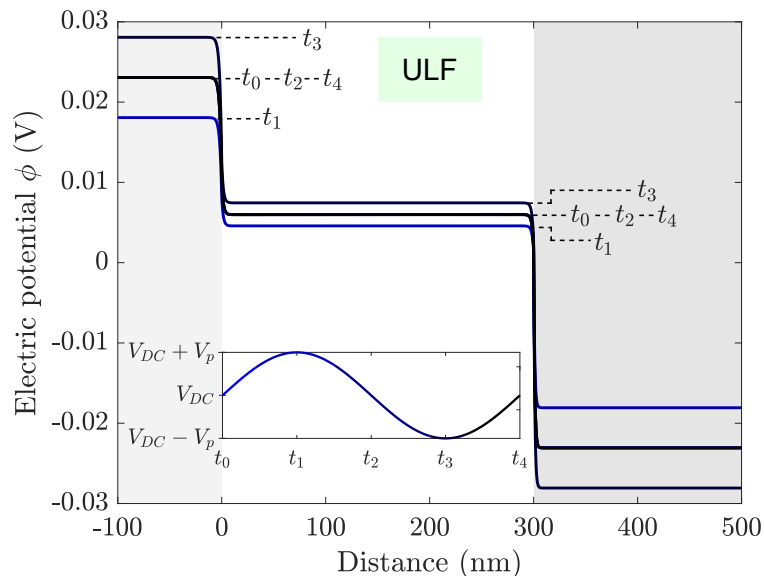


FIGURE 4.12: Electric potential at five equally spaced points in time during an ultra-low frequency impedance measurement, as indicated by Figure 4.11. The value of the applied voltage at the time points t_{0-4} is shown. Specifically, this is at 1 mHz but represents the electric potential for any perturbation with a frequency less than ~ 10 mHz. See, Figures 4.2 and 4.3 ($V_{DC} = 0.8$ V) for the full spectrum and simulation protocol.

The electric potential across the perovskite and adjacent Debye layers is largely determined by the applied voltage via the high density of anion vacancies [4–6]. This is shown in Figure 4.13 which plots the anion vacancy density across the perovskite layer at five equally spaced time points, in a similar fashion to Figure 4.12. The inset shows the filling and depleting of the right Debye layer (perovskite/HTL interface) by the anion vacancies relative to the steady-state (V_{DC}) distribution. Similarly, the charge contained within the Debye layer at the ETL/perovskite interface increases and decreases over a period. At these ultra-low frequencies, the slow drift of the anion vacancies can keep up with the ultra-low frequency voltage perturbation. Therefore, the ions (in approximate quasi-equilibrium) migrate in phase with the applied voltage and effectively screen the bulk electric field. The motion of ions into and out of the Debye layers modify the perovskite/TL potentials. These interfacial potentials modulate the current output of the cell via carrier recombination and collection.

The impact of the modulation of the interfacial potentials on the electron and hole distributions is shown in Figure 4.14. As the bulk electric field is screened by the ionic distribution throughout

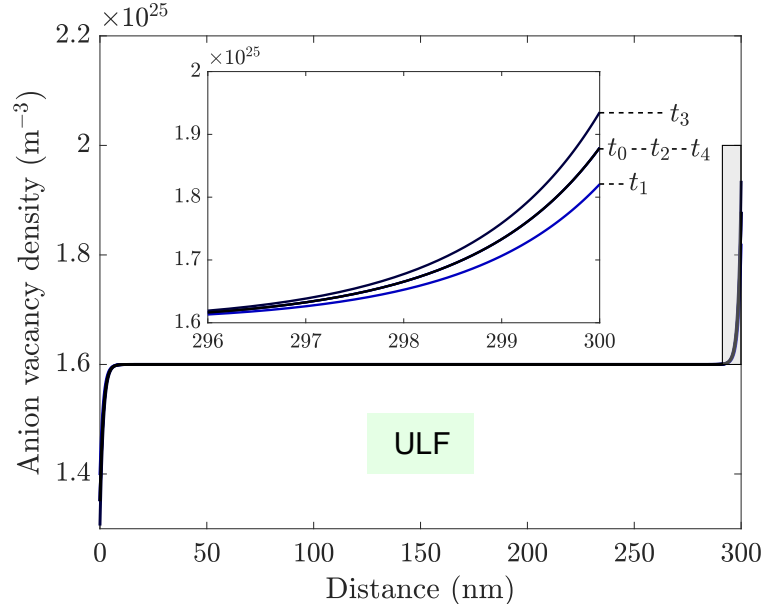


FIGURE 4.13: Anion vacancy density across the perovskite layer at five equally spaced points in time during an ultra-low frequency (ULF) impedance measurement. The inset shows a magnified view to capture the variation of the anion vacancy density within the perovskite/HTL Debye layer. The time points t_{0-4} are equivalent to those labelled in Figure 4.12.

an ultra-low frequency perturbation, the electrons and holes diffuse to a roughly uniform distribution across the bulk. These electron and hole distributions are equivalent to their steady-state distributions at the particular voltage $V(t_i)$. Increasing the voltage from steady-state ($t_0 - t_1$) causes an overall increase in the electron and hole densities. This is because reducing the size of the interfacial potential drops (via an increase to the applied voltage), impedes the transport of carriers to their respective transport layer. This results in a reduced current output (or increase in the recombination current). Conversely, reducing the applied voltage improves the transport and collection of carriers resulting in an increase in current.

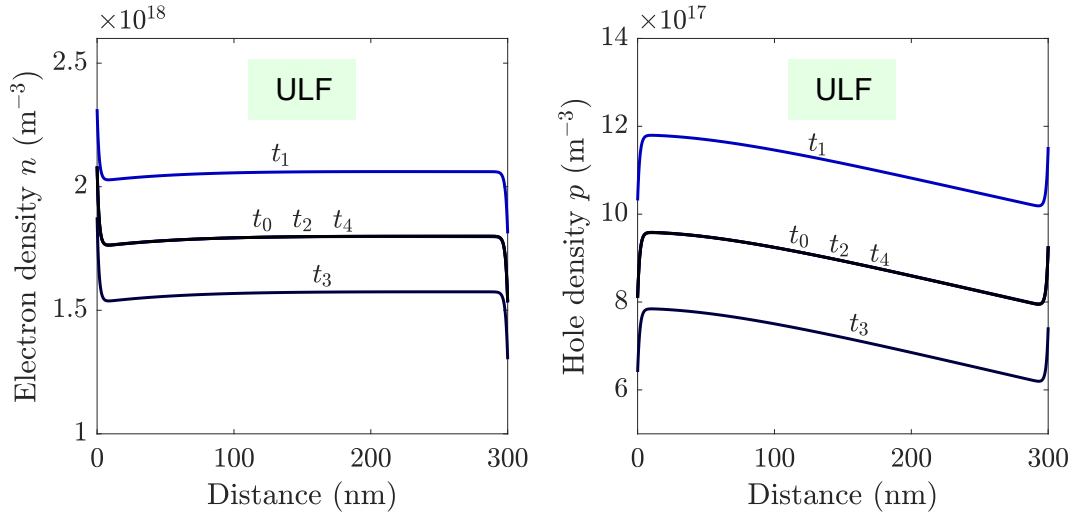


FIGURE 4.14: Electron density (left) and hole density (right) across the perovskite layer at five points in time over an ultra-low frequency perturbation. The time points t_{0-4} are equivalent to those labelled in Figure 4.12.

4.4.2 Intermediate frequency regime

The intermediate frequency regime characterises the response of a PSC to perturbations with frequencies of $10^1 \lesssim f \lesssim 10^3$ Hz. Figure 4.15 shows the variation of the electric potential during an intermediate (and ultra-high, see next subsection) frequency impedance measurement.

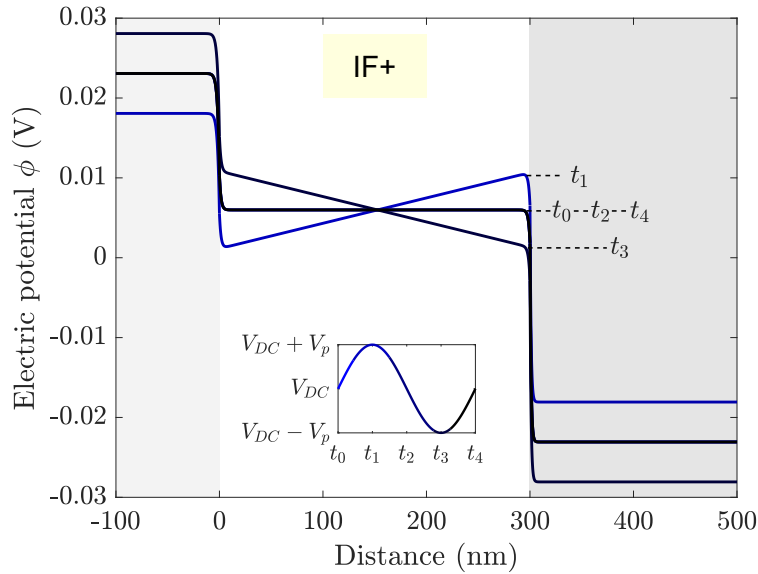


FIGURE 4.15: Electric potential at five equally spaced points in time during an intermediate frequency impedance measurement or above (IF+), as indicated by Figure 4.11. The value of the applied voltage at the time points t_{0-4} is shown. This figure is equivalent to Figure 4.12 but is valid for frequencies greater than ~ 10 Hz.

Over a period, the electric potential across the bulk of the transport layers remains flat and the applied potential is spread uniformly across the bulk of the perovskite. This results in an oscillating uniform bulk electric field which is in phase with the applied voltage. The size of the potential drops at the perovskite/TL interfaces remains constant. This is because at frequencies within and above the intermediate frequency regime, the ionic vacancies do not have time to move significantly over the course of a period. Therefore, the ionic vacancy distribution (to a very good approximation) remains fixed at the steady-state (V_{DC}) configuration as shown in Figure 4.16.

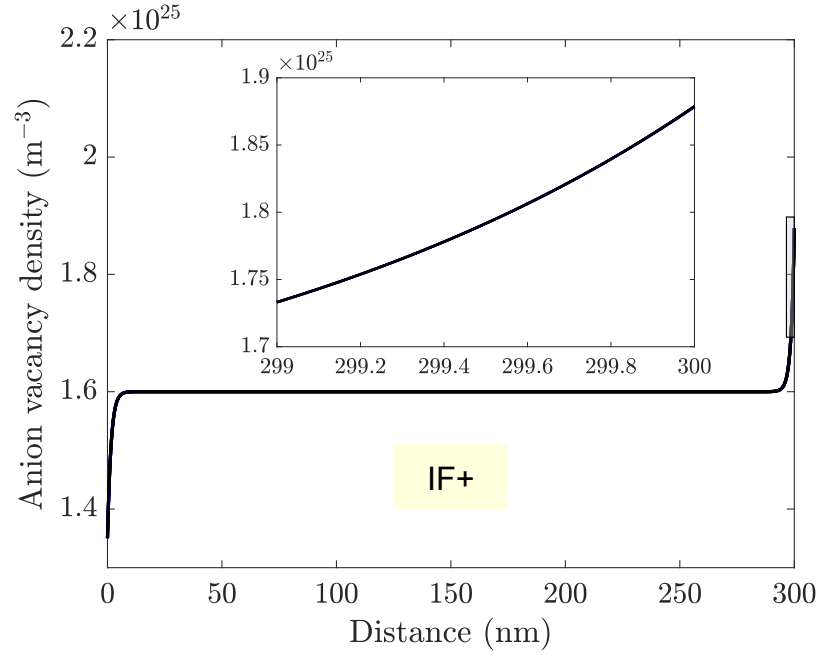


FIGURE 4.16: Anion vacancy density across the perovskite layer at five equally spaced points in time during an intermediate frequency impedance measurement or above (IF+). This is equivalent to Figure 4.13 but for frequencies above ~ 10 Hz. The inset shows that the anion vacancy density effectively remains static at the steady-state V_{DC} distribution.

Figure 4.17 shows how the sinusoidal components of the Debye layer charge and the electric field are dependent on the frequency of the perturbation. The Debye layer charge Q can be approximated by integrating the total ionic charge over the right-hand side of the perovskite layer as follows

$$Q(t) = q \int_{b/2}^b P(x, t) - N_0 \, dx, \quad (4.47)$$

where P is the anion vacancy density and N_0 is the static uniform cation vacancy density. The integration range is much larger than the width of the Debye layer. This is reasonable as within the bulk of the perovskite $P(x, t) \approx -N_0$. The ionic charge contained within the left-hand perovskite Debye layer is equal and opposite to the charge contained within the right-hand perovskite Debye layer. This Debye layer charge is a key component of the ‘surface polarisation model’, which is detailed in the following chapter. The electric field $E(t)$ is calculated at the

centre of the perovskite layer. This is illustrative of the entire bulk of the perovskite as the electric field is approximately uniform across it.

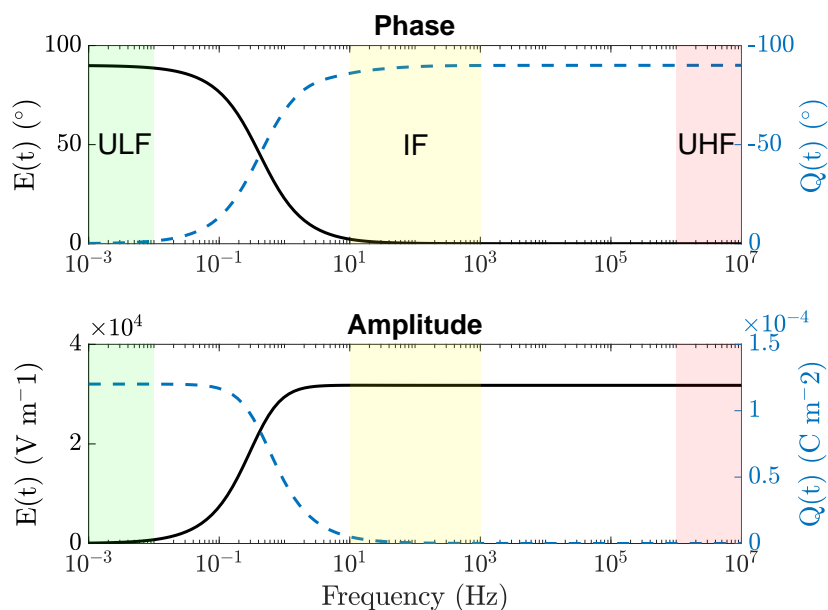


FIGURE 4.17: Phase and amplitude of the sinusoidal components of the bulk electric field E and Debye layer charge Q across an impedance spectrum. The electric field (black solid line) is calculated at the centre of the perovskite layer. The Debye layer charge (blue dashed line) is the excess ionic charge in the perovskite/HTL Debye layer. Note that the axis for the phase of the Debye layer charge is negative. Both phases have been shifted by 180° to be in line with the current convention (increasing $V \rightarrow$ increases J).

For each frequency, the sinusoidal component of the Debye layer charge and electric field is analysed using the same method presented in Section 4.2 to extract the amplitude and phase. Here we note that the phases of E and Q have been shifted by 180° . This is in line with the phase shift applied to the current perturbation and maintains the convention that an increase in voltage results in an increase in current. Therefore, the phase and amplitude of the bulk electric field and Debye layer charge can be plotted for each frequency as shown in Figure 4.17. With this representation it is clear that the amplitude of the electric field within the ultra-low frequency regime is negligible and the Debye layer charge amplitude is maximum. Conversely, within the IF frequency regime (and above), the Debye layer charge oscillation amplitude is negligible and the electric field oscillates with a maximum amplitude. This figure also shows that the relative phase between E and Q is approximately 90° throughout the frequency range.

In contrast to the ultra-low frequency regime, the carrier densities are strongly modulated by the alternating positive/negative bulk electric field. This is shown in Figure 4.18. Increasing the voltage from steady-state ($t_0 \rightarrow t_1$) induces a negative electric field across the bulk of the perovskite. This drives the electrons and holes away from their respective transport layers, reducing the current output. Conversely, reducing the voltage ($t_2 \rightarrow t_3$) forms a positive electric field, promoting the collection of carriers and increasing the current. As the fast-moving electronic carriers are in quasi-equilibrium, the electron and hole currents are in phase with the applied

voltage perturbation. Hence, the total current is in phase with the applied voltage within the intermediate frequency regime.

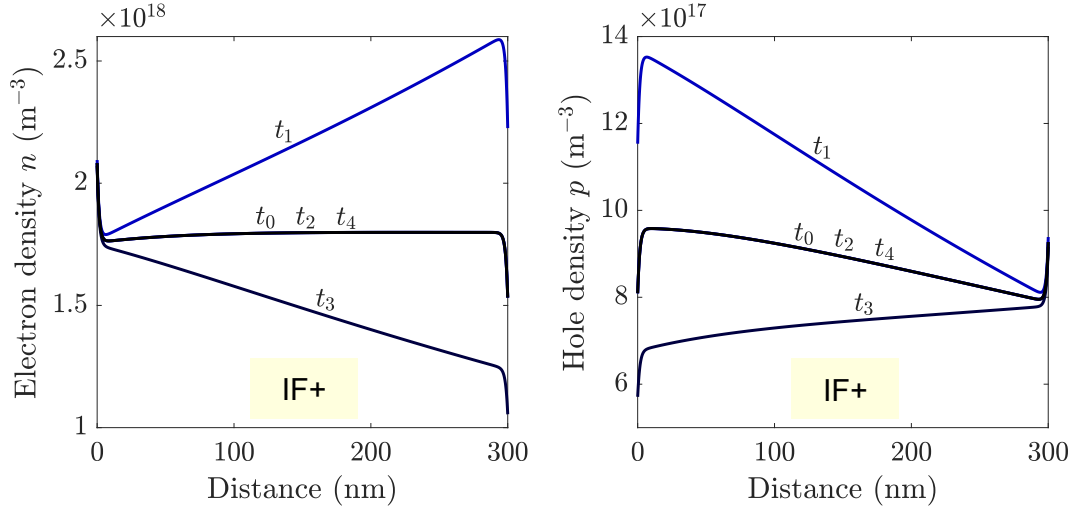


FIGURE 4.18: Electron density (left) and hole density (right) across the perovskite layer at five points in time over an impedance measurement above ~ 10 Hz. The time points t_{0-4} are equivalent to those labelled in Figure 4.15.

4.4.3 Ultra-high frequency regime

This regime describes the behaviour of a PSC during impedance measurements at frequencies above around 10^6 Hz. Within this regime, the electric potential over a period matches that within the IF regime (Figure 4.15). This is because for perturbation frequencies greater than around 100 Hz the anion vacancy distribution effectively remains static. However, in contrast to the intermediate frequency regime, the displacement current dominates the total current response at ultra-high frequencies. The displacement current, that contributes to the total current via eq.(4.37) is given by

$$j_d(x, t) = \epsilon_p \frac{\partial E(x, t)}{\partial t}. \quad (4.38 \text{ reprinted})$$

This current arises from the polarisation of the perovskite layer, in which the conductive transport layers act as the capacitor plates and the perovskite as the dielectric insulator³. Within the ultra-high frequency regime, the electric field across the bulk of the perovskite varies sinusoidally, in phase with the applied potential. As shown above, the displacement current is proportional to the rate of change of the electric field. Hence, during ultra-high frequency impedance measurements it has a phase relative to the voltage (and by definition E) of 90° . The amplitude of the displacement current only becomes non-negligible when the voltage across the device is modulated extremely quickly (i.e. at high frequencies).

Figure 4.19 shows how the sinusoidal components of the total current vary with frequency. The electron j_n , hole j_p and displacement currents j_d are all calculated at the centre of the

³This assumes sufficiently doped transport layers, which is reasonable for efficient PSCs.

perovskite layer. This figure shows that at frequencies within the ultra-high frequency regime, the amplitude of the electron and hole currents is insignificant compared to the amplitude of the displacement current. Therefore, the response of a PSC within the ultra-high frequency regime is characterised by the displacement current, which is purely capacitive. Consequently the total current has a positive phase and *leads* the voltage.

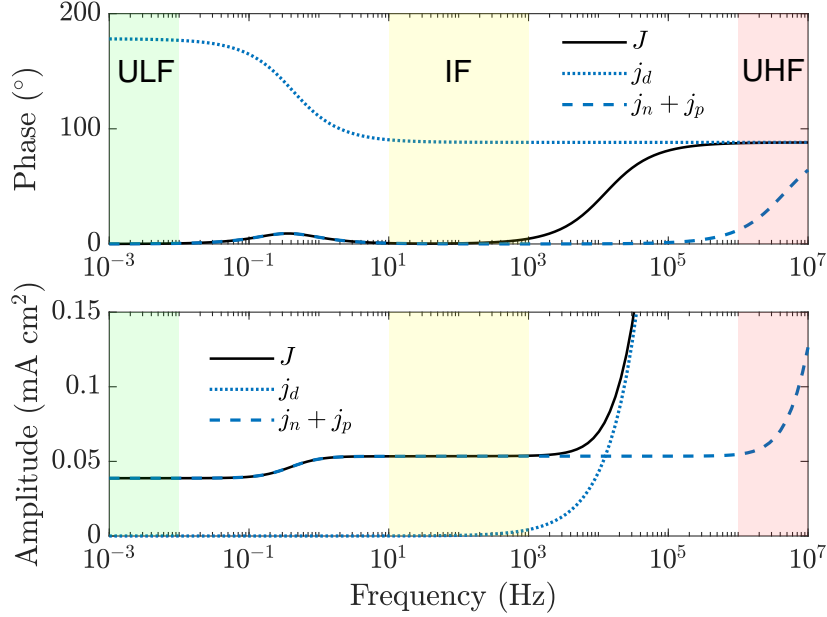


FIGURE 4.19: Amplitude and phase of the sinusoidal components of current versus frequency. The total current density is composed of the sum of the electron and hole currents $j_n + j_p$ and the displacement current j_d . This shows how the components of the total current vary according to frequency.

4.4.4 Low frequency feature

The numerical solutions find the characteristic frequency of the low frequency feature to be around 0.1-1 Hz, which is in line with experimental measurements [171, 175]. Additionally, the so-called giant capacitance associated with the LF feature and its dependence on illumination, as observed in experiment, is reproduced by the model [177]. This is demonstrated in Figure 4.8, which shows values ranging from 10-1000 mF cm⁻²; concordant with experimental calculations [115, 147, 157, 162].

As stated previously, the features apparent on the Nyquist plots of the spectra are produced in the transition between two different frequency regimes. The low frequency feature is produced over frequencies that span the transition between the ultra-low frequency and intermediate frequency regimes. Over these frequencies, the mobile ions can no longer move sufficiently quickly to remain in phase with voltage perturbation and are therefore unable to fully screen the electric field from the central region of the perovskite layer. This means that the interfacial potentials are modulated *and* there is a bulk electric field, which is out of phase with the applied voltage perturbation. This is shown in Figure 4.17, where the amplitudes of both $E(t)$ and $Q(t)$ are

non-negligible and have an absolute phase between 0° and 90° . As a result, the electron and hole currents are modulated by both the interfacial potentials, and the bulk electric field.

As reported experimentally, the numerical solutions show that the low frequency feature can be ‘capacitive’ (positive) and also ‘inductive’ (negative). This numerical model helps to probe and understand the underlying physics responsible for the low frequency feature. In the case of a ‘capacitive’ or positive LF feature, the changes to the interfacial potentials from the slow movement of ions within the ultra-low frequency regime modulates the current less strongly (i.e. the amplitude of the current is smaller) than in the intermediate frequency regime where the electric field modulates the current. Conversely, an ‘inductive’ or negative LF feature is observed when the motion of the ions within the ultra-low frequency regime modulates the current more strongly than the bulk electric field does in the intermediate frequency regime. This negative feature corresponds to the current lagging the voltage. In other words, the phase of the current is negative. This phase is usually indicative of an inductance; however, the relationship with frequency means that this feature is more appropriately classified as a negative ‘capacitance’. Nonetheless, the positive or negative capacitance associated with the low frequency feature is not a true capacitance. Similarly, the resistance associated with this feature, which is also negative when the capacitance is negative, is not true resistance. An RC element (resistor and capacitor in parallel) should only be used to extract the diameter of the semicircle and the time constant of the feature.

4.4.5 High frequency feature

The properties of the HF feature, as shown in the numerical solutions for the impedance spectra, are consistent experimental measurements. The HF feature is visible as a semicircle above the axis on the Nyquist plots, for example see Figures 4.2, 4.6, 4.9 and 4.10. The HF feature is produced in the frequency range between the intermediate frequency and the ultra-high frequency regimes. Over this frequency range, the ionic vacancies are effectively static, since they move too slowly to significantly adjust their position in response to the high frequency forcing. They thus remain fixed in the same configuration that they would adopt at the DC voltage. The electric field, which is in phase with the applied voltage perturbation, modulates the electron and hole currents. Additionally, the displacement current, which is 90° out of phase with the electric field, contributes to the total current. A more detailed description of the current response at high frequencies is given in Section 4.4.3.

With the perovskite solar cell parameters listed in Table 4.1, the characteristic frequency of the HF feature in the numerical spectra is around 10 - 100 kHz. This is in line with experimental reports [96, 147]. The resistance associated with the HF feature, displays the same dependence on illumination and DC voltage as observed in experiment [3, 96, 131]. Calculating the theoretical geometric capacitance of the PSC using eq.(3.20) and the device parameters from Table 4.1 returns a capacitance of 71 nF cm^{-2} . This value closely matches the value of C_{HF} determined by fitting to the numerical impedance spectra, as shown in Figure 4.8. Here, the value of the

capacitance is around a factor of 10 times less than that measured experimentally [96, 131, 147]. This discrepancy has been attributed to the roughness of the perovskite/transport layer interfaces and is accounted for by introducing a qualitative roughness factor, as described in Section 3.4.1 [131].

4.5 Conclusion

To summarise, a drift-diffusion model that includes mobile anion vacancies within the perovskite layer has been presented. We follow the particular model formulation specified by Courtier *et al.* [4]. Numerical solutions to this model are obtained using the open-source PSC simulation tool *IonMonger*. With the aid of an additional impedance module, developed especially for this thesis and the associated published works, we were able to simulate impedance spectroscopy measurements.

As shown in Section 4.3, the numerical solutions for the impedance response of a PSC are consistent with experiment. For example, the HF feature is a semicircular feature above the axis on a Nyquist plot, and observed at around 10 - 100 kHz. The associated capacitance is approximately independent of voltage and illumination, with a value predicted from eq.(3.20), indicating a geometric capacitance. The high frequency resistance displays a linear dependence on the light intensity, indicating that it is proportional to a recombination resistance. As observed in experiment, the LF feature is semicircular and can lie either above or below the axis, corresponding to a positive or negative ‘capacitance’ respectively. The numerical model correctly predicts the so-called giant capacitances measured in experiment and demonstrates how mobile ions can impact the charge injection, extraction, and recombination of electrons and holes during a LF impedance measurement. The more unusual intermediate frequency features, including loops and additional arcs, can also be reproduced by the drift-diffusion model. This is demonstrated in Figure 4.10 which qualitatively matches the experimental spectra presented in Figure 3.11.

In Section 4.3, it is shown that the low and high frequency features displayed within the simulated spectra display the same dependencies on illumination as observed for experimental spectra [147]. Additionally, Riquelme *et al.* showcase results that reproduce these trends for cell parameters that describe mesoporous and inverted cells [3]. Furthermore, a direct comparison of simulated spectra, obtained using this numerical model, to experimental measurements has been made by Riquelme *et al.* [3]. In this work, a semi-quantitative fit to both impedance spectra and J - V measurements is obtained after fitting device parameters for the drift-diffusion model [3]. It is found that interfacial recombination is required to match the observed hysteresis and the approximate features within the impedance spectra.

A framework to understand the impedance response of PSCs, depending on the frequency of perturbation, is established. We classify three frequency regimes, in which the impedance response is approximately constant and is the result of particular physical processes. For each

regime, the spatial distribution of charge and potential during impedance measurements are examined, helping to relate the temporal response to the frequency response. The impact of the bulk electric field and the ionic charge within the Debye layers on the current response is examined. Classifying and understanding the cell's response for each of the frequency regimes, helps to elucidate the causes of the high and low frequency features, which are observed as the cell transitions between two frequency regimes.

Understanding the exact processes responsible for the exotic IF features remains a challenge. We note that for spectra that display only a HF and LF feature, the electric field perturbation over all frequencies is a constant 90° out of phase with the Debye layer charge oscillations, as shown in Figure 4.17. However, when IF features are observed, this phase difference is no longer exactly equal to 90° in the IF regime. This indicates that IF features are produced when the charge carrier distribution is high enough to impact the ionic vacancy distribution. In general, this is not the case. However, at high voltages (at or above V_{oc} at 1-Sun) the charge carrier densities are high enough to accumulate and impact the ionic distribution. These findings are in line with the drift-diffusion simulations by Jacobs *et al.*, where it was found that loops could be obtained when the density of the carriers within the perovskite was increased [125]. While interesting, these features are not a universal feature of the impedance response of PSCs. Hence, a more detailed investigation of the IF features is left for future work.

The simulated spectra presented in this chapter were produced using the IS module for the open-source PSC simulator `IonMonger` [206]. This module will be released as an update to `IonMonger` to provide an accessible and fast tool for researchers to simulate IS measurements of PSCs.

The numerical model presented in this chapter is capable of simulating PSCs under a wide parameter regime, including regimes that result in an extremely stiff set of PDEs. The impact of specific parameters on the spectra can be examined. For example, the ionic density, or the type of recombination, can be modified to understand their effect on the impedance response of a PSC. It is not always straightforward to obtain quantitative agreement with experiment via parameter fitting because each parameter, or measurement condition, does not necessarily have a linear effect on the resulting spectra. Additionally, changing the size of one parameter impacts how other parameters modify the spectra. Even with the optimisations made to the IS module for speed of simulation, with over 20 parameters it is a time-consuming and challenging task to obtain a good fit to experiment. Analytic solutions, derived from the same underlying drift-diffusion model can show the impact of each parameter on the features, and more directly describe the fundamental impedance response of a PSC. A comparison of these analytic solutions to the numerical model will enable validation of their accuracy.

The drift-diffusion model employed in this chapter was originally developed to accurately simulate current-voltage measurements across a range of scan rates [4, 6]. Accordingly, the model contains the device physics required to accurately simulate both short and long timescales and, as a result, is ideal to simulate the impedance response across a wide frequency range. In general,

the model uses the simplest, but physically accurate, descriptions to approximate the workings of PSCs. More sophisticated descriptions are only added when necessary to reproduce experiment. For example, in contrast to other solar cell models, it was found that the high density of mobile ions within the perovskite layer played a considerable role in device operation and therefore must be included in a device model [6, 69]. Additionally, it was determined that the transport layers played a significant role in the observed characteristics of PSCs [4]. This approach results in a minimally complex model that describes the mobile charge and electric potential within the three core layers. Additional physics, such as multiple ionic species, photogeneration of ions, steric effects, or inclusion of two-dimensional geometries may be necessary to more accurately simulate the physics of PSCs. For example, to explain the HF capacitance without a roughness factor or the flattening of the semicircles. Furthermore, the planar ‘three-layer’ model employed here is not directly suitable for PSCs with less standard architectures, such as those that employ novel layers [230] or Ruddlesden-Popper phases [231].

Overall, the simulated impedance spectra show favourable agreement with experiment, thereby providing validation for the underlying drift-diffusion model of a PSC. It is found that a high density of mobile anion vacancies coupled with electrons and holes in the perovskite layer and appropriately modelled transport layers is sufficient to describe the fundamental impedance response of PSCs. This agreement with experiment motivates the derivation of an analytic model, via systematic approximations of the full drift-diffusion model, to describe the impedance response. This is the aim of the following chapter.

Chapter 5

Deriving an analytic model for IS simulation

In this chapter the surface polarisation, or ionic capacitance, model of a PSC is described. This is a systematically derived approximation (see refs. [4, 5]) to the coupled ionic-electronic drift-diffusion model for a PSC presented in the previous chapter. This model forms the basis for which analytic formulae can be derived; however, in order to arrive at tractable final solutions, further approximations are made. It is shown that for efficient PSCs the charge carriers (electrons and holes) can be approximated by a Boltzmann distribution. This allows the recombination equations for five different pathways to be simplified and enables a straightforward, yet general, equation for the total current output of a PSC to be derived. Finally, through linearisation, simple analytic relations are determined that describe the low and high frequency features of PSC impedance spectra.

To date, accounting for and understanding the impacts of mobile ions on the impedance response of PSCs has been challenging. Approaches thus far either use one of many proposed equivalent circuit models, whose physical origin are not suitably justified [157, 232] or use numerical methods to determine the solution to a drift-diffusion model [3, 125, 158, 183], which can involve a time consuming fitting process to match experimental spectra. The approach we present in this chapter addresses the drawbacks associated with both of these methods, yielding analytic solutions that justify a particular equivalent circuit and defines the associated resistances and capacitances in terms of physical device parameters. In the following chapter these analytic relations are examined and verified against numerical solutions to the full drift-diffusion model.

This chapter is set out as follows. Section 5.1 details the surface polarisation model for a perovskite solar cell. Section 5.2 presents the Boltzmann approximation for the carrier densities and its accuracy is confirmed on comparison to numerical solutions. Next, in Section 5.3, a general form for the recombination current for different recombination types is systematically derived, which includes a factor which we term the *electronic ideality factor*. Following this, the

current is linearised and analytic relations for the impedance of a PSC are determined in Section 5.4. Finally, in Section 5.5, we summarise the chapter and present our conclusions.

5.1 The surface polarisation model

The surface polarisation model of a PSC is a systematically derived (and highly accurate) approximation to the standard coupled drift-diffusion model for charge carrier transport across the cell and the motion of a single ion species in the perovskite absorber [4–6]. This model greatly reduces the complexity of the underlying drift-diffusion model and enables analytic results to be obtained after further analysis. Accordingly, the surface polarisation model is a key component in the derivation of an analytic model for impedance spectroscopy simulation.

To derive the surface polarisation model, Richardson *et al.* and Courtier *et al.* employed the technique of matched asymptotic analysis for a single-layer model of a PSC [5, 6]. In this model, the transport layers are assumed to be very highly doped such that they can be considered ‘quasi-metals’. Consequently, the electric potential across the transport layers is uniform and equal to the applied potential at the metal contacts. Additionally, the majority carrier density is uniform and equal to the doping density within the transport layers. Extension of the surface polarisation model to a three-layer model was later made by Courtier *et al.* [4]. Here, the transport layers are no longer assumed to be quasi-metals resulting in the correct description of the potential drops that form within the transport layers at the perovskite/TL interfaces. This model provides a more accurate description of PSCs and demonstrates how transport layer properties impact their operation. In more recent work by Courtier, the three-layer surface polarisation model was employed to determine an analytic relation for the current density at steady-state [135]. This enabled comparison to the traditional diode equation and identified the ideality factor. This is detailed further in Chapter 3.1.

5.1.1 Model description

Unlike other photovoltaics the response of PSCs is determined not only by the motion of the charge carriers but also by that of mobile ion vacancies. This makes their physics more complex than that of other solar cells. In the case of MAPbI₃ it is known, both from experiment [102, 233] and from *ab-initio* molecular calculations [69], that there is significant motion of the relatively mobile iodide ion vacancies. These vacancies move much more slowly than the (electronic) charge carriers and occur at much higher densities. In addition, mobile ion vacancies are known to occur at sufficiently high densities to result in the formation of narrow Debye (or double) layers at the interfaces between the perovskite and the transport layers. See, for example, [69, 195]. Figure 5.1 shows a schematic of these Debye layers and the electric potential across a PSC. Indeed Debye layers are a requirement for simulations to reproduce the behaviours that are characteristic of PSCs [4, 6, 125, 158, 183, 234, 235].

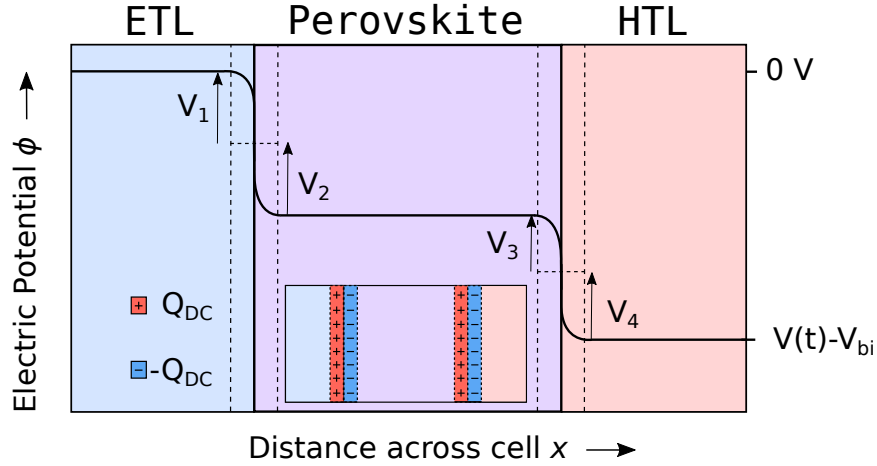


FIGURE 5.1: Diagram illustrating the potential drops V_1 - V_4 across a perovskite solar cell at steady-state. Dashed lines indicate the four Debye layers located at the perovskite/TL interfaces. Inset shows the charge contained within the perovskite Debye layers at steady-state Q_{DC} . Not to scale.

The properties of PSCs described above enable Richardson *et al.* [6] and Courtier *et al.* [4, 5] to derive the surface polarisation model from the underlying charge-transport model of the cell. Firstly, the approximate, yet highly accurate, physical insights that this model provide are described ahead of presentation of the equations. The comparatively high density of mobile charged ion vacancies in the perovskite crystal structure means that the internal electric potential within the device is, to a very good approximation, determined almost solely by the ion vacancy distribution, and is almost completely unaffected by the charge carrier distributions. Below the built-in voltage, the iodide vacancies accumulate at the perovskite/HTL interface. The total amount of excess ionic charge within this right Debye layer is given by Q . This is balanced by an equal and opposite ionic charge $-Q$ at the ETL/perovskite Debye layer. The Debye layers within the selective contacts contain an equal and opposite (electronic) charge to that contained within the adjacent perovskite Debye layer.

Additionally, it is found that the electric potential varies significantly within the narrow Debye layers around the transport layer interfaces but is well-approximated as linear in the perovskite bulk and flat in the bulk of the highly-doped transport layers (see Figure 5.2). Therefore, no electric field forms within the bulk of the transport layers and the electric field in the bulk of the perovskite is uniform. The uniform bulk electric field drives ionic vacancies into or out of the perovskite Debye layers. The redistribution of ionic vacancies is such that at steady-state, the bulk electric field within the perovskite is zero. Under non-steady-state conditions the total potential drop $V_{bi} - V(t)$ across the cell is composed of five components, as illustrated in Figure 5.2, such that

$$V_{bi} - V(t) = V_1(t) + V_2(t) + bE(t) + V_3(t) + V_4(t). \quad (5.1)$$

Here, $V_1(t)$ is the potential drop across the portion of the left-hand Debye layer lying within

the ETL; $V_2(t)$ is the potential drop across the portion of the left-hand Debye layer lying within the perovskite; $bE(t)$ is the potential drop occurring across the central region of the perovskite; $V_3(t)$ is the potential drop across the portion of the right-hand Debye layer lying within the perovskite; and, $V_4(t)$ is the potential drop across the portion of the right-hand Debye layer lying within the HTL.

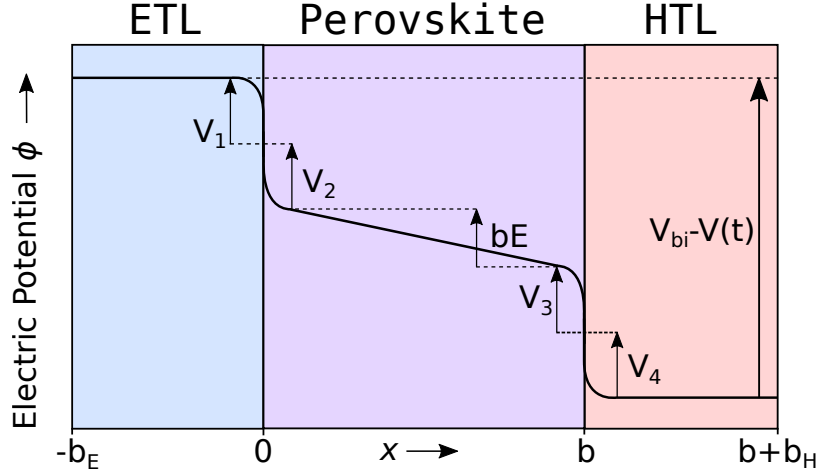


FIGURE 5.2: Diagram illustrating the electric potential across a PSC with a non-zero bulk electric field after a rapid reduction to the applied voltage.

The bulk electric field is related to the ionic charge contained within the perovskite/HTL Debye layer (per unit area), $Q(t)$, via

$$E(t) = \frac{V_T}{qD_+N_0} \frac{dQ}{dt}, \quad (5.2)$$

in which V_T is the thermal voltage, D_+ is the vacancy diffusion coefficient and N_0 is the uniform static cation vacancy density (equal to the average anion vacancy density). A full list of the material parameters that appear in the equations that follow are defined in Table 4.1. On rearranging eq.(5.1), and using eq.(5.2) for the bulk electric field, the evolution of the Debye layer charge in time is given by the ordinary differential equation (ODE)

$$\frac{dQ}{dt} = \frac{qD_+N_0}{V_Tb} \left(V_{bi} - V(t) - V_1(Q(t)) - V_2(Q(t)) - V_3(Q(t)) - V_4(Q(t)) \right). \quad (5.3)$$

As the ion motion is relatively slow, the charge within the Debye layers lags behind the changes in the applied voltage. The potential drops V_{1-4} are a function of the Debye layer surface charge Q . The exact functional forms of $V_1(Q)$, $V_2(Q)$, $V_3(Q)$ and $V_4(Q)$ are contingent on the physics of the device. In the widely considered scenario in which a single positively charged ion vacancy species is constrained to the perovskite layer, the potential drops V_{1-4} are given by [4]

$$\begin{aligned} V_1(Q) &= -\mathcal{V}(-\Omega_E Q), & V_2(Q) &= -\mathcal{V}(-Q), \\ V_3(Q) &= \mathcal{V}(Q), & V_4(Q) &= -\mathcal{V}(-\Omega_H Q), \end{aligned} \quad (5.4)$$

where the dimensionless parameters Ω_E and Ω_H set the relative magnitudes of V_1 and V_4 respectively and are defined

$$\Omega_E = \sqrt{\frac{\varepsilon_p N_0}{\varepsilon_E d_E}}, \quad \Omega_H = \sqrt{\frac{\varepsilon_p N_0}{\varepsilon_H d_H}}. \quad (5.5)$$

The capacitance relation $\mathcal{V}(Q)$ ¹ is given by

$$\mathcal{V}(Q) = \begin{cases} V_T \log \left[-\text{LambertW}_0 \left(-e^{-\left(\frac{q N_0 \varepsilon_p V_T Q^2}{2} + 1 \right)} \right) \right] & \text{for } Q \leq 0, \\ V_T \log \left[-\text{LambertW}_{-1} \left(-e^{-\left(\frac{q N_0 \varepsilon_p V_T Q^2}{2} + 1 \right)} \right) \right] & \text{for } Q > 0. \end{cases} \quad (5.7)$$

Here, the W_0 and W_{-1} correspond to the 0th and the -1st branches of the Lambert W function respectively. Figure 5.3 plots this non-linear capacitance relation. Figure 5.4a) shows the Debye layer charge calculated for different steady-state applied voltages for the cell parameters listed in Table 4.1. This was achieved using a numerical root finding algorithm to solve eq.(5.1). Note that steady-state values are denoted as ‘DC’. This is in line with the notation used later in this chapter. Additionally, Figure 5.4b) shows the dependence of the potential drops V_{1-4} on the Debye layer charge.

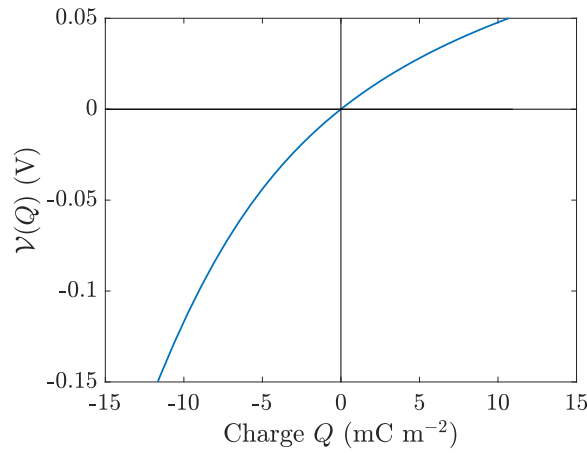


FIGURE 5.3: Non-linear capacitance relation from the surface polarisation model [4–6] given by equation (5.7).

¹The inverse of $\mathcal{V}(Q)$, is a more simple relation and is given by

$$Q(\mathcal{V}) = \sqrt{q N_0 \varepsilon_p V_T} \text{sign}(\mathcal{V}) \sqrt{2} \left(e^{\mathcal{V}/V_T} - \mathcal{V}/V_T - 1 \right)^{\frac{1}{2}}. \quad (5.6)$$

Evaluating this can be less numerically intensive than its inverse.

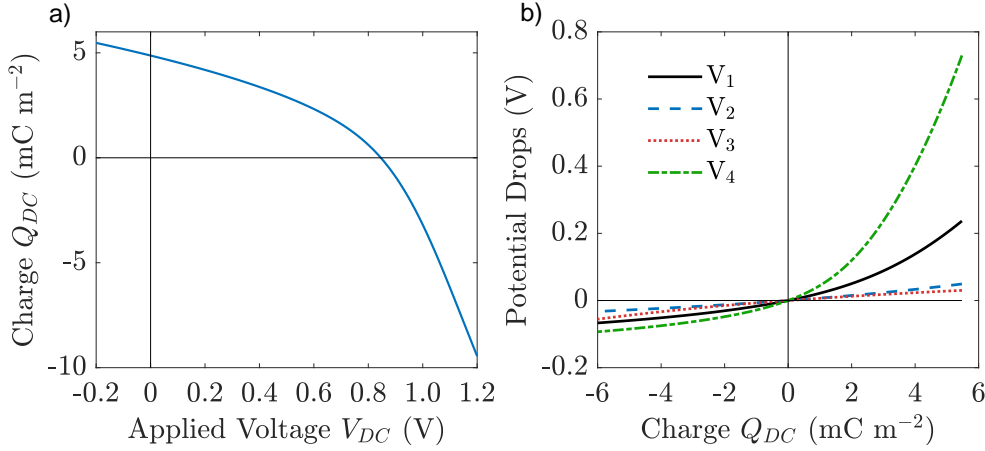


FIGURE 5.4: Left: Charge within the Debye layers for different steady-state (DC) applied voltages. Right: Potential drops across the interfaces of a PSC at steady-state with varying Debye layer charge. See Figure 5.1 for an illustration of these potential drops across the cell. The relative magnitudes of V_{1-4} are dependent on perovskite and transport layer properties via eq.(5.5). Table 4.1 lists the parameters used for these examples.

5.1.2 Drift-diffusion equations within the surface polarisation model

The drift-diffusion equations that describe the electron and hole densities within the perovskite bulk ($0 < x < b$) are given by

$$-\frac{1}{q} \frac{\partial j_n}{\partial x} = G_{\text{bulk}}(x) - R_{\text{bulk}}(n, p), \quad (5.8)$$

$$\frac{1}{q} \frac{\partial j_p}{\partial x} = G_{\text{bulk}}(x) - R_{\text{bulk}}(n, p), \quad (5.9)$$

$$j_n = qD_n \left(\frac{\partial n}{\partial x} + \frac{n}{V_T} E(t) \right), \quad (5.10)$$

$$j_p = -qD_p \left(\frac{\partial p}{\partial x} - \frac{p}{V_T} E(t) \right), \quad (5.11)$$

where G_{bulk} and R_{bulk} are the generation and recombination rates in the bulk respectively. The same rates are used as those defined in equations (4.20) and (4.21). Note that in contrast to equations (4.1) and (4.2) the time derivatives of the electron and hole densities, $\partial n / \partial t$ and $\partial p / \partial t$, have been neglected. This is because, for physically accurate parameter estimates, the electronic motion is extremely fast relative to the other timescales within the system. Consequently, the electron and hole densities are in quasi-equilibrium, even during rapid changes to the potential, i.e. during high frequency impedance measurements. Therefore, it is a reasonable approximation to disregard these time derivatives. Further justification can be found in ref. [5].

At the ETL/perovskite interface the hole current is subject to the following boundary condition:

$$j_p|_{x=0^+} = -qR_l \quad (5.12)$$

where R_l is the recombination rate at the left boundary. The interfacial recombination rates are defined in equations (4.24) and (4.25) and are functions of the carrier densities given by (5.16) and (5.17) respectively. The electron density within the perovskite at the interface is subject to

$$n|_{x=0+} = k_E d_E \exp\left(-\frac{V_1 + V_2}{V_T}\right), \quad (5.13)$$

where k_E is the ratio between the electron densities across the boundary, given by equation (4.27). At the perovskite/HTL interface the electron current is specified as

$$j_n|_{x=b-} = -qR_r, \quad (5.14)$$

where R_r is recombination rate at right interface. The boundary condition for the hole density at the perovskite/HTL interface is given by

$$p|_{x=b-} = k_H d_H \exp\left(-\frac{V_3 + V_4}{V_T}\right), \quad (5.15)$$

where k_H is defined in eq.(4.28) and is the ratio between the hole densities across the interface. The interfacial recombination rates, R_l and R_r , are functions of the carrier densities within the Debye layers at each interface. In their analysis, Courtier *et al.* find that at leading order the charge carrier densities are Boltzmann-distributed within the Debye layers [4]. Hence, at the ETL/perovskite interface (on $x = 0$) the carrier densities are given by [4]

$$\begin{aligned} n_{\text{ETL}}^{(l)}(t) &= d_E \exp\left(-\frac{V_1}{V_T}\right), \\ p^{(l)}(t) &= p|_{x=0+} \exp\left(-\frac{V_2}{V_T}\right), \end{aligned} \quad (5.16)$$

where, the electron density within the ETL is denoted by $n_{\text{ETL}}^{(l)}$ and the hole density within the perovskite is denoted by $p^{(l)}$. Correspondingly, at the perovskite/HTL interface ($x = b$) the electron density within the perovskite, $n^{(r)}$ and the hole density within the HTL, $p_{\text{HTL}}^{(r)}$ are given by

$$\begin{aligned} n^{(r)}(t) &= n|_{x=b-} \exp\left(-\frac{V_3}{V_T}\right), \\ p_{\text{HTL}}^{(r)}(t) &= d_H \exp\left(-\frac{V_4}{V_T}\right). \end{aligned} \quad (5.17)$$

The exponential functions of the potential drops V_{1-4} account for the steep variation in carrier densities over the Debye layers.

5.1.3 The total current

The total current within the perovskite layer is given by

$$J(t) = j_n(x, t) + j_p(x, t) + j_d(x, t) + j_P(x, t). \quad (4.37 \text{ reprinted})$$

The displacement current j_d is defined in eq.(4.38) and, with this approximate model, is not spatially dependent as the bulk electric field is uniform. The ionic current j_P , resulting from the motion of ions across the perovskite width, is at least four orders of magnitude less than the other current contributions. This is true across the full impedance spectrum and therefore it is reasonable to neglect this ionic current contribution. Evaluating the total current (4.37) at $x = b^-$ yields

$$J(t) = -qR_r + j_p|_{x=b^-} + j_d(t), \quad (5.18)$$

where the boundary condition (5.14) is used to specify $j_n|_{x=b^-}$. To determine the hole current at $x = b^-$, we integrate eq.(5.9) as follows

$$\frac{1}{q} \int_{0^+}^{b^-} \frac{\partial j_p}{\partial x} dx = \int_{0^+}^{b^-} G_{\text{bulk}}(x) - R_{\text{bulk}}(n, p) dx, \quad (5.19)$$

to give

$$\frac{1}{q} j_p|_{x=b^-} - \frac{1}{q} j_p|_{x=0^+} = \int_{0^+}^{b^-} G_{\text{bulk}}(x) - R_{\text{bulk}}(n, p) dx. \quad (5.20)$$

Here, $j_p|_{x=0^+}$ is defined via the boundary condition eq.(5.12). Substituting the relation above for $j_p|_{x=b^-}$ into eq.(5.18) an expression for the total current is obtained

$$J = q \int_{0^+}^{b^-} G_{\text{bulk}}(x) - R_{\text{bulk}}(n, p) dx - qR_r - qR_l + j_d. \quad (5.21)$$

For the following analysis it is helpful to define the generation current density

$$j_{\text{gen}} = q \int_{0^+}^{b^-} G_{\text{bulk}}(x) dx, \quad (5.22)$$

which, on integration using the generation rate (eq.(4.20)) gives

$$j_{\text{gen}} = qF_{ph} (1 - e^{-\alpha b}). \quad (5.23)$$

Additionally, the recombination or equivalently *dark* current density is defined

$$j_{\text{rec}} = q \int_{0^+}^{b^-} R_{\text{bulk}}(n, p) dx + qR_r + qR_l. \quad (5.24)$$

As such, the total current density can be expressed as

$$J(t) = j_{\text{gen}} - j_{\text{rec}}(t) + j_d(t). \quad (5.25)$$

5.1.4 Summary of the surface polarisation model

In comparison to the full drift-diffusion model presented in Chapter 4, the surface polarisation model is a greatly simplified set of equations. The coupled PDEs are reduced to a single first order ordinary differential equation for $Q(t)$, namely (5.3), that describes the evolution of ionic and electronic charge within the Debye layers and a quasi-steady state boundary value problem for the charge carriers within the perovskite bulk. The temporal and spatial stiffness has been eliminated through the decoupling of the electronic and ionic dynamics, and by explicitly resolving the solution in the Debye layers. As such, the surface polarisation model not only enables numerical solutions to be obtained more easily, it facilitates analytical solution. Specifically, to obtain solutions for the current output of a PSC, equation (5.3) is integrated in time for a given applied voltage $V(t)$. This determines the Debye layer charge $Q(t)$ which allows the bulk electric field $E(t)$ and voltage drops $V_{1-4}(t)$ to be determined as functions of time, from equations (5.8-5.11). At a given time point t_i , the boundary value problem (5.8-5.15) can be solved to determine the electron and hole densities across the perovskite layer. This enables the current output of the cell, at the time t_i , to be computed from eq.(5.25). Solving the boundary value problem repeatedly at different time points for which $Q(t)$ is known, enables the current flow $J(t)$ across the cell to be determined as a function of time.

The solutions obtained from the surface polarisation model have been verified against those determined from the full drift-diffusion model [4, 5, 135]. Excellent agreement is observed between the drift-diffusion model and the surface polarisation model in the relevant parameter regimes, validating the approximations employed to derive the surface polarisation model. On employing the surface polarisation model a variety of experimental observations have been reproduced including current-voltage hysteresis, dark current decay transients and voltage-dependent ideality factors [4, 6, 135, 236].

5.2 Boltzmann approximation to the carrier densities

Analytic solutions can be determined from the surface polarisation model without further simplification [210]. However, in order to arrive at a tractable final solution that can be interpreted relatively easily, we employ the further approximation that the charge carriers in the perovskite are Boltzmann distributed. This approximation has also been employed in ref. [135]. To justify this approximation, we need to analyse the typical size of the parameters within the drift-diffusion equations. This is done via non-dimensionalisation which involves rescaling the dimensional variables by parameters with magnitudes (and units) that are intrinsic to the cell. Here, we use

the same scaling as in [206] with the dimensionless variables labelled with a *

$$\begin{aligned} x &= bx^*, & p &= d_H p^*, & n &= d_E n^*, \\ j_p &= qF_{ph} j_p^*, & j_n &= qF_{ph} j_n^*, & E &= \frac{V_T}{b} E^*. \end{aligned} \quad (5.26)$$

Ideally, this rescaling would result in dimensionless variables that all have magnitudes of order 1. However, this is not always the case; under typical operational conditions the magnitudes of variables such as the carrier densities are strongly dependent on factors such as the applied voltage, illumination and recombination. Therefore, the magnitudes of the non-dimensional variables should still be considered when comparing the sizes of different variables. On applying the rescaling as specified above to equations (5.10) and (5.11) for the electron and hole currents, one obtains

$$j_n^* = \kappa_n \left(\frac{\partial n^*}{\partial x^*} + n^* E^*(t) \right), \quad (5.27)$$

$$j_p^* = -\kappa_p \left(\frac{\partial p^*}{\partial x^*} - p^* E^*(t) \right), \quad (5.28)$$

where the dimensionless variables are defined

$$\kappa_n = \frac{D_n d_E}{F_{ph} b}, \quad \kappa_p = \frac{D_p d_H}{F_{ph} b}. \quad (5.29)$$

With device parameters from Table 4.1 these have magnitudes

$$\kappa_n = \kappa_p \approx 2 \times 10^7. \quad (5.30)$$

It is implicitly assumed in conducting the non-dimensionalisation that the electron and hole currents across the perovskite have sizes

$$j_n^* \approx \mathcal{O}(1), \quad j_p^* \approx \mathcal{O}(1). \quad (5.31)$$

As such it is apparent that the following approximation can be made

$$\frac{\partial n^*}{\partial x^*} \approx -n^* E^*(t), \quad \frac{\partial p^*}{\partial x^*} \approx p^* E^*(t). \quad (5.32)$$

This approximation is accurate for cells operating near their built-in voltage that have long carrier diffusion lengths with respect to the total perovskite layer width, as is the case in state-of-the-art PSCs [31, 222]. Integrating and applying the boundary conditions (eq.(5.13) and eq.(5.15)) one obtains

$$\begin{aligned} n^* &= k_E \exp \left(-\frac{V_1 + V_2}{V_T} - x^* E^* \right), \\ p^* &= k_H \exp \left(-\frac{V_3 + V_4}{V_T} + (x^* - 1) E^* \right). \end{aligned} \quad (5.33)$$

These approximate expressions describe the carrier densities as Boltzmann distributed. Figure 5.5 plots these approximate expressions at different applied voltages together with numerical solutions from the full drift-diffusion model. Specifically, the distributions at five equally spaced time points are calculated for a high frequency impedance perturbation of the form of eq.(3.7), with $V_p = 10$ mV. The spacing of the five time points over a perturbation is illustrated in Figure 4.12. A HF perturbation is chosen to observe the effect of the bulk electric field. It is clear that the approximate solutions closely match the numerical solutions in the bulk of the perovskite at open-circuit (0.93 V). The correspondence is reasonable at the maximum power point (0.82 V), however, it is poor at voltages much below this. Between 0.7 V and open-circuit, the average carrier density in the perovskite increases by around two orders of magnitude. Therefore, at voltages close to open-circuit many more carriers are present in the perovskite. This enhances conductivity and, in turn, leads to the establishment of a quasi-equilibrium (i.e. Boltzmann) carrier distribution.

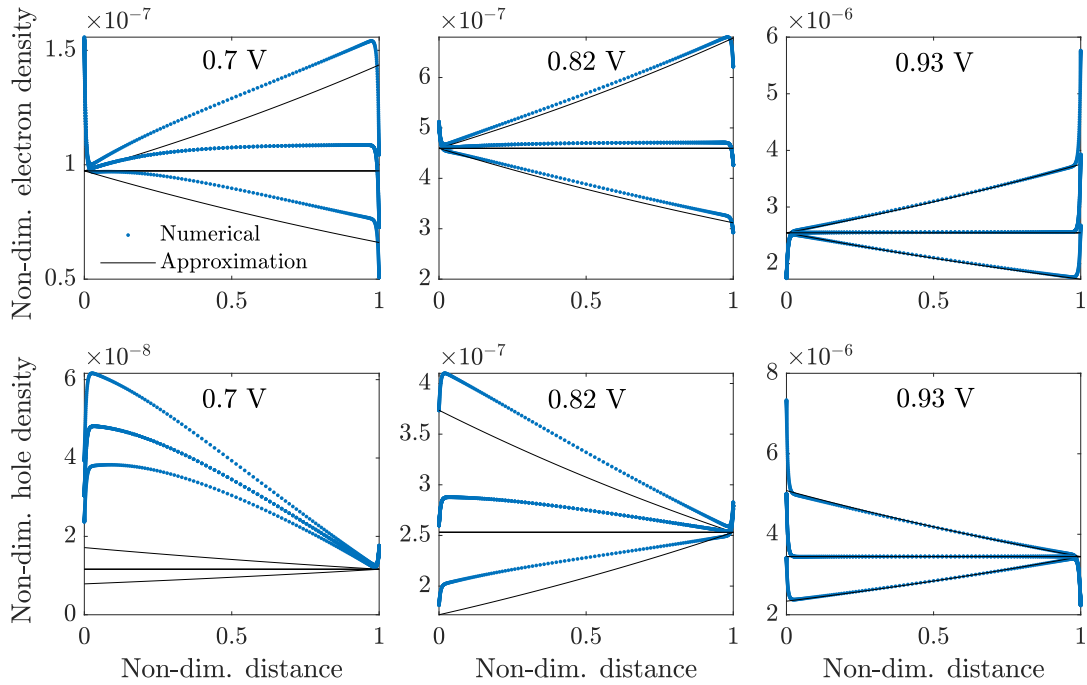


FIGURE 5.5: Comparison between solutions obtained for the electron and hole densities from the full drift-diffusion model and the Boltzmann approximation, given by 5.33. Solutions during a high frequency impedance perturbation (25 kHz) at different DC voltages are shown, including maximum power point (0.82 V) and open-circuit (0.93 V). The parameters used are detailed in Table 4.1, under 0.1-Sun equivalent illumination and with recombination at the ETL/perovskite interface (R_l) from Table 5.1.

On re-dimensionalising the approximate Boltzmann distributions given by (5.33) one obtains

$$\begin{aligned} n(x, t) &= k_E d_E \exp \left(-\frac{V_1(t) + V_2(t) + xE(t)}{V_T} \right), \\ p(x, t) &= k_H d_H \exp \left(-\frac{V_3(t) + V_4(t) + (b-x)E(t)}{V_T} \right). \end{aligned} \quad (5.34)$$

An additional example showing the agreement between these approximate relations and the full drift-diffusion model is shown in Figure 5.6. Simulation and cell parameters remain the same as those used for Figure 5.5, with the addition of calculating the carrier densities over an ultra-low frequency perturbation (1 mHz in this case). Insets show the left and right perovskite Debye layers.

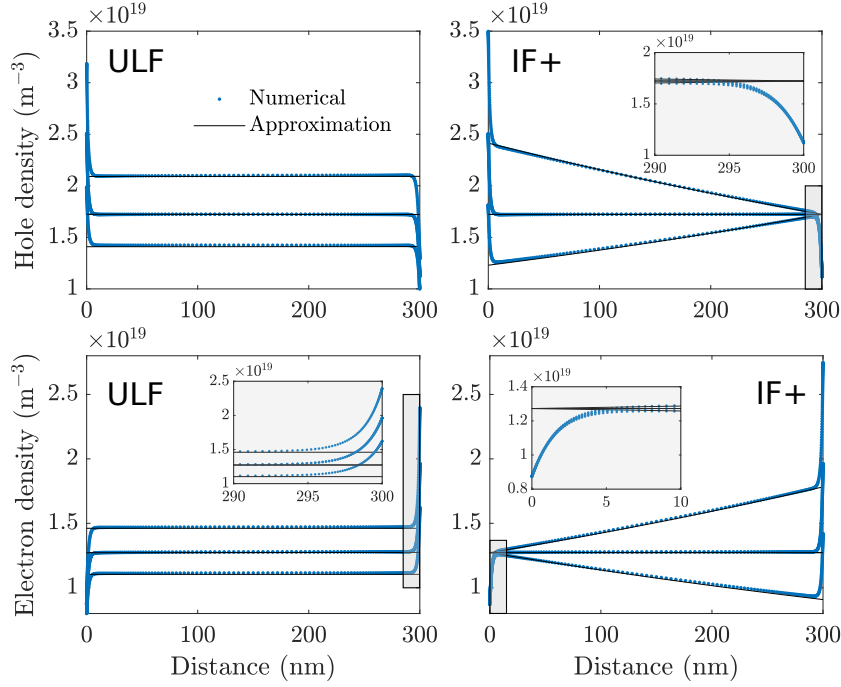


FIGURE 5.6: Comparison between solutions obtained for the electron and hole densities from the full drift-diffusion model and the Boltzmann approximation, given by (5.34). In both cases $V_{DC} = V_{oc}$. Left: carrier density at equally spaced intervals over an ultra-low frequency period (specifically, 1 mHz). Right: the equivalent but over a period of frequency 25 kHz. IF+ refers to frequencies within the intermediate frequency regime and above, i.e. greater than around 100 Hz. The parameters used are detailed in Table 4.1, under 0.1-Sun equivalent illumination and with recombination at the ETL/perovskite interface (R_l) from Table 5.1.

To further verify the effectiveness of the Boltzmann approximation, Figure 5.7 plots the carrier densities at maximum power point. Good agreement is shown, although it is not as good as at open-circuit. Additionally, Figure 5.7 shows solutions for a reduced anion vacancy density (at V_{oc}). Specifically, the mean anion vacancy density is $1.6 \times 10^{23} \text{ m}^{-3}$ which is two orders of magnitude less than the default used throughout. In this case, the solutions closely match in the perovskite bulk, however the lower anion vacancy density results in much wider Debye layers. This is expected as the Debye length is proportional to $1/\sqrt{N_0}$ [5].

Finally, Figure 5.8 shows a calculation of the error for the Boltzmann approximation eq.(5.34) at different DC voltages, both under illumination and in the dark. The relative error is calculated from the hole density determined from eq.(5.34) and the hole density determined from the numerical solution to the full drift-diffusion model. The mean relative error is then calculated at each time point during a sinusoidal perturbation, across 128 frequencies from 1 mHz to 10 MHz.

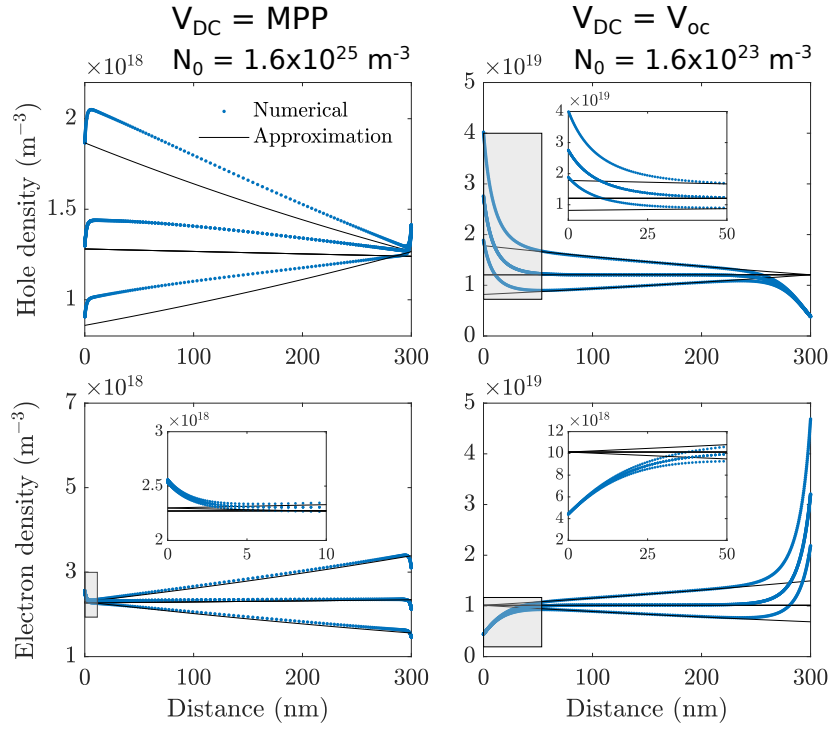


FIGURE 5.7: Verification of the Boltzmann approximation for the electron and hole densities at maximum power point (MPP) 0.82 V (left) and with a lower anion vacancy density at open-circuit 0.92 V (right). The carrier densities at five points in time over a period of frequency 25 kHz are shown. Illumination is 0.1-Sun with R_l recombination. Insets show the left Debye layer within the perovskite.

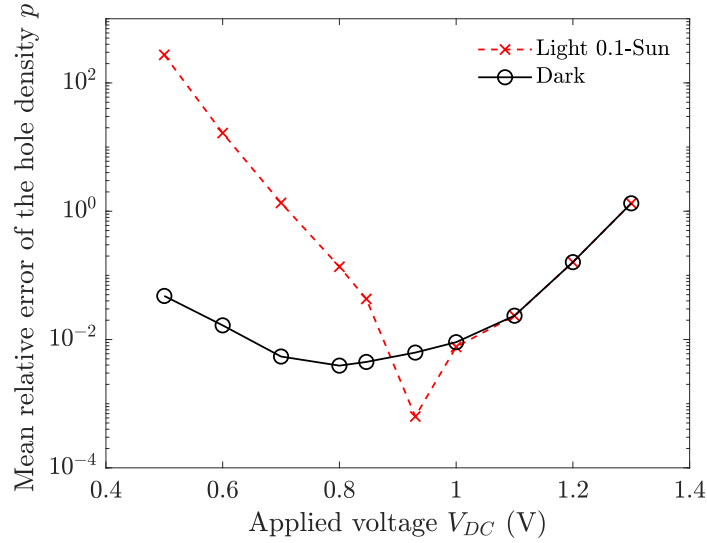


FIGURE 5.8: Mean relative error between the hole density calculated from the approximate relation eq.(5.34) and numerical solution to the full drift-diffusion model at different DC voltages. Hole densities calculated both under simulated illumination at 0.1-Sun and in the dark. Recombination is chosen to be at the ETL/perovskite interface (R_l) with device parameters from Table 4.1. For these parameters, the built-in voltage of the cell is 0.85 V and the open-circuit voltage at 0.1-Sun equivalent illumination is 0.93 V.

Overall, Figures 5.6-5.8 demonstrate that the carrier densities across the perovskite bulk during an impedance voltage perturbation are well approximated by (5.34) near the built-in voltage of the cell. The results presented in the following chapter demonstrate how well this approximation works when employed to model impedance spectroscopy measurements.

5.3 Recombination current

As derived earlier in this chapter, the total current density flowing across the cell $J(t)$, equation (5.25), is comprised of three components: the current generated by the incident radiation j_{gen} , the current loss due to charge carrier recombination $-j_{\text{rec}}$ and, at high frequencies, the displacement current j_d . Specifically, it is given by

$$J(t) = j_{\text{gen}} - j_{\text{rec}}(t) + j_d(t). \quad (5.25 \text{ reprinted})$$

The current density generated by the incident radiation j_{gen} can be determined via eq.(5.23) and the displacement current in time j_d can be evaluated via solution to the ODE for the Debye layer charge, given by equation (5.3), with a specified applied voltage. Therefore, on calculation of the recombination current given by

$$j_{\text{rec}} = qR_l \left(n_{\text{ETL}}^{(l)}(t), p^{(l)}(t) \right) + qR_r \left(n^{(r)}(t), p_{\text{HTL}}^{(r)}(t) \right) + q \int_0^b R_{\text{bulk}}(n(x, t), p(x, t)) dx, \quad (5.24 \text{ reprinted})$$

the total current density can be determined. With the approximated carrier distributions across the perovskite bulk given by eq.(5.34), the recombination current can be calculated straightforwardly using the bulk recombination rate R_{bulk} , and the interfacial rates R_l (on the interface with the ETL) and R_r (on the interface with the HTL). However, simplification to the recombination rates leads to a far more tractable relation for the recombination current. On analysing the typical sizes of the recombination parameters, the full forms of the five recombination mechanisms considered in this work can be approximated as either bimolecular or monomolecular, as shown in Table 5.1. The values for the recombination lifetimes used for each recombination type are also displayed. The simplified recombination rates provide very good approximations to the full rates and have been used in other modelling studies [4, 5]. In line with the rest of the approximations detailed in this chapter, the approximated recombination rates are verified against numerical solutions to the full model in Chapter 6.

In the case where there is a single dominant recombination mechanism, it is shown in the following subsections that the recombination current can be expressed in the general form

$$j_{\text{rec}}(t) = j_{R_i} \exp \left(- \frac{F_i(V_1(Q(t)), V_2(Q(t)), V_3(Q(t)), V_4(Q(t)))}{V_T} - \frac{b}{n_{\text{el}} V_T} E(t) \right). \quad (5.35)$$

Recombination Type	Full Form	Approximation	Parameter Values
Bimolecular, R_b	$R_{\text{bulk}} = \beta (np - n_i^2)$	$R_{\text{bulk}} \approx \beta np$	$\beta = 10^{-12} \text{ m}^3 \text{ s}^{-1}$
Hole-limited SRH, R_p	$R_{\text{bulk}} = \frac{np - n_i^2}{\tau_n p + \tau_p n + k_{SRH}}$	$R_{\text{bulk}} \approx \frac{p}{\tau_p}$	$\tau_n = 3 \times 10^{-10} \text{ s}$ $\tau_p = 3 \times 10^{-8} \text{ s}$
Electron-limited SRH, R_n	$R_{\text{bulk}} = \frac{np - n_i^2}{\tau_n p + \tau_p n + k_{SRH}}$	$R_{\text{bulk}} \approx \frac{n}{\tau_n}$	$\tau_n = 3 \times 10^{-8} \text{ s}$ $\tau_p = 3 \times 10^{-10} \text{ s}$
ETL/Perovskite interfacial, R_l	$R_l = \frac{n_{\text{ETL}}^{(l)} p^{(l)} - n_i^2 / k_E}{p^{(l)} / v_{nE} + n_{\text{ETL}}^{(l)} / v_{pE} + k_l}$	$R_l \approx v_{pE} p^{(l)}$	$v_{nE} = 10^5 \text{ ms}^{-1}$, $v_{pE} = 5 \text{ ms}^{-1}$
Perovskite/HTL interfacial, R_r	$R_r = \frac{n^{(r)} p_{\text{HTL}}^{(r)} - n_i^2 / k_H}{p_{\text{HTL}}^{(r)} / v_{nH} + n^{(r)} / v_{pH} + k_r}$	$R_r \approx v_{nH} n^{(r)}$	$v_{nH} = 5 \text{ ms}^{-1}$ $v_{pH} = 10^5 \text{ ms}^{-1}$

TABLE 5.1: List of the recombination types and the relevant parameter values used in this work. The full and approximated rates are used in the numerical and analytic calculations respectively. Unless otherwise stated, the recombination parameter values used are those specified here. The intrinsic carrier density n_i , and the parameters k_{SRH} , k_l and k_r are defined in (4.22)-(4.28). The interfacial recombination rates are dependent on the carrier densities at the left and right interfaces; for the analytic model, these are defined by equations (5.16) and (5.17) respectively.

Here, $F_i(V_1, V_2, V_3, V_4)$ (the potential barrier to recombination for recombination type i , where $i = b, p, n, l$ or r), n_{el} (the *electronic* ideality factor) and j_{R_i} (the recombination current prefactor) all depend on the dominant recombination mechanism and, for the recombination mechanism stated in Table 5.1, are presented in Table 5.2. Notably, the electronic ideality factor n_{el} , takes either the value 1 or 2, depending on the recombination mechanism, and can thus be used as a diagnostic tool (just as the ideality factor is in conventional photovoltaics) in order to distinguish between different possible sources of recombination within the cell. Importantly, all the ionic effects are contained in the function F_i so that n_{el} depends only upon purely electronic effects. Further discussion of the electronic ideality factor can be found in Section 6.3, along with details of how it may be obtained experimentally.

Label R_i	Recombination	$F_i(V_1, V_2, V_3, V_4)$	j_{R_i}	n_{el}
R_b	$R_{\text{bulk}} = \beta np$	$V_1 + V_2 + V_3 + V_4$	$qb\beta k_E d_E k_H d_H$	1
R_p	$R_{\text{bulk}} = p / \tau_p$	$V_3 + V_4$	$\frac{qb k_H d_H}{\tau_p}$	2
R_n	$R_{\text{bulk}} = n / \tau_n$	$V_1 + V_2$	$\frac{qb k_E d_E}{\tau_n}$	2
R_l	$R_l = v_{pE} p^{(l)}$	$V_2 + V_3 + V_4$	$q k_H d_H v_{pE}$	1
R_r	$R_r = v_{nH} n^{(r)}$	$V_1 + V_2 + V_3$	$q k_E d_E v_{nH}$	1

TABLE 5.2: Recombination types with labelling convention and corresponding values for the electronic ideality factor. $F_i(V_1, V_2, V_3, V_4)$ is the potential barrier to recombination for recombination of type R_i , where $i = b, p, n, l, r$. This notation enables the recombination current (5.35) (and later the impedance parameters) to be written in a general form. The total potential drop across the cell at steady state is given by $V_1 + V_2 + V_3 + V_4 = V_{\text{bi}} - V_{\text{DC}}$.

Equation (5.35) is an extension of the recent work by Courtier to non-steady state conditions [135]. This enables the frequency-dependent current output, as required for IS simulation, to be

determined later in this chapter. The following subsections, detail the derivation of the recombination current for each of the five recombination types. This is to justify the representation given in eq.(5.35).

Bimolecular recombination. In this first example, only bimolecular recombination in the bulk of the perovskite, $R_{\text{bulk}} = \beta np$ takes place. Shockley-Read-Hall recombination in the bulk is zero as are the interfacial recombination rates R_l and R_r . In this case, from eq.(5.24), the recombination current is given by

$$j_{\text{rec}} = q\beta k_E d_E k_H d_H \int_0^b \exp\left(-\frac{V_1(t) + V_2(t) + V_3(t) + V_4(t) + bE(t)}{V_T}\right) dx. \quad (5.36)$$

Given that V_{1-4} and $E(t)$ are not spatially dependent

$$j_{\text{rec}} = qb\beta k_E d_E k_H d_H \exp\left(-\frac{V_1(t) + V_2(t) + V_3(t) + V_4(t) + bE}{V_T}\right). \quad (5.37)$$

On defining the following for bimolecular recombination, R_b

$$j_{R_b} = qb\beta k_E d_E k_H d_H, \quad F_b(t) = V_1(t) + V_2(t) + V_3(t) + V_4(t), \quad n_{\text{el}} = 1, \quad (5.38)$$

one can write the recombination current in the form

$$j_{\text{rec}}(t) = j_{R_b} \exp\left(-\frac{F_b(V_1(t), V_2(t), V_3(t), V_4(t))}{V_T} - \frac{b}{n_{\text{el}} V_T} E(t)\right). \quad (\text{eq.(5.35) for } R_b)$$

Table 5.2 details the definitions of j_{R_b} , $F_b(t)$ and the electronic ideality factor n_{el} for bimolecular (and the other forms of) recombination.

Hole-limited recombination. The following considers hole-limited SRH in the bulk of the perovskite layer. Therefore, $R_{\text{bulk}} = p/\tau_p$ while the bimolecular and interfacial recombination rates are zero. The recombination current is given by

$$j_{\text{rec}} = \frac{qk_H d_H}{\tau_p} \int_0^b \exp\left(-\frac{V_3(t) + V_4(t) + (b-x)E(t)}{V_T}\right) dx. \quad (5.39)$$

Integrating this over the cell width, one obtains

$$j_{\text{rec}} = \frac{qk_H d_H}{\tau_p} \exp\left(-\frac{V_3(t) + V_4(t)}{V_T}\right) V_T \frac{1 - \exp(-\frac{bE(t)}{V_T})}{E}. \quad (5.40)$$

Making the substitution $\bar{E} = bE/V_T$, one can write

$$j_{\text{rec}} = \frac{qb k_H d_H}{\tau_p} \exp\left(-\frac{V_3(t) + V_4(t)}{V_T}\right) \frac{1 - \exp(-\bar{E})}{\bar{E}}. \quad (5.41)$$

Considering small perturbations to the bulk potential drop (bE) relative to the thermal voltage, as is reasonable for impedance measurements, suggests expanding in powers of the small quantity

\bar{E}

$$\frac{1 - \exp(-\bar{E})}{\bar{E}} = 1 - \frac{\bar{E}}{2} + \mathcal{O}(\bar{E}^2). \quad (5.42)$$

Neglecting terms of order $\mathcal{O}(\bar{E}^2)$ and noting that

$$\exp(-\frac{\bar{E}}{2}) = 1 - \frac{\bar{E}}{2} + \mathcal{O}(\bar{E}^2), \quad (5.43)$$

allows us to rewrite the recombination current in the form

$$j_{\text{rec}} \approx \frac{qbk_H d_H}{\tau_p} \exp\left(-\frac{V_3(t) + V_4(t)}{V_T} - \frac{b}{2V_T} E(t)\right). \quad (5.44)$$

where \bar{E} has been eliminated. Defining the following for hole-limited recombination

$$j_{R_p} = \frac{qbk_H d_H}{\tau_p}, \quad F_p(t) = V_3(t) + V_4(t), \quad n_{\text{el}} = 2, \quad (5.45)$$

one can write the recombination current in the form of equation (5.35).

Electron-limited recombination. Here the bulk recombination rate $R_{\text{bulk}} = n/\tau_n$ and $R_l = R_r = 0$. The recombination current is given by

$$j_{\text{rec}} = \frac{qk_E d_E}{\tau_n} \int_0^b \exp\left(-\frac{V_1(t) + V_2(t) + xE(t)}{V_T}\right) dx. \quad (5.46)$$

Integrating one obtains

$$j_{\text{rec}} = \frac{qk_E d_E}{\tau_n} \exp\left(-\frac{V_1(t) + V_2(t)}{V_T}\right) V_T \frac{1 - \exp(-\frac{bE}{V_T})}{E(t)}. \quad (5.47)$$

Using the same approximations detailed in equations (5.42) and (5.43), the recombination current can be written

$$j_{\text{rec}} = \frac{qbk_E d_E}{\tau_n} \exp\left(-\frac{V_1(t) + V_2(t)}{V_T} - \frac{b}{2V_T} E(t)\right) + \mathcal{O}(E^2). \quad (5.48)$$

Defining the following for electron-limited bulk SRH recombination

$$j_{R_n} = \frac{qbk_E d_E}{\tau_n}, \quad F_n(t) = V_1(t) + V_2(t), \quad n_{\text{el}} = 2, \quad (5.49)$$

one can write the recombination current in the form of equation (5.35).

ETL/perovskite interfacial SRH recombination. Here $R_l = v_{pE} p^{(l)}$. The recombination

at the perovskite/HTL interface and in the bulk is set to zero. The hole density at the ETL/Perovskite interface is given by

$$p^{(l)} = p|_{x=0^+} \exp\left(-\frac{V_2}{V_T}\right), \quad (5.50)$$

$$p^{(l)} = k_H d_H \exp\left(-\frac{V_2(t) + V_3(t) + V_4(t) + bE(t)}{V_T}\right). \quad (5.51)$$

Therefore the recombination current is given by

$$j_{\text{rec}} = q k_H d_H v_{pE} \exp\left(-\frac{V_2 + V_3 + V_4 + bE}{V_T}\right). \quad (5.52)$$

Defining the following for ETL/Perovskite interfacial SRH recombination

$$j_{R_l} = q k_H d_H v_{pE}, \quad F_l(t) = V_2(t) + V_3(t) + V_4(t), \quad n_{\text{el}} = 1, \quad (5.53)$$

one can write the recombination current in the form of equation (5.35).

Perovskite/HTL interfacial SRH recombination. Finally, we consider the case where $R_r = v_{n_H} n^{(r)}$ with zero recombination in the bulk or at the ETL/Perovskite interface. The electron density at the Perovskite/HTL interface is given by

$$n^{(r)} = n|_{x=b^-} \exp\left(-\frac{V_3}{V_T}\right), \quad (5.54)$$

$$n^{(r)} = k_E d_E \exp\left(-\frac{V_1(t) + V_2(t) + V_3(t) + bE(t)}{V_T}\right). \quad (5.55)$$

Therefore the recombination current is given by

$$j_{\text{rec}} = q v_{n_H} k_E d_E \exp\left(-\frac{V_1(t) + V_2(t) + V_3(t) + bE(t)}{V_T}\right). \quad (5.56)$$

Defining the following for Perovskite/HTL interfacial SRH recombination

$$j_{R_r} = q v_{n_H} k_E d_E, \quad F_r(t) = V_1(t) + V_2(t) + V_3(t), \quad n_{\text{el}} = 1, \quad (5.57)$$

one can write the recombination current in the form of equation (5.35).

This section has described how the general form for the recombination current is valid for each recombination mechanism. It is found that a factor, which takes an integer value of 1 or 2, is required in order to express the recombination current in a general form. In light of its relationship to the type of recombination mechanism and its equivalence to the ideality factor for traditional solar cells, we term this factor the *electronic ideality factor*. Further analysis of the electronic ideality factor is presented in Chapter 6.

Here, we note that it is a simplification to only consider a single recombination mechanism occurring at one time. Particularly, in physical devices bimolecular recombination is always

non-zero; however, it is reasonable to expect that a single mechanism might dominate over all others. Furthermore, it is worthwhile producing a model that describes the simplest operation of a PSC before adding complexity. Nonetheless, cells with losses via multiple recombination pathways are considered in Appendix A.

5.4 Linearisation and impedance spectroscopy

Now that we have a recipe to determine the current density in time for a general voltage perturbation, we consider the current response during an impedance measurement. To measure the impedance of a solar cell, a ‘DC’ (or constant) voltage is applied with an additional small sinusoidal signal to perturb the cell about a steady-state. The applied perturbation is small to induce a linear current response. By design, this enables the technique of linearisation to be employed in the analysis of impedance spectroscopy measurements.

Linearisation involves determining solutions at a given steady-state (in this case at a given DC voltage and illumination) and approximating the general (non-linear) behaviour close to steady-state as linear. Equivalently, linearisation can be thought of as a first order Taylor expansion about the steady-state. This technique is highly accurate for small deviations from the equilibrium, and hence, is ideal for the analysis of IS measurements. The general form of the applied voltage for an impedance measurement is

$$V(t) = V_{\text{DC}} + V_p \exp(i\omega t), \quad (5.58)$$

where, V_{DC} is the DC voltage, ω is the angular frequency of the sinusoidal perturbation and V_p is its amplitude. Here, the applied voltage perturbation given in eq.(3.7) has been presented in complex form to simplify the subsequent analysis. The size of the perturbations can be characterised by the following non-dimensional parameter

$$\delta = V_p/V_T, \quad (5.59)$$

where V_T is the thermal voltage (which is around 25 mV at room temperature). Impedance measurements require δ to be small for the analysis to be valid. In experiment, the perturbation amplitude (typically 10-20 mV) is such that it is small enough to ensure a linear response, but large enough that the response is significant compared to noise². For the purposes of this work, we assume that δ is sufficiently small such that a linear response is observed and terms of order δ^2 and higher can be neglected. The applied voltage can be written in the form

$$V(t) = V_{\text{DC}} + \delta V^{(1)}(t), \quad V^{(1)}(t) = V_T e^{i\omega t}, \quad (5.60)$$

²In practice, a perturbation amplitude of 20 mV suffices, even though this is not particularly small in comparison to the thermal voltage. In addition to the perturbation amplitude and temperature, the linearity of the current response is dependent on the DC voltage that the cell is perturbed from. This can be understood by looking at the gradient of a J - V curve at different voltages (see, for example, Figure 2.4).

where ⁽¹⁾ is used to denote first order terms. The Debye layer charge Q and the bulk electric field E can be expressed in terms of the leading and first order terms as follows

$$Q(t) = Q_{\text{DC}} + \delta Q^{(1)}(t) + \mathcal{O}(\delta^2), \quad (5.61)$$

$$E(t) = \underbrace{E_{\text{DC}}}_{=0} + \delta E^{(1)}(t) + \mathcal{O}(\delta^2). \quad (5.62)$$

At steady-state, the charge contained within the left and right Debye layers within the perovskite is $-Q_{\text{DC}}$ and Q_{DC} respectively with zero bulk electric field. Using eq.(5.1) we see that the leading order (or steady-state) Debye layer charge Q_{DC} is given by the solution to

$$V_{\text{DC}} - V_{\text{bi}} + V_1(Q_{\text{DC}}) + V_2(Q_{\text{DC}}) + V_3(Q_{\text{DC}}) + V_4(Q_{\text{DC}}) = 0. \quad (5.63)$$

To condense the notation, we define $F_T(t)$ the total potential drop across all four Debye layers, by

$$F_T(t) = V_1(t) + V_2(t) + V_3(t) + V_4(t), \quad (5.64)$$

which, at steady-state is simply

$$\begin{aligned} F_T(Q_{\text{DC}}) &= V_1(Q_{\text{DC}}) + V_2(Q_{\text{DC}}) + V_3(Q_{\text{DC}}) + V_4(Q_{\text{DC}}), \\ &= V_{\text{bi}} - V_{\text{DC}}. \end{aligned} \quad (5.65)$$

This equation can be solved to determine Q_{DC} as a function of the applied voltage V_{DC} . Owing to the complexity of the capacitance relations that set the potential drops V_{1-4} , it is not possible to determine an analytic solution for Q_{DC} . Therefore, a numerical root finding algorithm must be used to determine Q_{DC} in terms of the applied potential V_{DC} . This is the only part of the model that requires numerical evaluation, the rest is analytic. On linearising equation (5.3), we obtain the following ODE for the first order Debye layer charge, $Q^{(1)}(t)$

$$\frac{dQ^{(1)}(t)}{dt} = -\frac{qD_+N_0}{V_Tb} \left(V^{(1)}(t) + Q^{(1)}(t)F'_T(Q_{\text{DC}}) \right). \quad (5.66)$$

Here the prime denotes a derivative with respect to Q , hence

$$F'_T(Q_{\text{DC}}) = \left. \frac{dV_1}{dQ} \right|_{Q_{\text{DC}}} + \left. \frac{dV_2}{dQ} \right|_{Q_{\text{DC}}} + \left. \frac{dV_3}{dQ} \right|_{Q_{\text{DC}}} + \left. \frac{dV_4}{dQ} \right|_{Q_{\text{DC}}}. \quad (5.67)$$

On solving this first order ordinary differential equation one obtains

$$Q^{(1)}(t) = G_+ V_T \frac{-G_+ F'_T(Q_{\text{DC}}) + i\omega}{G_+^2 F'_T(Q_{\text{DC}})^2 + \omega^2} e^{i\omega t}, \quad (5.68)$$

where we have defined

$$G_+ = \frac{qD_+N_0}{V_Tb}. \quad (5.69)$$

On recalling that the electric field is given by

$$E(t) = \frac{1}{bG_+} \frac{dQ}{dt}, \quad (5.2 \text{ reprinted})$$

the electric field at first order is therefore given by

$$\begin{aligned} E^{(1)}(t) &= \frac{1}{bG_+} \frac{dQ^{(1)}}{dt}, \\ &= \frac{i\omega}{bG_+} Q^{(1)}, \end{aligned} \quad (5.70)$$

where the derivative was calculated using (5.68) for $Q^{(1)}$. Linearising the recombination current, one can write

$$j_{\text{rec}}(t) = j_{\text{rec}}(V_{\text{DC}}) + \delta j_{\text{rec}}^{(1)}(t) + \mathcal{O}(\delta^2), \quad (5.71)$$

where

$$j_{\text{rec}}(V_{\text{DC}}) = j_{R_i} \exp\left(-\frac{F_i(Q_{\text{DC}})}{V_T}\right), \quad (5.72)$$

$$j_{\text{rec}}^{(1)}(t) = Q^{(1)}(t) \left. \frac{dj_{\text{rec}}}{dQ} \right|_{Q=Q_{\text{DC}}}. \quad (5.73)$$

We use the notation in Table 5.2 to keep this derivation general. Taking the derivative of eq.(5.35), one obtains the first order recombination current

$$j_{\text{rec}}^{(1)}(t) = Q^{(1)}(t) j_{\text{rec}}(V_{\text{DC}}) \left(-\frac{F'_i(Q_{\text{DC}})}{V_T} - \frac{b}{n_{\text{el}} V_T} \frac{dE^{(1)}}{dQ^{(1)}} \right), \quad (5.74)$$

where a prime denotes a derivative with respect to the Debye layer charge Q . The short-circuit, displacement and total current can be expressed as

$$j_{\text{gen}} = j_{\text{gen}}(V_{\text{DC}}) + \underbrace{\delta j_{\text{gen}}^{(1)}}_{=0}, \quad (5.75)$$

$$j_d(t) = \underbrace{j_d(V_{\text{DC}})}_{=0} + \delta j_d^{(1)}(t) + \mathcal{O}(\delta^2), \quad (5.76)$$

$$J(t) = J(V_{\text{DC}}) + \delta J^{(1)}(t) + \mathcal{O}(\delta^2). \quad (5.77)$$

Using these linearised expressions and equation (5.25), the leading and first order current are given by

$$\begin{aligned} J(V_{\text{DC}}) &= j_{\text{gen}}(V_{\text{DC}}) - j_{\text{rec}}(V_{\text{DC}}), \\ &= qF_{ph} \left(1 - e^{-\alpha b}\right) - j_{R_i} \exp\left(-\frac{F_i(Q_{\text{DC}})}{V_T}\right), \end{aligned} \quad (5.78)$$

$$\begin{aligned} J^{(1)}(t) &= -j_{\text{rec}}^{(1)}(t) + j_d^{(1)}(t), \\ &= -Q^{(1)}(t)j_{\text{rec}}(V_{\text{DC}}) \left(-\frac{F'_i(Q_{\text{DC}})}{V_T} - \frac{b}{n_{\text{el}}V_T} \frac{dE^{(1)}}{dQ^{(1)}}\right) + \varepsilon_p \frac{dE^{(1)}}{dt}. \end{aligned} \quad (5.79)$$

After numerical evaluation of eq.(5.63) for the steady-state Debye layer charge Q_{DC} , the current response to an impedance perturbation (5.77) is given by the analytic relations (5.78-5.79). This enables the impedance for a given frequency perturbation to be determined, as shown in the following section.

5.4.1 Impedance parameters

Now that we have the linearised current output, specifically the first order current given by eq.(5.79), analytic relations for the impedance of a PSC can be determined. Electrical impedance is defined

$$Z(\omega) = \frac{V^{(1)}}{J^{(1)}} = R + iX, \quad (5.80)$$

where R is resistance and X is reactance. When considering the impedance of a system, it is conventional to define the current such that an increase in voltage results in an increase in current. Hence, for the rest of this section the current has been redefined to be consistent with this convention. Therefore, on using (5.60) and (5.79), the impedance is given by

$$Z(\omega) = \frac{V_T e^{i\omega t}}{Q^{(1)}(t)j_{\text{rec}}(V_{\text{DC}}) \left(-\frac{F'_i(Q_{\text{DC}})}{V_T} - \frac{b}{n_{\text{el}}V_T} \frac{dE^{(1)}}{dQ^{(1)}}\right) - \varepsilon_p \frac{dE^{(1)}}{dt}}, \quad (5.81)$$

which includes a sign change of eq.(5.79) due to this convention. Equation (5.81) is most straightforwardly related to the admittance $Y = 1/Z$ given by

$$Y(\omega) = G + iB. \quad (5.82)$$

Hence, using equations (5.70) for the electric field and (5.61)-(5.68), the admittance is found to be

$$G(\omega) = \frac{1}{G_+^2 F_T'(Q_{DC})^2 + \omega^2} \left(\frac{G_+^2}{V_T} j_{\text{rec}}(V_{DC}) F_i'(Q_{DC}) F_T'(Q_{DC}) + \omega^2 \left(\frac{j_{\text{rec}}(V_{DC})}{V_T n_{\text{el}}} - \frac{G_+ \varepsilon_p}{b} F_T'(Q_{DC}) \right) \right), \quad (5.83)$$

$$B(\omega) = \frac{\omega}{G_+^2 F_T'(Q_{DC})^2 + \omega^2} \left(\frac{G_+}{V_T} j_{\text{rec}}(V_{DC}) \left(\frac{F_T'(Q_{DC})}{n_{\text{el}}} - F_i'(Q_{DC}) \right) + \frac{\varepsilon_p}{b} \omega^2 \right). \quad (5.84)$$

It is worthwhile removing the variables F_i' and F_T' in favour of the ectypal factor. This is because the ectypal factor is commonly measured (and mistaken for an ideality factor) and is therefore something that can be easily identified and determined from experimental measurements [135]. Further description of the ectypal factor is given in Section 3.1. On investigation it can be shown that the measured ectypal factor \bar{n}_{ec} is related to the variables F_i' and F_T' via³

$$\bar{n}_{\text{ec}}(Q_{DC}) = \frac{F_T'(Q_{DC})}{F_i'(Q_{DC})}. \quad (5.89)$$

The above combined with the definition of F_T' given by

$$F_T'(Q_{DC}) = \frac{d}{dQ} (V_{\text{bi}} - V) \big|_{Q_{DC}} = -\frac{dV_{DC}}{dQ_{DC}}, \quad (5.90)$$

enables the variables F_i' and F_T' to be eliminated. On eliminating the variables F_i' and F_T' in (5.83) and (5.84), and using

$$R = \frac{G}{G^2 + B^2}, \quad X = -\frac{B}{G^2 + B^2}, \quad (5.91)$$

³The following justifies equation (5.89). Using eq.(5.64), which defines the total potential drop F_T across the Debye layers, one can write

$$\frac{F_T'(Q_{DC})}{F_i'(Q_{DC})} = \frac{\frac{d}{dQ} (V - V_{\text{bi}}) \big|_{Q=Q_{DC}}}{\frac{d}{dQ} (F_i) \big|_{Q=Q_{DC}}}. \quad (5.85)$$

Using the chain rule, the derivatives can be taken with respect to voltage such that

$$\frac{\frac{d}{dQ} (V - V_{\text{bi}}) \big|_{Q=Q_{DC}}}{\frac{d}{dQ} (F_i) \big|_{Q=Q_{DC}}} = \frac{\frac{d}{dV} (V - V_{\text{bi}}) \big|_{V=V_{DC}}}{\frac{d}{dV} (F_i) \big|_{V=V_{DC}}}. \quad (5.86)$$

Using the definition of the ectypal factor n_{ec} , eq.(3.5), to eliminate F_i , one obtains

$$\frac{F_T'(Q_{DC})}{F_i'(Q_{DC})} = \frac{\frac{d}{dV} (V - V_{\text{bi}}) \big|_{V=V_{DC}}}{\frac{d}{dV} (V - V_{\text{bi}}) \big|_{V=V_{DC}} \frac{1}{n_{\text{ec}}} - (V_{DC} - V_{\text{bi}}) \frac{1}{n_{\text{ec}}^2} \frac{dn_{\text{ec}}}{dV} \big|_{V=V_{DC}}}. \quad (5.87)$$

Finally, noting that $\frac{d}{dV} (V - V_{\text{bi}}) = 1$, one finds

$$\begin{aligned} \frac{F_T'(Q_{DC})}{F_i'(Q_{DC})} &= n_{\text{ec}}(V_{DC}) \left[1 - \frac{V_{DC} - V_{\text{bi}}}{n_{\text{ec}}} \frac{dn_{\text{ec}}}{dV} \bigg|_{V=V_{DC}} \right]^{-1} \\ &= \bar{n}_{\text{ec}}(V_{DC}). \end{aligned} \quad (5.88)$$

The right hand side of this equation is exactly the measured ectypal factor as defined by eq.(3.6) [135].

one obtains the resistance and reactance of a PSC as a function of frequency

$$R(\omega) = \frac{\frac{j_{\text{rec}}(V_{\text{DC}})}{V_T \bar{n}_{\text{ec}}} (G_+ + \frac{dV_{\text{DC}}}{dQ_{\text{DC}}})^2 + \omega^2 \left(\frac{j_{\text{rec}}(V_{\text{DC}})}{V_T n_{\text{el}}} + \frac{\varepsilon_p}{b} G_+ + \frac{dV_{\text{DC}}}{dQ_{\text{DC}}} \right)}{\left(\frac{j_{\text{rec}}(V_{\text{DC}})}{V_T \bar{n}_{\text{ec}}} G_+ + \frac{dV_{\text{DC}}}{dQ_{\text{DC}}} \right)^2 + \omega^2 \left(\frac{j_{\text{rec}}(V_{\text{DC}})^2}{V_T^2 n_{\text{el}}^2} + 2 \frac{\varepsilon_p}{b} \frac{j_{\text{rec}}(V_{\text{DC}})}{V_T \bar{n}_{\text{ec}}} G_+ + \frac{dV_{\text{DC}}}{dQ_{\text{DC}}} + \frac{\varepsilon_p^2}{b^2} \omega^2 \right)}, \quad (5.92)$$

$$X(\omega) = \frac{\omega \left(\frac{j_{\text{rec}}(V_{\text{DC}})}{V_T} G_+ + \frac{dV_{\text{DC}}}{dQ_{\text{DC}}} \left(\frac{1}{n_{\text{el}}} - \frac{1}{\bar{n}_{\text{ec}}} \right) - \frac{\varepsilon_p}{b} \omega^2 \right)}{\left(\frac{j_{\text{rec}}(V_{\text{DC}})}{V_T \bar{n}_{\text{ec}}} G_+ + \frac{dV_{\text{DC}}}{dQ_{\text{DC}}} \right)^2 + \omega^2 \left(\frac{j_{\text{rec}}(V_{\text{DC}})^2}{V_T^2 n_{\text{el}}^2} + 2 \frac{\varepsilon_p}{b} \frac{j_{\text{rec}}(V_{\text{DC}})}{V_T \bar{n}_{\text{ec}}} G_+ + \frac{dV_{\text{DC}}}{dQ_{\text{DC}}} + \frac{\varepsilon_p^2}{b^2} \omega^2 \right)}. \quad (5.93)$$

These relations describe the general impedance response of a PSC, including the impact of mobile ions, in terms of fundamental cell properties. The Nyquist spectra generated by these relations, for cell parameters from Table 4.1, consist of a high frequency semicircle above the axis and a low frequency semicircle that lies either above or below the axis. Spectra calculated using these relations are validated against those obtained numerically from the full drift-diffusion model in the following chapter.

5.4.2 Resistances, capacitances, and an RC-RC circuit

On analysing the frequency dependent relations for the real and imaginary components of the impedance, (5.92)-(5.93), the diameters of (or equivalently resistances associated with) the LF and HF semicircles are given by

$$R_{\text{HF}} = \frac{V_T n_{\text{el}}}{j_{\text{rec}}(V_{\text{DC}})}, \quad (5.94)$$

$$R_{\text{LF}} = \frac{V_T}{j_{\text{rec}}(V_{\text{DC}})} (\bar{n}_{\text{ec}}(V_{\text{DC}}) - n_{\text{el}}), \quad (5.95)$$

which have units $\Omega \text{ m}^2$. The characteristic frequencies corresponding to the location of the peaks in the reactance $-X$ versus frequency plots are

$$\omega_{\text{HF}} = \frac{b j_{\text{rec}}(V_{\text{DC}})}{\varepsilon_p V_T n_{\text{el}}}, \quad (5.96)$$

$$\omega_{\text{LF}} = G_+ \frac{n_{\text{el}}}{\bar{n}_{\text{ec}}(V_{\text{DC}})} \left(-\frac{dQ_{\text{DC}}}{dV_{\text{DC}}} \right)^{-1}. \quad (5.97)$$

See Figure 3.6 for a Nyquist and frequency plot labelling these impedance parameters. The capacitances, related to the resistances and characteristic frequencies via $C = 1/(R\omega)$, are given by

$$C_{\text{HF}} = \frac{\varepsilon_p}{b}, \quad (5.98)$$

$$C_{\text{LF}} = \frac{\bar{n}_{\text{ec}}(V_{\text{DC}}) j_{\text{rec}}(V_{\text{DC}})}{G_+ V_T n_{\text{el}} (\bar{n}_{\text{ec}}(V_{\text{DC}}) - n_{\text{el}})} \left(-\frac{dQ_{\text{DC}}}{dV_{\text{DC}}} \right). \quad (5.99)$$

and have units of capacitance per unit area, F m^{-2} . On substitution of these resistances and capacitances, given by (5.94-5.99), into (5.92) and (5.93) the impedance relations take the form

$$R(\omega) = \frac{(R_{HF} + R_{LF})(1 - \omega^2 R_{HF} C_{HF} R_{LF} C_{LF}) + \omega^2 R_{HF} R_{LF}^2 C_{LF}^2}{(1 - \omega^2 R_{HF} C_{HF} R_{LF} C_{LF})^2 + \omega^2 R_{LF}^2 C_{LF}^2}, \quad (5.100)$$

$$X(\omega) = -\frac{\omega R_{LF}^2 C_{LF} (1 + \omega^2 R_{HF}^2 C_{HF} C_{LF})}{(1 - \omega^2 R_{HF} C_{HF} R_{LF} C_{LF})^2 + \omega^2 R_{LF}^2 C_{LF}^2}. \quad (5.101)$$

Notably, these relations are not identical to the impedance of an RC - RC circuit, given by eq.(3.17), or any of the circuit models presented in Figure 3.7 that produce two semicircular features. However, while not exact, we note that the frequency dependent impedance relations derived here are extremely well-approximated by an RC - RC equivalent circuit with component values specified by equations (5.94-5.99). This is true provided the time constants of the two features are very different ($\tau_{HF} \ll \tau_{LF}$), as is the case for typical parameter estimates for PSCs.

The close equivalence between (5.92-5.93) and an RC - RC circuit is shown in Figure 5.9, with panel c) showing the error between the two. An example of the spectra produced from (5.92)-(5.93) and an RC - RC , when the time constants of the low and high frequency features are similar, is also shown in Figure 5.9b) and d). Specifically, $\tau_{HF} \approx \tau_{LF}/4$. This demonstrates the fundamental difference between (5.92)-(5.93) and an RC - RC circuit.

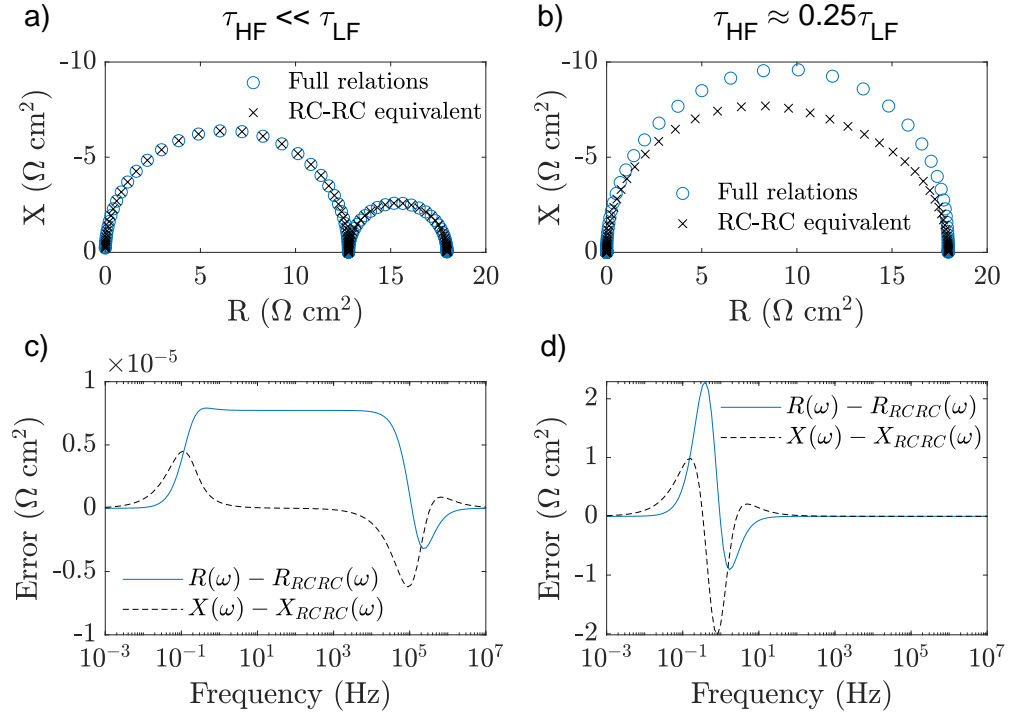


FIGURE 5.9: Comparison between the full impedance relations (5.92-5.93) and an RC - RC equivalent circuit approximation using the component values specified by equations (5.94-5.99). The Nyquist plot shown in a) uses cell parameters from Table 4.1, resulting in time constants that differ by 6 orders of magnitude. Panel b) shows an example of a spectrum with time constants that are similar. c) and d) show the difference, as an estimate of error, between the full impedance relations (5.92-5.93) and an RC - RC equivalent circuit approximation.

5.5 Summary

In this chapter, we derived analytic relations that describe the impedance response of PSCs. To summarise our approach, we began by employing the surface polarisation model to approximate the coupled ionic-electronic drift-diffusion model for a PSC. This approximate, yet highly accurate, model correctly describes the evolution of the mobile ion vacancies and the electric potential. Therefore, it can be used to predict the results of impedance measurements. However, in order to arrive at tractable analytic expressions (i.e. a set of transcendental equations) for the impedance of the device, the electron and hole distributions are also assumed to be Boltzmann distributed throughout the device. As demonstrated, this is a suitable approximation for efficient PSCs when the applied voltage lies in the vicinity of the open-circuit voltage and the maximum power point. After linearisation, we obtain analytic expressions, in terms of the fundamental physical properties of the cell, for an appropriately defined (electronic) ideality factor and for the high and low frequency resistances and capacitances typically extracted from the impedance spectra of PSCs.

Although analytic solutions that are valid under a wider parameter regime can be determined directly from the surface polarisation model, further approximations have been made to lead to tractable relations. These offer greater insight and can be more easily employed by experimentalists. Notably, we derive a general equation for the recombination current (5.35), valid for a PSC with either SRH, bimolecular or interfacial recombination. This serves as an equivalent to the traditional diode equation, but is valid for the mixed ionic-electronic behaviour of PSCs. Additionally, we identify an ideality factor, which we term the *electronic ideality factor* n_{el} . In contrast to the empirical factor (which is what is actually determined from typical measurements of an ideality factor for PSCs), the electronic ideality factor has the advantage that it is not dependent on the applied voltage or ionic parameters, and can be related straightforwardly to the dominant form of recombination, according to Table 5.2. The following chapter provides more detail on the electronic ideality factor, and a recipe to determine it using impedance spectroscopy.

The analytic model derived in this chapter produces a low and high frequency semicircle on a Nyquist plot, corresponding to two time constants. Without reference to equivalent circuits, this model is derived directly from the drift-diffusion model from which it approximates. When the time constants for the low and high frequency features differ significantly (as is the case for PSCs), we find that the analytic model can be well-approximated by the impedance response of an RC - RC equivalent circuit. Therefore, we have justified the use of an RC - RC equivalent circuit and defined the associated resistances and capacitances in terms of physical device parameters. The analytic relations for the impedance response of a PSC are examined and verified against numerical solutions to the full drift-diffusion model in the following chapter.

Finally, we remark on the generality of the approach that has been adopted to arrive at the analytic model. For ease of interpretation, it has been assumed that the cell response is dominated

by a single recombination mechanism. However, this model can describe cells with multiple concurrent recombination pathways (see Appendix A) as well as full (non-approximated) recombination equations. Furthermore, the analytic model is compatible with capacitance relations derived from other versions of a drift-diffusion model, which describe a modified physical picture of a PSC (for example, one in which both anion and cation vacancies are mobile, or one in which the charge carriers in the transport layers obey degenerate statistics). Indeed, it should be noted that our approach can be applied more widely to other devices based on mixed ionic-electronic semiconductors.

Chapter 6

Analytic model results

In the previous chapter an analytic model was constructed to describe the impedance response of PSCs. This chapter seeks to validate this model against the more complex drift-diffusion model (see Chapter 4) from which it is derived. In a regime where the applied voltage approaches built-in voltage, the analytic model and the drift-diffusion model solutions agree very closely. This is demonstrated for impedance spectra produced at different DC voltages, including maximum power point, and at different levels of illumination. Additionally, the trends observed in the resistances, capacitances and time constants are concordant with those observed experimentally [3, 96, 147].

It is found that the shape of the spectra are shown to be closely related to the type of recombination losses occurring within the cell, through the particular values of the electronic ideality factor n_{el} and ectypal factor \bar{n}_{ec} . For the first time, this provides a simple explanation for when and why negative LF features are observed. The relations for the high and low frequency resistances and capacitances are examined and employed to further explain the processes responsible for their origin. The properties of the electronic ideality factor and the ectypal factor are detailed and their values are calculated from analytic and numerical impedance spectra. It is demonstrated that the electronic ideality factor can be determined from the HF resistance as a means by which to infer the type of recombination occurring within a PSC. This is a significant result and shows that this new factor (the electronic ideality factor) plays an analogous role in PSCs to that played by the ideality factor in conventional photovoltaics. Lastly, cells with multiple recombination mechanisms are considered and good agreement is observed between the analytic and numerical models.

The analytic model provides a practical and useful tool with which to interpret PSC impedance data and extract physical parameters from IS experiments. A novel physical parameter n_{el} , the electronic ideality factor, which is of particular significance to PSC physics, is identified. By measuring the n_{el} and \bar{n}_{ec} from experimental impedance measurements, using the recipes detailed in this chapter, the main form and in certain cases the location of recombination losses

within the cell can be identified. This will aid the development of more efficient PSCs by enabling researchers to identify losses easily using impedance spectroscopy.

In the first section of this chapter the analytic model solutions are presented and validated against numerical solutions at different DC voltages, illuminations and recombination mechanisms. Next, in Section 6.2, the analytic relations are examined to provide insight into the origins of the low and high frequency features. Section 6.3 shows how the shape of impedance spectra are related to the values of the ectypal and electronic ideality factors. Recipes to determine them from experimental impedance measurements are also laid out. In Section 6.4, the results from the analytic model with multiple concurrent recombination mechanisms are validated against numerical solutions. It is demonstrated how multiple concurrent recombination mechanisms affect the values measured for the electronic ideality factor. Finally, the conclusions are outlined in Section 6.5.

6.1 Comparison between the analytic and numerical drift-diffusion models.

In the previous chapter, analytic relations for the impedance response of a PSC were derived. It is found that the low and high frequency resistances and capacitances are given by

$$R_{HF} = \frac{V_T n_{el}}{j_{rec}(V_{DC})}, \quad C_{HF} = \frac{\varepsilon_p}{b}, \quad (6.1)$$

$$R_{LF} = \frac{V_T}{j_{rec}(V_{DC})} (\bar{n}_{ec}(V_{DC}) - n_{el}), \quad C_{LF} = \frac{\bar{n}_{ec}(V_{DC}) j_{rec}(V_{DC})}{G_+ V_T n_{el} (\bar{n}_{ec}(V_{DC}) - n_{el})} \left(-\frac{dQ_{DC}}{dV_{DC}} \right). \quad (6.2)$$

Here, $j_{rec}(V_{DC})$ is the steady-state recombination current density, ε_p is the perovskite layer permittivity, \bar{n}_{ec} is the measured ectypal factor determined by the standard techniques used to obtain the ideality factor (such as the Suns- V_{oc} or dark- JV methods), n_{el} is the electronic ideality factor, and G_+ quantifies the ionic conductance per unit area of the perovskite layer, and is given by

$$G_+ = \frac{qD_+N_0}{V_T b}, \quad (5.69 \text{ reprinted})$$

where D_+ and N_0 are the ionic vacancy density and diffusion coefficient in the perovskite layer. The final term in (6.2) is the ionic capacitance of the cell (per unit area) and is found by solving (5.1) to obtain an expression for Q_{DC} as a function of V_{DC} and then differentiating this function with respect to V_{DC} . An example plot of Q_{DC} as a function of V_{DC} is made in Figure 5.4.

Numerical and analytic solution protocol

Numerical solutions are obtained using the impedance spectroscopy module for the open-source PSC simulation tool `IonMonger` [206], as developed for this thesis and associated works [2, 3]. This solves the fully coupled ionic-electronic drift-diffusion equations for a planar PSC with a

single positively charged mobile ion vacancy species and mobile charge carriers in the perovskite layer (as described in ref. [4] and Chapter 4). The IS module for `IonMonger` is detailed in Section 4.2. In line with the spectra presented in Chapter 4, the numerical and analytic impedance spectra presented in this work (unless otherwise stated) are simulated at open-circuit under monochromatic (520 nm) illumination with intensity that produces a photocurrent equivalent to 0.1-Sun. Cell and recombination parameters are listed in Tables 4.1 and 5.1 respectively. Impedance spectra are composed of 128 and 256 frequencies for the numerical and analytic solutions respectively over a range of 10^{-3} - 10^7 Hz. The voltage perturbation amplitude is 10 mV throughout.

For transparency, we note that the analytic solutions are calculated using the frequency dependent equations (5.92)-(5.93) rather than equations (6.1)-(6.2) as part of an RC - RC circuit. For physically realistic device parameters these are indistinguishable and so equations (6.1)-(6.2) are referenced for ease of interpretation. In this section, comparison between the analytic model and numerical solutions is first made for different DC voltages and illuminations. Following this, we examine the impact of different recombination mechanisms on impedance spectra.

6.1.1 DC voltage and illumination

Figure 6.1 shows a Nyquist plot for simulated impedance spectra, all with the same device parameters (given in Table 4.1), but at different DC voltages, including open-circuit. In this example, recombination takes place on the ETL/perovskite interface (R_l). See Table 5.1 for the values chosen for the recombination parameters. Figure 6.2 represents these spectra as the real and imaginary components of impedance versus frequency. It is clear that across these DC voltages, the agreement between the analytic model and the numerical solutions is remarkably good. The best agreement is observed at open-circuit. This is expected as the carrier densities are closer to a Boltzmann distribution at open-circuit, in comparison to lower voltages.

In line with Figure 4.8, the dependence of the resistances, capacitances, and time constants on open-circuit voltage is shown in Figure 6.3. Specifically, five spectra are calculated at open-circuit with voltages 0.85 V to 1.02 V, corresponding to illumination intensities from 10-1000 W m^{-2} equivalent illumination. Here, the sole source of recombination is at the ETL/perovskite interface (R_l). The impedance spectra display two positive semicircular features at all illuminations, with diameters that decrease significantly with increasing illumination. The resistances and capacitances are extracted from the numerical spectra by fitting to an RC - RC equivalent circuit. The impedance parameters from the analytic model are calculated using equations (6.1)-(6.2) and (5.96)-(5.97). Figure 6.3 demonstrates that the analytic model successfully captures the dependence of the HF and LF features on illumination (or equivalently open-circuit voltage).

A considerable advantage of using the (approximate) analytic model, as opposed to the drift-diffusion model, to interpret impedance spectra is that ‘trends’ (such as the dependence of the spectra on illumination, open-circuit voltage and steady-state voltage) observed in real spectra

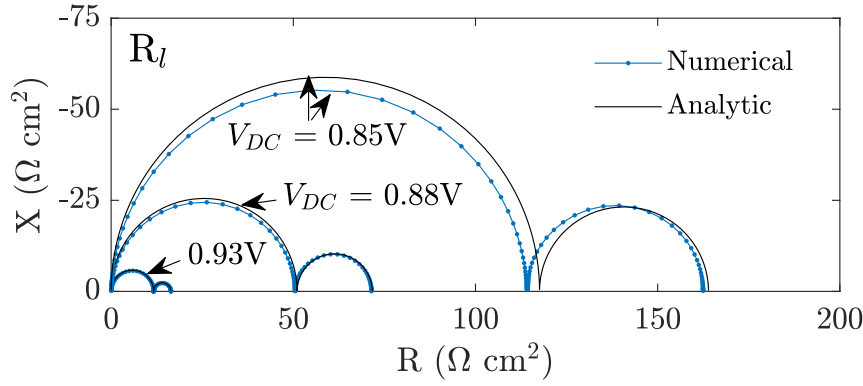


FIGURE 6.1: Simulated impedance spectra for a PSC with recombination at the ETL/perovskite interface (R_l) under 0.1-Sun equivalent illumination with a perturbation amplitude of 10 mV. Spectra for three DC voltages are shown, including at open-circuit where $V_{DC} = V_{oc} = 0.93V$. The cell parameters used in the numerical and analytic model are listed in Table 4.1. The recombination parameters for the approximate rates (as used for the analytic solution) and full rates (as used for the numerical solution) are listed in Table 5.1.

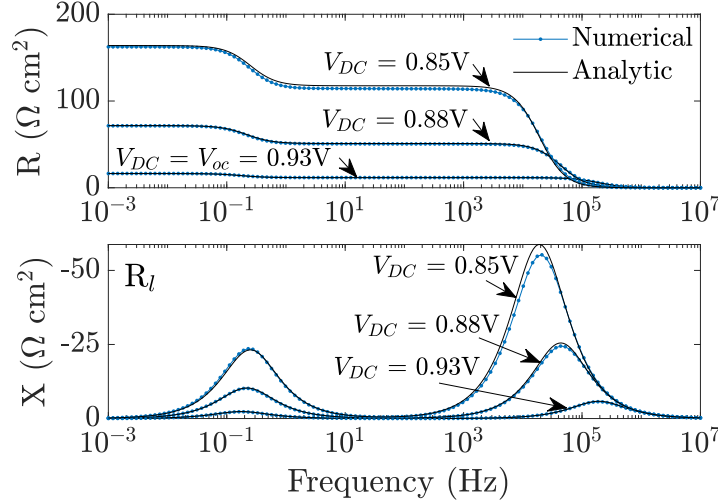


FIGURE 6.2: Real (top) and imaginary (bottom) components of impedance versus frequency for the spectra presented in Figure 6.1.

can be much more easily understood. Furthermore, the key physical parameters of the device may be obtained much more easily from impedance data by comparing to the explicit formulae for R_{HF} , C_{HF} , R_{LF} and C_{LF} , generated by the analytic model, than by repeatedly solving the drift-diffusion model until a parameter set is found that matches the data.

Approximations such as a high anion vacancy density in comparison to the carrier densities and narrow Debye layers with respect to cell width, were made in order to arrive at the analytic model. To demonstrate that the accuracy of the analytic model is not solely attributable to the relatively high anion vacancy density chosen in the parameter set given in Table 4.1, we calculate equivalent impedance spectra with identical parameters except for an anion vacancy density of $N_0 = 1.6 \times 10^{23} \text{ m}^{-3}$. Specifically, Figure 6.4 shows impedance spectra equivalent to Figure 6.1 but calculated for a simulated PSC with an anion vacancy density that is two orders of magnitude

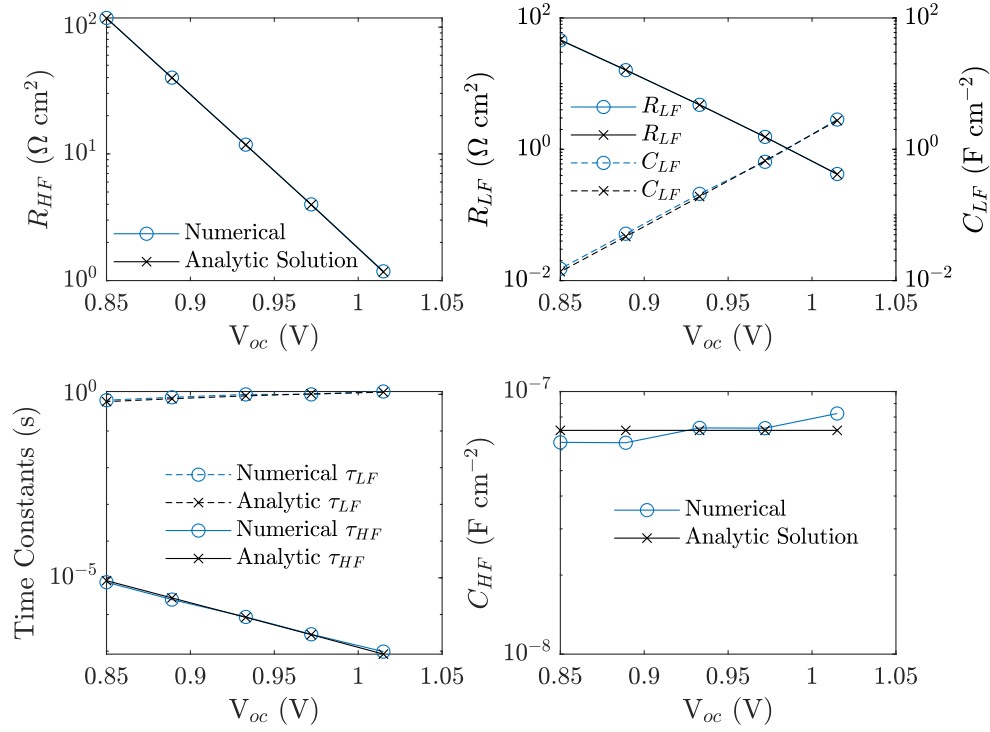


FIGURE 6.3: High and low frequency resistances, capacitances and time constants, calculated at different open-circuit voltages from impedance spectra obtained analytically and numerically. Parameters calculated from numerical spectra are indicated by blue (solid or dotted) lines with circle markers and parameters calculated numerically are indicated by black (solid or dotted) lines with crosses. Parameters used to calculate the numerical and analytic spectra are those from Table 4.1 for a cell with hole-limited interfacial recombination (R_l). The time constants are related to the angular frequency via, $\tau_f = 1/\omega_f$. The ectypal factor determined from the gradient of the HF resistance versus V_{oc} (see Section 6.3.2 eq.(6.14)) is approximately 1.4.

lower than the value used throughout the rest of this thesis. The close agreement between the analytic and numerical solutions confirms that the analytic model is capable of describing cells with lower anion vacancy densities, as for example used by some other groups [183, 237].

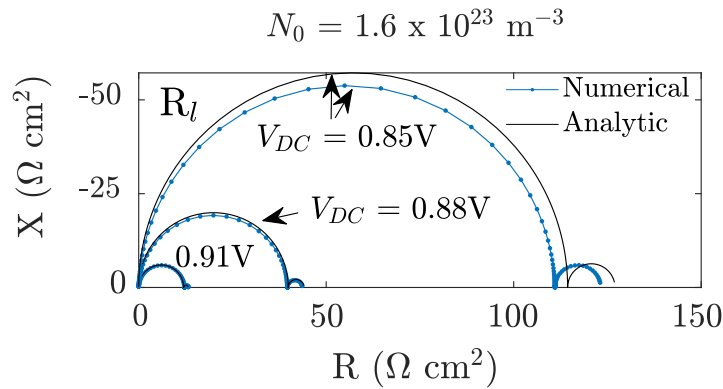


FIGURE 6.4: Nyquist plot showing analytic and numerical impedance spectra, under equivalent simulation conditions to Figure 6.1 but with an anion vacancy density of $1.6 \times 10^{23} \text{ m}^{-3}$.

Finally, Figure 6.5 is equivalent to Figure 6.1 but for lower DC voltages. Specifically, Figure 6.5 shows two Nyquist plots of simulated spectra under 0.1-Sun equivalent illumination with recombination at the ETL/perovskite interface (R_l). These plots show that the agreement is good at 0.82 V (the maximum power point for 0.1-Sun illumination); however, below this, the analytic solution poorly approximates the numerical solution. This is because approximating the carrier densities as Boltzmann distributed is not accurate at lower voltages. This is shown in Figure 5.5, which plots the carrier densities for these cell and recombination parameters at 0.82 V and 0.7 V. See Figure 6.11 for additional evidence showing the accuracy of the analytic model at different DC voltages.

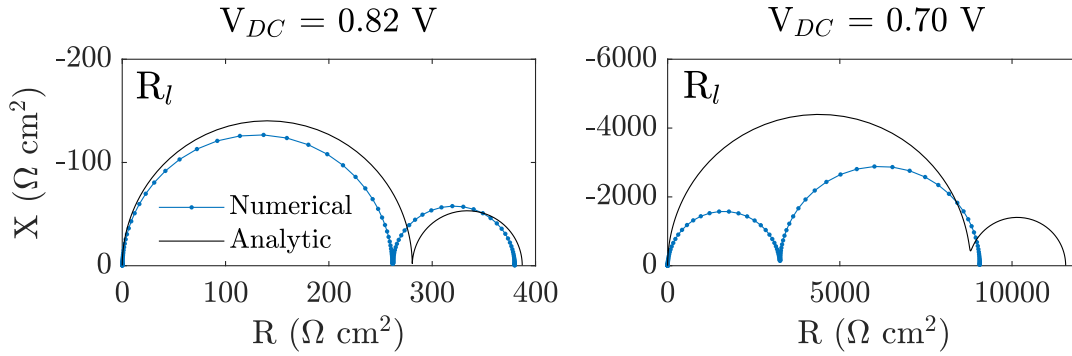


FIGURE 6.5: Nyquist plots showing analytic and numerical impedance spectra, at the maximum power point (left) and at 0.7 V (right) under 0.1-Sun equivalent illumination with recombination at the ETL/perovskite interface (R_l). Cell and recombination parameters are listed in Tables 4.1 and 5.1 respectively.

6.1.2 Recombination mechanisms

Thus far in this chapter, the impedance spectra have only been presented for a PSC with recombination on the ETL/perovskite interface. Here, we consider the impact that the type of recombination has on the shape of the impedance spectra but again using the parameter set given in Table 4.1. Figure 6.6 shows four Nyquist plots, each for a simulated PSC with different recombination mechanisms under 0.1-Sun illumination at open-circuit. Electron-limited and hole-limited SRH are shown, in addition to bimolecular recombination and interfacial recombination on the perovskite/HTL interface. The recombination types and equations are listed in Table 5.1. Here, we reiterate that the approximate rates are used for the analytic model, while the numerical model uses the full rates. This figure shows that the position and appearance of the LF feature are dependent on the type of recombination. With the device parameters specified in Table 4.1, electron-limited SRH recombination in the bulk results in a positive (or ‘capacitive’ LF feature), while hole-limited SRH recombination results in a negative (or ‘inductive’) LF feature. Additionally, Figure 6.6c) shows that a cell with only bimolecular recombination does not display a low frequency feature. This is discussed in Section 6.2.2.

Figure 6.7 shows the corresponding frequency plots for the spectra presented in Figure 6.6. In this representation, the similarities and differences between the spectra are apparent. The HF

peaks for the SRH recombination types R_n and R_p overlap very closely. Similarly, the bimolecular R_b and perovskite/HTL interfacial R_r recombination types overlap at HF. Conversely, the LF feature is different for all the recombination types. The rich behaviour of the LF feature is examined more closely in Section 6.2.2.

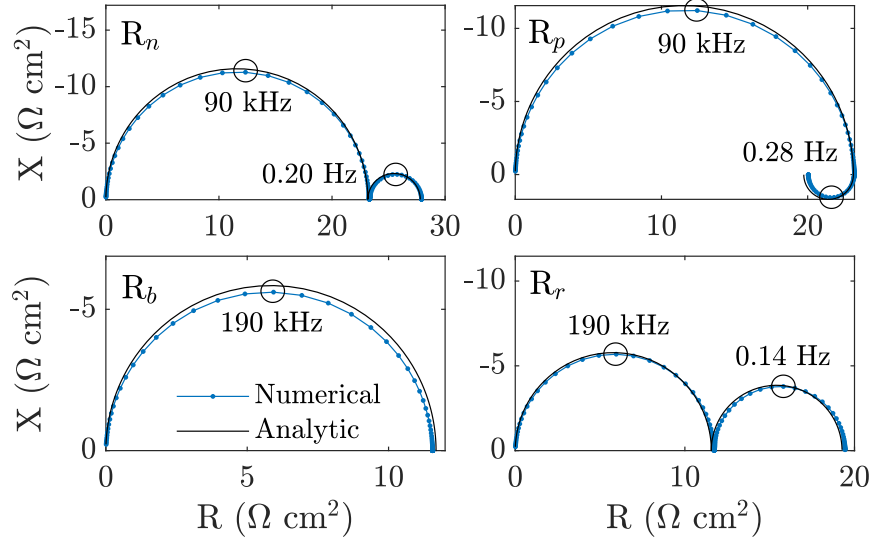


FIGURE 6.6: Simulated impedance spectra at open-circuit with different recombination mechanisms at 0.1-Sun illumination. R_n : electron-limited bulk SRH ($V_{oc} = 0.94$ V), R_p : hole-limited bulk SRH ($V_{oc} = 0.92$ V), R_b : bimolecular bulk recombination ($V_{oc} = 0.95$ V) and R_r : perovskite/HTL interfacial ($V_{oc} = 0.95$ V). Cell and recombination parameters are listed in Tables 4.1 and 5.1 respectively.

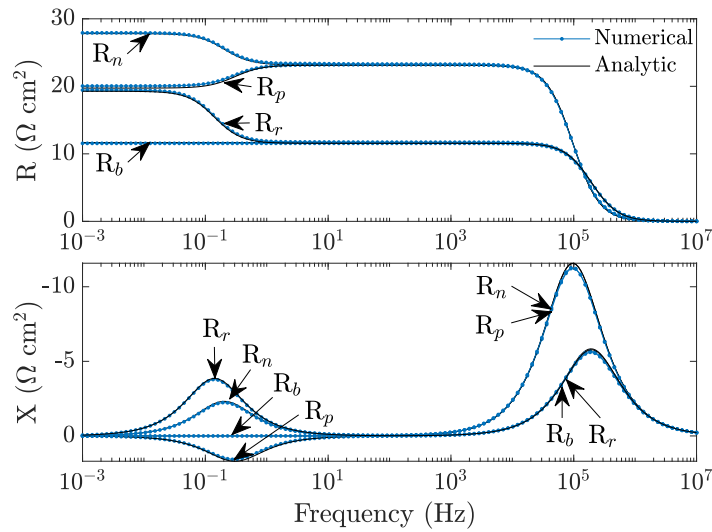


FIGURE 6.7: Real (top) and imaginary (bottom) components of impedance versus frequency for the spectra presented in Figure 6.6.

Figures 6.8 and 6.9 are equivalent to Figures 6.6 and 6.7 above but under 1-Sun equivalent illumination. Good agreement is observed between the numerical and analytic spectra; however, numerical solutions for electron-limited and hole-limited SRH recombination in the bulk show intermediate frequency (IF) features that are not reproduced by the analytic model. These IF

features appear as a small bulge between the HF feature and the LF feature in Figure 6.8. While not observed here, the IF feature can also emerge as a loop between the high and low frequency semicircles on the Nyquist plane. The analytic model does not reproduce the wide range of IF features observed in experiment. However, although interesting, these features are not universally observed in experimental measurements and do not seem to be an intrinsic part of the impedance response of PSCs [96, 134, 147, 238].

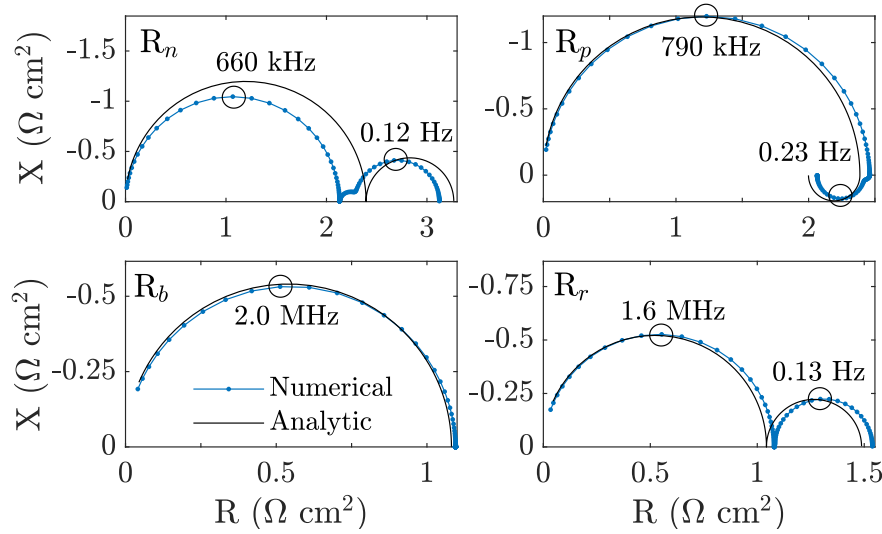


FIGURE 6.8: Simulated impedance spectra at open-circuit with different recombination mechanisms at 1-Sun illumination. R_n : electron-limited bulk SRH ($V_{oc} = 1.08$ V), R_p : hole-limited bulk SRH ($V_{oc} = 1.02$ V), R_b : bimolecular bulk recombination ($V_{oc} = 1.01$ V) and R_r : perovskite/HTL interfacial ($V_{oc} = 1.04$ V). Cell and recombination parameters are listed in Tables 4.1 and 5.1 respectively.

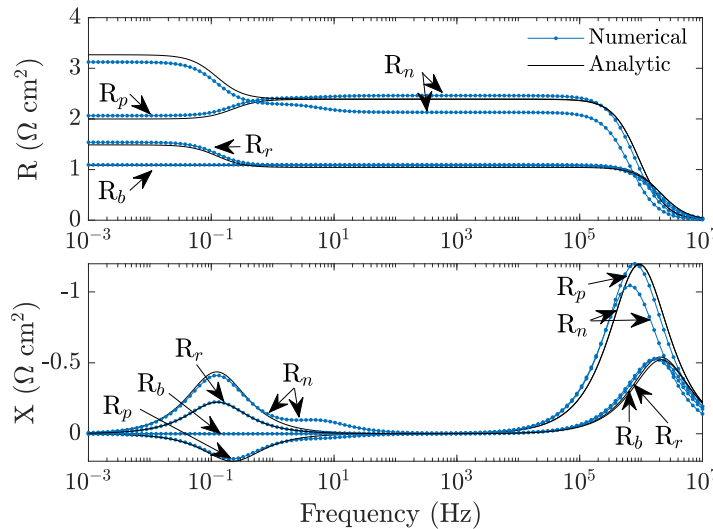


FIGURE 6.9: Frequency plot of the spectra presented in Figure 6.8.

As shown by Figures 6.8 and 6.9, at 1-Sun the agreement of the analytic model with numerical solutions varies from excellent to relatively poor, depending on the type of recombination and, in general, the device parameters. For this reason, the application of the analytic model should

be more carefully considered, particularly at illuminations above 1-Sun or higher DC voltages. Nonetheless, the analytic model still provides accurate qualitative understanding for impedance spectra that display two features. Additionally, the ideality factors extracted from impedance spectra at 1-Sun are likely to be accurate enough to identify the sources of efficiency losses (for example, see Figure 6.16 at 1.02 V). Finally, Figure 6.10 presents impedance spectra at maximum power point under 0.1-Sun equivalent illumination.

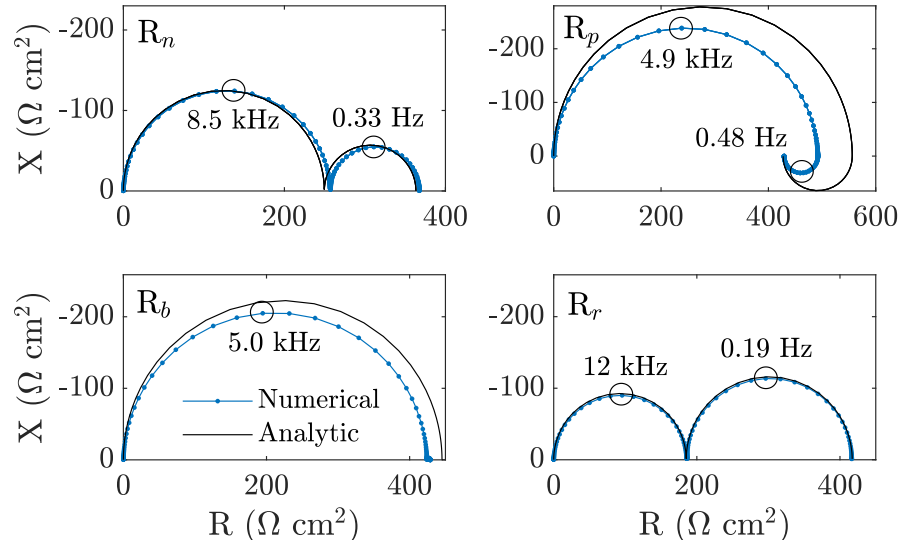


FIGURE 6.10: Simulated impedance spectra at maximum power point at 0.1-Sun illumination with different recombination mechanisms. R_n : electron-limited bulk SRH ($V_{DC} = 0.78$ V), R_p : hole-limited bulk SRH ($V_{DC} = 0.79$ V), R_b : bimolecular bulk recombination ($V_{DC} = 0.86$ V) and R_r : perovskite/HTL interfacial ($V_{DC} = 0.81$ V). Cell and recombination parameters are listed in Tables 4.1 and 5.1 respectively. This figure is equivalent to Figure 6.6 but at maximum power point rather than at V_{oc} .

In this section, we have demonstrated the capability of the analytic model to reproduce solutions to the full drift-diffusion model. Excellent agreement is observed at 0.1-Sun (and below) at open-circuit for all recombination types. At 1-Sun, the agreement is still very good, though noticeably worse than at 0.1-Sun, particularly where an intermediate frequency feature is observed. Similarly, at maximum power point, the agreement is good. However, much below the maximum power point, as shown in Figure 6.5 the analytic solutions poorly approximate the full model.

6.1.3 Analytic model accuracy

Figure 6.11 shows the approximate error of the analytic model with respect to numerical solutions at different DC voltages at 0.1-Sun equivalent illumination and in the dark. The relative error in the magnitude of the impedance $|Z|$ between the numerical solution and the approximate analytic solution is determined at each frequency. The mean relative error in $|Z|$ is then

calculated for a complete impedance spectrum, in this case 128 frequencies, for a given illumination and DC voltage. Calculating the error at different steady-state conditions demonstrates when the approximate analytic model can be deemed accurate.

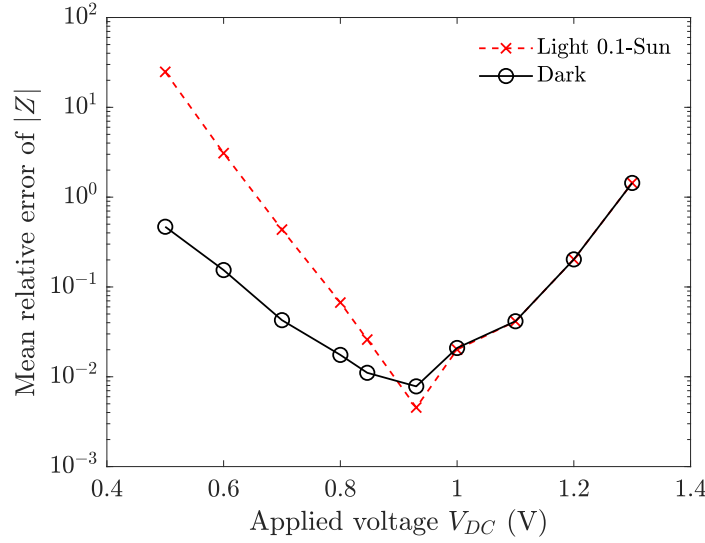


FIGURE 6.11: Mean relative error between the approximate analytic model solutions and the numerical solutions to the full drift-diffusion model at different DC voltages. Impedance calculated both under simulated illumination at 0.1-Sun and in the dark. Recombination is chosen to be at the ETL/perovskite interface (R_I) with device parameters from Table 4.1. The mean relative error is shown at the built-in voltage of the cell (0.85 V) and at open-circuit for 0.1-Sun equivalent illumination (0.93 V).

It is clear that the analytic model provides a good approximation when the applied voltage is close to the built-in voltage of the cell ($V_{bi} = 0.85$ V for the parameters from Table 4.1). This is true both in the dark, and under light (provided illumination is at most around 1-Sun). Significantly above the open-circuit voltage (0.93 V at 0.1-Sun), or below the maximum power point (0.82 V at 0.1-Sun) the analytic model poorly approximates the full model. The accuracy of the analytic model is limited by the Boltzmann approximation for the charge carriers (5.34) which, as shown in Figure 5.8, is only accurate in the vicinity of the built-in voltage of the cell.

6.2 Qualitative behaviour of the IS response

A key benefit of the analytic model over purely numerical solutions, is the ability to analyse the relations to determine a deeper understanding of the impedance response. In this section, the analytic relations given by (6.1) and (6.2) are examined to provide physical descriptions for the low and high frequency features.

6.2.1 High frequency feature

The analytic and numerical results show a high frequency feature in the form of a semicircle above the axis on a Nyquist plot. This is consistent across all recombination types (light intensities and DC voltages) and matches that reported in experiment [96, 134, 147, 238]. A series resistance associated with the metal contacts and measurement apparatus is not observed [151]. The analytic model identifies the high frequency resistance (6.1) as inversely proportional to the recombination current. This is in line with the interpretation of a recombination resistance [131, 239].

$$R_{HF} = \frac{V_T n_{el}}{j_{rec}(V_{DC})}, \quad C_{HF} = \frac{\varepsilon_p}{b}, \quad (6.1 \text{ reprinted})$$

In addition, it identifies the high frequency capacitance (6.1) as a purely geometric capacitance [157, 166], which is consistent with other reports found in the literature [96, 125, 131, 147, 152, 166, 239, 240]. The HF, or geometric, capacitance is the result of the contribution to the total current at high frequencies from the out-of-phase displacement current, given by eq.(4.38). The displacement current arises from the polarisation of the perovskite layer, in which the conductive transport layers act as the capacitor plates and the perovskite as the dielectric insulator (assuming sufficiently doped transport layers). The displacement current is proportional to the rate of change of the electric field. Hence, it has a phase relative to the voltage (and by definition E) of 90° . Its magnitude only becomes non-negligible when the voltage across the device is modulated extremely quickly (i.e. at HF). The displacement current is purely capacitive and consequently introduces a phase to the total current (5.25). This causes the total current to *lead* the voltage at high frequency.

Figure 6.12 shows the evolution of the potential across a PSC over a period for perturbations with frequencies greater than around 100 Hz. This corresponds to the intermediate frequency regime and above (IF+), as described in Section 4.4.2. The applied potential induces a uniform electric field across the perovskite layer (which cannot be screened by the motion of ions into and out of the Debye layers). This electric field is in phase with the applied voltage and modulates the current extracted from the device. At these high frequencies, the ion vacancy distribution remains fixed at its steady-state V_{DC} configuration [3]. Unlike many other measurement techniques, high frequency impedance removes the transient effects of ion motion and leads to a response that is determined by the electronic properties of the PSC.

We note that calculating the geometric capacitance from the perovskite permittivity and perovskite width returns capacitances up to 10-100 times less than those extracted experimentally. This is a commonly observed feature of such experiments and may be explained by the roughness of the interfaces. With this in mind, a roughness factor has been proposed to reconcile the values of C_{HF} measured experimentally with those predicted from theory [3, 131]. The low values of the HF capacitance from our simulations (in both numerical and analytic impedance spectra) are reflected in the frequency plots, which show that the HF peak is shifted to slightly higher frequencies than is measured in experiment [96, 147]. Given the amount of evidence supporting the interpretation of this capacitance as a geometric capacitance, and that our models

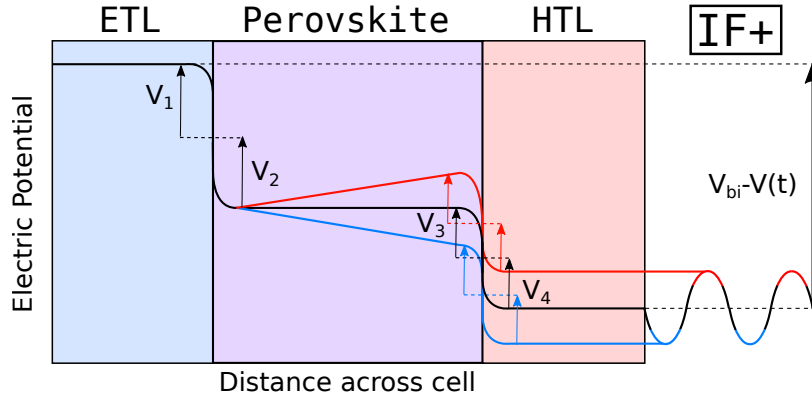


FIGURE 6.12: Schematic of the electric potential across a PSC during impedance measurements at intermediate frequencies and above ($\gtrsim 100$ Hz). The ion distribution is unable to adjust significantly over the short timescale of an impedance oscillation and so the potential drops V_{1-4} , across the Debye layers, remain in their steady-state configuration. The time-dependent changes in applied potential thus lead to corresponding changes in electric field $E(t)$ within the perovskite layer.

assume completely planar interfaces, we expect that roughness of the interfaces could explain this discrepancy between the theoretical and measured HF capacitance.

Jacobs *et al.* report that a two-dimensional model simulating a mesoporous interface does not result in a higher geometric capacitance (i.e. no roughness factor due to the non-planar interface) [125]. However, the exact model details were not specified. Interestingly, experimental measurements have found that even polished surfaces can have roughness factors of around 4 [241]. Clearly, the discrepancy between the capacitances predicted and those measured experimentally indicates that further investigation is needed using models that suitably account for two- or three-dimensional geometries.

In summary, the potential across the cell during impedance measurements at frequencies above around 100 Hz is well described by Figure 6.12. The resistance associated to the HF feature is the so-called recombination resistance and the capacitance is the geometric capacitance of the cell. Notably, the HF feature encapsulates information on the type of recombination losses occurring within the cell, through its dependence on the value of the electronic ideality factor n_{el} . Section 6.3.1 describes the electronic ideality factor and details a recipe to determine it experimentally from the HF resistance.

6.2.2 Low frequency feature

In the ultra-low frequency limit (below $\sim 10^{-2}$ Hz), the modulation of the applied potential is so slow that the ionic distribution remains in approximate quasi-equilibrium throughout the perturbation and, as a result, the electric field within the perovskite layer is almost entirely screened (i.e. $E(t) \approx 0$), as illustrated in Figure 6.13. During an ultra-low frequency measurement the evolving potential drops across the Debye layers $V_{1-4}(t)$ modulate the recombination current

(5.35) and thus lead to an impedance response that is dependent on the properties of the ion motion. More generally, over the frequencies that the LF feature is observed, the bulk electric field is only partially screened from the flow of charge into and out of the Debye layers. The resulting cell potential is best described by a state *between* that of the ultra-low frequency regime (Figure 6.13) and the intermediate and UHF regime illustrated in Figure 6.12. As such, the current output of the cell is modulated by both the potentials V_{1-4} and the bulk electric field, which have a phase relative to the oscillating applied potential. This interpretation is in line with the discussions of IS of PSCs found in [96, 125, 158]. Further description of the LF feature is given in Section 4.4.4.

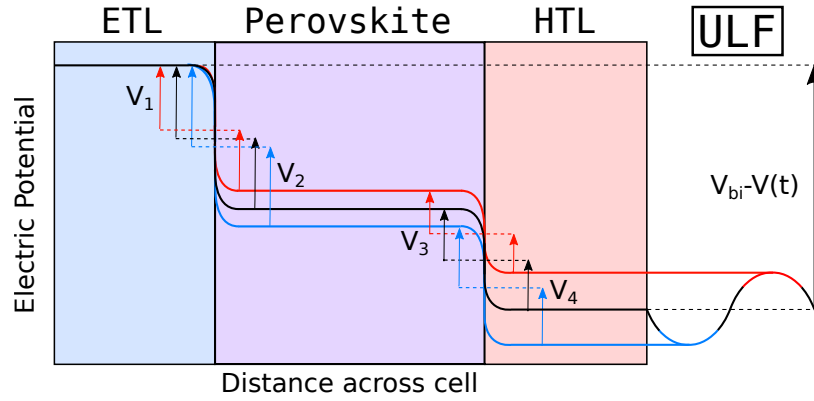


FIGURE 6.13: Illustration of the effect of an oscillating potential difference on the distribution of the electric potential across a PSC during impedance measurements at ultra-low frequencies (below ~ 10 mHz). The slow modulation of applied voltage allows ionic charge to fill and deplete the perovskite Debye layers in-phase with the applied potential. The charging and discharging of Debye layers effectively screens the bulk electric field.

$$R_{LF} = \frac{V_T}{j_{\text{rec}}(V_{\text{DC}})} (\bar{n}_{\text{ec}}(V_{\text{DC}}) - n_{\text{el}}), \quad C_{LF} = \frac{\bar{n}_{\text{ec}}(V_{\text{DC}}) j_{\text{rec}}(V_{\text{DC}})}{G_+ V_T n_{\text{el}} (\bar{n}_{\text{ec}}(V_{\text{DC}}) - n_{\text{el}})} \left(-\frac{dQ_{\text{DC}}}{dV_{\text{DC}}} \right). \quad (6.2 \text{ reprinted})$$

At low frequency, the possible impedance response of a PSC can be more varied. The analytic model shows that, depending upon the cell parameters, three different LF responses may be observed in the Nyquist plane. Either: (i) a ‘capacitive’ semicircle above the axis; or (ii) an ‘inductive’ semicircle below the axis; or (iii) no visible LF feature. See Figures 6.6 and 6.8 for examples of impedance spectra with these three LF features. The forms of the relations for R_{LF} and C_{LF} , given in eq.(6.2), provide insight into why certain features are observed in the IS response of a PSC. This enables the three different LF responses to be characterised, depending on the values of the ectypal and the electronic ideality factors, as illustrated in Figure 6.14.

For example, when the recombination in a cell is dominated by bimolecular recombination, the low frequency resistance shrinks to zero. This is because, from Table 5.2 and eq.(3.5), $\bar{n}_{\text{ec}} = n_{\text{el}} = 1$. As a result, only a high frequency semicircle is observed in the Nyquist plot. This is shown Figures 6.6c) and 6.8c). While it is not realistic to entirely eliminate all other sources of

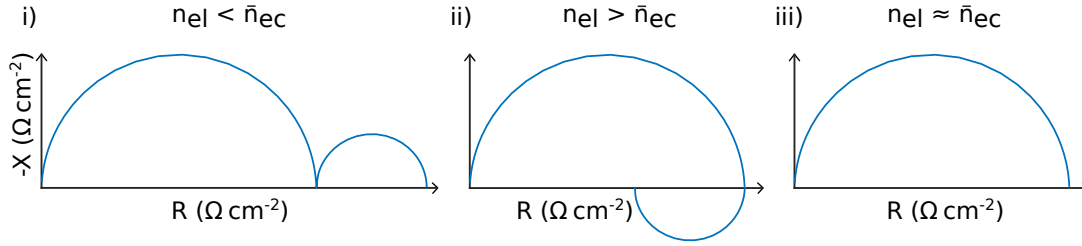


FIGURE 6.14: Illustration of how the shape of an impedance spectrum (near V_{oc}) of a PSC is related to the electronic ideality factor n_{el} and the measured ectypal factor \bar{n}_{ec} .

recombination, this result is nevertheless interesting, since it demonstrates that the absence of a LF feature does not necessarily signify the absence of ion motion. Indeed, the LF feature may also disappear where other types of recombination are present, provided $\bar{n}_{ec} \approx n_{el}$, see Table 6.1 for further details.

The low frequency feature appears ‘inductive’ (i.e. lies below the axis on a Nyquist plot) when both both $R_{LF} < 0$ and $C_{LF} < 0$. This can be seen from eq.(6.2) when

$$n_{el} > \bar{n}_{ec}. \quad (6.3)$$

A notable result is that a negative LF feature never occurs where the recombination occurs predominantly on one of the interfaces with the transport layers. Reframing this point, if a negative low frequency feature is observed on a Nyquist plot, we can infer from the model that the dominant efficiency loss is due to bulk SRH within the perovskite layer. More details about when negative LF features can be expected to appear, for the particular types of recombination considered here, are provided in Table 6.1.

Recombination	Conditions for no LF feature	Can R_{LF} & C_{LF} be negative?
$R_b: R_{bulk} = \beta np$	always (since $\bar{n}_{ec} = n_{el}$)	No ($R_{LF} = 0, C_{LF} = \infty$)
$R_p: R_{bulk} = p/\tau_p$	if $V_1 + V_2 = V_3 + V_4$	Yes if $V_1 + V_2 < V_3 + V_4$
$R_n: R_{bulk} = n/\tau_n$	if $V_1 + V_2 = V_3 + V_4$	Yes if $V_3 + V_4 < V_1 + V_2$
$R_l = v_{pE}p^{(l)}$	if $V_1 \ll V_2 + V_3 + V_4$	No ($R_{LF} \geq 0, C_{LF} > 0$)
$R_r = v_{nH}n^{(r)}$	if $V_4 \ll V_1 + V_2 + V_3$	No ($R_{LF} \geq 0, C_{LF} > 0$)

TABLE 6.1: Table showing the relationship between the recombination mechanism and the observed low frequency feature. These conditions are derived assuming V_{DC} is sufficiently close to V_{bi} , such that $\bar{n}_{ec} \approx n_{ec}$, in addition to the inequality given by (6.3) and the definition of n_{ec} (3.5). At steady-states further from V_{bi} , the conditions remain the same except the potentials V_{1-4} are replaced with their derivatives with respect to Debye layer charge

$$V'_{1-4} = dV_{1-4}/dQ_{DC}.$$

We remark that the conventional interpretation of the low frequency feature in terms of a resistance and a capacitance does not have a direct physical interpretation and should be viewed only as a tool for extracting information from the spectra. In particular, equivalent circuit components with negative values are unphysical. An inductive element can be employed in an effort to describe the negative LF feature. However, this does not particularly help with interpretation, as

a negative (positive) LF response is not related to storage of energy in magnetic (electric) fields. Therefore, for simplicity, we use the RC - RC equivalent circuit model presented in Figure 3.6 and emphasise that equations (6.1) and (6.2) should be used to interpret the IS response.

From the analytic model the characteristic low and high frequencies, ω_{LF} and ω_{HF} , which give the locations of the maxima in $X(\omega)$ (e.g. see Figure 6.9), are given by

$$\omega_{LF} = G_+ \frac{n_{el}}{\bar{n}_{ec}(V_{DC})} \left(-\frac{dQ_{DC}}{dV_{DC}} \right)^{-1}, \quad \omega_{HF} = \frac{bj_{rec}(V_{DC})}{\varepsilon_p V_T n_{el}}, \quad (5.96 \text{ and } 5.97 \text{ reprinted})$$

where it should be noted that dQ_{DC}/dV_{DC} is negative for all V_{DC} , as shown in Figure 5.4. The characteristic frequency of the LF feature ω_{LF} is proportional to G_+ . This parameter is defined in (5.69) and quantifies the ionic conductance, which explains why ω_{LF} increases with higher anion vacancy densities or mobilities, as shown in ref. [3]. Additionally, as $\bar{n}_{ec}dQ_{DC}/dV_{DC}$ is not strongly temperature dependent, the activation energy extracted from the LF time constant is the result of the temperature dependence of $G_+(T)$ [96, 147, 185, 242].

6.3 Ideality factors

The analytic relations (6.1)-(6.2) show that the impedance response of a PSC is closely related to the values of the ionic and the electronic ideality factors. In this section, we evaluate how these factors are related and how they can be determined experimentally from impedance spectroscopy measurements.

6.3.1 Electronic ideality factor

For the recombination mechanisms studied in this work (see Table 5.1) the electronic ideality factor n_{el} takes a value of either 1 or 2, depending on the dominant recombination mechanism. The relationship between the recombination type and the value of the electronic ideality factor is stated in Table 5.2. Specifically, n_{el} takes a value of 2 if the dominant source of recombination occurs via an electron- or hole-limited SRH mechanism within the perovskite absorber layer bulk. Otherwise, n_{el} takes a value of 1 which corresponds to either bimolecular recombination in the perovskite bulk, or recombination at a perovskite/TL interface.

From an experimental perspective the electronic ideality factor can be determined from the high frequency resistance (6.1) and the recombination current via the formula

$$n_{el} = \frac{R_{HF}(V_{DC})j_{rec}(V_{DC})}{V_T}, \quad (6.4)$$

where the recombination current j_{rec} may be estimated from

$$j_{rec}(V_{DC}) = j_{gen} - J(V_{DC}). \quad (6.5)$$

Here, j_{gen} is the photo-generated current ($j_{\text{gen}} \approx J(V = 0)$) and $J(V_{\text{DC}})$ is the steady-state current output of the cell at V_{DC} . This result is key to analysing the behaviour of real cells from experimental data as it is straightforward to obtain n_{el} given that both $R_{\text{HF}}(V_{\text{DC}})$ and $j_{\text{rec}}(V_{\text{DC}})$ are readily measured. This is the method used later in Section 6.3.3 to determine n_{el} from impedance spectra calculated via numerical solution to the drift-diffusion model.

In order to demonstrate how the analytic model and the electronic ideality factor are related to conventional solar cell theory, we consider a three-layer cell in which there are no mobile ions present in the perovskite capable of forming interfacial Debye layers and screening the field from the absorber. In this scenario the interfacial potential drops are all zero, that is $V_1 = V_2 = V_3 = V_4 = 0$. The potential profile no longer has the form depicted in Figure 5.1 but is instead similar to that typically portrayed for an ideal ‘p-i-n’ junction, where the built-in voltage and applied potential is dropped uniformly across the central intrinsic (i.e. perovskite) layer. Hence, the uniform electric field in the perovskite (see equations (5.2) and (5.3)) is given by

$$E(t) = \frac{1}{b} (V_{\text{bi}} - V(t)). \quad (6.6)$$

Using the relation above, $V_{1-4} = 0$ and $F_i(V_{1-4}) = 0$, equation (5.35) for the recombination current simplifies to

$$j_{\text{rec}}(t) = j_{R_i}^* \exp\left(\frac{V(t)}{n_{\text{el}} V_T}\right), \quad (6.7)$$

where we define $j_{R_i}^* = j_{R_i} \exp(-V_{\text{bi}}/(n_{\text{el}} V_T))$. Ignoring the contribution from the displacement current, the total current is given by

$$J(t) = j_{\text{gen}} - j_{R_i}^* \exp\left(\frac{V(t)}{n_{\text{el}} V_T}\right). \quad (6.8)$$

This can be compared to the classical non-ideal diode equation [14]

$$J(t) = j_{\text{gen}} - j_0 \left[\exp\left(\frac{V(t)}{n_{\text{id}} V_T}\right) - 1 \right], \quad (3.2 \text{ reprinted})$$

where j_0 is the dark saturation current density and n_{id} is the diode ideality factor. At voltages above around 0.1 V the exponential term dominates and the -1 in the brackets can be neglected. It is clear from this comparison that, in the absence of ions in the perovskite layer, the electronic ideality factor is analogous to the ideality factor that appears in standard semiconductor diode theory. Finally, by removing the ions in this way it is evident, from equation (6.2), that the LF impedance response disappears, leaving only the HF semicircle described by equation (6.1).

To summarise, the derivation of the analytic model for impedance spectroscopy simulation has led to the identification of a dimensionless constant, which we term the *electronic ideality factor* n_{el} . This factor plays an analogous role to that played by the traditional ideality factor in conventional photovoltaics. Therefore, n_{el} can be used as a tool to deduce the dominant form of recombination losses that take place in a PSC cell. In contrast to the ectypal factor \bar{n}_{ec} , which is

commonly used to analyse PSC behaviour in the literature [135], the electronic ideality factor is not inherently voltage dependent or influenced by the distribution of potential drops V_{1-4} across the cell. More specifically, it is a purely electronic parameter, which is not directly influenced by the behaviour of the ions in the perovskite material. In order to justify this assertion, we note that n_{el} is obtained using only the high frequency impedance measurements via equation (6.4). At high frequencies, the cell is perturbed about its steady-state ionic configuration and the ions are effectively immobile, because they move too slowly to respond to the voltage oscillations. As a result, the oscillating applied potential is dropped fully across the interior of the perovskite, producing an oscillating internal electric field which only modulates the electron and hole densities (this is illustrated in Figure 6.12). Even at these high frequencies, the electron and hole concentrations remain in quasi-equilibrium. As such, only HF impedance is capable of probing the electronic properties of a PSC about a particular steady-state. Although the drift-diffusion model of a PSC leads us to conclude, at least where there is only a single source of recombination, that n_{el} is independent of applied voltage, from a practical perspective it is probably best practice to determine n_{el} from experiments conducted at the maximum power point. This provides the best picture of the cell working under typical operating conditions.

6.3.2 The ectypal factor

On referring to (6.1)-(6.2) it is clear that the measured ectypal factor can be determined from the low and high frequency resistances extracted from the impedance spectra via

$$\bar{n}_{ec}(V_{DC}) = \frac{j_{rec}(V_{DC})}{V_T} \left(R_{HF}(V_{DC}) + R_{LF}(V_{DC}) \right). \quad (6.9)$$

This method enables the ectypal factor to be calculated from impedance spectra (at a single DC voltage) without having to determine the gradient of a linear fitted function, as is required by the Suns- V_{oc} , dark- JV (and $R_{HF} - V_{oc}$, see below) techniques. Notably, once \bar{n}_{ec} has been determined, it can be used to estimate the potential barrier for recombination F_i at steady state by inverting the formula (3.5) to obtain

$$F_i|_{V_{DC}} \approx \frac{V_{bi} - V_{DC}}{\bar{n}_{ec}(V_{DC})}. \quad (6.10)$$

See ref. [135] for further details. In practice, we note that using equation (6.9) as a method of obtaining the ectypal factor from impedance measurements may be challenging. It relies on the PSC remaining stable over the long periods required to accurately determine R_{LF} . Additionally, spectra can exhibit more than two features or show non-ideal behaviour, suggesting that the validity of this method is uncertain.

The ectypal factor from the HF resistance versus open-circuit voltage. It is common in the literature to extract an ‘ideality factor’ for PSCs from the dependence of the high frequency resistance R_{HF} on open-circuit voltage (as illumination intensity is adjusted). Specifically,

plotting $\ln(R_{HF})$ versus V_{oc} (as shown in Figures 4.8 and 6.3) typically produces a straight line with a gradient that can be related to an ‘ideality factor’ [3, 96, 134]. The analytic model enables us to derive what the gradient of $\ln(R_{HF})$ versus V_{oc} actually determines. Taking the log of the high frequency resistance (6.1) at V_{oc} one obtains

$$\ln(R_{HF}(V_{oc})) = \ln(V_T n_{el}) - \ln(j_{rec}(V_{oc})). \quad (6.11)$$

Using the definition of the ectypal factor (3.5), the recombination current (5.35) at open-circuit can be written in the form

$$j_{rec}(V_{oc}) = j_{R_i} \exp\left(\frac{V_{oc} - V_{bi}}{V_T n_{ec}(V_{oc})}\right), \quad (6.12)$$

Therefore, on substituting above into (6.11) one obtains

$$\ln(R_{HF}(V_{oc})) = \ln(V_T n_{el}) - \frac{V_{oc} - V_{bi}}{V_T n_{ec}(V_{oc})} - \ln(j_{R_i}), \quad (6.13)$$

which can be rewritten

$$\ln(R_{HF}(V_{oc})) = -\frac{1}{V_T n_{ec}(V_{oc})} V_{oc} + C, \quad \text{where } C = \ln\left(\frac{V_T n_{el}}{j_{R_i}}\right) + \frac{V_{bi}}{V_T n_{ec}(V_{oc})}. \quad (6.14)$$

This shows that by plotting the logarithm of the high frequency resistance versus open-circuit voltage ($\ln(R_{HF})$ versus V_{oc}), one obtains the ectypal factor from the gradient. This result is concordant with the findings of Pockett *et al.*, where it is found that the gradients of the Suns- V_{oc} and the $\ln(R_{HF}) - V_{oc}$ plots are approximately equivalent. A similar argument can be made from the fact that R_{HF} is proportional to the derivative of the recombination current with respect to voltage. Note that in general the ectypal factor is dependent on voltage and hence its value is expected to vary over the voltage range that fitting takes place. Unlike other measurement techniques, such as Suns- V_{oc} and dark- JV methods, this $\ln(R_{HF})$ versus V_{oc} method returns the value of the true ectypal factor, and not the measured ectypal factor. See ref. [135] for an explanation of this distinction.

Very similarly to the derivation above, we note that the ectypal factor can also be determined from $\ln(R_{HF} + R_{LF})$ versus V_{oc} . Specifically,

$$\begin{aligned} \ln(R_{HF}(V_{oc}) + R_{LF}(V_{oc})) &= -\frac{1}{V_T n_{ec}(V_{oc})} V_{oc} + D, \\ \text{where, } D &= \ln\left(\frac{V_T \bar{n}_{ec}(V_{oc})}{j_{R_i}}\right) + \frac{V_{bi}}{V_T n_{ec}(V_{oc})}. \end{aligned} \quad (6.15)$$

To summarise, we demonstrate that the ectypal factor can be determined using experimental IS measurements at a given DC voltage using equation (6.9). Furthermore, the ideality factor determined from the gradient of $\ln(R_{HF})$ versus V_{oc} returns the true ectypal factor.

6.3.3 Comparison between the ectypal and the electronic ideality factors

Figure 6.15 illustrates how the ectypal factor and the electronic ideality factor, are related to J - V measurements. This helps to associate the somewhat abstract representation of impedance to the more straightforward measurements of current versus voltage.

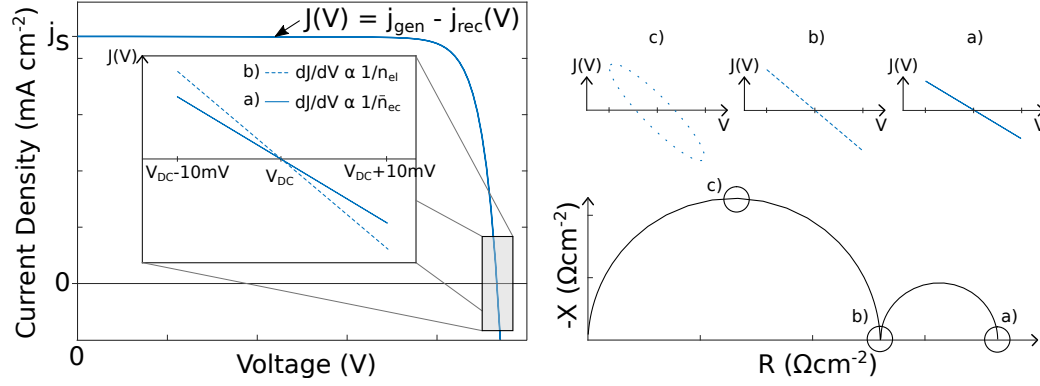


FIGURE 6.15: Left: steady-state JV curve with a Lissajous plot ($J(t)$ versus $V(t)$) inset showing the gradient, as measured by impedance spectroscopy. Right: Lissajous plots illustrating the current response at points a), b) and c) indicated on the Nyquist plot. The gradients shown in a) and b) are proportional to the measured ectypal factor and the electronic ideality factor respectively. For simplicity, a series resistance has not been included.

Plots of the electronic ideality factor n_{el} and the ectypal factor \bar{n}_{ec} against open-circuit voltages V_{oc} (corresponding to different illumination intensities) are shown in Figure 6.16. These are both computed from equations (6.4) and (6.9). The analytic calculations use the relations given by (6.1)-(6.2) while the low and high frequency resistances are obtained from numerical impedance spectra via fitting to extract the diameters of the semicircular features. Additionally, the recombination current for the numerical calculations is estimated using eq.(6.5). The results show the voltage independence of n_{el} for a single dominant source of recombination and additionally demonstrates that a non-integer value of \bar{n}_{ec} is obtained, even in cells with a single recombination mechanism. Caprioglio *et al.* corroborate these results with their simulations, determining non-integer values for a single recombination process. [132]. This supports the interpretation of \bar{n}_{ec} as an ectypal factor rather than a true ideality factor. The impedance spectra from which these factors are obtained are the same as those used for Figure 6.3. The gradient of $\ln(R_{HF})$ versus V_{oc} returns an estimate for the ectypal factor of 1.4. This value is in line with the values of the measured ectypal factor given in Figure 6.16.

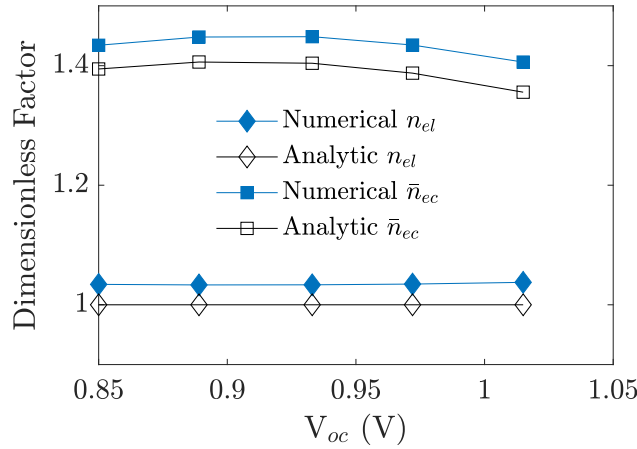


FIGURE 6.16: Electronic ideality factor, n_{el} , and ectypal factor, \bar{n}_{ec} , calculated at different open-circuit voltages from impedance spectra obtained analytically and numerically. Calculated from the same spectra as used for Figure 6.3. Parameters used to calculate the numerical and analytic spectra are those from Table 1 for a cell with hole-limited interfacial recombination (R_l).

To further demonstrate the differences between the ectypal and electronic ideality factors, we compute these quantities for the five different forms of recombination detailed in Table 5.1. Additionally, n_{el} and \bar{n}_{ec} are calculated for a cell with multiple recombination mechanisms, as described in the following section. These results are displayed in Figure 6.17. Here, the numerical and analytic spectra from which the ectypal and electronic ideality factors are computed are simulated at 0.1-Sun illumination and at V_{oc} with device parameters from Table 4.1. We remark that while \bar{n}_{ec} for this cell lies within the range that typically would be expected for an ideality factor (i.e. mainly between 1 and 2), it is highly sensitive to device parameters (such as ion density or transport layer doping). This is demonstrated in Figure 6.18, which shows an equivalent figure but with modified parameters to describe a cell with less optimal ETL properties. With these modified ETL parameters, the relative sizes of the potentials V_{1-4} are significantly different, resulting in different values of the ectypal factor for each recombination type (except for bimolecular recombination).

From Figures 6.17 and 6.18, it is clear that the factors calculated from the drift-diffusion model closely match those predicted by the analytic model (at V_{oc}). Even when only a single source of recombination is present, the ectypal factor \bar{n}_{ec} is non-integer (except for purely bimolecular recombination). This highlights the challenge of attributing a particular form of recombination to a value of \bar{n}_{ec} . However, in contrast, when a single recombination mechanism dominates, the electronic ideality factor n_{el} is an integer and its value can be used to distinguish between bulk SRH recombination $n_{el} = 2$ and interfacial recombination $n_{el} = 1$. For multiple recombination mechanisms, the electronic ideality factor quantifies the proportion of bulk SRH to interfacial (and bimolecular) recombination via equation (A.15) and lies between 1 and 2. This is discussed further in the following section. If the size/proportion of some of the potentials V_{1-4} are known it is then theoretically possible, by pairing this information about n_{el} and \bar{n}_{ec}

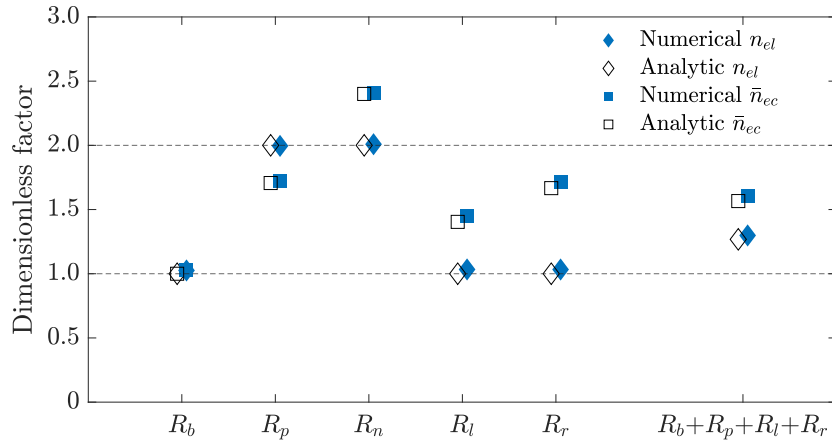


FIGURE 6.17: Electronic ideality factor and the ectypal factor calculated from impedance spectra at open-circuit for the five recombination types considered in this work and cell parameters from Table 4.1. The rightmost entry is for multiple recombination mechanisms, as displayed in Figure 6.19. We note that the values of the ectypal factor determined from the gradient of $\ln(R_{HF})$ versus V_{oc} in Figures 4.8 and 6.3 for R_p and R_l are approximately 1.7 and 1.4 respectively. These values are consistent with the values calculated here using eq.(6.9).

(using equation (3.5)), to diagnose the exact form and location of the recombination which is limiting cell performance.

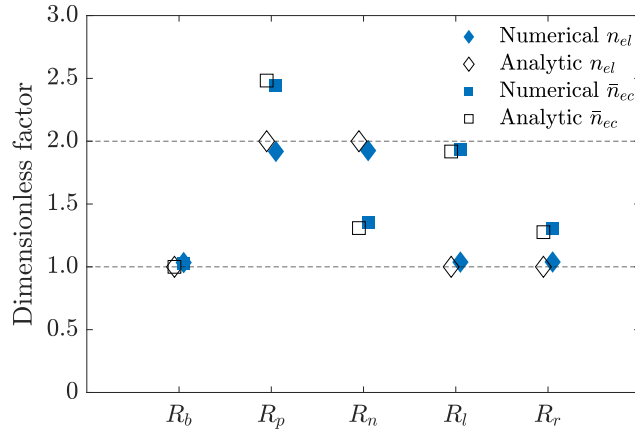


FIGURE 6.18: Electronic ideality factor and the ectypal factor calculated from impedance spectra at open-circuit for the five recombination types considered in this work. This is equivalent to Figure 6.17 but calculated from simulated impedance spectra with modified ETL parameters; namely, the width $b_E = 30$ nm, the effective doping density $d_E = 5 \times 10^{22} \text{ m}^{-3}$ and the effective density of states $g_{cE} = 10^{24} \text{ m}^{-3}$. All other cell and recombination parameters are the same and listed in Tables 4.1 and 5.1 respectively.

6.4 General recombination mechanisms

Until now we have only considered scenarios where there is a single recombination mechanism. Whilst in general this is unrealistic, there is usually a dominant form of recombination for any particular applied voltage V_{DC} , and therefore for any given impedance measurement. The results

from one of these simple cases, with a single recombination mechanism, is therefore likely to give a good qualitative understanding of any particular impedance measurement conducted on a PSC. Nevertheless, it is possible to generalise our analytic model to describe cells with any combination of recombination mechanisms. Furthermore, the analytic model is compatible with full recombination rates and is not restricted to the approximate forms listed in Table 5.1. However, we note that more general sets of recombination mechanisms lead to unwieldy equations for the HF and LF resistances and capacitances that are difficult to interpret. In order to illustrate the sort of behaviour that might be expected in a real cell, whilst retaining some ease of interpretation, we provide a representative example of a PSC with a combination of the recombination pathways given in Table 5.1. These more general expressions are given in Appendix A.

As an example, we consider the additive combination of bimolecular and hole-limited recombination in the perovskite ($R_b + R_p$), as given in Table 5.1, and the surface recombination pathways R_l (on the ETL/perovskite interface) and R_r (on the perovskite/HTL interface), again as given in Table 5.1. The analytic results for this cell (as computed from equations (A.6)-(A.7)) are compared to the numerical solutions of the drift-diffusion model, in which the full recombination rates are used. Figure 6.19 shows a comparison between the two approaches for this cell (i.e. the analytic model versus drift-diffusion model) and demonstrates good agreement between the two across the full frequency range. The corresponding frequency plots are presented in Figure 6.20. As expected, the combination of these four different recombination mechanisms leads to a decrease in open-circuit voltage ($V_{oc} = 0.88$ V for $R_p + R_l + R_r + R_b$ as compared to $V_{oc} = 0.93$ V with just R_l).

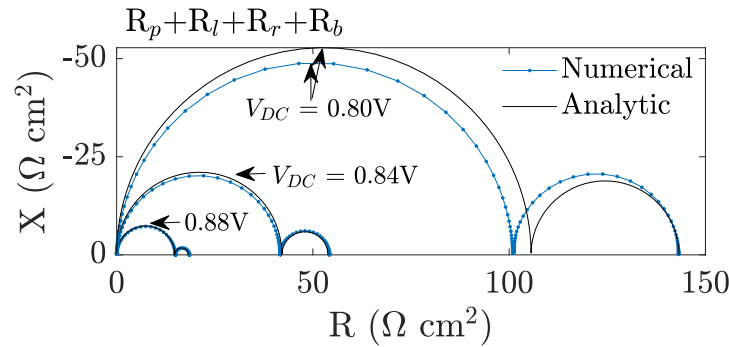


FIGURE 6.19: Simulated impedance spectra for a PSC with four types of recombination under 0.1-Sun equivalent illumination. Spectra at three DC voltages are shown, including $V_{oc} = 0.88$ V. Specifically, the recombination taking place is bimolecular (R_b) and hole-limited SRH (R_p) in the bulk and at both the ETL/perovskite (R_l) and perovskite/HTL (R_r) interfaces. Recombination parameters for each type are specified in Table 5.1 and the additional parameters are given in Table 4.1. Figure 6.20 presents the corresponding frequency plot for this Nyquist diagram.

For a cell with multiple recombination pathways the interpretation of the high and low frequency features remains the same. Interpretation of the ectypal factor, is more complex and left as an opportunity for future research. In Appendix A, it is shown that the electronic ideality factor,

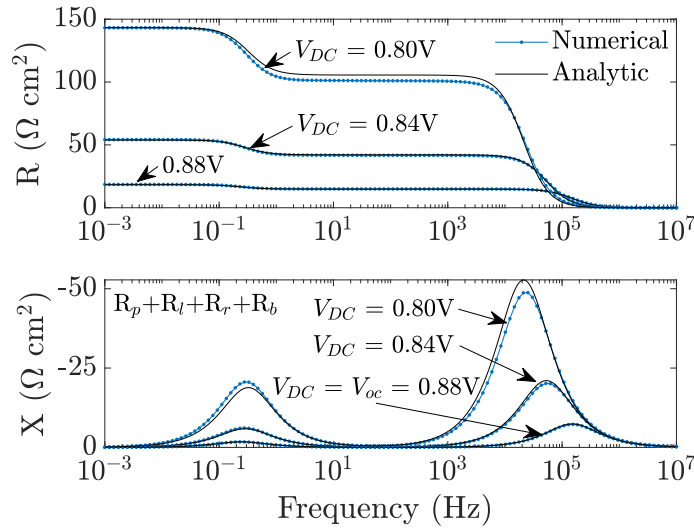


FIGURE 6.20: Corresponding frequency plot for the Nyquist diagram presented in Figure 6.19.

calculated from an impedance spectrum using (6.4), is given by

$$n_{\text{el}} = \frac{2}{2 - r_{\text{SRH}}} \quad (\text{A.15 reprinted})$$

where r_{SRH} is the ratio of the bulk SRH recombination current to the total recombination current. Therefore, the electronic ideality factor lies close to 1 when SRH recombination is negligible relative to interfacial (or bimolecular) recombination. Correspondingly, a value for the electronic ideality factor that is close to 2 indicates that the dominant form of recombination is SRH in the perovskite bulk.

Figure 6.17 shows the electronic ideality factor calculated for the analytic and numerical impedance spectra in Figure 6.19 at open-circuit. Once again good agreement is observed between the analytic and the full drift-diffusion model. This shows that a non-integer electronic ideality factor is expected if multiple recombination mechanisms are present, and its value can be interpreted using equation A.15.

6.5 Conclusion

We have shown excellent agreement between the solutions of the analytic model and the drift-diffusion model for impedance simulations conducted on a physically realistic set of parameters at V_{oc} and very good agreement at the maximum power point. Notably, no fitting is required in order to obtain this agreement between the analytic model and the drift-diffusion model; they only require that the same set of physical parameters are used in both.

It is important to note that there are some limitations to the analytic model that we have derived. The chief amongst these is that it is reliant on the charge carriers being close to quasi-equilibrium, so that in this particular instance they are close to being Boltzmann distributed. This is a reasonable assumption for cells with long carrier diffusion lengths operating fairly close to V_{oc} , where many more carriers are present in the perovskite, but breaks down as the device is brought towards short-circuit. Approximated recombination rates as opposed to the full SRH recombination equations are used in the analytic model. Additionally, the surface polarisation model assumes that the ionic vacancy density is greater than the charge carrier densities and therefore the electric potential is controlled almost solely by the ionic distribution. As demonstrated by comparison of the analytic model solutions to the numerical solutions, these approximations are accurate for realistic PSC parameters and recombination lifetimes.

The approximations to the underlying drift-diffusion model of a PSC have enabled the derivation of analytic formulae for R_{LF} , C_{LF} , R_{HF} , C_{HF} that account for the ionic characteristics within the perovskite layer. This enables physical meaning to be assigned to these commonly measured quantities and for experimental IS measurements to be used to infer PSC properties. Interestingly, it is found that the shape of an impedance spectrum is related to the dominant form of recombination. For example, if a negative LF feature is observed then the dominant form of recombination is SRH in the bulk of the perovskite. In general, the relationship between the type of recombination and the shape of the spectra is expressed through the specific values of n_{el} and \bar{n}_{ec} .

From a practical perspective, a key result of this work is the identification of an ideality factor that is appropriate for analysing the behaviour of PSCs. This can be determined from the high frequency resistance and the recombination current via the relation

$$n_{el} = \frac{R_{HF}(V_{DC})j_{rec}(V_{DC})}{V_T}, \quad (6.4 \text{ reprnted})$$

which has the property that it is independent of V_{DC} provided the dominant source of recombination does not change as the steady-state applied voltage V_{DC} is varied. This is a consequence of it depending purely on electronic (as opposed to ionic) parameters. Crucially, when there is a single dominant source of recombination loss within the cell, n_{el} takes an integer value. In particular, if this dominant loss mechanism occurs via SRH recombination within the perovskite layer, then $n_{el} = 2$. Whereas, if the dominant loss mechanism is bimolecular, or occurs at one of the perovskite/TL interfaces, then $n_{el} = 1$. As a result, we have identified a straightforward experimental method to determine a true ideality factor for PSCs through measurement of the high frequency resistance. This is valuable as this enables the key efficiency losses to be determined using a quick and inexpensive method that can be employed both in the lab and in operation.

During development in the lab, if the recombination type is known, this can inform future device development to help minimise losses. For example, if SRH recombination in the bulk limits the performance, then efforts could be targeted towards improving the perovskite crystallinity. On the other hand, a particular interface may be identified (using both n_{el} and n_{ec}). In this

case, efficiency losses could be mitigated by passivating the interface or even by modifying the doping level of the transport layers to change the potential distribution V_{1-4} . The non-destructive nature of IS means that it can be used to monitor device stability over time. When paired with the accurate interpretation provided by the analytic model, this opens up the prospect of an inexpensive tool to help understand the causes of degradation.

It has been reported that even cells produced using identical methods can display very different properties [131]. Measuring the impedance spectra of the cells and fitting to an RC - RC circuit can be used to characterise and compare cells from the same batch. Differences between the resistances and capacitances can highlight defective, or suboptimal cells. For example, differences in the high frequency capacitance C_{HF} could indicate that the perovskite width b is not consistent between different cells.

While mobile ions greatly impact the operation of PSCs, it is challenging to study their ionic properties. The analytic model shows that the characteristic frequency of the LF feature ω_{LF} , given by eq.(5.97), is directly proportional to the ionic conductivity of the perovskite. From this expression, it is evident that the activation energy of the ionic vacancies can be extracted through the dependence of ω_{LF} on temperature. Furthermore, using innovative experiment design, it may be possible to obtain an accurate estimate for the ionic conductivity to better understand the density and mobility of the ionic vacancies present in PSCs.

Finally, numerically solving the drift-diffusion model and fitting the device parameters to reproduce experimental data is extremely challenging. The analytic model provides a much more accessible means to fit device parameters, either manually or via automated parameter tuning. This opens up the possibility of determining realistic estimates for device properties, such as recombination lifetimes and diffusion coefficients.

Chapter 7

Summary and Conclusions

The purpose of this thesis has been to develop models to simulate the impedance response of perovskite solar cells. This is with the aim of better understanding the features observed in their impedance spectra and to enable physical properties to be inferred from these measurements. A coupled ionic-electronic drift-diffusion model was used to model the operation of PSCs. This suitably accounts for the properties of the three core layers of a PSC, including the high density of mobile anion vacancies in the perovskite layer. Two approaches were taken; the first was to solve the drift-diffusion equations numerically by adding the capability to simulate IS measurements to the open-source PSC simulation tool `IonMonger` [106, 206]. The second approach, involved determining analytic solutions to describe the impedance response of PSCs through the application of a number of approximations to the coupled ionic-electronic drift-diffusion model. At applied voltages close to open-circuit, this analytic model demonstrates excellent agreement with the more complex drift-diffusion model from which it is derived. Both of these models provide new insights into the fundamental impedance response of PSCs, helping researchers to more effectively employ IS to understand and improve the efficiency of PSCs.

This thesis begins by presenting an introduction to the field of perovskite solar cells. The significant interest in recent years in PSCs is largely due to their excellent optoelectronic properties, high efficiencies and potential for low-cost, high-volume production. However, interpretation of standard characterisation techniques for PSCs can be challenging. This is due to the presence of a high density of mobile ionic vacancies, which gives rise to fundamental differences in behaviour between PSCs and other photovoltaic devices. One such characterisation technique, impedance spectroscopy, relies on accurate device models in order to analyse and extract useful information from its results. In Chapter 3, the present understanding for the commonly observed features in the impedance spectra are detailed, the models used to interpret the spectra are reviewed and an opportunity for the application of drift-diffusion models in the analysis of impedance data from PSCs is identified. These drift-diffusion models can significantly enhance our understanding of the physical processes that give rise to the unusual features observed in the impedance spectra of PSCs.

In Chapter 4, a drift-diffusion model that includes mobile anion vacancies within the perovskite layer is set out. The particular formulation is the same as that used by Richardson *et al.* [6] and Courtier *et al.* [4, 210] and is in line with the drift-diffusion models used by other groups [118, 183, 192]. Impedance spectroscopy measurements were simulated using a bespoke module, developed in this thesis and associated works [2, 3], for the open-source software `IonMonger` [106, 206]. This enables impedance spectra to be simulated relatively quickly under realistic parameter and measurement regimes.

The simulated impedance spectra display features that are consistent with experimental measurements. For example, the HF feature has a characteristic frequency of around 10 - 100 kHz and is visible as a semicircle above the axis on a Nyquist plot. At different voltages, its diameter varies in size proportionally to a recombination resistance and the associated capacitance is equal to the geometric capacitance of the cell, calculated from eq.(3.20). The low frequency feature is semicircular and can lie above or below the axis on a Nyquist plot. The numerical model demonstrates how ionic redistribution can impact the charge injection, extraction and recombination of electrons and holes at low frequencies. This interpretation for the LF feature as an ionic modulation of current is in line with reports from the literature [96, 125, 158, 183]. In addition to the low and high frequency features, the numerical model reproduces the unusual intermediate frequency features, that are sometimes observed in PSC impedance spectra. These features include a loop between the LF and HF features and additional arcs. Figure 4.10 shows examples of these exotic features, which qualitatively match the experimental spectra presented in Figure 3.11.

Section 4.3, demonstrates that the low and high frequency features display the same dependencies on illumination as observed in experimental spectra. Additionally, the simulation results by Riquelme *et al.* using the `IonMonger` IS module reproduce these trends for cell parameters that describe mesoporous and inverted cells [3]. Furthermore, Riquelme *et al.* show a direct comparison of simulated spectra, obtained using the numerical model, to experimental measurements [3]. A semi-quantitative fit to both impedance spectra and J - V measurements is obtained through fitting device parameters and the inclusion of interfacial recombination.

A framework to understand the impedance response of PSCs depending on the frequency of perturbation is established through the classification of three frequency regimes. Over each frequency regime, the impedance response is approximately constant and is the result of particular physical processes. Examining the potential profile and spatial distribution of charge over each of these frequency regimes helps to relate the temporal response to the frequency response. With this framework, the physical processes responsible for the high and low frequency features, which are observed as the cell transitions between two frequency regimes, can be better understood.

The impedance module will be released as part of `IonMonger` version 2.0 [*release paper in preparation by W. Clarke, L.J Bennett, Y. Grudeva, J.M Foster, G. Richardson, and N. E. Courtier*]. This update provides an accessible tool for PSC impedance spectroscopy simulation,

helping researchers to study the impact of specific device parameters and recombination mechanisms on the impedance response of PSCs. Overall, the simulated impedance spectra obtained via numerical solution to the drift-diffusion model show very good agreement with experiment, and capture all of the qualitative features of the IS response of PSCs observed in practice.

In Chapter 5, a systematic asymptotic analysis of the drift-diffusion model (presented in Chapter 4) was used to obtain an approximate analytic model of the impedance response of a PSC. The resulting simplified analytic model retains all the physical parameters used in the drift-diffusion model and thus greatly simplifies the procedure of deducing device parameters from IS data. In order to arrive at a simplified model for the impedance response, we were required to make a number of physically reasonable assumptions, the most important of which are that: (i) the ion vacancies occur at much higher densities than the charge carriers, (ii) the ion vacancy density is sufficiently high to lead to narrow space charge layers at the interfaces with the transport layers, (iii) the transport layers are doped, and (iv) the electrons and holes in the perovskite are Boltzmann distributed at the voltage at which the impedance measurement is made. To further reduce the complexity of the recombination current equation, approximate recombination rates for each of the five mechanisms were used, as listed in Table 5.1. The approximations summarised above enabled a general, yet simple, relation for the total current to be derived. Finally, the model equations could be linearised to derive analytic expressions for the impedance response of PSCs. Notably, the analytic model predicts a response that can be related to an RC - RC equivalent circuit (approximately but accurately for realistic PSC parameters). As such, this model defines the commonly measured low and high frequency resistances and capacitances in terms of device properties and measurement conditions.

In Chapter 6, the analytic model solutions are compared to the full drift-diffusion model from which it is derived. Excellent agreement is demonstrated between the two models, in a regime where the applied voltage is close to the open-circuit voltage. In particular, the effect of the type of recombination on the impedance spectra at open-circuit is examined. Through plotting the spectra and examining the analytic model, it is found that the appearance of the LF feature is dependent on the type of recombination. Specifically, for a cell with only bimolecular radiative recombination, a LF feature is not visible. For recombination at either the ETL/perovskite or perovskite/HTL interfaces, the LF feature always lies above the axis on a Nyquist plot. When recombination is bulk SRH, the relative size of the interfacial potentials on the ETL/perovskite interface ($V_1 + V_2$) versus those on the perovskite/HTL interface ($V_3 + V_4$) determine whether or not the LF feature lies above or below the axis. The general relationship between the type of recombination and the shape of the spectra is expressed through the specific values of the electronic ideality factor n_{el} and the measured ectypal factor \bar{n}_{ec} (where \bar{n}_{ec} is what is actually determined for PSCs when using the Suns- V_{oc} and dark- J - V methods).

Through the derivation of the analytic model, a factor which we term, the *electronic ideality factor* n_{el} , is identified for PSCs. In contrast to the ectypal factor (commonly mistaken for an ‘ideality factor’), the electronic ideality factor is not directly dependent on the ionic properties of the cell, and its value is directly related to the type of recombination losses occurring within

the cell. This dimensionless factor can be determined from the high frequency resistance and the recombination current via the relation

$$n_{\text{el}} = \frac{R_{\text{HF}}(V_{\text{DC}})j_{\text{rec}}(V_{\text{DC}})}{V_T}. \quad (6.4 \text{ reprinted})$$

When there is single source of recombination n_{el} takes an integer value. Specifically, if recombination is SRH in the bulk of the perovskite, then $n_{\text{el}} = 2$, whereas, if the loss mechanism is radiative recombination in the bulk, or occurs at one of the perovskite/transport layer interfaces, then $n_{\text{el}} = 1$. As a result, we have identified an experimental method to determine a true ideality factor for PSCs through measurement of the high frequency resistance. As derived in Appendix A, and demonstrated in Section 6.4, the analytic model is compatible with multiple recombination mechanisms. Non-integer values of the electronic ideality factor are expected when multiple recombination mechanisms limit the performance, with the closeness to 1 or 2 indicating the relative amount of each type of recombination.

The analytic model describes the fundamental impedance response of PSCs, in terms of device properties and measurement conditions. The identification of the electronic ideality factor n_{el} and a recipe to determine it from impedance measurements, is an important discovery that has the potential to transform how efficiency losses are identified in PSCs. In summary, the numerical and analytic models formed in this work provide much needed insight into the impedance response of PSCs. This will help researchers to use impedance spectroscopy more effectively to study and monitor the properties of PSCs and other related devices with substantial ionic motion.

7.1 Further research

While the models formed in this work are able to accurately reproduce the common features and experimental trends of IS measurements of PSCs, further quantitative comparison to experimental spectra should be attempted. This task is now more easily achievable as the analytic relations show the approximate dependence of the low and high frequency features on device and measurement parameters. Additional validation of the analytic model and theory presented in Chapter 5 could be obtained via measurement of the electronic ideality factor. For example, the electronic ideality factor could be calculated at different temperatures and illuminations (as long as the dominant recombination mechanism is not expected to vary). In theory, the electronic ideality factor should remain approximately constant, whereas the ideality factor (the ‘ideality factor’) determined from Suns- V_{oc} or dark- $J-V$ methods) is expected to vary.

There is scope to further investigate the physical origin of the intermediate frequency features using the IS module. In this work, these features have been linked to an accumulation of electronic charge within the perovskite, i.e. they are visible for DC voltages at or above V_{oc} at 1-Sun. However, additional investigation is required to discern why the intermediate frequency features can appear below the axis, as a bulge or as a loop between the LF and HF features. While this

work has demonstrated that additional processes or mechanisms are not *required* to explain the IF features, it is not yet clear the effect that these may have on the impedance spectra. For example, the drift-diffusion model and `IonMonger` can be extended to describe PSCs with multiple species of mobile anion vacancies, or mobile cation vacancies. The resulting impedance response would be interesting to investigate.

The analytic model is compatible with other non-linear capacitance relations. These can be derived from other versions of the drift-diffusion model, which describe a modified physical picture of a PSC (for example, one in which there are multiple mobile ionic species or one in which the charge carriers in the transport layers obey degenerate statistics). Extension of the analytic model to describe these scenarios would provide much more insight into the cell response than a numerical model could provide.

It is possible to derive an analytic model from the surface polarisation model (equations 5.1-5.17) without the assumption of the carrier densities being Boltzmann distributed. In order to decouple the PDEs for the charge carriers, the recombination in the bulk must be either electron- or hole-limited SRH (i.e. dependent on only one carrier type). Additionally, interface recombination relies on a Boltzmann distribution at the interface. This alternative model would be accurate under approximately the same conditions as the surface polarisation model, i.e. for DC voltages between around 0 – 1.1 V and up to around 1-Sun illumination. Therefore, in comparison to the analytic model developed in this work, it would be applicable for a wider range of voltages and device parameters; however, it would be more limited in the types of recombination that it could model. If developed, this would be a useful intermediate tool between the full numerical model and the simpler analytic model. From a preliminary investigation, it was found that the alternative analytic model results in relatively unwieldy expressions for the impedance response that are challenging to interpret. However, these could be related to the analytic model presented here in order to gain a better physical understanding.

Intensity modulated photocurrent spectroscopy (IMPS) and intensity modulated photovoltage spectroscopy (IMVS) are similar techniques to impedance spectroscopy that probe the frequency response of a solar cell. In contrast to impedance spectroscopy, it is the incident illumination that is perturbed about a steady-state rather than the voltage. Specifically, for IMPS the cell is held at short-circuit and the photocurrent is measured. For IMVS, the cell is held at open-circuit and the (photo)voltage is measured. Similarly to IS, the results from these techniques are not as well understood for PSCs as they are for dye-sensitised solar cells and other more established technologies.

Analytic models that describe the IMPS and IMVS response of PSCs could be derived using the same mathematical methods as employed in this thesis. IMVS is carried out at open-circuit and therefore the Boltzmann approximation for the carrier densities (as described in Section 5.2) can be employed. This would result in relatively simple analytic relations for the high and low frequency features. As IMPS is performed at short-circuit, the Boltzmann approximation is not suitable. However, analytic solutions could still be obtained directly from linearisation

of the surface polarisation model. Furthermore, extension of the IS module for `IonMonger` to simulate IMVS and IMPS would be relatively straightforward. Models for IMPS and IMVS would further improve our understanding of the operation of PSCs and would be a valuable contribution to the field.

Appendix A

Multiple concurrent recombination mechanisms

In this appendix, the analytic model presented in Chapter 5 is extended to describe multiple (concurrent) recombination mechanisms that take the approximate forms listed in Table 5.1. In Section A.1, notation is defined and the resistances and capacitances given in the main text eq.(6.1) and (6.2) are extended to describe the impedance of a PSC with multiple recombination mechanisms. Following this, Section A.2 considers the value that would be determined for the electronic ideality factor for a cell with more than one dominant recombination mechanism.

A.1 The low and high frequency resistances and capacitances

Chapter 5 considers cells that have a single form of recombination that dominates over the others. Here, we consider the more general case in which cell losses occur via multiple recombination pathways. In line with the main text, it is assumed that the recombination rates listed in Table 5.1 are good approximations to the full recombination rates. As such, the recombination current (5.24) can be composed as follows

$$j_{\text{rec}} = j_{\text{rec}_b} + j_{\text{rec}_{\text{SRH}}} + j_{\text{rec}_l} + j_{\text{rec}_r}, \quad (\text{A.1})$$

where each component is the recombination current resulting from the specific form of recombination. SRH recombination is either electron-limited (R_n) or hole-limited (R_p). To reduce the length of the formula, we define the following

$$j_{\text{rec}} = \sum_{i=b,p,n,l,r} j_{\text{rec}_i}. \quad (\text{A.2})$$

The abbreviations used for the different types of recombination pathways are given in Table 5.1. Additionally, we use n_{el_i} and \bar{n}_{ec_i} to distinguish the different values of the electronic ideality

factor and the measured ectypal factor respectively for the corresponding recombination type. For example, for bimolecular recombination (R_b) and electron-limited bulk SRH recombination (R_n), the total recombination current is

$$j_{\text{rec}} = j_{\text{rec}_b} + j_{\text{rec}_n} = \sum_{i=b,n} j_{\text{rec}_i}, \quad (\text{A.3})$$

with

$$n_{\text{el}_b} = 1, \quad n_{\text{el}_n} = 2, \quad (\text{A.4})$$

$$\bar{n}_{\text{ec}_b}(V_{\text{DC}}) = 1, \quad \bar{n}_{\text{ec}_n}(V_{\text{DC}}) = \frac{F'_T(Q_{\text{DC}})}{F'_n(Q_{\text{DC}})} = \frac{V'_1 + V'_2 + V'_3 + V'_4}{V'_1 + V'_2}. \quad (\text{A.5})$$

With this notation, the general form for the resistances and capacitances associated with the high and low frequency features can be written as

$$R_{HF} = V_T \left(\sum_i \frac{j_{\text{rec}_i}(V_{\text{DC}})}{n_{\text{el}_i}} \right)^{-1} \quad C_{HF} = \frac{\varepsilon_p}{b} \quad (\text{A.6})$$

$$R_{LF} = V_T \left(\sum_i \frac{j_{\text{rec}_i}(V_{\text{DC}})}{\bar{n}_{\text{ec}_i}} \right)^{-1} - R_{HF} \quad C_{LF} = \frac{(\sum_i j_{\text{rec}_i}(V_{\text{DC}})/n_{\text{el}_i})^2 \frac{dQ_{\text{DC}}}{dV_{\text{DC}}}}{G_+ V_T \sum_i j_{\text{rec}_i}(V_{\text{DC}}) (1/\bar{n}_{\text{ec}_i} - 1/n_{\text{el}_i})}, \quad (\text{A.7})$$

where the sum over i is the sum over recombination pathways, $i = b, p, n, l, r$ as defined in Table 5.1.

A.2 The electronic ideality factor

Here, we consider what value is obtained for the electronic ideality factor when there is more than one source of recombination. We start by writing (A.1) in the form

$$j_{\text{rec}} = j_{\text{recSRH}} + j_{\text{recnon-SRH}}, \quad (\text{A.8})$$

where

$$j_{\text{recSRH}} = j_{\text{rec}_n} \quad \text{or} \quad j_{\text{rec}_p}, \quad (\text{A.9})$$

$$j_{\text{recnon-SRH}} = \sum_{i=b,l,r} j_{\text{rec}_i}, \quad (\text{A.10})$$

we see that the HF resistance, as defined in (A.6), can be written in the form

$$R_{HF} = V_T \left(\frac{j_{\text{recSRH}}(V_{\text{DC}})}{2} + j_{\text{recnon-SRH}}(V_{\text{DC}}) \right)^{-1}, \quad (\text{A.11})$$

where appropriate values of the electronic ideality factor n_{el_i} , from Table 5.2, are used for each recombination type. On defining r_{SRH} as the ratio of the SRH recombination current to the total recombination current, as follows

$$r_{\text{SRH}} = \frac{j_{\text{recSRH}}(V_{\text{DC}})}{j_{\text{rec}}(V_{\text{DC}})}, \quad (\text{A.12})$$

we can express the HF resistance as

$$R_{\text{HF}}(V_{\text{DC}}) = V_T \left(j_{\text{rec}}(V_{\text{DC}}) \left(\frac{r_{\text{SRH}}}{2} + 1 - r_{\text{SRH}} \right) \right)^{-1}. \quad (\text{A.13})$$

This simplifies to

$$R_{\text{HF}}(V_{\text{DC}}) = \frac{V_T}{j_{\text{rec}}(V_{\text{DC}}) \left(\frac{2-r_{\text{SRH}}}{2} \right)}. \quad (\text{A.14})$$

On comparison of the above with (5.94), or by substituting it into the following

$$n_{\text{el}} = \frac{R_{\text{HF}}(V_{\text{DC}}) j_{\text{rec}}(V_{\text{DC}})}{V_T}, \quad (6.4 \text{ reprinted})$$

we see that the electronic ideality factor determined for a cell with multiple recombination pathways is given by

$$n_{\text{el}} = \frac{2}{2 - r_{\text{SRH}}}, \quad (\text{A.15})$$

where r_{SRH} is the ratio of the SRH recombination current to the total recombination current. Therefore, the electronic ideality factor takes a value between 1 and 2, depending on the relative proportion of recombination current to SRH or non-SRH losses.

References

- [1] Alejandra Castro-Chong, Antonio J Riquelme, Tom Aernouts, Laurence J Bennett, Giles Richardson, Gerko Oskam, and Juan A Anta. Illumination intensity dependence of the recombination mechanism in mixed perovskite solar cells. *ChemPlusChem*, 86(9):1347–1356, 2021.
- [2] Laurence J Bennett, Antonio J Riquelme, Nicola E Courtier, Juan A Anta, and Giles Richardson. A new ideality factor for perovskite solar cells and an analytical theory for their impedance spectroscopy response. *arXiv preprint arXiv:2105.11226*, 2021.
- [3] Antonio Riquelme, Laurence J Bennett, Nicola E Courtier, Matthew J Wolf, Lidia Contreras-Bernal, Alison B Walker, Giles Richardson, and Juan A Anta. Identification of recombination losses and charge collection efficiency in a perovskite solar cell by comparing impedance response to a drift-diffusion model. *Nanoscale*, 12(33):17385–17398, 2020.
- [4] Nicola E Courtier, James M Cave, Jamie M Foster, Alison B Walker, and Giles Richardson. How transport layer properties affect perovskite solar cell performance: insights from a coupled charge transport/ion migration model. *Energy & Environmental Science*, 12(1):396–409, 2019.
- [5] Nicola E Courtier, Jamie M Foster, Simon EJ O’Kane, Alison B Walker, and Giles Richardson. Systematic derivation of a surface polarisation model for planar perovskite solar cells. *European Journal of Applied Mathematics*, pages 1–31, 2018.
- [6] Giles Richardson, Simon EJ O’Kane, Ralf G Niemann, Timo A Peltola, Jamie M Foster, Petra J Cameron, and Alison B Walker. Can slow-moving ions explain hysteresis in the current–voltage curves of perovskite solar cells? *Energy & Environmental Science*, 9(4):1476–1485, 2016.
- [7] IEA International Energy Agency. World Energy Outlook 2021. <https://www.iea.org/reports/world-energy-outlook-2021>. Accessed: 20-11-2021.
- [8] Intergovernmental Panel on Climate Change (IPCC). AR6 Climate Change 2021: The Physical Science Basis. <https://www.ipcc.ch/report/ar6/wg1/>. Accessed: 20-11-2021.
- [9] Nancy M Haegel, Robert Margolis, Tonio Buonassisi, David Feldman, Armin Froitzheim, Raffi Garabedian, Martin Green, Stefan Glunz, Hans-Martin Henning, Burkhard Holder, et al. Terawatt-scale photovoltaics: Trajectories and challenges. *Science*, 356(6334):141–143, 2017.
- [10] IEA. International Energy Agency, Technology Roadmap: Solar Photovoltaic Energy 2016 Edition. <https://webstore.iea.org/technology-roadmap-solar-photovoltaic-energy-2014>, 2014. Accessed: 08-06-2018.

- [11] International Energy Agency (IEA). Renewables 2020 - Analysis and forecast to 2025. <https://www.iea.org/reports/renewables-2020?mode=overview>, 2020. Accessed: 21-11-2021.
- [12] Fraunhofer Institute for Solar Energy Systems (ISE). Photovoltaics Report. <https://www.ise.fraunhofer.de/content/dam/ise/de/documents/publications/studies/Photovoltaics-Report.pdf>, 2018. Accessed: 21-11-2021.
- [13] Yang Yu, Hong Li, and Haibo Bao. Price dynamics and market relations in solar photovoltaic silicon feedstock trades. *Renewable Energy*, 86:526–542, 2016.
- [14] Jenny Nelson. *The physics of solar cells*. World Scientific Publishing Company, 2003.
- [15] Sven Rühle. Tabulated values of the Shockley–Queisser limit for single junction solar cells. *Solar Energy*, 130:139–147, 2016.
- [16] Arvind Shah, Pedro Torres, Reto Tscharnner, Nicolas Wyrsh, and Herbert Keppner. Photovoltaic technology: the case for thin-film solar cells. *science*, 285(5428):692–698, 1999.
- [17] Jian Gong, Seth B Darling, and Fengqi You. Perovskite photovoltaics: life-cycle assessment of energy and environmental impacts. *Energy & Environmental Science*, 8(7):1953–1968, 2015.
- [18] Erik A Alsema and Mariska J de Wild-Scholten. The real environmental impacts of crystalline silicon PV modules: an analysis based on up-to-date manufacturers data. In *Presented at the 20th European Photovoltaic Solar Energy Conference*, volume 6, page 10, 2005.
- [19] Henry J Snaith. Perovskites: the emergence of a new era for low-cost, high-efficiency solar cells. *The Journal of Physical Chemistry Letters*, 4(21):3623–3630, 2013.
- [20] Juan-Pablo Correa-Baena, Antonio Abate, Michael Saliba, Wolfgang Tress, T Jesper Jacobsson, Michael Grätzel, and Anders Hagfeldt. The rapid evolution of highly efficient perovskite solar cells. *Energy & Environmental Science*, 10(3):710–727, 2017.
- [21] Chuantian Zuo, Doojin Vak, Dechan Angmo, Liming Ding, and Mei Gao. One-step roll-to-roll air processed high efficiency perovskite solar cells. *Nano Energy*, 46:185–192, 2018.
- [22] Martin A Green, Anita Ho-Baillie, and Henry J Snaith. The emergence of perovskite solar cells. *Nature Photonics*, 8(7):nphoton–2014, 2014.
- [23] Dian Wang, Matthew Wright, Naveen Kumar Elumalai, and Ashraf Uddin. Stability of perovskite solar cells. *Solar Energy Materials and Solar Cells*, 147:255–275, 2016.
- [24] Yasuhiro Yamada, Toru Nakamura, Masaru Endo, Atsushi Wakamiya, and Yoshihiko Kanemitsu. Near-band-edge optical responses of solution-processed organic–inorganic hybrid perovskite CH₃NH₃PbI₃ on mesoporous TiO₂ electrodes. *Applied Physics Express*, 7(3):032302, 2014.
- [25] Giles E Eperon, Victor M Burlakov, Pablo Docampo, Alain Goriely, and Henry J Snaith. Morphological control for high performance, solution-processed planar heterojunction perovskite solar cells. *Advanced Functional Materials*, 24(1):151–157, 2014.
- [26] Mingzhen Liu, Michael B Johnston, and Henry J Snaith. Efficient planar heterojunction perovskite solar cells by vapour deposition. *Nature*, 501(7467):395, 2013.

- [27] Md Shahiduzzaman, Mohammad Ismail Hossain, Sem Visal, Tetsuya Kaneko, Wayesh Qarony, Shinjiro Umez, Koji Tomita, Satoru Iwamori, Dietmar Knipp, Yuen Hong Tsang, et al. Spray pyrolyzed TiO₂ embedded multi-layer front contact design for high-efficiency perovskite solar cells. *Nano-micro letters*, 13(1):1–17, 2021.
- [28] Ioannis B Koutselas, Laurent Ducasse, and George C Papavassiliou. Electronic properties of three-and low-dimensional semiconducting materials with Pb halide and Sn halide units. *Journal of Physics: Condensed Matter*, 8(9):1217, 1996.
- [29] Qianqian Lin, Ardalan Armin, Ravi Chandra Raju Nagiri, Paul L Burn, and Paul Meredith. Electro-optics of perovskite solar cells. *Nature Photonics*, 9(2):106, 2015.
- [30] Muhammad I Asghar, Jun Zhang, H Wang, and Peter D Lund. Device stability of perovskite solar cells—a review. *Renewable and Sustainable Energy Reviews*, 77:131–146, 2017.
- [31] Samuel D Stranks, Giles E Eperon, Giulia Grancini, Christopher Menelaou, Marcelo JP Alcocer, Tomas Leijtens, Laura M Herz, Annamaria Petrozza, and Henry J Snaith. Electron-hole diffusion lengths exceeding 1 micrometer in an organometal trihalide perovskite absorber. *Science*, 342(6156):341–344, 2013.
- [32] Dongqin Bi, Wolfgang Tress, M Ibrahim Dar, Peng Gao, Jingshan Luo, Clémentine Renevier, Kurt Schenk, Antonio Abate, Fabrizio Giordano, Juan-Pablo Correa Baena, et al. Efficient luminescent solar cells based on tailored mixed-cation perovskites. *Science advances*, 2(1):e1501170, 2016.
- [33] Mojtaba Abdi-Jalebi, Zahra Andaji-Garmaroudi, Stefania Cacovich, Camille Stavrakas, Bertrand Philippe, Johannes M Richter, Mejd Alsari, Edward P Booker, Eline M Hutter, Andrew J Pearson, et al. Maximizing and stabilizing luminescence from halide perovskites with potassium passivation. *Nature*, 555(7697):497, 2018.
- [34] Norman Pellet, Peng Gao, Giuliano Gregori, Tae-Youl Yang, Mohammad K Nazeeruddin, Joachim Maier, and Michael Grätzel. Mixed-organic-cation perovskite photovoltaics for enhanced solar-light harvesting. *Angewandte Chemie International Edition*, 53(12):3151–3157, 2014.
- [35] Giles E Eperon, Samuel D Stranks, Christopher Menelaou, Michael B Johnston, Laura M Herz, and Henry J Snaith. Formamidinium lead trihalide: a broadly tunable perovskite for efficient planar heterojunction solar cells. *Energy & Environmental Science*, 7(3):982–988, 2014.
- [36] Henry J Snaith. Present status and future prospects of perovskite photovoltaics. *Nature materials*, 17(5):372, 2018.
- [37] Akihiro Kojima, Kenjiro Teshima, Tsutomu Miyasaka, and Yasuo Shirai. Novel photoelectrochemical cell with mesoscopic electrodes sensitized by lead-halide compounds (2). In *Meeting Abstracts*, pages 397–397. The Electrochemical Society, 2006. number 7.
- [38] Akihiro Kojima, Kenjiro Teshima, Yasuo Shirai, and Tsutomu Miyasaka. Organometal halide perovskites as visible-light sensitizers for photovoltaic cells. *Journal of the American Chemical Society*, 131(17):6050–6051, 2009.
- [39] Hui-Seon Kim, Chang-Ryul Lee, Jeong-Hyeok Im, Ki-Beom Lee, Thomas Moehl, Arianna Marchioro, Soo-Jin Moon, Robin Humphry-Baker, Jun-Ho Yum, Jacques E Moser, et al. Lead iodide perovskite sensitized all-solid-state submicron thin film mesoscopic solar cell with efficiency exceeding 9%. *Scientific reports*, 2:591, 2012.

- [40] Michael M Lee, Joël Teuscher, Tsutomu Miyasaka, Takuro N Murakami, and Henry J Snaith. Efficient hybrid solar cells based on meso-superstructured organometal halide perovskites. *Science*, page 1228604, 2012.
- [41] James M Ball, Michael M Lee, Andrew Hey, and Henry J Snaith. Low-temperature processed meso-superstructured to thin-film perovskite solar cells. *Energy & Environmental Science*, 6(6):1739–1743, 2013.
- [42] Silver-Hamill Turren-Cruz, Michael Saliba, Matthew T Mayer, Hector Juárez-Santisteban, Xavier Mathew, Lea Nienhaus, Wolfgang Tress, Matthew P Erodici, Meng-Ju Sher, Mounsi G Bawendi, et al. Enhanced charge carrier mobility and lifetime suppress hysteresis and improve efficiency in planar perovskite solar cells. *Energy & Environmental Science*, 2018.
- [43] Wei EI Sha, Xingang Ren, Luzhou Chen, and Wallace CH Choy. The efficiency limit of CH₃NH₃PbI₃ perovskite solar cells. *Applied Physics Letters*, 106(22):221104, 2015.
- [44] F Meillaud, Arvind Shah, C Droz, Evelyne Vallat-Sauvain, and C Miazza. Efficiency limits for single-junction and tandem solar cells. *Solar energy materials and solar cells*, 90(18-19):2952–2959, 2006.
- [45] Jun Hong Noh, Sang Hyuk Im, Jin Hyuck Heo, Tarak N Mandal, and Sang Il Seok. Chemical management for colorful, efficient, and stable inorganic–organic hybrid nanostructured solar cells. *Nano letters*, 13(4):1764–1769, 2013.
- [46] National Renewable Energy Laboratory. NREL, Best Research-Cell Efficiencies. <https://www.nrel.gov/pv/cell-efficiency.html>. Accessed: 20-11-2021.
- [47] Stefaan De Wolf, Jakub Holovsky, Soo-Jin Moon, Philipp Löper, Bjoern Niesen, Martin Ledinsky, Franz-Josef Haug, Jun-Ho Yum, and Christophe Ballif. Organometallic halide perovskites: sharp optical absorption edge and its relation to photovoltaic performance. *The journal of physical chemistry letters*, 5(6):1035–1039, 2014.
- [48] Konrad Wojciechowski, Michael Saliba, Tomas Leijtens, Antonio Abate, and Henry J Snaith. Sub-150 C processed meso-superstructured perovskite solar cells with enhanced efficiency. *Energy & Environmental Science*, 7(3):1142–1147, 2014.
- [49] Zhengguo Xiao, Cheng Bi, Yuchuan Shao, Qingfeng Dong, Qi Wang, Yongbo Yuan, Chenggong Wang, Yongli Gao, and Jinsong Huang. Efficient, high yield perovskite photovoltaic devices grown by interdiffusion of solution-processed precursor stacking layers. *Energy & Environmental Science*, 7(8):2619–2623, 2014.
- [50] Stefano Razza, Francesco Di Giacomo, Fabio Matteocci, Lucio Cina, Alessandro Lorenzo Palma, Simone Casaluci, Petra Cameron, Alessandra D’epifanio, Silvia Licoccia, Andrea Reale, et al. Perovskite solar cells and large area modules (100 cm²) based on an air flow-assisted PbI₂ blade coating deposition process. *Journal of Power Sources*, 277:286–291, 2015.
- [51] Jaeki Jeong, Minjin Kim, Jongdeuk Seo, Haizhou Lu, Paramvir Ahlawat, Aditya Mishra, Yingguo Yang, Michael A Hope, Felix T Eickemeyer, Maengsuk Kim, et al. Pseudo-halide anion engineering for α -FAPbI₃ perovskite solar cells. *Nature*, 592(7854):381–385, 2021.
- [52] Jason J Yoo, Gabkyung Seo, Matthew R Chua, Tae Gwan Park, Yongli Lu, Fabian Rotermund, Young-Ki Kim, Chan Su Moon, Nam Joong Jeon, Juan-Pablo Correa-Baena, et al. Efficient perovskite solar cells via improved carrier management. *Nature*, 590(7847):587–593, 2021.

- [53] Aslihan Babayigit, Anitha Ethirajan, Marc Muller, and Bert Conings. Toxicity of organometal halide perovskite solar cells. *Nature materials*, 15(3):247, 2016.
- [54] Guangda Niu, Xudong Guo, and Liduo Wang. Review of recent progress in chemical stability of perovskite solar cells. *Journal of Materials Chemistry A*, 3(17):8970–8980, 2015.
- [55] International Electrotechnical Commission. IEC, Terrestrial photovoltaic (PV) modules. <https://webstore.iec.ch/publication/24312>. Accessed: 08-04-2019.
- [56] I. W. Wendells. Solar Panel Performance Standards IEC 61215/61646. <https://www.solarguidebook.com/solar-panel-performance-standards-iec-61215-61646>. Accessed: 09-04-2019.
- [57] NREL National Renewable Energy Laboratory. IEC 61215: What it is and isn't. <https://www.nrel.gov/docs/fy12osti/54714.pdf>. Accessed: 09-04-2019.
- [58] Bert Conings, Jeroen Drijkoningen, Nicolas Gauquelin, Aslihan Babayigit, Jan D'Haen, Lien D'Olieslaeger, Anitha Ethirajan, Jo Verbeeck, Jean Manca, Edoardo Mosconi, et al. Intrinsic thermal instability of methylammonium lead trihalide perovskite. *Advanced Energy Materials*, 5(15):1500477, 2015.
- [59] Giorgio Divitini, Stefania Cacovich, Fabio Matteocci, Lucio Cinà, A Di Carlo, and Caterina Ducati. In situ observation of heat-induced degradation of perovskite solar cells. *Nature Energy*, 1(2):15012, 2016.
- [60] Jinli Yang, Braden D Siempelkamp, Dianyi Liu, and Timothy L Kelly. Investigation of $\text{CH}_3\text{NH}_3\text{PbI}_3$ degradation rates and mechanisms in controlled humidity environments using in situ techniques. *ACS nano*, 9(2):1955–1963, 2015.
- [61] Zhaoning Song, Antonio Abate, Suneth C Watthage, Geethika K Liyanage, Adam B Phillips, Ullrich Steiner, Michael Graetzel, and Michael J Heben. Perovskite solar cell stability in humid air: Partially reversible phase transitions in the $\text{PbI}_2\text{-CH}_3\text{NH}_3\text{I-H}_2\text{O}$ system. *Advanced Energy Materials*, 6(19):1600846, 2016.
- [62] Daniel Bryant, Nicholas Aristidou, Sebastian Pont, Irene Sanchez-Molina, Thana Chotchunangatchaval, Scot Wheeler, James R Durrant, and Saif A Haque. Light and oxygen induced degradation limits the operational stability of methylammonium lead triiodide perovskite solar cells. *Energy & Environmental Science*, 9(5):1655–1660, 2016.
- [63] Daniel J Slotcavage, Hemamala I Karunadasa, and Michael D McGehee. Light-induced phase segregation in halide-perovskite absorbers. *ACS Energy Letters*, 1(6):1199–1205, 2016.
- [64] Tomas Leijtens, Giles E Eperon, Sandeep Pathak, Antonio Abate, Michael M Lee, and Henry J Snaith. Overcoming ultraviolet light instability of sensitized TiO_2 with meso-superstructured organometal tri-halide perovskite solar cells. *Nature communications*, 4:2885, 2013.
- [65] Konrad Domanski, Juan-Pablo Correa-Baena, Nicolas Mine, Mohammad Khaja Nazeeruddin, Antonio Abate, Michael Saliba, Wolfgang Tress, Anders Hagfeldt, and Michael Grätzel. Not all that glitters is gold: metal-migration-induced degradation in perovskite solar cells. *ACS nano*, 10(6):6306–6314, 2016.

- [66] Fabio Matteocci, Lucio Cinà, Enrico Lamanna, Stefania Cacovich, Giorgio Divitini, Paul A Midgley, Caterina Ducati, and Aldo Di Carlo. Encapsulation for long-term stability enhancement of perovskite solar cells. *Nano Energy*, 30:162–172, 2016.
- [67] Konrad Domanski, Bart Roose, Taisuke Matsui, Michael Saliba, Silver-Hamill Turren-Cruz, Juan-Pablo Correa-Baena, Cristina Roldan Carmona, Giles Richardson, Jamie M Foster, Filippo De Angelis, et al. Migration of cations induces reversible performance losses over day/night cycling in perovskite solar cells. *Energy & Environmental Science*, 10(2):604–613, 2017.
- [68] Felix Utama Kosasih and Caterina Ducati. Characterising degradation of perovskite solar cells through in-situ and operando electron microscopy. *Nano energy*, 47:243–256, 2018.
- [69] Christopher Eames, Jarvist M Frost, Piers RF Barnes, Brian C O'Regan, Aron Walsh, and M Saiful Islam. Ionic transport in hybrid lead iodide perovskite solar cells. *Nature communications*, 6:7497, 2015.
- [70] Jon M Azpiroz, Edoardo Mosconi, Juan Bisquert, and Filippo De Angelis. Defect migration in methylammonium lead iodide and its role in perovskite solar cell operation. *Energy & Environmental Science*, 8(7):2118–2127, 2015.
- [71] Stefania Cacovich, Giorgio Divitini, Christopher Ireland, Fabio Matteocci, Aldo Di Carlo, and Caterina Ducati. Elemental mapping of perovskite solar cells by using multivariate analysis: an insight into degradation processes. *ChemSusChem*, 9(18):2673–2678, 2016.
- [72] Yongbo Yuan and Jinsong Huang. Ion migration in organometal trihalide perovskite and its impact on photovoltaic efficiency and stability. *Accounts of chemical research*, 49(2):286–293, 2016.
- [73] Jin Hyuck Heo, Hye Ji Han, Dasom Kim, Tae Kyu Ahn, and Sang Hyuk Im. Hysteresis-less inverted CH₃NH₃PbI₃ planar perovskite hybrid solar cells with 18.1% power conversion efficiency. *Energy & Environmental Science*, 8(5):1602–1608, 2015.
- [74] Lingling Zheng, Yao-Hsien Chung, Yingzhuang Ma, Lipei Zhang, Lixin Xiao, Zhijian Chen, Shufeng Wang, Bo Qu, and Qihuang Gong. A hydrophobic hole transporting oligothiophene for planar perovskite solar cells with improved stability. *Chemical communications*, 50(76):11196–11199, 2014.
- [75] Zhiping Wang, David P. McMeekin, Nobuya Sakai, Stephan van Reenen, Konrad Wojciechowski, Jay B. Patel, Michael B. Johnston, and Henry J. Snaith. Efficient and air-stable mixed-cation lead mixed-halide perovskite solar cells with n-doped organic electron extraction layers. *Advanced Materials*, 29(5):1604186, 2017.
- [76] Michael Saliba, Taisuke Matsui, Konrad Domanski, Ji-Youn Seo, Amita Ummadisingu, Shaik M Zakeeruddin, Juan-Pablo Correa-Baena, Wolfgang R Tress, Antonio Abate, Anders Hagfeldt, et al. Incorporation of rubidium cations into perovskite solar cells improves photovoltaic performance. *Science*, 354(6309):206–209, 2016.
- [77] Bart Roose, Juan-Pablo Correa Baena, Karl C Gödel, Michael Graetzel, Anders Hagfeldt, Ullrich Steiner, and Antonio Abate. Mesoporous SnO₂ electron selective contact enables uv-stable perovskite solar cells. *Nano Energy*, 30:517–522, 2016.

- [78] Sandeep K Pathak, A Abate, P Ruckdeschel, B Roose, Karl C Gödel, Yana Vaynzof, Aditya Santhala, Shun-Ichiro Watanabe, Derek J Hollman, Nakita Noel, et al. Performance and stability enhancement of dye-sensitized and perovskite solar cells by Al doping of TiO₂. *Advanced Functional Materials*, 24(38):6046–6055, 2014.
- [79] Michael Saliba, Taisuke Matsui, Ji-Youn Seo, Konrad Domanski, Juan-Pablo Correa-Baena, Mohammad Khaja Nazeeruddin, Shaik M Zakeeruddin, Wolfgang Tress, Antonio Abate, Anders Hagfeldt, et al. Cesium-containing triple cation perovskite solar cells: improved stability, reproducibility and high efficiency. *Energy & environmental science*, 9(6):1989–1997, 2016.
- [80] Antonio Abate, Sanghyun Paek, Fabrizio Giordano, Juan-Pablo Correa-Baena, Michael Saliba, Peng Gao, Taisuke Matsui, Jaejung Ko, Shaik M Zakeeruddin, Klaus H Dahmen, et al. Silolothiophene-linked triphenylamines as stable hole transporting materials for high efficiency perovskite solar cells. *Energy & Environmental Science*, 8(10):2946–2953, 2015.
- [81] Kevin A Bush, Colin D Bailie, Ye Chen, Andrea R Bowring, Wei Wang, Wen Ma, Tomas Leijtens, Farhad Moghadam, and Michael D McGehee. Thermal and environmental stability of semi-transparent perovskite solar cells for tandems enabled by a solution-processed nanoparticle buffer layer and sputtered ITO electrode. *Advanced Materials*, 28(20):3937–3943, 2016.
- [82] Kevin A Bush, Axel F Palmstrom, J Yu Zhengshan, Mathieu Boccard, Rongrong Cheacharoen, Jonathan P Mailoa, David P McMeekin, Robert LZ Hoyer, Colin D Bailie, Tomas Leijtens, et al. 23.6%-efficient monolithic perovskite/silicon tandem solar cells with improved stability. *Nature Energy*, 2(4):17009, 2017.
- [83] Simone Guarnera, Antonio Abate, Wei Zhang, Jamie M Foster, Giles Richardson, Annamaria Petrozza, and Henry J Snaith. Improving the long-term stability of perovskite solar cells with a porous Al₂O₃ buffer layer. *The journal of physical chemistry letters*, 6(3):432–437, 2015.
- [84] Anyi Mei, Yusong Sheng, Yue Ming, Yue Hu, Yaoguang Rong, Weihua Zhang, Shulin Luo, Guangren Na, Chengbo Tian, Xiaomeng Hou, et al. Stabilizing perovskite solar cells to IEC61215: 2016 standards with over 9,000-h operational tracking. *Joule*, 4(12):2646–2660, 2020.
- [85] Eui Hyuk Jung, Nam Joong Jeon, Eun Young Park, Chan Su Moon, Tae Joo Shin, Tae-Youl Yang, Jun Hong Noh, and Jangwon Seo. Efficient, stable and scalable perovskite solar cells using poly (3-hexylthiophene). *Nature*, 567(7749):511, 2019.
- [86] Jiupeng Cao and Feng Yan. Recent progress in tin-based perovskite solar cells. *Energy & Environmental Science*, 14(3):1286–1325, 2021.
- [87] Po-Yen Chen, Jifa Qi, Matthew T Klug, Xiangnan Dang, Paula T Hammond, and Angela M Belcher. Environmentally responsible fabrication of efficient perovskite solar cells from recycled car batteries. *Energy & Environmental Science*, 7(11):3659–3665, 2014.
- [88] Kira L Gardner, Jeffrey G Tait, Tamara Merckx, Weiming Qiu, Ulrich W Paetzold, Lucinda Kootstra, Manoj Jaysankar, Robert Gehlhaar, David Cheyins, Paul Heremans, et al. Nonhazardous solvent systems for processing perovskite photovoltaics. *Advanced Energy Materials*, 6(14):1600386, 2016.
- [89] Aslihan Babayigit, Dinh Duy Thanh, Anitha Ethirajan, Jean Manca, Marc Muller, Hans-Gerd Boyen, and Bert Conings. Assessing the toxicity of Pb-and Sn-based perovskite solar cells in model organism danio rerio. *Scientific reports*, 6(1):1–11, 2016.

- [90] Aleksandra B Djurišić, Fangmeng Z Liu, Hannah W Tam, Man-Kin Wong, Andrew H Ng, Chen Surya, Weifeng Chen, and Zhangxing B He. Perovskite solar cells-an overview of critical issues. *Progress in Quantum Electronics*, 53:1–37, 2017.
- [91] Parikhith Sinha, Sukhwant Raju, Karen Drozdak, and Andreas Wade. Life cycle management and recycling of pv systems. *PV-Tech Power*, 13:47–50, 2017.
- [92] Henry J Snaith, Antonio Abate, James M Ball, Giles E Eperon, Tomas Leijtens, Nakita K Noel, Samuel D Stranks, Jacob Tse-Wei Wang, Konrad Wojciechowski, and Wei Zhang. Anomalous hysteresis in perovskite solar cells. *The journal of physical chemistry letters*, 5(9):1511–1515, 2014.
- [93] Eva Lisa Unger, Eric T Hoke, Colin D Bailie, William H Nguyen, Andrea Ruth Bowring, T Heumüller, Mark Greyson Christoforo, and Michael D McGehee. Hysteresis and transient behavior in current–voltage measurements of hybrid-perovskite absorber solar cells. *Energy & Environmental Science*, 7(11):3690–3698, 2014.
- [94] Wolfgang Tress, Nevena Marinova, Thomas Moehl, Shaik Mohammad Zakeeruddin, Mohammad Khaja Nazeeruddin, and Michael Grätzel. Understanding the rate-dependent J–V hysteresis, slow time component, and aging in CH₃NH₃PbI₃ perovskite solar cells: the role of a compensated electric field. *Energy & Environmental Science*, 8(3):995–1004, 2015.
- [95] Rafael S Sanchez, Victoria Gonzalez-Pedro, Jin-Wook Lee, Nam-Gyu Park, Yong Soo Kang, Ivan Mora-Sero, and Juan Bisquert. Slow dynamic processes in lead halide perovskite solar cells. Characteristic times and hysteresis. *The journal of physical chemistry letters*, 5(13):2357–2363, 2014.
- [96] Adam Pockett, Giles E Eperon, Nobuya Sakai, Henry J Snaith, Laurence M Peter, and Petra J Cameron. Microseconds, milliseconds and seconds: deconvoluting the dynamic behaviour of planar perovskite solar cells. *Physical Chemistry Chemical Physics*, 19(8):5959–5970, 2017.
- [97] Jeffrey A Christians, Joseph S Manser, and Prashant V Kamat. Best practices in perovskite solar cell efficiency measurements. Avoiding the error of making bad cells look good, 2015.
- [98] Eugen Zimmermann, Ka Kan Wong, Michael Müller, Hao Hu, Philipp Ehrenreich, Markus Kohlstädt, Uli Würfel, Simone Mastroianni, Gayathri Mathiazhagan, Andreas Hinsch, et al. Characterization of perovskite solar cells: Towards a reliable measurement protocol. *APL Materials*, 4(9):091901, 2016.
- [99] Mariona Coll, Andrés Gomez, Elena Mas-Marza, Osbel Almora, Germà Garcia-Belmonte, Mariano Campoy-Quiles, and Juan Bisquert. Polarization switching and light-enhanced piezoelectricity in lead halide perovskites. *The journal of physical chemistry letters*, 6(8):1408–1413, 2015.
- [100] Zhen Fan, Juanxiu Xiao, Kuan Sun, Lei Chen, Yating Hu, Jianyong Ouyang, Khuong P Ong, Kaiyang Zeng, and John Wang. Ferroelectricity of CH₃NH₃PbI₃ perovskite. *The journal of physical chemistry letters*, 6(7):1155–1161, 2015.
- [101] Simone Meloni, Thomas Moehl, Wolfgang Tress, Marius Franckevičius, Michael Saliba, Yong Hui Lee, Peng Gao, Mohammad Khaja Nazeeruddin, Shaik Mohammed Zakeeruddin, Ursula Rothlisberger, et al. Ionic polarization-induced current–voltage hysteresis in CH₃NH₃PbX₃ perovskite solar cells. *Nature communications*, 7(1):1–9, 2016.

- [102] Tae-Youl Yang, Giuliano Gregori, Norman Pellet, Michael Grätzel, and Joachim Maier. The significance of ion conduction in a hybrid organic–inorganic lead-iodide-based perovskite photosensitizer. *Angewandte Chemie*, 127(27):8016–8021, 2015.
- [103] Wei Zhang, Victor M Burlakov, Daniel J Graham, Tomas Leijtens, Anna Osherov, Vladimir Bulović, Henry J Snaith, David S Ginger, Samuel D Stranks, et al. Photo-induced halide redistribution in organic–inorganic perovskite films. *Nature communications*, 7:11683, 2016.
- [104] Yong Zhao, Chunjun Liang, Huimin Zhang, Dan Li, Ding Tian, Guobao Li, Xiping Jing, Wenguan Zhang, Weikang Xiao, Qian Liu, et al. Anomalously large interface charge in polarity-switchable photovoltaic devices: an indication of mobile ions in organic–inorganic halide perovskites. *Energy & Environmental Science*, 8(4):1256–1260, 2015.
- [105] Philip Calado, Andrew M Telford, Daniel Bryant, Xiaoe Li, Jenny Nelson, Brian C O'Regan, and Piers RF Barnes. Evidence for ion migration in hybrid perovskite solar cells with minimal hysteresis. *Nature communications*, 7:13831, 2016.
- [106] Nicola E Courtier, Giles Richardson, and Jamie M Foster. A fast and robust numerical scheme for solving models of charge carrier transport and ion vacancy motion in perovskite solar cells. *Applied Mathematical Modelling*, 2018.
- [107] Junichiro Mizusaki, Kimiyasu Arai, and Kazuo Fueki. Ionic conduction of the perovskite-type halides. *Solid State Ionics*, 11(3):203–211, 1983.
- [108] Titilayo A Kuku. Ionic transport and galvanic cell discharge characteristics of CuPbI₃ thin films. *Thin Solid Films*, 325(1-2):246–250, 1998.
- [109] Aron Walsh, David O Scanlon, Shiyu Chen, XG Gong, and Su-Huai Wei. Self-regulation mechanism for charged point defects in hybrid halide perovskites. *Angewandte Chemie International Edition*, 54(6):1791–1794, 2015.
- [110] Jun Haruyama, Keitaro Sodeyama, Liyuan Han, and Yoshitaka Tateyama. First-principles study of ion diffusion in perovskite solar cell sensitizers. *Journal of the American Chemical Society*, 137(32):10048–10051, 2015.
- [111] Giles E Eperon and David S Ginger. B-site metal cation exchange in halide perovskites. *ACS Energy Letters*, 2(5):1190–1196, 2017.
- [112] Daniel Bryant, Scot Wheeler, Brian C O'Regan, Trystan Watson, Piers RF Barnes, Dave Worsley, and James Durrant. Observable hysteresis at low temperature in “hysteresis free” organic–inorganic lead halide perovskite solar cells. *The Journal of Physical Chemistry Letters*, 6(16):3190–3194, 2015.
- [113] Luis K Ono, Sonia R Raga, Shenghao Wang, Yuichi Kato, and Yabing Qi. Temperature-dependent hysteresis effects in perovskite-based solar cells. *Journal of Materials Chemistry A*, 3(17):9074–9080, 2015.
- [114] Hui-Seon Kim and Nam-Gyu Park. Parameters affecting I–V hysteresis of CH₃NH₃PbI₃ perovskite solar cells: effects of perovskite crystal size and mesoporous TiO₂ layer. *The journal of physical chemistry letters*, 5(17):2927–2934, 2014.

- [115] Hui-Seon Kim, In-Hyuk Jang, Namyoun Ahn, Mansoo Choi, Antonio Guerrero, Juan Bisquert, and Nam-Gyu Park. Control of I–V hysteresis in $\text{CH}_3\text{NH}_3\text{PbI}_3$ perovskite solar cell. *The journal of physical chemistry letters*, 6(22):4633–4639, 2015.
- [116] Konrad Wojciechowski, Samuel D Stranks, Antonio Abate, Golnaz Sadoughi, Aditya Sadhanala, Nikos Kopidakis, Garry Rumbles, Chang-Zhi Li, Richard H Friend, Alex K-Y Jen, et al. Heterojunction modification for highly efficient organic–inorganic perovskite solar cells. *ACS nano*, 8(12):12701–12709, 2014.
- [117] Yuchuan Shao, Zhengguo Xiao, Cheng Bi, Yongbo Yuan, and Jinsong Huang. Origin and elimination of photocurrent hysteresis by fullerene passivation in $\text{CH}_3\text{NH}_3\text{PbI}_3$ planar heterojunction solar cells. *Nature communications*, 5:5784, 2014.
- [118] Stephan van Reenen, Martijn Kemerink, and Henry J Snaith. Modeling anomalous hysteresis in perovskite solar cells. *The journal of physical chemistry letters*, 6(19):3808–3814, 2015.
- [119] Jordi Carrillo, Antonio Guerrero, Sara Rahimnejad, Osbel Almora, Issac Zarazua, Elena Mas-Marza, Juan Bisquert, and Germà Garcia-Belmonte. Ionic reactivity at contacts and aging of methylammonium lead triiodide perovskite solar cells. *Advanced Energy Materials*, 6(9), 2016.
- [120] Antonio Guerrero, Jingbi You, Clara Aranda, Yong Soo Kang, Germà Garcia-Belmonte, Huanping Zhou, Juan Bisquert, and Yang Yang. Interfacial degradation of planar lead halide perovskite solar cells. *Acs Nano*, 10(1):218–224, 2015.
- [121] Heetae Yoon, Seong Min Kang, Jong-Kwon Lee, and Mansoo Choi. Hysteresis-free low-temperature-processed planar perovskite solar cells with 19.1% efficiency. *Energy & Environmental Science*, 9(7):2262–2266, 2016.
- [122] Zhengguo Xiao, Qingfeng Dong, Cheng Bi, Yuchuan Shao, Yongbo Yuan, and Jinsong Huang. Solvent annealing of perovskite-induced crystal growth for photovoltaic-device efficiency enhancement. *Advanced Materials*, 26(37):6503–6509, 2014.
- [123] Wanyi Nie, Hsinhan Tsai, Reza Asadpour, Jean-Christophe Blancon, Amanda J Neukirch, Gautam Gupta, Jared J Crochet, Manish Chhowalla, Sergei Tretiak, Muhammad A Alam, et al. High-efficiency solution-processed perovskite solar cells with millimeter-scale grains. *Science*, 347(6221):522–525, 2015.
- [124] James M Cave, Nicola E Courtier, Isabelle A Blakborn, Timothy W Jones, Dibyajyoti Ghosh, Kenrick F Anderson, Liangyou Lin, Andrew A Dijkhoff, Gregory J Wilson, Krishna Feron, et al. Deducing transport properties of mobile vacancies from perovskite solar cell characteristics. *Journal of Applied Physics*, 128(18):184501, 2020.
- [125] Daniel A Jacobs, Heping Shen, Florian Pfeffer, Jun Peng, Thomas P White, Fiona J Beck, and Kylie R Catchpole. The two faces of capacitance: New interpretations for electrical impedance measurements of perovskite solar cells and their relation to hysteresis. *Journal of Applied Physics*, 124(22):225702, 2018.
- [126] William Shockley. The theory of p-n junctions in semiconductors and p-n junction transistors. *Bell System Technical Journal*, 28(3):435–489, 1949.
- [127] Chih-Tang Sah, Robert N Noyce, and William Shockley. Carrier generation and recombination in pn junctions and pn junction characteristics. *Proceedings of the IRE*, 45(9):1228–1243, 1957.

- [128] Wolfgang Tress, Mozghan Yavari, Konrad Domanski, Pankaj Yadav, Bjoern Niesen, Juan Pablo Correa Baena, Anders Hagfeldt, and Michael Graetzel. Interpretation and evolution of open-circuit voltage, recombination, ideality factor and subgap defect states during reversible light-soaking and irreversible degradation of perovskite solar cells. *Energy & Environmental Science*, 11(1):151–165, 2018.
- [129] Juan-Pablo Correa-Baena, Silver-Hamill Turren-Cruz, Wolfgang Tress, Anders Hagfeldt, Clara Aranda, Leyla Shooshtari, Juan Bisquert, and Antonio Guerrero. Changes from bulk to surface recombination mechanisms between pristine and cycled perovskite solar cells. *ACS Energy Letters*, 2(3):681–688, 2017.
- [130] David Kiermasch, Andreas Baumann, Mathias Fischer, Vladimir Dyakonov, and Kristofer Tvingstedt. Revisiting lifetimes from transient electrical characterization of thin film solar cells; a capacitive concern evaluated for silicon, organic and perovskite devices. *Energy & Environmental Science*, 11(3):629–640, 2018.
- [131] Adam Pockett, Giles E Eperon, Timo Peltola, Henry J Snaith, Alison Walker, Laurence M Peter, and Petra J Cameron. Characterization of planar lead halide perovskite solar cells by impedance spectroscopy, open-circuit photovoltage decay, and intensity-modulated photovoltage/photocurrent spectroscopy. *The Journal of Physical Chemistry C*, 119(7):3456–3465, 2015.
- [132] Pietro Caprioglio, Christian M Wolff, Oskar J Sandberg, Ardan Armin, Bernd Rech, Steve Albrecht, Dieter Neher, and Martin Stollerfoht. On the origin of the ideality factor in perovskite solar cells. *Advanced Energy Materials*, 10(27):2000502, 2020.
- [133] Phil Calado, Dan Burkitt, Jizhong Yao, Joel Troughton, Trystan M Watson, Matt J Carnie, Andrew M Telford, Brian C O'Regan, Jenny Nelson, and Piers RF Barnes. Identifying dominant recombination mechanisms in perovskite solar cells by measuring the transient ideality factor. *Physical Review Applied*, 11(4):044005, 2019.
- [134] Osbel Almora, Kyung Taek Cho, Sadig Aghazada, Iwan Zimmermann, Gebhard J Matt, Christoph J Brabec, Mohammad Khaja Nazeeruddin, and Germà Garcia-Belmonte. Discerning recombination mechanisms and ideality factors through impedance analysis of high-efficiency perovskite solar cells. *Nano Energy*, 48:63–72, 2018.
- [135] Nicola Courtier. Interpreting ideality factors for planar perovskite solar cells: Ectypal diode theory for steady-state operation. *Physical Review Applied*, 2020.
- [136] Adriano Sacco. Electrochemical impedance spectroscopy: Fundamentals and application in dye-sensitized solar cells. *Renewable and Sustainable Energy Reviews*, 79:814–829, 2017.
- [137] Sheng S Zhang, Kang Xu, and TR Jow. EIS study on the formation of solid electrolyte interface in Li-ion battery. *Electrochimica acta*, 51(8-9):1636–1640, 2006.
- [138] Jan Philipp Schmidt, Philipp Berg, Michael Schönleber, André Weber, and Ellen Ivers-Tiffée. The distribution of relaxation times as basis for generalized time-domain models for Li-ion batteries. *Journal of Power Sources*, 221:70–77, 2013.
- [139] TE Springer, TA Zawodzinski, MS Wilson, and S Gottesfeld. Characterization of polymer electrolyte fuel cells using AC impedance spectroscopy. *Journal of the Electrochemical Society*, 143(2):587–599, 1996.

- [140] Zhen He and Florian Mansfeld. Exploring the use of electrochemical impedance spectroscopy (EIS) in microbial fuel cell studies. *Energy & Environmental Science*, 2(2):215–219, 2009.
- [141] Florian Mansfeld. Electrochemical impedance spectroscopy (EIS) as a new tool for investigating methods of corrosion protection. *Electrochimica Acta*, 35(10):1533–1544, 1990.
- [142] A Amirudin and D Thieny. Application of electrochemical impedance spectroscopy to study the degradation of polymer-coated metals. *Progress in organic coatings*, 26(1):1–28, 1995.
- [143] RA Armas, Claudio A Gervasi, Alejandro R Di Sarli, SG Real, and Jorge R Vilche. Zinc-rich paints on steels in artificial seawater by electrochemical impedance spectroscopy. *Corrosion*, 48(5):379–383, 1992.
- [144] Allen J Bard, Larry R Faulkner, Johna Leddy, and Cynthia G Zoski. *Electrochemical methods: fundamentals and applications*, volume 2. Wiley New York, 1980.
- [145] J Ross Macdonald and E Barsoukov. Impedance spectroscopy: theory, experiment, and applications. *History*, 1(8):1–13, 2005.
- [146] Andrzej Lasia. Electrochemical impedance spectroscopy and its applications. In *Modern aspects of electrochemistry*, pages 143–248. Springer, 2002.
- [147] Lidia Contreras, Susana Ramos-Terrón, Antonio Riquelme, Pablo P Boix, Jesús Antonio Idígoras, Iván Mora Seró, and Juan A Anta. Impedance analysis of perovskite solar cells: a case study. *Journal of Materials Chemistry A*, 2019.
- [148] Ian D Raistrick. Application of impedance spectroscopy to materials science. *Annual Review of Materials Science*, 16(1):343–370, 1986.
- [149] Digby D Macdonald. Reflections on the history of electrochemical impedance spectroscopy. *Electrochimica Acta*, 51(8-9):1376–1388, 2006.
- [150] Elizabeth von Hauff. Impedance spectroscopy for emerging photovoltaics. *The Journal of Physical Chemistry C*, 2019.
- [151] Monojit Bag, Lawrence A Renna, Ramesh Y Adhikari, Supravat Karak, Feng Liu, Paul M Lahti, Thomas P Russell, Mark T Tuominen, and D Venkataraman. Kinetics of ion transport in perovskite active layers and its implications for active layer stability. *Journal of the American Chemical Society*, 137(40):13130–13137, 2015.
- [152] Anna Todinova, Lidia Contreras-Bernal, Manuel Salado, Shahzada Ahmad, Neftalí Morillo, Jesús Idígoras, and Juan A Anta. Towards a universal approach for the analysis of impedance spectra of perovskite solar cells: equivalent circuits and empirical analysis. *ChemElectroChem*, 4(11):2891–2901, 2017.
- [153] Mark E Orazem and Bernard Tribollet. *Electrochemical impedance spectroscopy*, volume 48. John Wiley & Sons, 2011.
- [154] Elena Guillén, F Javier Ramos, Juan A Anta, and Shahzada Ahmad. Elucidating transport-recombination mechanisms in perovskite solar cells by small-perturbation techniques. *The Journal of Physical Chemistry C*, 118(40):22913–22922, 2014.

- [155] Emilio J Juarez-Perez, Michael Wußler, Francisco Fabregat-Santiago, Kerstin Lakus-Wollny, Eric Mankel, Thomas Mayer, Wolfram Jaegermann, and Ivan Mora-Sero. Role of the selective contacts in the performance of lead halide perovskite solar cells. *The journal of physical chemistry letters*, 5(4):680–685, 2014.
- [156] Zhen Li, Candy C Mercado, Mengjin Yang, Ethan Palay, and Kai Zhu. Electrochemical impedance analysis of perovskite–electrolyte interfaces. *Chemical Communications*, 53(16):2467–2470, 2017.
- [157] Antonio Guerrero, Germá Garcia-Belmonte, Ivan Mora-Sero, Juan Bisquert, Yong Soo Kang, T Jesper Jacobsson, Juan-Pablo Correa-Baena, and Anders Hagfeldt. Properties of contact and bulk impedances in hybrid lead halide perovskite solar cells including inductive loop elements. *The Journal of Physical Chemistry C*, 120(15):8023–8032, 2016.
- [158] Davide Moia, Ilario Gelmetti, Phil Calado, William Fisher, Michael Stringer, Onkar Game, Yinghong Hu, Pablo Docampo, David Lidzey, Emilio Palomares, et al. Ionic-to-electronic current amplification in hybrid perovskite solar cells: ionically gated transistor-interface circuit model explains hysteresis and impedance of mixed conducting devices. *Energy & Environmental Science*, 12(4):1296–1308, 2019.
- [159] Amalie Dualeh, Thomas Moehl, Nicolas Tétreault, Joël Teuscher, Peng Gao, Mohammad Khaja Nazeeruddin, and Michael Grätzel. Impedance spectroscopic analysis of lead iodide perovskite-sensitized solid-state solar cells. *ACS nano*, 8(1):362–373, 2013.
- [160] Hui-Seon Kim, Ivan Mora-Sero, Victoria Gonzalez-Pedro, Francisco Fabregat-Santiago, Emilio J Juarez-Perez, Nam-Gyu Park, and Juan Bisquert. Mechanism of carrier accumulation in perovskite thin-absorber solar cells. *Nature communications*, 4:2242, 2013.
- [161] Elnaz Ghahremanirad, Agustín Bou, Saeed Olyaei, and Juan Bisquert. Inductive loop in the impedance response of perovskite solar cells explained by surface polarization model. *The Journal of Physical Chemistry Letters*, 8(7):1402–1406, 2017.
- [162] Isaac Zarazua, Juan Bisquert, and Germà Garcia-Belmonte. Light-induced space-charge accumulation zone as photovoltaic mechanism in perovskite solar cells. *The journal of physical chemistry letters*, 7(3):525–528, 2016.
- [163] Adam Pockett. *Characterization of Perovskite Solar Cells*. PhD thesis, University of Bath, 2016.
- [164] Arava Zohar, Nir Kedem, Igal Levine, Dorin Zohar, Ayelet Vilan, David Ehre, Gary Hodes, and David Cahen. Impedance spectroscopic indication for solid state electrochemical reaction in (CH₃NH₃) PbI₃ films. *The journal of physical chemistry letters*, 7(1):191–197, 2015.
- [165] Francisco Fabregat-Santiago, Germà Garcia-Belmonte, Ivan Mora-Sero, and Juan Bisquert. Characterization of nanostructured hybrid and organic solar cells by impedance spectroscopy. *Physical Chemistry Chemical Physics*, 13(20):9083–9118, 2011.
- [166] Osbel Almora, Clara Aranda, Elena Mas-Marzá, and Germà Garcia-Belmonte. On mott-schottky analysis interpretation of capacitance measurements in organometal perovskite solar cells. *Applied Physics Letters*, 109(17):173903, 2016.
- [167] Alexander R Pascoe, Noel W Duffy, Andrew D Scully, Fuzhi Huang, and Yi-Bing Cheng. Insights into planar CH₃NH₃PbI₃ perovskite solar cells using impedance spectroscopy. *The Journal of Physical Chemistry C*, 119(9):4444–4453, 2015.

- [168] Juan Bisquert, Luca Bertoluzzi, Ivan Mora-Sero, and Germà Garcia-Belmonte. Theory of impedance and capacitance spectroscopy of solar cells with dielectric relaxation, drift-diffusion transport, and recombination. *The Journal of Physical Chemistry C*, 118(33):18983–18991, 2014.
- [169] Germà Garcia-Belmonte, Pablo P Boix, Juan Bisquert, Michele Sessolo, and Henk J Bolink. Simultaneous determination of carrier lifetime and electron density-of-states in P3HT: PCBM organic solar cells under illumination by impedance spectroscopy. *Solar Energy Materials and Solar Cells*, 94(2):366–375, 2010.
- [170] Hongxia Wang, Antonio Guerrero, Agustín Bou, Abdullah M Al-Mayouf, and Juan Bisquert. Kinetic and material properties of interfaces governing slow response and long timescale phenomena in perovskite solar cells. *Energy & Environmental Science*, 12(7):2054–2079, 2019.
- [171] Alexander Kovalenko, Jan Pospisil, Oldrich Zmeskal, Jozef Krajcovic, and Martin Weiter. Ionic origin of a negative capacitance in lead halide perovskites. *physica status solidi (RRL)–Rapid Research Letters*, 11(3):1600418, 2017.
- [172] Qidong Tai, Peng You, Hongqian Sang, Zhike Liu, Chenglong Hu, Helen LW Chan, and Feng Yan. Efficient and stable perovskite solar cells prepared in ambient air irrespective of the humidity. *Nature communications*, 7:11105, 2016.
- [173] Francisco Fabregat-Santiago, Michael Kulbak, Arava Zohar, Marta Vallés-Pelarda, Gary Hodes, David Cahen, and Iván Mora-Seró. Deleterious effect of negative capacitance on the performance of halide perovskite solar cells. *ACS Energy Letters*, 2(9):2007–2013, 2017.
- [174] Mohd Taukeer Khan, Peng Huang, Abdullah Almohammed, Samrana Kazim, and Shahzada Ahmad. Mechanistic origin and unlocking of negative capacitance in perovskites solar cells. *Iscience*, 24(2):102024, 2021.
- [175] Firouzeh Ebadi, Nima Taghavinia, Raheleh Mohammadpour, Anders Hagfeldt, and Wolfgang Tress. Origin of apparent light-enhanced and negative capacitance in perovskite solar cells. *Nature communications*, 10(1):1–9, 2019.
- [176] Juan Bisquert, Antonio Guerrero, and Cedric Gonzales. Theory of hysteresis in halide perovskites by integration of the equivalent circuit. *ACS Physical Chemistry Au*, 2021.
- [177] Emilio J Juarez-Perez, Rafael S Sanchez, Laura Badia, Germà Garcia-Belmonte, Yong Soo Kang, Ivan Mora-Sero, and Juan Bisquert. Photoinduced giant dielectric constant in lead halide perovskite solar cells. *The journal of physical chemistry letters*, 5(13):2390–2394, 2014.
- [178] Darryl P Almond and Chris R Bowen. An explanation of the photoinduced giant dielectric constant of lead halide perovskite solar cells. *The journal of physical chemistry letters*, 6(9):1736–1740, 2015.
- [179] Osbel Almora, Clara Aranda, and Germà Garcia-Belmonte. Do capacitance measurements reveal light-induced bulk dielectric changes in photovoltaic perovskites? *The Journal of Physical Chemistry C*, 122(25):13450–13454, 2017.
- [180] Kenjiro Miyano, Neeti Tripathi, Masatoshi Yanagida, and Yasuhiro Shirai. Lead halide perovskite photovoltaic as a model p–i–n diode. *Accounts of chemical research*, 49(2):303–310, 2016.

- [181] Mehran Samiee, Siva Konduri, Balaji Ganapathy, Ranjith Kottokkaran, Hisham A Abbas, Andrew Kitahara, Pranav Joshi, Liang Zhang, Max Noack, and Vikram Dalal. Defect density and dielectric constant in perovskite solar cells. *Applied Physics Letters*, 105(15):153502, 2014.
- [182] Hsin-Sheng Duan, Huanping Zhou, Qi Chen, Pengyu Sun, Song Luo, Tze-Bin Song, Brion Bob, and Yang Yang. The identification and characterization of defect states in hybrid organic–inorganic perovskite photovoltaics. *Physical chemistry chemical physics*, 17(1):112–116, 2015.
- [183] Martin T Neukom, Andreas Schiller, Simon Züfle, Evelyne Knapp, Jorge Ávila, Daniel Pérez-del Rey, Chris Dreessen, Kassio PS Zanoni, Michele Sessolo, Henk J Bolink, et al. Consistent device simulation model describing perovskite solar cells in steady-state, transient, and frequency domain. *ACS Applied Materials & Interfaces*, 11(26):23320–23328, 2019.
- [184] Lidia Contreras, Jesús Idígoras, Anna Todinova, Manuel Salado, Samrana Kazim, Shahzada Ahmad, and Juan A Anta. Specific cation interactions as the cause of slow dynamics and hysteresis in dye and perovskite solar cells: a small-perturbation study. *Physical Chemistry Chemical Physics*, 18(45):31033–31042, 2016.
- [185] Rodrigo García-Rodríguez, Dominic Ferdani, Samuel Pering, Peter J Baker, and Petra J Cameron. Influence of bromide content on iodide migration in inverted MAPb (I 1- x Br x) 3 perovskite solar cells. *Journal of Materials Chemistry A*, 7(39):22604–22614, 2019.
- [186] Agustin O Alvarez, Ramon Arcas, Clara A Aranda, Loengrid Bethencourt, Elena Mas-Marza, Michael Saliba, and Francisco Fabregat-Santiago. Negative capacitance and inverted hysteresis: Matching features in perovskite solar cells. *arXiv preprint arXiv:2005.11828*, 2020.
- [187] Dino Klotz. Negative capacitance or inductive loop?—a general assessment of a common low frequency impedance feature. *Electrochemistry Communications*, 98:58–62, 2019.
- [188] FLUXiM AG: Switzerland. Semiconducting Thin Film Optics Simulator (SETFOS). <https://www.fluxim.com/>. Accessed: 05-12-2021.
- [189] COMSOL Multiphysics software. <https://uk.comsol.com/>. Accessed: 06-12-2021.
- [190] MATLAB with COMSOL Multiphysics via LiveLink for MATLAB. https://uk.mathworks.com/products/connections/product_detail/comsol-multiphysics.html. Accessed: 06-12-2021.
- [191] Philip Calado, Piers RF Barnes, Ilario Gelmetti, Mohammed Azzouzi, and Benjamin Hilton. Drift-diffusion. <https://doi.org/10.5281/zenodo.3670155>, 2017.
- [192] Philip Calado, Ilario Gelmetti, Benjamin Hilton, Mohammed Azzouzi, Jenny Nelson, and Piers RF Barnes. Driftdiffusion: an open source code for simulating ordered semiconductor devices with mixed ionic-electronic conducting materials in one dimension. *Journal of Computational Electronics*, pages 1–32, 2022.
- [193] Sandheep Ravishankar, Osbel Almora, Carlos Echeverría-Arrondo, Elnaz Ghahremanirad, Clara Aranda, Antonio Guerrero, Francisco Fabregat-Santiago, Arie Zaban, Germà Garcia-Belmonte, and Juan Bisquert. Surface polarization model for the dynamic hysteresis of perovskite solar cells. *The Journal of Physical Chemistry Letters*, 8(5):915–921, 2017.

- [194] Miguel Anaya, Wei Zhang, Bruno Clasen Hames, Yuelong Li, Francisco Fabregat-Santiago, Mauricio E Calvo, Henry J Snaith, Hernán Míguez, and Iván Mora-Seró. Electron injection and scaffold effects in perovskite solar cells. *Journal of Materials Chemistry C*, 5(3):634–644, 2017.
- [195] Stefan AL Weber, Ilka M Hermes, Silver-Hamill Turren-Cruz, Christopher Gort, Victor W Bergmann, Laurent Gilson, Anders Hagfeldt, Michael Graetzel, Wolfgang Tress, and Rüdiger Berger. How the formation of interfacial charge causes hysteresis in perovskite solar cells. *Energy & Environmental Science*, 11(9):2404–2413, 2018.
- [196] Ilka M Hermes, Yi Hou, Victor W Bergmann, Christoph J Brabec, and Stefan AL Weber. The interplay of contact layers: How the electron transport layer influences interfacial recombination and hole extraction in perovskite solar cells. *The journal of physical chemistry letters*, 9(21):6249–6256, 2018.
- [197] Molang Cai, Nobuyuki Ishida, Xing Li, Xudong Yang, Takeshi Noda, Yongzhen Wu, Fengxian Xie, Hiroyoshi Naito, Daisuke Fujita, and Liyuan Han. Control of electrical potential distribution for high-performance perovskite solar cells. *Joule*, 2(2):296–306, 2018.
- [198] Joseph W Jerome. *Analysis of charge transport: a mathematical study of semiconductor devices*. Springer Science & Business Media, 2012.
- [199] Siegfried Selberherr. *Analysis and simulation of semiconductor devices*. Springer Science & Business Media, 2012.
- [200] RS Eisenberg. Computing the field in proteins and channels. *The Journal of membrane biology*, 150(1):1–25, 1996.
- [201] Giles Richardson. A multiscale approach to modelling electrochemical processes occurring across the cell membrane with application to transmission of action potentials. *Mathematical medicine and biology: a journal of the IMA*, 26(3):201–224, 2009.
- [202] Brian E Conway, John O’M Bockris, and Ernest Yeager. *Thermodynamic and transport properties of aqueous and molten electrolytes*. Plenum Press, New York, NY, USA, 1983.
- [203] Giles Richardson, Guy Denuault, and CP Please. Multiscale modelling and analysis of lithium-ion battery charge and discharge. *Journal of Engineering Mathematics*, 72(1):41–72, 2012.
- [204] Bartłomiej Matejczyk, J-F Pietschmann, M-T WOLFRAM, and Giles Richardson. Asymptotic models for transport in large aspect ratio nanopores. *European Journal of Applied Mathematics*, pages 1–28, 2018.
- [205] Brian J Kirby. *Micro-and nanoscale fluid mechanics: transport in microfluidic devices*. Cambridge university press, 2010.
- [206] Nicola E Courtier, James M Cave, Alison B Walker, Giles Richardson, and Jamie M Foster. Ion-monger: a free and fast planar perovskite solar cell simulator with coupled ion vacancy and charge carrier dynamics. *Journal of Computational Electronics*, 18(4):1435–1449, 2019.
- [207] Fluxim AG, Large Area Organic Semiconductor Simulation (LAOSS), 2020. <https://www.fluxim.com/laoss>. Accessed: 07-06-2022.

- [208] COMSOL Multiphysics Software Understand, Predict, and Optimize Physics-Based Designs and Processes with COMSOL Multiphysics. <https://www.comsol.com/comsol-multiphysics>. Accessed: 07-06-2022.
- [209] Yuchuan Shao, Yanjun Fang, Tao Li, Qi Wang, Qingfeng Dong, Yehao Deng, Yongbo Yuan, Haotong Wei, Meiyu Wang, Alexei Gruverman, et al. Grain boundary dominated ion migration in polycrystalline organic–inorganic halide perovskite films. *Energy & Environmental Science*, 9(5):1752–1759, 2016.
- [210] Nicola E Courtier. *Modelling ion migration and charge carrier transport in planar perovskite solar cells*. PhD thesis, University of Southampton, 2019.
- [211] Yuichi Kato, Luis K Ono, Michael V Lee, Shenghao Wang, Sonia R Raga, and Yabing Qi. Silver iodide formation in methyl ammonium lead iodide perovskite solar cells with silver top electrodes. *Advanced Materials Interfaces*, 2(13):1500195, 2015.
- [212] Sharada Govinda, Bhushan P Kore, Menno Bokdam, Pratibha Mahale, Abhinav Kumar, Somnath Pal, Biswajit Bhattacharyya, Jonathan Lahnsteiner, Georg Kresse, Cesare Franchini, et al. Behavior of methylammonium dipoles in MAPbX₃ (X= Br and I). *The journal of physical chemistry letters*, 8(17):4113–4121, 2017.
- [213] Samuel D Stranks, Victor M Burlakov, Tomas Leijtens, James M Ball, Alain Goriely, and Henry J Snaith. Recombination kinetics in organic-inorganic perovskites: excitons, free charge, and subgap states. *Physical Review Applied*, 2(3):034007, 2014.
- [214] Jamie M Foster, Henry J Snaith, Tomas Leijtens, and Giles Richardson. A model for the operation of perovskite based hybrid solar cells: formulation, analysis, and comparison to experiment. *SIAM Journal on Applied Mathematics*, 74(6):1935–1966, 2014.
- [215] Giles Richardson and Alison Walker. Drift diffusion modelling of charge transport in photovoltaic devices. In *Unconventional Thin Film Photovoltaics*, pages 297–331. Royal Society of Chemistry, 2016.
- [216] Lawrence F Shampine and Mark W Reichelt. The MATLAB ODE suite. *SIAM journal on scientific computing*, 18(1):1–22, 1997.
- [217] Lawrence F Shampine, Mark W Reichelt, and Jacek A Kierzenka. Solving index-1 DAEs in MATLAB and Simulink. *SIAM review*, 41(3):538–552, 1999.
- [218] Gaurav Sharma and Jos Martin. Matlab®: a language for parallel computing. *International Journal of Parallel Programming*, 37(1):3–36, 2009.
- [219] Philipp Löper, Michael Stuckelberger, Bjoern Niesen, Jérémie Werner, Miha Filipič, Soo-Jin Moon, Jun-Ho Yum, Marko Topič, S Wolf De, and Christophe Ballif. Complex refractive index spectra of CH₃NH₃PbI₃ perovskite thin films determined by spectroscopic ellipsometry and spectrophotometry. *The journal of physical chemistry letters*, 6(1):66–71, 2015.
- [220] Federico Brivio, Keith T Butler, Aron Walsh, and Mark Van Schilfgaarde. Relativistic quasiparticle self-consistent electronic structure of hybrid halide perovskite photovoltaic absorbers. *Physical Review B*, 89(15):155204, 2014.

- [221] Philip Schulz, Eran Edri, Saar Kirmayer, Gary Hodes, David Cahen, and Antoine Kahn. Interface energetics in organo-metal halide perovskite-based photovoltaic cells. *Energy & Environmental Science*, 7(4):1377–1381, 2014.
- [222] Constantinos C Stoumpos, Christos D Malliakas, and Mercouri G Kanatzidis. Semiconducting tin and lead iodide perovskites with organic cations: phase transitions, high mobilities, and near-infrared photoluminescent properties. *Inorganic chemistry*, 52(15):9019–9038, 2013.
- [223] Jun-ichi Fujisawa, Takumi Eda, and Minoru Hanaya. Comparative study of conduction-band and valence-band edges of TiO₂, SrTiO₃, and BaTiO₃ by ionization potential measurements. *Chemical Physics Letters*, 685:23–26, 2017.
- [224] Gamry Instruments. Quick Check of EIS System Performance. <https://www.gamry.com/application-notes/EIS/quick-check-of-eis-system-performance>. Accessed: 13-06-2022.
- [225] Jean-Baptiste Jorcin, Mark E Orazem, Nadine Pébère, and Bernard Tribollet. CPE analysis by local electrochemical impedance spectroscopy. *Electrochimica Acta*, 51(8-9):1473–1479, 2006.
- [226] Sumayya M Abdulrahim, Zubair Ahmad, Jolly Bahadra, and Noora J Al-Thani. Electrochemical impedance spectroscopy analysis of hole transporting material free mesoporous and planar perovskite solar cells. *Nanomaterials*, 10(9):1635, 2020.
- [227] Evelyne Knapp, Mattia Battaglia, Thilo Stadelmann, Sandra Jenatsch, and Beat Ruhstaller. Xgboost trained on synthetic data to extract material parameters of organic semiconductors. In *8th Swiss Conference on Data Science, Lucerne, Switzerland, 9 June 2021*. IEEE, 2021.
- [228] Sandheep Ravishankar, Clara Aranda, Sandy Sanchez, Juan Bisquert, Michael Saliba, and Germà Garcia-Belmonte. Perovskite solar cell modeling using light and voltage modulated techniques. *The Journal of Physical Chemistry C*, 2019.
- [229] Sandheep Ravishankar, Marisé García-Batlle, Juan Bisquert, Germà Garcia-Belmonte, Jann Odobina, and Carl-Albrecht Schiller. Removing instability-caused low-frequency features in small perturbation spectra of perovskite solar cells. *The Journal of Physical Chemistry C*, 124(29):15793–15799, 2020.
- [230] Meiyang Liang, Adnan Ali, Abdelhak Belaidi, Mohammad Istiaque Hossain, Oskar Ronan, Clive Downing, Nouar Tabet, Stefano Sanvito, Fedwa EI-Mellouhi, and Valeria Nicolosi. Improving stability of organometallic-halide perovskite solar cells using exfoliation two-dimensional molybdenum chalcogenides. *npj 2D Materials and Applications*, 4(1):1–8, 2020.
- [231] Hsinhan Tsai, Wanyi Nie, Jean-Christophe Blancon, Constantinos C Stoumpos, Reza Asadpour, Boris Harutyunyan, Amanda J Neukirch, Rafael Verduzco, Jared J Crochet, Sergei Tretiak, et al. High-efficiency two-dimensional Ruddlesden–Popper perovskite solar cells. *Nature*, 536(7616):312–316, 2016.
- [232] So-Min Yoo, Seog Joon Yoon, Juan A Anta, Hyo Joong Lee, Pablo P Boix, and Ivan Mora-Sero. An equivalent circuit for perovskite solar cell bridging sensitized to thin film architectures. *Joule*, 3(10):2535–2549, 2019.

- [233] Alessandro Senocrate, Igor Moudrakovski, Gee Yeong Kim, Tae-Youl Yang, Giuliano Gregori, Michael Grätzel, and Joachim Maier. The nature of ion conduction in methylammonium lead iodide: a multimethod approach. *Angewandte Chemie International Edition*, 56(27):7755–7759, 2017.
- [234] Martin Thomas Neukom, Simon Züfle, Evelyne Knapp, Mohammed Makha, Roland Hany, and Beat Ruhstaller. Why perovskite solar cells with high efficiency show small IV-curve hysteresis. *Solar Energy Materials and Solar Cells*, 169:159–166, 2017.
- [235] Philip Calado and Piers RF Barnes. Ionic screening in perovskite p–n homojunctions. *Nature Energy*, 6(6):589–591, 2021.
- [236] Simon EJ O’Kane, Giles Richardson, Adam Pockett, Ralf G Niemann, James M Cave, Nobuya Sakai, Giles E Eperon, Henry J Snaith, Jamie M Foster, Petra J Cameron, et al. Measurement and modelling of dark current decay transients in perovskite solar cells. *Journal of Materials Chemistry C*, 5(2):452–462, 2017.
- [237] Luca Bertoluzzi, Caleb C Boyd, Nicholas Rolston, Jixian Xu, Rohit Prasanna, Brian C O’Regan, and Michael D McGehee. Mobile ion concentration measurement and open-access band diagram simulation platform for halide perovskite solar cells. *Joule*, 4(1):109–127, 2020.
- [238] Victoria Gonzalez-Pedro, Emilio J Juarez-Perez, Waode-Sukmawati Arsyad, Eva M Barea, Francisco Fabregat-Santiago, Ivan Mora-Sero, and Juan Bisquert. General working principles of CH₃NH₃PbX₃ perovskite solar cells. *Nano letters*, 14(2):888–893, 2014.
- [239] Lidia Contreras-Bernal, Manuel Salado, Anna Todinova, Laura Calio, Shahzada Ahmad, Jesús Idígoras, and Juan A Anta. Origin and whereabouts of recombination in perovskite solar cells. *The Journal of Physical Chemistry C*, 121(18):9705–9713, 2017.
- [240] Isaac Zarazua, Guifang Han, Pablo P Boix, Subodh Mhaisalkar, Francisco Fabregat-Santiago, Ivan Mora-Seró, Juan Bisquert, and Germà Garcia-Belmonte. Surface recombination and collection efficiency in perovskite solar cells from impedance analysis. *The journal of physical chemistry letters*, 7(24):5105–5113, 2016.
- [241] Eugene F Douglass Jr, Peter F Driscoll, Deli Liu, Nancy A Burnham, Christopher R Lambert, and W Grant McGimpsey. Effect of electrode roughness on the capacitive behavior of self-assembled monolayers. *Analytical chemistry*, 80(20):7670–7677, 2008.
- [242] Daniele Meggiolaro, Edoardo Mosconi, and Filippo De Angelis. Formation of surface defects dominates ion migration in lead-halide perovskites. *ACS Energy Letters*, 4(3):779–785, 2019.